

*Characterization of hydroxypropyl methylcellulose acetate succinate
solid dispersions in the solid-state and during dissolution*

A DISSERTATION
SUBMITTED TO THE FACULTY OF
UNIVERSITY OF MINNESOTA
BY

Ralm Gerick Ricarte

IN PARTIAL FULFILLMENT OF THE REQUIREMENTS
FOR THE DEGREE OF
DOCTOR OF PHILOSOPHY

Timothy P. Lodge
Marc A. Hillmyer

December 2016

© Ralm Gerick Ricarte 2016
All Rights Reserved

Acknowledgements

Graduate school, to be quite honest, is a slog. Regardless, the decision to pursue a Ph.D. in chemical engineering is one of the best choices I ever made in my life. I must thank many folks for helping me cultivate my scientific aptitude and compassion over the past five years.

I owe an endless amount of gratitude to my advisors Profs. Marc Hillmyer and Timothy Lodge for molding me into the scientist that I am today. These two were never easy on me. In fact, I vividly remember their disbelieving and unimpressed responses to all the data I presented during my post-first-summer-in-the-lab meeting with them. Their strict approach, however, was born neither out of malice nor condescension. Rather, the aim of their constructive criticism was to teach me to be objective and to carefully consider every hypothesis until proven otherwise. Like Tim told me during one of our meetings, “A good scientist is always skeptical.” I also learned a lot from each advisor individually. From Marc, I absorbed his enthusiasm for exploring cutting-edge polymer science and undertaking high risk/high reward research endeavors. He also taught me how to manage a large, and sometimes cranky, group of people. From Tim, I internalized his methodical approach to science and willingness to engage in critical, but respectful, discussions with his colleagues and peers. I also want to thank Tim for helping me during my struggles with my qualification exams. Those one-on-one coaching sessions were stressful, but your patience with me was instrumental in rebuilding my confidence. Although I will soon graduate from the University of Minnesota, I suspect I will still turn to Marc and Tim for advice in the coming years (I hope they’re cool with that).

In addition to my advisors, my interactions with the other faculty members of the Polymer Group also fostered my growth as a scientist. I want to express much gratitude to Prof. Frank Bates for being an excellent role model and pillar of support. I also want to

thank Profs. Theresa Reineke, David Morse, Chris Macosko, Mahesh Mahanthappa, and Christopher Ellison.

At the U, I have worked with several brilliant and talented colleagues. During my first two years, I worked closely with Ligeng Yin and Sara Arvidson; they were patient mentors who always made time to answer my questions and engage in scientific discussions. During my last three years, I directly collaborated with Lindsay Johnson, Jeff Ting, and Ziang Li. These three are not only excellent scientists, but also wonderful human beings who were always willing to help whenever I needed assistance. I also want to acknowledge the scores of other scientists who helped me along the way, including (in no particular order) Peter Schmidt, Aakriti Kharel, Ingrid Haugan, Sujay Chopade, Prof. Jennifer Laaser, Dr. Debbie Schneiderman, Dr. James Gallagher, Dr. Morgan Schulze, Marie Vanderlaan, Dr. Paula Delgado, Dr. Henry Martinez, Dr. Thodoris Vasilakopoulos, Jacob Brutman, Guilhem De Hoe, Stacey Saba, Annabelle Watts, Dr. Madalyn Radlauer, Dr. Thomas Vidil, Dr. Soonyong So, Dr. Yuewen Xu, Dr. Yuanyan Gu, Dr. Matthew Irwin, Dr. Ameara Mansour, Dr. John McAllister, Dr. Lucas McIntosh, Dr. Chris Thurber, Dr. Can Zhou, Megan Sonnenberg, Dr. Megan Hoarfrost, Ron Lewis, Dr. Maryam Khaleel, and Dr. Joshua Speros.

Almost all the work in the dissertation was performed at user facilities (both on and off campus) that were maintained by hard-working and friendly staff. Specifically, I want to thank Dr. Chris Frethem, Dr. Jason Myers, Dr. Wei Zhang, Dr. Robert Hafner, Dr. Fang Zhou, Dr. Hanseung Lee, Dr. David Giles, Dr. Seema Thakral, Dr. Nicholas Seaton, Dr. Yimin Mao, and Dr. Paul Butler.

Several benefactors funded the studies discussed in this dissertation (and enabled my lavish grad student lifestyle). These works were sponsored by The Dow Chemical Company (Dow) through Agreement 224249AT with the University of Minnesota. I thank

Dr. Jodi Mecca, Dr. Timothy Young, Dr. Steven J. Guillaudeu, Dr. Robert L. Schmitt, and Dr. William Porter for their feedback on my work. I was additionally supported by the National Science Foundation Graduate Research Fellowship under Grant No. 00039202 and the Robert V. Mattern Fellowship.

Along with my thesis work, I invested a significant portion of my grad school career co-founding and running Science For All, a non-profit outreach program dedicated to teaching science to the urban Twin Cities community. You can learn more about the program here: <https://sfa.cems.umn.edu/>. Specifically, I want to thank Laura Seifert for advising me on how to run an outreach program and connecting me to a variety of educators in the Twin Cities area, my co-founders Rebecca Mackenzie, Nancy Trejo, Joseph DeWilde, Debbie Schneiderman, Lafe Purvis, and Bryan Baxter, and our partner teachers Heidi Smith (KIPP Northstar Academy) and Joe Kaliszewski (American Indian Magnet School). Of course, I must thank the students I mentored: Ashley, Khaylah, Le'Amor, Niswey, Thai, and Chong.

I also must give a shout-out to all the friends I have made during grad school: Dr. Tim Gillard, Colleen Crook, Melissa Johnson, Kevin Pustulka, Lawrence Stern, Sadie Johnson, Dayne Plemmons, Koustav "K.G." Ganguly, Scott White, Frankie Pelaez, Grayson Jackson, Prof. Rob Hickey, and Danielle Hickey. Ph.D. life is tough, but y'all made it fun.

Finally, I thank my family for supporting me over the past five years. Although I didn't come home as often as you wanted, I love you very much.

Dedication

To those who seek knowledge for knowledge's sake, regardless of race, color, age, gender, orientation, or creed.

Abstract

The use of a solid dispersion (SD), a mixture of an active pharmaceutical ingredient and a polymer excipient, may significantly enhance the aqueous solubility and oral bioavailability of a hydrophobic drug, but the role of the polymer is poorly understood. For example, hydroxypropyl methylcellulose acetate succinate (HPMCAS) is considered to be one of the best performing excipients, but its effectiveness is not universal to all drugs. Elucidation of the critical properties of HPMCAS is inhibited due to the poor spatial resolution and sensitivity of the techniques traditional used to characterize SDs. To address this shortcoming, the studies in this dissertation focus on the development of novel analytical methods for characterizing SDs in both the solid-state and during dissolution. First, transmission electron microscopy (TEM) and electron diffraction evaluates drug crystallinity in SDs with a spatial resolution and sensitivity superior to the traditional methods. Second, energy-dispersive X-ray spectroscopy probes the spatial distribution of drug and polymer in a SD particle. Third, electron energy-loss spectroscopy quantitatively measures the concentration of drug and polymer in a SD with both high concentration and spatial resolution. Fourth, cryogenic TEM and small-angle X-ray scattering reveal a direct correlation between SD dissolution and nanostructure evolution in solution. Finally, the utility of these novel tools and possible future research directions are discussed.

Table of Contents

Acknowledgements	i
Dedication	iv
Abstract.....	v
List of Tables	x
List of Figures.....	xi
Chapter 1: Introduction	1
<i>1.1 Motivation.....</i>	<i>1</i>
<i>1.2 Background.....</i>	<i>6</i>
1.2.1 Hydroxypropyl methylcellulose acetate succinate (HPMCAS)	6
1.2.2 Solid-state characterization of solid dispersions.....	9
1.2.2.1 Wide-angle X-ray Scattering	11
1.2.2.2 Polarized optical microscopy	13
1.2.2.3 Thermal analysis	15
1.2.2.4 Dielectric relaxation spectroscopy	20
1.2.2.5 Solid-state nuclear magnetic resonance spectroscopy	21
1.2.2.6 Atomic force microscopy.....	22
1.2.3 Solution characterization of solid dispersions	24
1.2.3.1 Dissolution of drug and polymer from SD particles.....	25
1.2.3.2 Phase behavior of SDs during dissolution	26
<i>1.3 Unresolved questions and dissertation outline.....</i>	<i>28</i>
Chapter 2: Materials and methods.....	31
<i>2.1 Introduction.....</i>	<i>31</i>
<i>2.2 Hydroxypropyl methylcellulose acetate succinate samples.....</i>	<i>31</i>
<i>2.3 Preparation of solid dispersions.....</i>	<i>32</i>
<i>2.4 Wide-angle X-ray scattering.....</i>	<i>33</i>
<i>2.5 Modulated differential scanning calorimetry.....</i>	<i>33</i>
<i>2.6 Transmission electron microscopy (TEM).....</i>	<i>34</i>
2.6.1 Basic TEM theory	34
2.6.2 TEM imaging and electron diffraction	35

2.6.5 Scanning TEM (STEM) and high-angle annular dark-field (HAADF) imaging	38
2.6.6 Energy dispersive X-ray spectroscopy	39
2.6.7 Electron energy-loss spectroscopy	41
2.6.8 Cryogenic transmission electron microscopy (cryo-TEM)	44
2.6.9 TEM sample preparation and instrumentation	45
2.7 Microcentrifuge dissolution and solubility assays	47
2.8 Light and X-ray scattering of polymer solutions and dissolution media	48
2.8.1 Basic scattering theory	48
2.8.2 Static light scattering (SLS)	49
2.8.3 Dynamic light scattering (DLS)	51
2.8.4 Light scattering sample preparation and instrumentation	53
2.8.5 Small-angle X-ray scattering sample preparation and instrumentation	54
Chapter 3: Detection of pharmaceutical drug crystallites in solid dispersions by transmission electron microscopy[†]	56
3.1 Introduction	56
3.2 Experimental details	57
3.2.1 Materials	57
3.2.2 Preparation of solid dispersions by spray drying	57
3.2.3 Wide-angle X-ray scattering (WAXS)	58
3.2.4 Modulated differential scanning calorimetry (MDSC)	58
3.2.5 Transmission electron microscopy (TEM)	59
3.2.6 In situ WAXS	59
3.2.7 Growth of GF crystals from a 50 wt% GF solid dispersion on a TEM grid	60
3.3 Results	60
3.3.1 Wide-angle X-ray scattering of solid dispersions	60
3.3.2 MDSC of solid dispersions	62
3.3.3 TEM of spray dried GF	65
3.3.4 TEM analysis of solid dispersions	68
3.4 Discussion	75
3.5 Conclusion	77
Chapter 4: Energy-dispersive X-ray spectroscopy of solid dispersions	78
4.1 Introduction	78
4.2 Experimental details	78
4.2.1 Materials	78
4.2.2 Preparation of solid dispersions by spray drying	79
4.2.3 STEM electron beam trajectory simulations	79
4.2.4 STEM EDS sample preparation and instrumentation	79
4.3 Results and discussion	80
4.3.1 Simulations of STEM electron beam trajectory	80
4.3.2 Elemental spectrum maps of griseofulvin and HPMCAS	81

4.3.3 Quantification of EDS spectra	85
4.4 Conclusions.....	89
Chapter 5: Nanoscale concentration quantification of pharmaceutical actives in amorphous polymer matrices by electron energy-loss spectroscopy[†]	90
5.1 Introduction.....	90
5.2 Experimental details	91
5.2.1 Materials	91
5.2.2 Preparation of SDs by spin coating.....	91
5.2.3 High-angle annular dark-field scanning transmission electron microscopy and electron energy-loss spectroscopy	91
5.2.4 Quantification of drug concentration in spin-coated SDs from EELS spectra	92
5.2.5 Annealing of 25 wt% phenytoin spin-coated SD TEM sample.....	94
5.3 Results and discussion	94
5.3.1 EELS of HPMCAS and phenytoin	94
5.3.2 Quantification of phenytoin concentration for spin-coated HPMCAS and phenytoin.....	96
5.3.3 EELS of spin-coated SDs with varying phenytoin concentration	97
5.3.4 Quantification of phenytoin concentration in spin-coated SDs	98
5.3.5 EELS of an annealed 25 wt% phenytoin spin-coated SD.....	103
5.4 Conclusions.....	108
Chapter 6: Direct observation of nanostructures during dissolution of polymer/drug particles.....	110
6.1 Introduction.....	110
6.2 Experimental Section	111
6.2.1 Materials	111
6.2.2 Preparation of SDs by spray drying.....	112
6.2.3 Dynamic light scattering (DLS).....	112
6.2.4 Static light scattering (SLS).....	112
6.2.5 Microcentrifuge dissolution and solubility assays.....	113
6.2.6 Cryogenic transmission electron microscopy (Cryo-TEM).....	114
6.2.7 Small-angle X-ray scattering (SAXS)	115
6.3 Results	115
6.3.1 Characterization of HPMCAS solutions.....	115
6.3.2 Dissolution of phenytoin and HPMCAS SDs.....	123
6.3.3 Dissolution of probucol and HPMCAS SDs.....	138
6.4 Discussion.....	148
6.5 Conclusions.....	150
Chapter 7: Conclusion.....	151
7.1 Project summary.....	151

7.2 Future research directions.....	153
Bibliography	157
Appendix A: Supporting information for detection of pharmaceutical drug crystallites in solid dispersions by transmission electron microscopy[†]	167
<i>A.1 GF/HPMCAS solid dispersion particle morphology.....</i>	<i>167</i>
<i>A.2 Indexing of GF electron diffraction patterns.....</i>	<i>168</i>
<i>A.3 Beam Sensitivity of GF crystals.....</i>	<i>170</i>
<i>A.4 Fourier transform infrared (FTIR) spectroscopy of solid dispersions.....</i>	<i>171</i>
<i>A.5. References.....</i>	<i>172</i>
Appendix B: Supporting information for energy-dispersive X-ray spectroscopy of solid dispersions	173
<i>B.1 Modulated differential scanning calorimetry of griseofulvin:hydroxypropyl methylcellulose acetate succinate solid dispersions.....</i>	<i>173</i>
Appendix C: Supporting information for nanoscale concentration quantification of pharmaceutical actives in amorphous polymer matrices by electron energy-loss spectroscopy[†]	175
<i>C.1 Cross-section and mean free path length of inelastic scattering for various species</i>	<i>175</i>
<i>C.2 Conventional TEM EELS characterization of phenytoin:HPMCAS spin-coated solid dispersions</i>	<i>176</i>
<i>C.3. Subtraction of amorphous C film contribution of EELS spectra</i>	<i>179</i>
<i>C.4 Modulated differential scanning calorimetry of a 25 wt% phenytoin spray-dried dispersion.....</i>	<i>182</i>
<i>C.5. References</i>	<i>183</i>
Appendix D: Supporting Information for direct observation of nanostructures during dissolution of polymer/drug particles	184
<i>D.1 Comparison of physical properties for various active pharmaceutical ingredients</i>	<i>184</i>
<i>D.2. Solid-state characterization of phenytoin and probucol solid dispersions.....</i>	<i>186</i>
<i>D.3. PHY and PRB SDs dissolved in HPMCAS solutions</i>	<i>189</i>
<i>D.4. Dissolution of poly(N-isopropylacrylamide-co-N,N-dimethylacrylamide) SDs .</i>	<i>192</i>
<i>D.5. Small-angle neutron scattering of HPMCAS solutions.....</i>	<i>193</i>
<i>D.6. References</i>	<i>194</i>

List of Tables

Table 2.1. Grade, molar mass, and acetate and succinate composition of AFFINISOL™ HPMCAS batches used for dissertation studies.....	32
Table 2.2. Comparison of λ and q for light and X-ray scattering.	49
Table 4.1. Full-width half-maximum (FWHM) of incident electrons at various sample depths.	81
Table 4.2. Comparison of theoretical and experimental EDS spectrum peak intensities for GF.	87
Table 4.3. Measured peak ratio intensities for spray dried GF particles with varying thickness.....	88
Table 4.4. Measured peak ratio intensities for 300 nm thick GF SD particle with varying drug loading.	88
Table 6.1. Fitted parameters from double exponential fit of second-order autocorrelation functions for 9 mg/mL HPMCAS in PBS at 37°C.	119
Table 6.2. Fitted parameters from triaxial ellipsoid form factor model fit of 10 wt% PHY SD dissolution media SAXS patterns.	131
Table 6.3. Fitted parameters from polydisperse sphere form factor model fit of 10 wt% PHY SD dissolution media SAXS patterns.	134
Table 6.4. Fitted parameters from polydisperse sphere form factor model fit of 10 wt% PRB SD dissolution media SAXS patterns.....	143
Table 6.5. Fitted parameters from Ostwald ripening model fit of 10 wt% PRB SD dissolution media nanoparticles.	143
Table C.1. Z_{eff} , molecular weight, and ξ for various molecules.	175
Table D.1. Crystalline and expected glassy aqueous solubility at 37°C for phenytoin and probucol.	185

List of Figures

Figure 1.1. (A) Chemical structures of hydroxypropyl methylcellulose acetate succinate (HPMCAS), phenytoin, and probucol.	5
Scheme 1.1. Synthesis of (A) hydroxypropyl methylcellulose and (B) hydroxypropyl methylcellulose acetate succinate.	7
Figure 1.2. Wide-angle X-ray scattering patterns of pure phenytoin and SDs with 10 wt% phenytoin and various HPMC esters of substituted succinates.	12
Figure 1.3. Polarized optical micrographs from undercooled melts of (a) pure felodipine and mixtures of 97 wt% felodipine and 3 wt% of (b) PVP, (c) HPMCAS, (d) poly(vinyl pyrrolidone- <i>co</i> -vinyl acetate), and (e) poly(vinyl acetate).	14
Figure 1.4. Differential scanning calorimetry trace of HPMCAS H-grade for a heating ramp of 10 °C/min.	18
Figure 1.5. Modulated differential scanning calorimetry traces of a 10 wt% griseofulvin and 90 wt% HPMCAS H-grade SD.	19
Figure 1.6. (A) AFM topological map of a telaprevir:HPMC 6:4 w/w SD.	23
Figure 1.7. Schematic of the dissolution of a slab of hydrophilic glassy polymer.	26
Figure 1.8. UV extinction and fluorescence data for glassy phenylbutazone in phosphate-buffered saline.	28
Figure 2.1. Simplified ray diagram of the electron beam in a transmission electron microscope.	35
Figure 2.2. Bright-field TEM image of 10 wt% griseofulvin and 90 wt% HPMCAS 126 SD particles.	36
Figure 2.3. (A) Bright-field TEM image, (B) electron diffraction pattern, and (C) dark-field TEM image of a spin coated griseofulvin film.	37
Figure 2.4. Electron diffraction pattern of a spin coated phenytoin thin film after a cumulative electron dose of (A) 1000 and (B) 26000 e ⁻ /nm ²	38
Figure 2.5. Comparison of electron beam optics for conventional TEM and STEM.	39
Figure 2.6. Experimental EDS spectrum and chemical structure of griseofulvin.	41

Figure 2.7. Experimental EELS spectrum and chemical structure of griseofulvin.....	44
Figure 2.8. <i>Zimm</i> plot of methylcellulose in water at 20 °C.....	51
Figure 2.9. (A) Second-order time autocorrelation functions and (B) inverse Laplace transform results for dynamic light scattering measurements of multicompartment micelles at various time points.....	53
Scheme 3.1. Molecular structures of griseofulvin (GF) and hydroxypropyl methylcellulose acetate succinate (HPMCAS).....	57
Figure 3.1. WAXS of solid dispersions with varying GF loading.....	61
Figure 3.2. WAXS of the physical mixture of 5 vol% GF and 95 vol% hydroxypropyl methylcellulose.....	62
Figure 3.3. Modulated DSC heat flow curves of GF solid dispersions.....	63
Figure 3.4. Modulated DSC heat flow curves of 10 wt% GF solid dispersion.....	65
Figure 3.5. (a) Bright-field TEM of a spray dried GF particle.....	66
Figure 3.6. (a) Bright-field TEM of particles in a 3 vol% spray dried GF in spray dried HPMCAS physical mixture.....	67
Figure 3.7. Bright-field TEM images of (a) 5, (b) 10, and (c) 50 wt% GF solid dispersion particles.....	69
Figure 3.8. (a) <i>In situ</i> WAXS of 50 wt% GF solid dispersion before and after annealing at 130 °C.....	70
Figure 3.9. (a) <i>In situ</i> WAXS of 5 wt% GF solid dispersion before and after annealing at 140 °C.....	71
Figure 3.10. (a) <i>In situ</i> WAXS of 10 wt% GF solid dispersion before and after annealing at 140 °C.....	72
Figure 3.11. (a) Bright-field TEM image and (b) electron diffraction pattern of droplet observed in the post-annealed TEM sample of 50 wt% GF solid dispersion.....	73
Figure 3.12. (a) Bright-field TEM of 50 wt% GF solid dispersion that was annealed on a TEM grid at 130 °C for 12 hrs.....	74

Figure 3.13. (a) Bright-field TEM of a large crystal (30 μm long) in the post-annealed TEM sample of 50 wt% GF solid dispersion.....	75
Figure 4.1. (A) Simulated trajectories of 10^6 300 kV incident electrons traveling through a GF sample.	81
Figure 4.2. Comparison of EDS spectra for HPMCAS and GF. Inset is a magnification of the Cl peaks.....	82
Figure 4.3. HAADF TEM image (middle-top) and elemental maps of a spray dried GF particle.....	83
Figure 4.4. (A) HAADF TEM image and (B) Cl $K\alpha$ map of a spray dried HPMCAS particle.....	84
Figure 4.5. (A) HAADF TEM image and (B) Cl $K\alpha$ map of a 10 wt% GF SD particle.	85
Figure 4.6. (A) HAADF TEM image of spray dried GF particles.....	86
Figure 4.7. (A) EDS spectra for spray dried GF particles with different thicknesses.	87
Figure 5.1. High-angle annular dark-field (HAADF) STEM image of spin-coated (A) HPMCAS and (B) phenytoin films.....	95
Figure 5.2. Histograms of measured concentrations for (A) spin-coated HPMCAS and (B) spin-coated phenytoin.....	96
Figure 5.3. HAADF STEM images of (A) 10, (B) 25, and (C) 50 wt% phenytoin spin-coated dispersion films.	97
Figure 5.4. Comparison of experimental and predicted EELS spectra for 10, 25, and 50 wt% phenytoin (PHY) spin-coated dispersions.	98
Figure 5.5. Histograms of measured concentrations, as calculated by the EELS MLS noise-weighted algorithm, for 50 spots in (A) 10, (B) 25, and (C) 50 wt% spin-coated SDs.....	100
Figure 5.5. Phenytoin and HPMCAS EELS spectra for various collection area sizes. .	101
Figure 5.6. Histograms of measured concentrations, as calculated by the EELS MLS noise-weighted algorithm, for 50 spots in (A) 10, (B) 25, and (C) 50 wt% spin-coated SDs.....	103

Figure 5.7. Histograms of measured concentrations from 50 spots on a 10 wt% phenytoin spin-coated SD.	103
Figure 5.8. Histograms of measured concentrations from 50 spots on a 50 wt% phenytoin spin-coated SD.	103
Figure 5.9. (A) HAADF STEM image of a 25 wt% phenytoin spin-coated dispersion film that was annealed to 140 °C.	105
Figure 5.10. Low magnification HAADF TEM image of annealed 25 wt% phenytoin SD.	105
Figure 5.11. (A) Molecular structures of carbamazepine, naproxen, itraconazole, and griseofulvin.	106
Figure 5.12. Histograms of measured concentrations from 50 spots for 10 wt% drug solid dispersions featuring HPMCAS as the excipient and either (A) carbamazepine, (B) naproxen, (C) itraconazole, or (D) griseofulvin as the drug.	107
Scheme 6.1. Chemical structures of hydroxypropyl methylcellulose acetate succinate (HPMCAS), phenytoin, and probucol.	111
Figure 6.1. (A) Hydrodynamic radius distribution of HPMCAS in PBS buffer at 37 °C.	117
Figure 6.2. Additional DLS data of 9 mg/mL of HPMCAS in PBS at 37°C.	118
Figure 6.3. <i>Cryo-TEM of 9 mg/mL HPMCAS in PBS solution.</i>	120
Figure 6.4. (A) REPES analysis and (B) double exponential fit analysis for 8 mg/mL of HPMCAS in PBS at 25 °C.	121
Figure 6.5. Berry-modified Zimm plots of HPMCAS in PBS at (A) 25 and (B) 50°C.	123
Figure 6.6. Dissolution profiles of PHY:HPMCAS SDs with various drug loadings. ...	124
Figure 6.7. Measured solubility of crystalline phenytoin in HPMCAS solutions.	124
Figure 6.8. (A) Cryo-TEM image of 10 wt% phenytoin SD dissolution media at 10 min.	126
Figure 6.9. Cryo-TEM images of 10 wt% PHY SD dissolution media at (A) 4, (B) 20, (C) 40, and (D) 90 min.	127

Figure 6.10. Characterization of spray dried HPMCAS dissolution media (targeted concentration of 9 mg/mL).	128
Figure 6.11. SAXS patterns of centrifuged 10 wt% PHY SD dissolution media.	128
Figure 6.12. (A) Comparison of experimental SAXS data versus triaxial ellipsoid form factor model fit.....	130
Figure 6.13. Comparison of experimental SAXS data versus polydisperse sphere form factor model fit.....	132
Figure 6.14. (A) Average radius (R_{avg}) and (B) Schulz-Zimm distribution width parameter (z) extracted from polydisperse sphere form factor model fit for 10 wt% PHY SD dissolution media.	133
Figure 6.15. Cryo-TEM images of 25 wt% phenytoin dissolution media at (A) 4 min and (B) 10 min.	135
Figure 6.16. (A) Comparison of SAXS pattern and triaxial ellipsoid form model fit for 25 wt% PHY SD dissolution media at 10 min.....	135
Figure 6.17. Characterization of 50 wt% PHY SD dissolution media.....	136
Figure 6.18. Dissolution profiles for PHY SDs with a targeted drug concentration of 300 $\mu\text{g/mL}$	137
Figure 6.19. (A) Dissolution profiles of probucol:HPMCAS SDs with various drug loadings.	139
Figure 6.20. (A) Cryo-TEM image of 10 wt% probucol SD dissolution media at 4 min.	141
Figure 6.21. Cryo-TEM of 10 wt% PRB dissolution media at (A) 90 and (B) 360 min.	142
Figure 6.22. Comparison of SAXS patterns and polydisperse sphere form factor model fit for 10 wt% PRB SD dissolution media.	142
Figure 6.23. (A) Average radius (R_{avg}) and (B) Schulz-Zimm distribution width parameter (z) extracted from polydisperse sphere form factor model fit for 10 wt% PRB SD dissolution media.	143
Figure 6.24. 25 wt% probucol SD dissolution media at (A) 4 min and (B) 360 min. (D) Low-dose cryo-TEM image and (D) electron diffraction pattern at 360 min.....	145

Figure 6.25. SAXS patterns of 25 wt% SD PRB dissolution media.....	146
Figure 6.26. Cryo-TEM images of 50 wt% PRB SD dissolution media at (A) 4, (B) 40, and (C) 360 min. (D) SAXS patterns of 50 wt% PRB SD dissolution media.	147
Figure 6.27. Dissolution profiles for 10 wt% PRB SD with a targeted drug concentration of 300 $\mu\text{g/mL}$	148
Figure A.1. Scanning electron microscopy images of solid dispersion particles.	168
Figure A.2. (a) Bright-field TEM image and (b) electron diffraction pattern of GF crystal.....	170
Figure A.3. Bright-field TEM images of spray dried GF particles at (a) ambient temperature and (b) $-180\text{ }^{\circ}\text{C}$	171
Figure A.4. FTIR spectra of solid dispersions with varying GF loading.....	172
Figure B.1. MDSC reversing heat flow curves for GF SDs with varying drug loading, spray dried HPMCAS, and spray dried GF.	174
Figure C.1. Conventional bright-field TEM image of spin-coated (A) HPMCAS and (B) phenytoin films.	177
Figure C.2. Bright-field TEM images of (A) 10, (B) 25, and (C) 50 wt% phenytoin spin-coated dispersion films.	178
Figure C.3. Experimental and predicted conventional TEM EELS spectra for 10, 25, and 50 wt% phenytoin (PHY) spin-coated dispersions.	178
Figure C.4. Histogram of measured concentrations from 50 spots by conventional TEM EELS spectra, as calculated by the MLS noise-weighted algorithm, for (A) 10, (B) 25, and (C) 50 wt% phenytoin spin-coated dispersions.....	179
Figure C.5. Raw 10 wt% phenytoin (PHY) spin-coated SD, amorphous C film, and 10 wt% phenytoin spin-coated SD with C film subtracted EELS spectra.	180
Figure C.6. Histograms of measured concentrations from 50 spots on a 10 wt% phenytoin spin-coated SD.....	181
Figure C.7. Modulated DSC heat flow curves of a 25 wt% phenytoin spray-dried dispersion.	183

Figure D.1. Comparison of octanol-water partition coefficient versus free energy of crystallization at 37 °C for various active pharmaceutical ingredients.	185
Figure D.2. Scanning electron microscopy images of (A) 10 wt% PHY, (B) 25 wt% PHY, (C) 50 wt% PHY, (D) 10 wt% PRB, (E) 25 wt% PRB, and (F) 50 wt% PRB SDs.	187
Figure D.3. Scanning electron microscopy images of (A) 3.2 wt% PHY and (B) crystalline probucol.....	188
Figure D.4. Wide-angle X-ray scattering patterns of HPMCAS SDs featuring either (A) phenytoin or (B) probucol as the API.....	188
Figure D.5. Modulated differential scanning calorimetry reversing heat flow curves of HPMCAS SDs containing either (A) phenytoin and (B) probucol as the API.....	189
Figure D.6. (A) Dissolution profile 25 wt% phenytoin SD dissolved in HPMCAS solution compared with 10 and 25 wt% phenytoin SDs dissolved in PBS (same data as Figure 3A).....	191
Figure D.7. SAXS patterns of (A) 25 wt% PHY SD and (B) 25 wt% PRB SD dissolved in 6 mg/mL HPMCAS solution.	192
Figure D.8. (A) Dissolution profile of a 10 wt% PHY and 90 wt% poly(NIPAm-co-DMA) SD.....	193
Figure D.9. (A) Experimental SANS pattern and power law fit of 9 mg/mL HPMCAS in deuterated phosphate buffered saline (d-PBS).....	194

Chapter 1: Introduction

1.1 Motivation

During the early 1990s, simultaneous advances in genomics, combinatorial chemistry, and ultra-high-throughput automated assay technology initiated a new approach for rapidly discovering novel orally administered drug molecules. This paradigm shift caused the pharmaceutical industry to make brash predictions for the success rate of bringing new clinical candidates to market.¹ Although these techniques did lead to the discovery of drugs that had high binding affinity and selectivity for various enzyme targets, they were biased towards identifying molecules that had poor aqueous solubility ($< 100 \mu\text{g/mL}$)² and, consequently, low oral bioavailability. The poor solubility arose from a combination of crystallinity and the molecules containing hydrophobic moieties that facilitate drug potency. Due to this bias, 40% of currently marketed drugs and 90% of drugs in the discovery pipeline are insoluble in water.³ The shortcoming of this drug discovery paradigm—possibly the most challenging and critical issue facing the pharmaceutical industry today—motivates the development of several drug formulation strategies to overcome poor aqueous solubility and enhance bioavailability.⁴

Many of these strategies for surmounting solubility limitations rely on the use of polymers, molecular chains comprised of repeating subunits (*i.e.*, monomers) connected by covalent bonds. The chain-like nature of polymer molecules imparts fascinating

properties that may be precisely tuned by altering the chain length (molecular weight), repeat unit (chemical composition), and architecture.⁵ By striking a particular balance among these three parameters, polymers may exhibit properties (*e.g.*, amphiphilicity and pH-responsiveness) that are useful for increasing controlled delivery efficacy. Formulation strategies exploit these properties by using polymers to stabilize drug nanocrystals^{6,7,8} or incorporate drug into amphiphilic nanoparticles.^{9,10} Perhaps the most straightforward of these strategies is the use of a solid dispersion (SD), a mixture of an active pharmaceutical ingredient (API) and a polymer excipient. The two components are blended in such a way that the API transforms from a thermodynamically stable crystal to a metastable glass. Because the glass exists in a higher free energy state relative to the crystal, the API achieves a significantly higher aqueous solubility (often by orders of magnitude)^{11,12,13,14} and greatly improved efficacy. Furthermore, solid dispersions may be prepared at a large-scale by high-throughput processes like spray drying and hot melt extrusion.¹⁵ Due to the versatility and scalability of solid dispersions, this formulation strategy has attracted much attention from both academic and industrial communities.^{4,15,16} Nevertheless, a fundamental understanding of solid dispersion materials is needed to enable rational SD design.

In particular, the role of the polymer excipient needs to be clarified. Ideally, the polymer prevents the drug from crystallizing—both in the solid-state and in solution—and facilitates the dissolution of the drug in aqueous solvent. Thus, the choice of polymer significantly influences the physical stability and bioavailability of the API.^{15,17} Identification of an appropriate excipient for a particular drug, however, typically requires inefficient and expensive trial-and-error experiments.^{18,19} Expedition of this process is hindered by poor understanding of polymer-drug interactions and the metastable state of SDs. Moreover, formulation composition, processing conditions, and storage environment also affect the effectiveness of the polymer as an excipient.

In spite of these intricacies, several classes of polymers have been identified as effective excipients for a wide variety of drugs. Acrylic and methacrylic polymer excipients

may be judiciously designed to incorporate functional groups that interact with the drug. Eudragit[®], a family of copolymers derived from esters of acrylic and methacrylic acids, significantly improved the release of APIs like itraconazole and curcumin.^{20,21} Because Eudragit[®] copolymers are pH-responsive, they may be used to prevent solid dispersions from dissolving in the acidic environment of the stomach.²² Acrylic statistical copolymers featuring two, four, or five unique monomers also enhanced the supersaturation of various drugs.^{23,24,25} Unfortunately, acrylates and methacrylates offer poor protection from drug crystallization in the solid-state due to the flexibility of the polymers.²⁶ Conversely, poly(vinyl pyrrolidone) (PVP), a water-soluble polymer, is commonly used as an excipient because its relatively high rigidity (the glass transition temperature is 177 °C) impedes the mobility of amorphous drug, thereby inhibiting crystallization.²⁷ The polymer may also stabilize amorphous drug through hydrogen bonding between the drug and the carbonyl group of PVP.²⁸ Though PVP is highly hygroscopic (absorption of substantial amounts of water by the excipient will induce crystallization of drug),^{29,30} the hygroscopicity of the excipient may be reduced by copolymerizing vinyl pyrrolidone with vinyl acetate.³¹

While the aforementioned polymers are suitable excipients, cellulosic derivatives—the most prominent class of excipients—are especially effective at inhibiting crystallization and maintaining supersaturated drug concentrations in solution. These polymers exhibit little or no human toxicity because they are not absorbed by the GI tract and undergo minimal degradation during digestion. The rigid anhydroglucose backbone of cellulose imparts the polymers with a high glass transition temperature (typically above 100 °C) and hinders drug crystallization. While cellulose itself is insoluble in water due to its strong tendency to crystallize, the three hydroxyls on each anhydroglucose unit may be partially or fully reacted with various molecules to make the derivative soluble in solvent (either aqueous, organic, or both) and give specific functionality.³² Hydroxypropyl methylcellulose (HPMC), a water-soluble cellulose ether, provides exceptional crystallization inhibition and supersaturation enhancement for such drugs as nifedipine,

felodipine, and etravirine.^{33,34,35} Novel cellulose ω -carboxyesters (such as cellulose adipate, suberate, and sebacate derivatives) can prevent the nucleation and growth of drug crystals in solution.^{36,37,38,39,40}

The most remarkable cellulosic derivative—and perhaps polymer excipient, in general—is hydroxypropyl methylcellulose acetate succinate (HPMCAS). As seen in Figure 1.1A, the anhydroglucose backbone of the polymer is randomly substituted by five different substituents: hydroxyl, methoxyl, hydroxypropyl, acetate, and succinate. These moieties make HPMCAS both pH-responsive, due to the ionizable succinate, and amphiphilic, due to substituents that are either hydrophobic (methoxyl and acetate) or hydrophilic (hydroxyl, hydroxypropyl, and deprotonated succinate). Because HPMCAS is amphiphilic, it may be dissolved in the same organic solvent as the drug, unlike HPMC, allowing for simpler and more economical processing of spray dried SDs. HPMCAS-based SDs typically have longer shelf-life stability than HPMC and PVP-based SDs because the HPMCAS is less hygroscopic than the other two polymers. Moreover, HPMCAS regularly outperforms other polymers at maintaining supersaturated drug and impeding crystallization in solution. For these reasons, HPMCAS is considered to be the premier polymer excipient on the market today.^{41,42}

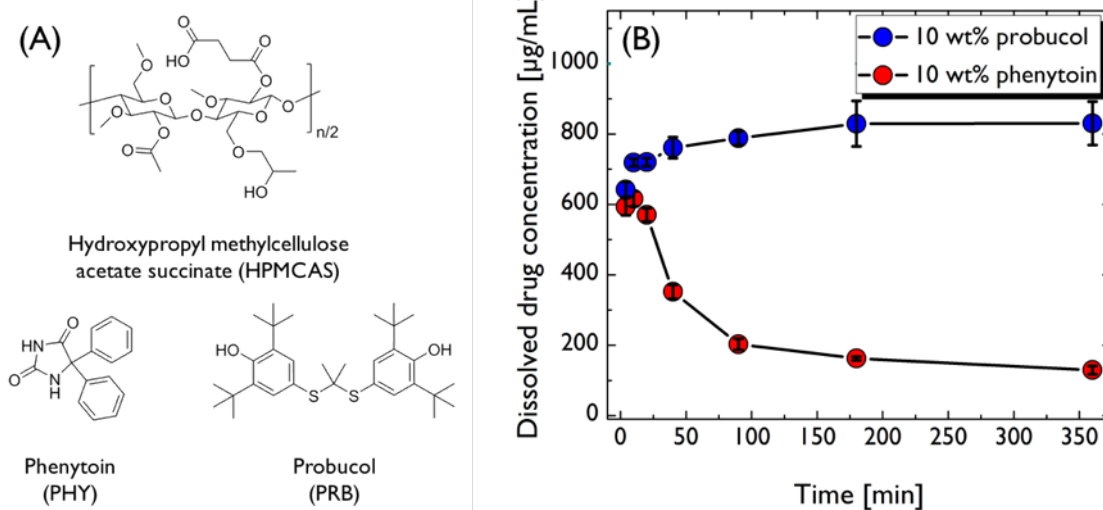


Figure 1.1. (A) Chemical structures of hydroxypropyl methylcellulose acetate succinate (HPMCAS), phenytoin, and probucol. The pictured structure of HPMCAS is merely illustrative and not representative of the actual substitution pattern. (B) Dissolution profiles of SDs featuring HPMCAS as the excipient and either probucol or phenytoin as the drug. The targeted drug concentration for both SDs is 1000 $\mu\text{g/mL}$. Each data point and error bar represent the average and standard deviation, respectively, of three measurements. HPMCAS maintains the concentration of probucol over 6 hours, but cannot stabilize the concentration of phenytoin.

Yet, HPMCAS is not a panacea. The polymer's effectiveness as an excipient is contingent on the identity of drug in the SD. As seen in Figure 1B, HPMCAS can maintain a high concentration of the drug probucol for over six hours, but cannot stabilize the drug phenytoin for more than 20 minutes. These opposing trends illustrate the need for a better understanding of the interactions between polymer and drug to allow for rational SD design.

To that end, the work described in this thesis expands the understanding of polymer-drug interactions by focusing on nanoscale (<100 nm) characterization of HPMCAS-based SDs for numerous poorly-soluble drugs. Though many hypotheses regarding polymer-drug interactions invoke nanoscale phenomena, the techniques traditionally used to characterize SDs either lack the resolution or sensitivity for probing these length scales and, consequently, only allow for incomplete understanding of SD structure-property

relationships. I addressed this shortcoming by developing novel nanoscale techniques for characterizing SDs in both the solid-state and during dissolution. These techniques not only achieved superior resolution and sensitivity compared to the traditional techniques, but also revealed critical information regarding the dissolution enhancement mechanism for SDs. The remainder of this chapter first details pertinent background on these three topics: (i) synthesis and characterization of HPMCAS, (ii) solid-state characterization of SDs, and (iii) solution characterization of SDs. Then, unresolved questions regarding solid dispersions and an outline of the dissertation are discussed.

1.2 Background

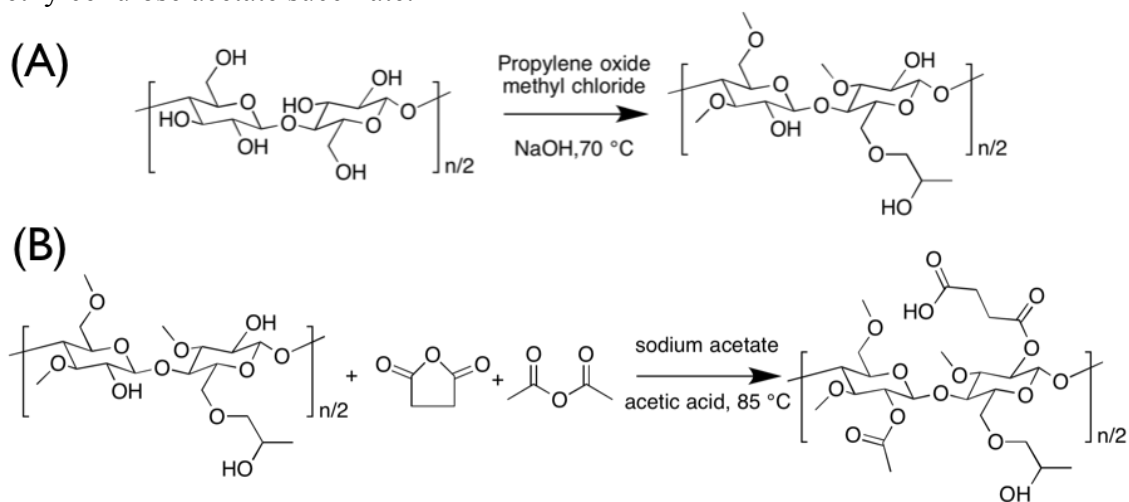
1.2.1 Hydroxypropyl methylcellulose acetate succinate (HPMCAS)

HPMCAS, first patented by the company Shin-Etsu in 1987,⁴³ is a derivative of cellulose, a ubiquitous polysaccharide that is a major component of wood, cotton, and plants, and is produced by sea organisms and microorganisms. Cellulose consists of linear chains of anhydroglucose units (AGU) connected by β -D-(1 \rightarrow 4) linkages. Each AGU has three hydroxyls that may undergo both intra- and interchain hydrogen bonding; as a result, cellulose is highly crystalline and insoluble in water. To solubilize and functionalize cellulose, the hydroxyls may be substituted with moieties (*e.g.*, ethers and esters) that disrupt the hydrogen bonding. The bulk and solution properties of these cellulose derivatives depend not only the identity of the substituents, but also on the degree of substitution (DS), which is the average hydroxyl substitution per AGU of the cellulose backbone; it ranges from 0 to 3.³²

HPMCAS features four unique substituents: methoxyl, hydroxypropyl, acetate, and succinate. As described in Scheme 1.1, the derivatization of the cellulose backbone is a two-step process. First, cellulose pulp is treated with chloromethane, propylene oxide, and sodium hydroxide to create HPMC. Second, the intermediate is reacted with acetic anhydride and succinic anhydride to form HPMCAS. The two anhydrides may be

introduced to the reaction vessel simultaneously or separately. The molar amount of each anhydride loaded into the reaction vessel is 1 to 10 times the desired degree of esterification of the AGUs.⁴⁵ The typical DS values for the methoxyl, hydroxypropyl, acetate, and succinate substituents range from 1.84–1.92, 0.23–0.26, 0.44–0.70, 0.13–0.43, respectively.⁴³ HPMCAS is further subdivided into different grades based on the molar ratio of acetate to succinate substituents on the polymer; L grade has a ratio less than 1, M grade has a ratio that is approximately 1, and H grade has a ratio that is greater than 1. This ratio affects not only the hydrophilicity, but also the pH-responsiveness of the polymer. To dissolve the polymer in aqueous buffer, the pH of the solvent must be above 5.5, 6, and 6.8 for HPMCAS-L, HPMCAS-M, and HPMCAS-H, respectively.⁴⁴

Scheme 1.1. Synthesis of (A) hydroxypropyl methylcellulose and (B) hydroxypropyl methylcellulose acetate succinate.



Although the synthesis of HPMCAS is relatively simple, the microstructure of the polymer is complex. Like most polysaccharides, HPMCAS has large molecular weight dispersity (\mathcal{D}) due to the natural dispersity of cellulose.³² The four moieties not only add to the hydroxyls on the AGU backbone in a random fashion, but may also react with the hydroxyl group on the hydroxypropyl substituent to form oligomeric side chains. Furthermore, the average molecular weight of commercially produced HPMCAS is much

higher than expected, based on the molecular weight of the precursor HPMC measured by size-exclusion chromatography. This discrepancy is posited to be caused by aggregation of HPMCAS in solution or crosslinking reactions between HPMCAS chains.⁴⁵ Because these heterogeneities make the structure of HPMCAS challenging to characterize, the structure of the polymer is still ambiguous.

The ill-defined complexities of the HPMCAS molecule potentially enable its unique solution behavior. By performing molecular dynamic simulations, Xiang *et al.* predicted that water molecules form clusters around the oxygen atoms of HPMCAS.⁴⁶ Fukasawa *et al.* observed that molecular weight measurements of HPMCAS in aqueous solvent agree with the expected values based on the molecular weight of the precursor HPMC, but measurements of HPMCAS in organic solvent produced much higher molecular weight values. To rationalize this behavior, they posited HPMCAS formed aggregates in organic solvent.⁴⁷ Chen reported unusually high molecular weights of HPMCAS in a mixed solvent of aqueous buffer and acetonitrile. Based on this observation, Chen hypothesized that HPMCAS formed aggregates in solution due to a heterogeneous distribution of the acetate and succinate moieties across the HPMCAS backbone. He also posited that HPMCAS underwent a conformation change in solution as the molecular weight increased.⁴⁸ In 2011, Chen *et al.* identified mixed solvents that minimized the molecular weight and, in theory, the tendency to aggregate for HPMCAS in solution.⁴⁹ Consistent with the SEC studies, many researchers presume HPMCAS forms colloids in solution by attributing amphiphilicity arguments.^{41,42,50}

Yet, to the best of my knowledge, no direct evidence of these colloids has been reported in the literature. Moreover, none of these studies considered the presence of cross-linked HPMCAS. To more accurately elucidate the dissolution enhancement mechanism of HPMCAS SDs, a rigorous characterization of HPMCAS in solution is needed.

1.2.2 Solid-state characterization of solid dispersions

The spatial distribution of drug throughout the polymer matrix of an SD significantly influences the properties of the material. An SD may potentially exhibit any of these three morphologies: (i) a single domain of drug molecularly dissolved in the polymer matrix; (ii) phase-separated domains enriched in amorphous drug or polymer; (iii) crystalline domains of drug in the polymer matrix. The contemporary SD design approach desires intimate mixing between the drug and polymer and considers phase separation and crystallization as signs of poor API stability and efficacy.²⁰

To identify appropriate excipients for various APIs, thermodynamic models have been used to predict the miscibility between drugs and polymers. One frequently used model is Flory-Huggins theory, which was independently developed by Paul Flory and Maurice Huggins in the early 1940s.^{51,52} It describes the free energy of mixing between a polymer and a small molecule, ΔG_m , by:

$$\frac{\Delta G_m}{kT} = \frac{\phi_p}{N_p} \ln \phi_p + \phi_d \ln \phi_d + \phi_p \phi_d \chi \quad (1.1)$$

where k is Boltzmann's constant, T is temperature, ϕ_p is the volume fraction of polymer in the blend, N_p is the degree of polymerization of the polymer, ϕ_d is the volume fraction of the small molecule, and χ is the Flory-Huggins interaction parameter, which quantifies the interaction between the two species. Because χ only considers short-ranged dispersion interactions between the two species, it may be expressed as:

$$\chi = \frac{\hat{V}_d}{RT} (\delta_d - \delta_p)^2 \quad (1.2)$$

where \hat{V}_d is the molar volume of the small molecule, R is the universal gas constant, δ_d is the solubility parameter of the small molecule, and δ_p is the solubility parameter of the polymer. Based on this equation, $\chi \geq 0$. Equation 1.2, however, is rarely quantitatively reliable for predicting experimental data of SDs because it fails to consider non-dispersion forces (*e.g.*, hydrogen bonding and π - π stacking) and non-ideal entropy of mixing. Instead, experimentalists typically fit data to an effective interaction parameter, χ_{eff} , that follows the form:

$$\chi_{eff} = \frac{\alpha}{T} + \beta \quad (1.3)$$

The constants α and β describe the non-ideal enthalpy of mixing and non-ideal entropy of mixing, respectively. For species that are miscible or have favorable non-dispersion interactions, χ_{eff} is 0.45 or lower. Using Flory-Huggins theory, Pajula *et al.* predicted the miscibility or immiscibility between blends of two different drug molecules. For 23 out of 26 of the blends, the Flory-Huggins model correctly predicted mixing or demixing between the two components.⁵³ Tian *et al.* used Flory-Huggins theory to develop phase diagrams for blends of the drug felodipine with either the HPMCAS or Soluplus[®] as the polymer excipient. Based on the phase diagram, they concluded that felodipine was more miscible with Soluplus[®].⁵⁴ Tian *et al.* also used Flory-Huggins to predict the miscibility of felodipine-PVP dispersions produced by spray drying and melt extrusion.⁵⁵

Despite the literature precedent, the use of Flory-Huggins theory or any thermodynamic model to predict the physical stability of SDs is insufficient. Flory-Huggins theory was derived for systems at equilibrium, not a metastable system like a SD,

where the drug is thermodynamically driven to crystallize. Therefore, rigorous solid-state characterization needs to be performed to confirm the morphology of a particular SD.

Identification of SD morphology, however, is non-trivial. If phase separation or crystallization occurs, the domains may be smaller than 100 nm because the crystal nucleus of a typical API is potentially on the order of 10 nm.⁵ Yet, sub-100 nm detection is challenging for most traditional SD characterization techniques. Furthermore, distinguishing between drug and polymer is difficult because both species are composed of similar constitutive atoms (*i.e.*, carbon, nitrogen, oxygen). Nevertheless, many techniques are used to probe the morphology of solid dispersions, such as wide-angle X-ray scattering, optical microscopy, calorimetry, dielectric relaxation spectroscopy, solid-state nuclear magnetic resonance, and atomic force microscopy. The following sections detail a broad overview of the application and weaknesses of these techniques for characterizing SDs.

1.2.2.1 Wide-angle X-ray Scattering

Lab-scale wide-angle X-ray scattering (WAXS, also known as X-ray diffraction) is the most common tool for detecting crystallinity in SDs. In WAXS, a collimated X-ray beam of a specific wavelength irradiates a sample while a detector is rotated around the sample stage to collect X-rays that are scattered from the material. This scattering produces an X-ray diffraction pattern (Figure 1.2). If the sample is glassy, the pattern will have a diffuse shape. This “amorphous halo” is due to the lack of order in the glassy structure; the X-rays are scattered over a wide range. If the sample is crystalline, the pattern will have relatively sharp peaks. These Bragg peaks are caused by the long-range order of crystalline structures; the X-rays mostly scatter at angles that are related to the arrangement of the atoms in the crystal. The intensity of the Bragg peaks relative to the whole diffraction

pattern is proportional to the crystalline fraction of the material, while the peak width is indicative of the minimum crystal grain size.⁵⁶

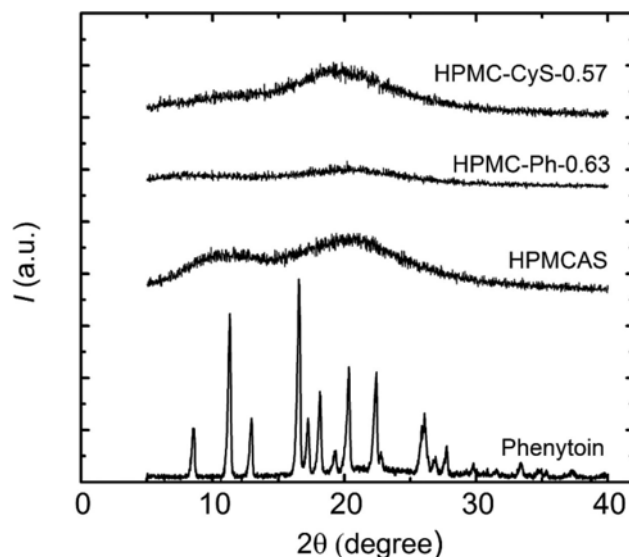


Figure 1.2. Wide-angle X-ray scattering patterns of pure phenytoin and SDs with 10 wt% phenytoin and various HPMC esters of substituted succinates. The scattering pattern of phenytoin, which is crystalline, exhibits sharp Bragg peaks, while the scattering patterns of the SDs, which contain amorphous phenytoin, each display a broad amorphous halo. Adapted with permission from Yin, L.; Hillmyer, M. A. *Mol. Pharm.* 2014, *11*, 175–185. Copyright 2014 American Chemical Society.⁵⁷

For SDs, WAXS is typically used to quickly screen API-polymer pairings and probe the mechanism of drug crystallization in the polymer matrix. Rumondor studied the influence of humidity on the crystallization of the drug felodipine in PVP or HPMCAS SDs. Based on changes in the Bragg peak intensity, the authors determined felodipine crystallization rates were sensitive to humidity for PVP SDs, but not HPMCAS SDs. They hypothesized that felodipine and PVP underwent moisture-induced phase separation, while HPMCAS stabilized amorphous felodipine, even at high levels of humidity.⁵⁸ Chiou confirmed the presence of griseofulvin crystals in pulverized dispersions of griseofulvin:polyethylene glycol using WAXS. A larger loading of griseofulvin in the dispersion led to the formation of larger crystals and, as a result, poorer dissolution

enhancement.⁵⁹ Yamamura *et al.* characterized the crystallization mechanism for griseofulvin. By comparing experimental and simulated diffraction patterns, they determined crystallization of the drug occurred over two distinct stages.⁶⁰

Although the use of laboratory-scale WAXS is routine, its sensitivity is limited. The practical lower limit of detection for WAXS is approximately 5 vol%, so the technique cannot distinguish between an SD that contains completely amorphous and one that has trace levels of crystallinity ($\lesssim 5$ vol%).⁶⁰ Thus, WAXS may potentially misdiagnose the miscibility between drug and polymer. Sensitive techniques are also required for elucidating the dissolution enhancement mechanism because trace levels of crystallinity can facilitate crystallization in solution.^{61,62}

1.2.2.2 Polarized optical microscopy

Polarized optical microscopy (POM) may be used to directly image anisotropic drug crystals within the polymer matrix of an SD. When light enters an isotropic material, which has a uniform index of refraction, it propagates at a velocity that is invariant to the material orientation. When light enters an anisotropic material, which has orientation-dependent indices of refraction, it is refracted into two orthogonal rays that travel at different velocities. This phenomenon is known as birefringence. When a birefringent crystal (*e.g.*, those with monoclinic, orthorhombic, or tetragonal lattices) is analyzed under cross-polarized white light illumination, as is the case with POM, interference between the components of the refracted rays that pass through the analyzer produces color contrast between the crystal and background.⁶³

Because drug molecules typically form anisotropic crystals, POM may be used to study a wide variety of APIs. Ghebremeskel *et al.* characterized the influence of surfactants on the physical stability of various SD systems. By using POM and WAXS, they determined that the surfactants inhibited crystallization and improved the API stability

within the SDs.⁶⁴ Kestur and Taylor investigated the relationship between drug-polymer hydrogen bonding and API crystallization inhibition for felodipine with various polymers. By measuring the size of drug crystals within the polymer matrices over a period of two days, they correlated the inhibition of crystallization with the presence of hydrogen bonding between the species (Figure 1.3).⁶⁵

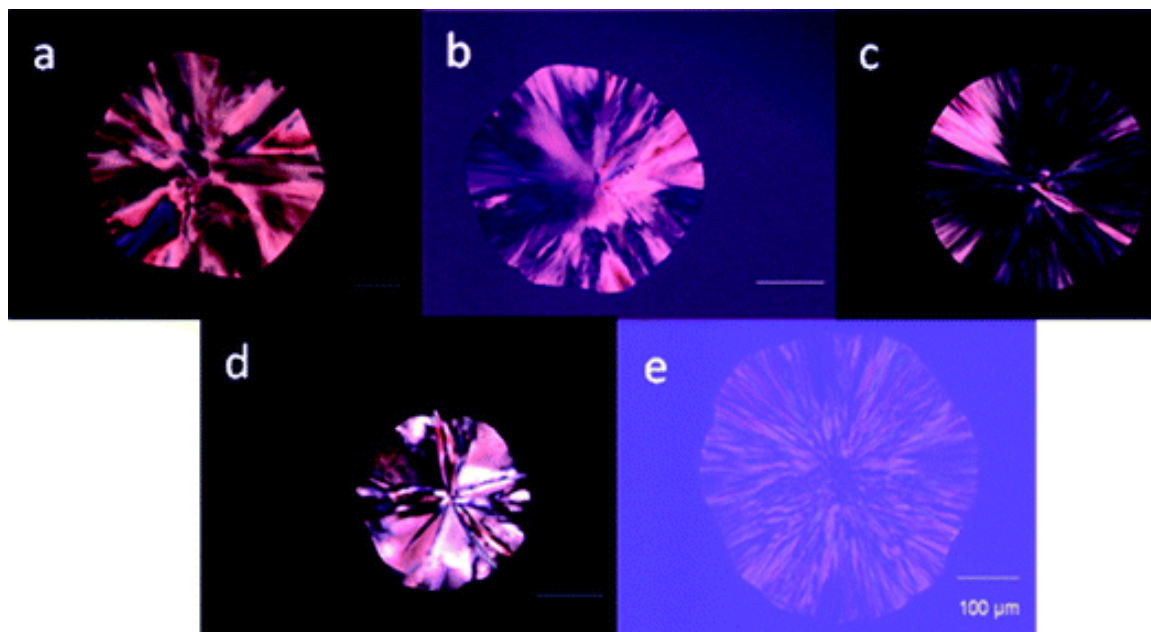


Figure 1.3. Polarized optical micrographs from undercooled melts of (a) pure felodipine and mixtures of 97 wt% felodipine and 3 wt% of (b) PVP, (c) HPMCAS, (d) poly(vinyl pyrrolidone-*co*-vinyl acetate), and (e) poly(vinyl acetate). The scale bar in each image represents 100 μm . Adapted with permission from Kestur, U. S.; Taylor, L. S. *CrystEngComm* 2010, 12, 2390. Copyright Royal Society of Chemistry 2010.⁶⁵

While POM is a versatile technique for characterizing SDs, it cannot be used to detect nanosize crystals because the diffraction-barrier limits its spatial resolution to 250 nm. Therefore, POM provides limited information regarding nucleation or early stages of crystal growth.⁶⁶

1.2.2.3 Thermal analysis

SDs have complex thermal properties because both drug and polymer excipient exist, ideally, as glasses. Unlike a crystalline solid, the structure of a glass (also known as an amorphous solid) resembles a liquid; the packing of the molecules lacks long-range order. The molecules are also essentially frozen, so that the material does not flow over relevant timescales. As a glass is heated over a particular temperature range, the heat capacity of the material increases, the density decreases, the molecular relaxations speed up, and the material becomes a liquid and flows. This progression is the *glass transition*, while the temperature range at which it occurs is the *glass transition temperature* (T_g). During this transition, thermodynamic variables (such as entropy, enthalpy, and volume) exhibit a change in slope with increasing temperature. Although this behavior may be suggestive of a second-order phase transition, a thermodynamic description of the glass transition is not completely appropriate because a glass is a non-equilibrium state; the measured value of T_g is affected by processing, aging, and characterization technique. As a result, the glass transition is typically classified as a pseudo second-order transition.⁵

For SDs, measurement of T_g gauges the physical stability of a particular formulation. Well below T_g , the drug cannot crystallize because both drug and polymer molecules do not have sufficient thermal energy to move. Near T_g , the drug may potentially phase separate or crystallize because drug and polymer molecular mobilities increase. These relaxations, however, are still relatively slow relative to the time scale of experimental observation, so the kinetics of phase separation and crystallization are slow. Above T_g , the drug has a strong tendency to phase separate or crystallize because the molecules may easily move. To minimize the risk of drug crystallization, formulations are designed so that the T_g of the drug:excipient blend is 50 °C above the storage temperature. The T_g of a binary blend, $T_{g,mix}$, may be estimated by the expression:

$$\ln T_{g,mix} = \frac{w_1 \Delta C_{p,1} \ln T_{g,1} + w_2 \Delta C_{p,2} \ln T_{g,2}}{w_1 \Delta C_{p,1} + w_2 \Delta C_{p,2}} \quad (1.4)$$

w_i is the weight fraction, $\Delta C_{p,i}$ is the change in heat capacity, and $T_{g,i}$ is the T_g of the i th component. Assuming $\ln(1+x) \approx x$, Equation 1.4 may be simplified to form the Couchman-Karas equation:

$$T_{g,mix} = \frac{w_1 T_{g,1} + w_2 \frac{\Delta C_{p,2}}{\Delta C_{p,1}} T_{g,2}}{w_1 + w_2 \frac{\Delta C_{p,2}}{\Delta C_{p,1}}} \quad (1.5)$$

This equation assumes that the two components only exhibit dispersive interactions and that their ideal volumes are additive.¹⁷ Other variations of the Couchman-Karas equation have been developed to account specific interactions.^{67,68} Though these models are not quantitatively robust, they do predict that $T_{g,mix}$ will be sufficiently larger than the storage temperature if the polymer excipient (which has a higher T_g than the drug) comprises a significant weight fraction of the SD, has an exceptionally high T_g , or both. Generally, polymers that have stiff backbones (like cellulose derivatives), large rigid side groups, high molecular weight, or high polarity have sufficiently high T_g s, though these correlations are not completely universal.⁵ The measurement of T_g of an SD is also performed to evaluate miscibility between drug and polymer. For this “miscibility evaluation”, if an SD exhibits only a single T_g , drug and polymer are judged to be miscible. Conversely, if an SD exhibits multiple T_g 's, drug and polymer are judged to be immiscible.¹⁷

The most common method for measuring T_g of an SD is differential scanning calorimetry (DSC). In this technique, a material is placed in an aluminum DSC pan and the pan is put on a heating stage alongside an empty reference pan that sits on a separate heating stage. The two pans simultaneously undergo a controlled temperature variation. The amount and direction of heat flow into the sample pan is adjusted to keep its temperature the same as the reference pan. The measurement of the heat flow reveals the thermal

transitions of the material.⁵ Figure 1.4 shows a DSC trace of HPMCAS. The temperature variation of the experiment proceeded in three stages. First, the polymer was heated to an elevated temperature that is high enough to erase thermal history. Second, it was rapidly cooled to the beginning temperature. Third, the sample was heated again. During this second heating cycle, the heat flow exhibited a gradual increase because the heat capacity of the material increases. The midpoint of the increase is taken to be the T_g of HPMCAS. While this protocol is commonly used for the T_g measurement of the pure polymer and, if experimentally accessible, pure drug, the T_g measurement of the SD should be performed on the first heating cycle because the influence of thermal history is critical to understanding the material properties. DSC may also be used to evaluate drug crystallinity and crystallization in SDs. The heat released during crystallization or heat consumed during melting appear as exothermic or endothermic peaks, respectively, in the DSC trace. The magnitudes of these peaks are related to the fraction of crystalline drug in the sample.^{5,17}

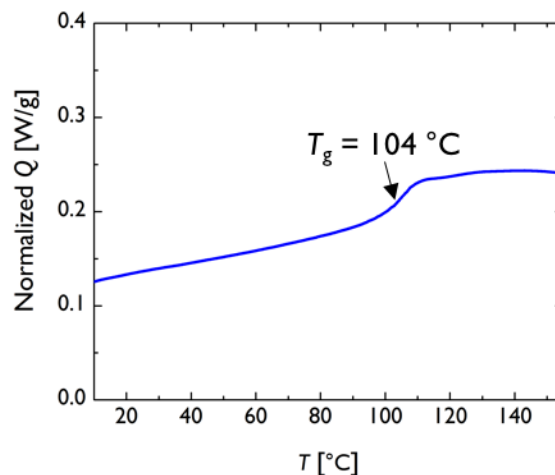


Figure 1.4. Differential scanning calorimetry trace of HPMCAS H-grade for a heating ramp of 10 °C/min. Only second heating ramp data is shown. The T_g of this polymer is defined as the midpoint of the transition region. This criterion is reliable only if enthalpic overshoot is not too large.

For many SD systems, the T_g and drug crystallization temperature (T_c) overlap. To separate these thermal events, modulated differential scanning calorimetry (MDSC) may be used. For MDSC, the sample and reference pan undergo a sinusoidal temperature ramp. For the material to achieve the required temperature profile, the heat flow for the sample is also sinusoidal. The measured heat flow may be deconvoluted into three signals (Figure 1.5). First, the Fourier transform of the heat flow signal generates a total heat curve, which is a facsimile of a conventional DSC trace. Second, the amplitude of the heat flow signal may be converted to a reversing heat curve, which accounts for heat capacity changes in the material (indicative of a glass transition event). Third, the difference between the total and reversing heat curves produces the non-reversing heat curve, which accounts for all other thermal events.

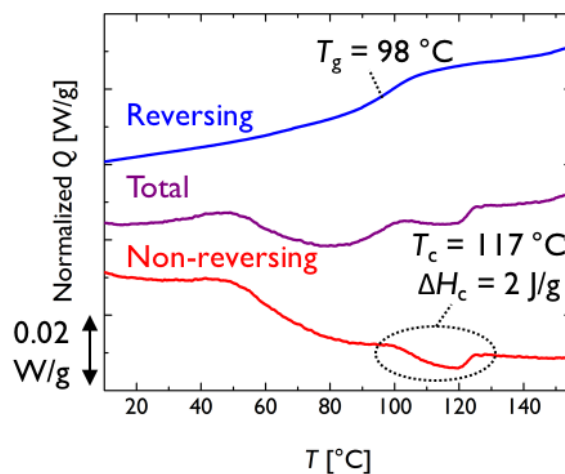


Figure 1.5. Modulated differential scanning calorimetry traces of a 10 wt% griseofulvin and 90 wt% HPMCAS H-grade SD. Data, shifted for clarity, were recorded upon first heating using an average temperature heating rate of 1 °C/min, a temperature modulation amplitude of 1 °C, and a temperature modulation period of 40 s. The reversing heat curve reveals T_g , while the non-reversing curve shows the crystallization temperature and enthalpy (T_c and ΔH_c , respectively) of griseofulvin.

The use of conventional DSC and MDSC has revealed critical physical properties of SDs. Gupta *et al.* studied the thermal transitions of ternary systems of the drug celecoxib, PVP, and the amino sugar meglumine. The T_g of these ternary blends deviated from theoretical predictions, which suggested the drug had favorable interactions with one of the other components.⁶⁹ Janssens *et al.* studied the influence of the preparation method on the ultimate thermal properties of various SD formulations. They observed that film cast SDs exhibited phase separation and crystallization at lower temperatures than spray dried SDs.²⁰ Marsac *et al.* probed the miscibility of crystalline drugs in various excipients by measuring the melting point depression of the drug. Systems that had been previously reported as miscible exhibited a significant melting point depression, whereas systems that had been reported as immiscible did not. By relating the melting point depression to Flory-Huggins theory, the authors also estimated χ for various drug:polymer pairings.⁷⁰

Although DSC is routinely used to evaluate SDs, its utility is limited because T_g is not a reliable gauge of miscibility and physical stability. Miscible blends may exhibit

multiple T_g s, whereas immiscible blends may exhibit a single T_g .^{71,72,73,74,75} Drugs that have identical T_g s can exhibit vastly different tendencies to crystallize from the amorphous state. T_g is also a poor indicator of the nucleation rate of drug in various polymers.^{76,77} Furthermore, similar to WAXS, trace levels of crystallinity are challenging to detect by DSC.¹⁷

1.2.2.4 Dielectric relaxation spectroscopy

Although T_g itself is a poor indicator of crystallization inhibition, the molecular motions of the drug and polymer below T_g may significantly influence the physical stability of the glassy drug in the SD. As the temperature of a liquid is cooled towards T_g , the viscosity and structural relaxation time (the time that it takes for a molecule to diffuse an interparticle distance) increase by orders of magnitude. The temperature dependence of the structural relaxation time, τ_α , may be described by the Vogel-Fulcher-Tammann model:

$$\tau_\alpha = \tau_0 \exp\left(\frac{DT_0}{T - T_0}\right) \quad (1.6)$$

τ_0 is the relaxation time constant for the unrestricted material ($\sim 10^{-14}$ s), D is the strength parameter, T is temperature, and T_0 is the zero-mobility or Kauzmann temperature. The molecular motions that affect τ_α (*i.e.*, molecule translation and rotation) are known as α -relaxations. These “global” α -relaxations (0.1–100 s) are affected by the diffusion and position of neighboring molecules. Glassy materials also exhibit β -relaxations, which are much faster than α -relaxations (< 0.1 s) and obey Arrhenius kinetics. These relaxations are presumably “local”, but the identity of the processes is not always well understood.^{5,20,78}

Both α - and β -relaxations may be probed by dielectric relaxation spectroscopy (DRS), where the dielectric properties of a material are measured under the influence of a

variable frequency electric field. The material's response to the electric field is a complex dielectric function, $\varepsilon^*(\omega)$, that may be expressed as:

$$\varepsilon^*(\omega) = \varepsilon'(\omega) + \varepsilon''(\omega) \quad (1.7)$$

ε' describes the energy stored by the material and ε'' is the energy dissipated by the material. These functions may be fit to mathematical models to extract relaxation times.⁷⁸ Kothari *et al.* used DRS to study the influence of drug loading on the physical stability of nifedipine:PVP SDs. They observed that lower drug loadings correlated with longer τ_α (*i.e.*, a decrease in molecular mobility) and slower nifedipine crystallization rates.⁷⁹ Mehta *et al.* measured τ_α , using DRS, and crystallization time, using synchrotron-sourced WAXS, as a function of water absorbed by the SD. For both dry and wet SDs, they determined that the crystallization had a power-law relationship with τ_α .^{80,81}

Though DRS provides deep insight into the physics of glass materials, the understanding of the relationship between molecular mobility and SD physical stability is primitive. The identity and role of β -relaxations is ambiguous, while interpretation of DRS data is also non-trivial. Low frequency data may be obscured by interference from conductivity and relaxation events in multi-component blends may overlap.^{17,78}

1.2.2.5 Solid-state nuclear magnetic resonance spectroscopy

Solid-state nuclear magnetic resonance spectroscopy (SS-NMR) may overcome the sensitivity and resolution limitations of WAXS and DSC to provide quantitative structural and composition information for SDs. This technique, in which a solid sample is exposed to magnetic fields, elucidates intermolecular interactions (such as hydrogen bonding) between any two molecular species. Tobyn *et al.* characterized SDs featuring a novel API and PVP by both MDSC and SS-NMR. While MDSC confirmed the two components were miscible, SS-NMR revealed that the API engaged in hydrogen bonding with PVP.⁸² SS-

NMR may also identify nanostructures within SDs through relaxometry experiments, where the relaxation of particular NMR signals are correlated with the domain size of heterogeneities in the formulation.⁸³ Aso *et al.* performed ¹⁹F-NMR relaxometry to track the crystallization of flufenamic acid in SDs containing PVP or HPMC as the excipient. By measuring the spin-lattice relaxation times of the fluorine atoms in the API, they determined that PVP was better than HPMC at inhibiting drug crystallization.⁸⁴ Yuan *et al.* used ¹H-NMR relaxometry to evaluate the miscibility of nifedipine:PVP SDs at various nifedipine loadings. For nifedipine loadings above 75 wt%, they observed that the drug formed amorphous domains 5–20 nm in size.⁸⁵

Although SS-NMR probes SDs at the molecular level, adoption of the technique as a routine characterization tool is hampered by many challenges. To obtain a sufficient signal-to-noise ratio, the acquisition times for the technique are long; single measurements may require a run time of 1 week.⁸⁶ Therefore, SS-NMR is inappropriate for systems that undergo structural evolution at timescales shorter than the acquisition time. Furthermore, the interpretation of the relaxometry experiments is challenging because the data may be obscured by heteronuclear coupling effects.⁸³

1.2.2.6 Atomic force microscopy

In recent years, many researchers used atomic force microscopy (AFM) techniques to qualitatively characterize SD morphology. For AFM, a sharp tip that is connected to a cantilever is rastered across a sample surface. Interatomic van der Waals interactions between the AFM tip and sample cause the cantilever to bend. The displacement of the cantilever correlates with sample height and material properties (*e.g.*, adhesion, modulus, and viscoelasticity). Because the AFM tip radius is ~ 10 nm, AFM may resolve structures that are tens of nanometers in size.⁸⁷

The high spatial resolution of AFM makes the technique appropriate for studying the onset of phase separation or crystallization in SDs. Marsac *et al.* used AFM to image moisture-induced phase separation in felodipine:PVP SDs. When a 50 wt% felodipine SD was exposed to a relative humidity of 94% for 1 hr, amorphous drug-rich domains approximately 100 nm in size were observed. After 4 hr of exposure, drug crystals 500 nm in size were detected.⁸⁸

Because imaging alone cannot distinguish between drug and polymer, some researchers have used photothermal-induced resonance (PTIR), a related technique that couples AFM and infrared spectroscopy, to evaluate local chemical composition. In PTIR, a laser irradiates an AFM sample to cause it to mechanically oscillate. By measuring the oscillations with the AFM cantilever, local composition and topology may be elucidated.⁸⁹ Using PTIR, Qi *et al.* unambiguously identified drug crystals in felodipine:Eudragit SDs that were processed by melt extrusion. In related work, Li *et al.* detected phase separated regions of amorphous telaprevir, ranging from 50 to 100s of nanometers in size, within matrices of various polymers (Figure 1.6). The spatial resolution of PTIR, however, is only ~ 100 nm, making this technique inappropriate for resolving the onset of phase separation or crystallization.^{90,91}

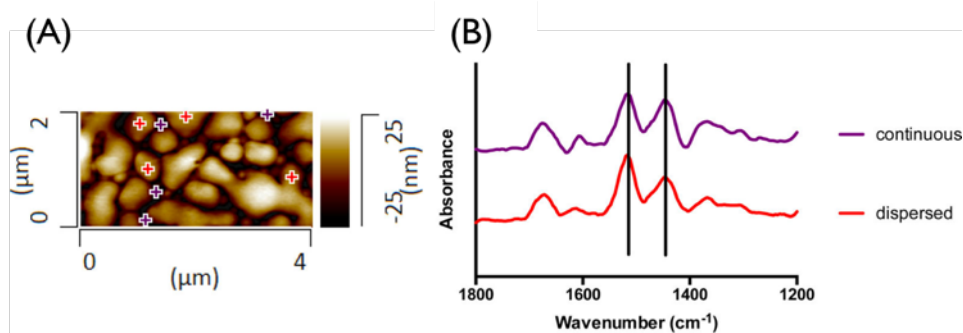


Figure 1.6. (A) AFM topological map of a telaprevir:HPMC 6:4 w/w SD. (B) Local infrared spectra from continuous or discrete domains in the film. Based on the differences in the spectra, the authors deduced that the dispersed phases were telaprevir rich, while the continuous phases were telaprevir poor. Adapted with permission from Li, N.; Taylor, L. S. *Mol. Pharm.* 2016, 13, 1123–1136. Copyright American Chemical Society 2016.⁹¹

1.2.3 Solution characterization of solid dispersions

SDs are designed so that upon dissolution the drug becomes supersaturated in the gastrointestinal fluid, thereby driving rapid absorption of drug into the blood stream. Supersaturation, S , is defined as:

$$S = \frac{C}{C_{crys}} \quad (1.8)$$

C is the concentration of drug in the supersaturated solution and C_{crys} is the solubility of the thermodynamically stable crystal. SDs achieve supersaturation because the drug in the formulation exists as a glass, which has a higher apparent solubility relative to the crystal. Although true equilibrium between glassy drug and drug dissolved in solution cannot exist because the glass is not the lowest free-energy state, a metastable partitioning of drug between the two phases is still obtained. The apparent solubility of the glassy drug, C_{glass} , may be estimated by:

$$C_{glass} = C_{crys} \gamma \exp \frac{\Delta G_{g \rightarrow c}}{RT} \quad (1.9)$$

$$\Delta G_{g \rightarrow c} = -\frac{\Delta H_f}{R} \left(\frac{T_m - T}{T_m T} \right) \quad (1.10)$$

γ is the activity coefficient of glassy drug saturated with water (ranges from 0.5-1 for various drugs),¹² $\Delta G_{g \rightarrow c}$ is the free energy difference between glassy and crystalline drug, ΔH_f is the enthalpy of fusion of crystalline drug, T_m is the melting temperature of crystalline drug, T is temperature, and R is the universal gas constant. Because C_{glass} is significantly larger than C_{crys} , SDs can achieve large values of S .^{12,13,14} Supersaturation, however, also induces crystallization of drug, so an optimal excipient for an API needs to

simultaneously stabilize glassy drug and inhibit crystallization. This stability of these phases affects not only the behavior of drug and polymer in aqueous solution, but also the release of both species from SD particles. The following sections discuss the physics and characterization of these stages of SD dissolution.

1.2.3.1 Dissolution of drug and polymer from SD particles

The release of drug from an SD particle is a fairly complex process. When an SD particle is submerged in aqueous solvent, it imbibes water molecules. Unlike the dissolution kinetics of particles of pure drug, which is limited by the diffusion and convection of the drug in water, the dissolution kinetics of SDs is controlled by both drug mass transfer and dissolution of the polymer matrix. Polymer dissolution, illustrated in Figure 1.7 for a slab of hydrophilic glassy polymer, occurs in three stages. (i) Water penetration causes the polymer to simultaneously swell and devitrify. The gel-water interface (front S) moves outward, while the gel-glassy polymer interface (front R) moves inward. (ii) Polymer chains begin to disentangle at the gel-water interface and dissolve into solution when the water concentration in the swollen polymer exceeds a critical concentration. The rate of disentanglement is affected by both molecular weight and the reptation time of the polymer chains. Both fronts S and R retreat towards the center of the film. (iii) Polymer chains at the gel-water interface continue to disentangle and dissolve after the glassy core disappears. Front S continues to move inward until all the polymer is dissolved.⁹²

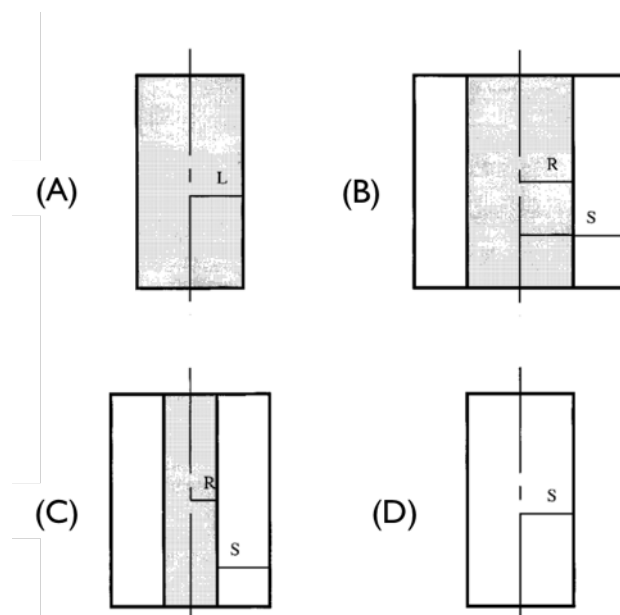


Figure 1.7. Schematic of the dissolution of a slab of hydrophilic glassy polymer. (A) Slab before immersion in solvent. L is the initial thickness. (B) Initial swelling of polymer. Solvent swelling causes the gel-solvent interface to move outwards (front S), while devitrification leads to the gel-glassy polymer interface to move inwards (front R). (C) Disentanglement of polymer from gel-solvent interface. Both fronts S and R move inwards. (D) Depletion of glassy polymer. Front S moves inward until all polymer dissolves. Adapted with permission from Narasimhan, B.; Peppas, N. A. *J. Pharm. Sci.* 1997, 86, 297–304. Copyright Wiley Periodicals and the American Pharmacists Association.⁹²

The coupled rates of dissolution for drug and polymer influence the ultimate dissolution profile of the drug. Faster dissolution of polymer relative to drug may also cause enrichment of drug at the dissolution interface and, consequently, crystallization.⁹³ Furthermore, high drug loadings decrease the dissolution rate of SDs.^{94,95,96} Although several mathematical models have been developed for predicting the dissolution rate of drug from polymer matrices,^{92,97,98,99} the influence of drug:polymer interactions on the dissolution rate is not fully understood.

1.2.3.2 Phase behavior of SDs during dissolution

For SD formulations that target a concentration of drug above the crystalline solubility, release of drug from SD particles during dissolution will cause the solution to

be supersaturated. However, studies of the phase behavior of drug and polymer in supersaturated solutions were rare until the late 2000's. In 2008 and 2009, Curatolo *et al.* published two studies focused on HPMCAS SDs. To rationalize the performance of HPMCAS as an excipient, the authors claimed the polymer formed nanosized aggregates with drug. They hypothesized that these aggregates replenished the concentration of fully dissolved drug in solution. In spite of the claims by the authors, these two publications did not include any characterization of the structures in the dissolution media.^{41,42}

In 2012, Taylor *et al.* developed a new assay for characterizing SD dissolution media using UV extinction. By irradiating the sample with UV light at a non-absorbing wavelength and measuring light transmission, they discovered the formation of structures in the dissolution media for a variety of SD systems.^{100,101,102,103,104} UV extinction, however, could not distinguish between amorphous structures and crystalline structures. To complement these studies, Taylor *et al.* developed a fluorescence spectroscopy assay for characterizing SD dissolution. This technique involves the addition of a fluorophore that interacts with amorphous drug (but not crystalline drug) in the dissolution media. By simultaneously monitoring both light transmission through the solution and the emission spectra of the sample, they determined that many SD systems formed amorphous drug-rich nanodroplets. They observed that these nanodroplets only formed when the concentration of drug in solution surpassed the glassy drug solubility (Figure 1.8).^{101,105,106} In agreement with the claims by Curatolo *et al.*, Taylor proposed that these nanodroplets serve as reservoirs that maintain the concentration of fully dissolved drug. The stability of the nanodroplets was contingent on the drug:polymer pairing and the structures typically coarsened over time. Furthermore, drug was removed from solution by crystallization, which led to accelerated depletion of the nanodroplets.¹⁶ Although polymers are recognized as necessary for inhibiting nanodroplet coalescence and drug crystallization, their interaction with drug during dissolution is still not well understood. Additional studies are needed to resolve this mechanism.

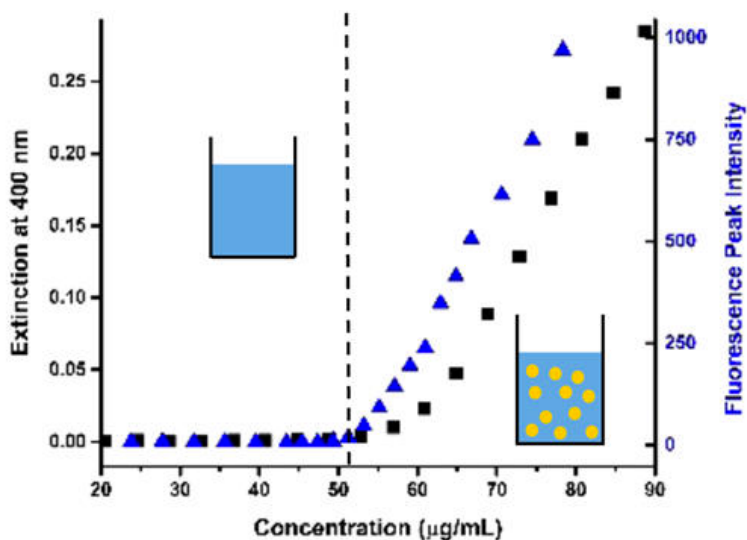


Figure 1.8. UV extinction and fluorescence data for glassy phenylbutazone in phosphate-buffered saline. When the concentration of the drug exceeded $\sim 50 \mu\text{g/mL}$, UV extinction detected the formation of structure, while fluorescence confirmed the structure was amorphous. Based on the data, the authors concluded the drug formed amorphous nanodroplets in solution. Adapted with permission Almeida e Sousa, L.; Reutzel-Edens, S. M.; Stephenson, G. A.; Taylor, L. S. *Mol. Pharm.* 2015, 12, 484–495. Copyright American Chemical Society.¹⁰⁵

1.3 Unresolved questions and dissertation outline

Although physical stability and dissolution performance are contingent on nanoscale phenomena, the tools routinely used to characterize SDs lack the spatial resolution and sensitivity for evaluating these properties. Correspondingly, reports of SD characterization often provide unclear and conflicting interpretations of structure-property relationships. For example, the relationship between SD morphology and dissolution is ambiguous. Do trace levels of crystallinity or phase separation significantly diminish solubility enhancement? How can trace levels of crystallinity or phase separation be detected? Furthermore, the behavior of drug and polymer during SD dissolution is not well understood. Some reports claim drug forms amorphous aggregates in solution, but what is their structure? Do all drugs form aggregates, or only some? What is the role of the polymer in forming and sustaining these aggregates?

To address the unresolved questions, the goal of the work in this thesis is to elucidate structure-property relationships of SDs by directly evaluating their nanoscale properties. I developed several SD characterization tools that achieved spatial resolutions and sensitivities superior to those of the traditional techniques. Using these novel tools, we discovered that the stability and performance of HPMCAS SDs are directly controlled by their nanoscale structures. This insight reveals crucial steps of the dissolution enhancement mechanism and will ultimately guide the efforts of the pharmaceutical community in establishing design principles for SDs. The following chapters discuss these findings in detail:

- Chapter 2 describes the materials and methods for all subsequent chapters.
- Chapter 3 focuses on the development of transmission electron microscopy and electron diffraction as tools for detecting trace amounts of crystalline drug within the polymer matrix of SDs.
- Chapter 4 explores the use of energy-dispersive X-ray spectroscopy as a potential, but ultimately limited, technique for mapping the spatial distribution of drug throughout SDs.
- Chapter 5 chronicles the development of electron energy-loss spectroscopy as a tool for quantifying, with high sensitivity and < 100 nm spatial resolution, concentration of drug and polymer in spin-coated SDs.
- Chapter 6 reports the use of cryogenic transmission electron microscopy and small-angle X-ray scattering for characterizing the dissolution media of HPMCAS SDs.

I discovered that the dissolution profiles of these SDs directly correlates with the presence of nanoscale structures in solution.

- Chapter 7 discusses the implications of the studies in the dissertation and proposes possible future directions.
- The appendices include experimental data not featured in the main chapters.

Chapter 2: Materials and methods

2.1 Introduction

This chapter details the hydroxypropyl methylcellulose acetate succinate (HPMCAS) samples, solid dispersion (SD) preparation methods, and characterization techniques used for the dissertation studies. The characterization techniques described in this chapter include wide-angle X-ray scattering (WAXS), modulated differential scanning calorimetry (MDSC), transmission electron microscopy (TEM), electron diffraction, energy-dispersive X-ray spectroscopy (EDS), electron energy-loss spectroscopy (EELS), cryogenic transmission electron microscopy (cryo-TEM), dynamic light scattering (DLS), static light scattering (SLS), and small-angle X-ray scattering.

2.2 Hydroxypropyl methylcellulose acetate succinate samples

All HPMCAS samples were provided by The Dow Chemical Company under the trade name AFFINISOL™. Similar to HPMCAS produced by Shin-Etsu, AFFINISOL™ is sub-divided into different grades based on the molar ratio of acetate to succinate moieties. 716 grade has a ratio that is less than 1, 912 grade has a ratio that is approximately 1, and 126 grade has a ratio that is greater than 1. Table 2.1 specifies the grade, molar mass, and weight percent of acetate and succinate moieties, as measured by Dow, for the three different HPMCAS batches used for the studies described in this dissertation.

Table 2.1 Grade, molar mass, and acetate and succinate composition of AFFINISOL™ HPMCAS batches used for dissertation studies. Molar mass was measured by size-exclusion chromatography with a multi-angle light scattering detector. Weight percents of methoxyl and hydroxypropyl moieties for all batches were 24 and 8 %, respectively.

Chapter	Grade	M_n [kg/mol]	\bar{D}	Weight percent [%]			
				Methoxyl	Hydroxy- propyl	Acetate	Succinate
3 & 4	126	32	3.4	24	8	14	6
5	126	80	2.1	24	8	12	7
6	912	60	24	24	8	10	11

2.3 Preparation of solid dispersions

To prepare SDs, targeted amounts of drug and HPMCAS were first dissolved in tetrahydrofuran to form a solution with a total solids loading of 2 wt%. The precursor solution was then processed by either spray drying (Chapters 3, 4, and 6) or spin coating (Chapter 5). For spray drying, the solution was spray dried by a mini spray dryer (Bend Research) using a nitrogen flow rate of 12.8 L/min, an inlet temperature of 68 °C, and a solution flow rate of 0.65 mL/min. The outlet temperature fluctuated between 24 and 27 °C. SD powder was recovered from filter paper placed in the outlet of the spray dryer. For spin coating, an approximately 10 μ L drop of the precursor solution was filtered through a 0.2 μ m PTFE syringe filter and placed onto a 200-mesh copper TEM grid that was supported by a 1 cm \times 1 cm silica wafer. The TEM grids had an ultrathin (nominally 5 nm) amorphous carbon film to support the SD. The samples were spun at 2500–3000 for 1 min. For both types of processing, the freshly-prepared SD was dried under reduced pressure at ambient temperature for at least 12 h and stored in a desiccator under reduced pressure at ambient temperature until use.

2.4 Wide-angle X-ray scattering

WAXS was used to evaluate crystallinity of drug in SDs (Chapter 3 and Appendix D.2). For ambient temperature measurements, approximately 50 mg of sample was loaded into a 0.5 mm-deep zero-background sample holder and analyzed using a Bruker-AXS D5005 diffractometer with a Cu K α source ($\lambda = 1.54 \text{ \AA}$). For *in situ* WAXS measurements (Chapter 3), approximately 50 mg of sample was loaded into a 0.8 mm-deep, zero-background, temperature-controlled sample holder and characterized by a Bruker D8 Discover diffractometer with a Cu K α source filtered with a nickel foil ($\lambda = 1.54 \text{ \AA}$). The holder was placed in a sample chamber and immersed under nitrogen gas at a flow rate of 15 mL/min. For both types of measurement, diffraction patterns were collected from a scattering vector (q) range of 4–28 nm⁻¹ with a scan rate of 0.01 nm⁻¹s⁻¹. The overall crystallinity (vol%) was calculated by dividing the area of the Bragg peaks after background subtraction by the total area of the diffraction pattern. The crystal grain size was calculated using the Scherrer equation, a routine procedure.¹⁰⁷

2.5 Modulated differential scanning calorimetry

Thermal properties of various drugs, HPMCAS, and SDs were evaluated by MDSC using a Discovery DSC (TA Instruments). 5–8 mg samples were put inside TzeroTM aluminum pans with standard lids. While immersed under nitrogen gas at a flow rate of 50 mL/min, each sample was heated from 0 to 160 °C using an average temperature heating rate of 1°C/min, a temperature modulation amplitude of 1 °C, and a temperature modulation period of 40 s. During the heat cycle, total, reversing, and non-reversing heat flow curves were measured. The glass transition temperature (T_g) was determined from the reversing heat flow curve, and the crystallization temperature and enthalpy (T_c and ΔH_c) were estimated from the non-reversing heat flow curve. All samples were analyzed by MDSC in triplicate.

2.6 Transmission electron microscopy (TEM)

A major aspect of this dissertation is the use of transmission electron microscopy (TEM) techniques to evaluate structure-property relationships of SDs at the nanoscale. To provide context for the dissertation studies, theory and application of TEM is detailed in the following sections.

2.6.1 Basic TEM theory

TEM is a workhorse characterization tool for nanoscale materials (defined as materials that have at least one dimension roughly 1 to 100 nm in size). The usefulness of the technique stems from the wave-like characteristics of the electron. The spatial resolution—*i.e.*, the minimum distance in which two separate objects may be distinguished—of both optical and transmission electron microscopy is proportional to the wavelength of the incident radiation. Because wavelengths of visible light are hundreds of nanometers, the best spatial resolution physically achievable by optical microscopy is ~ 250 nm, insufficient for resolving nanoscale objects. TEM, however, may theoretically resolve atomic detail because the electrons used in the technique, whose kinetic energies are ≥ 100 kV, have picometer wavelengths. Although lens aberrations may inhibit full atomic resolution, TEM easily resolves nanoscale structures.¹⁰⁸

Figure 2.1 displays a simplified ray diagram of a transmission electron microscope. The incident electron beam is produced by an electron source and passes through electron lenses and a condenser aperture for collimation (not shown). When the beam impinges the sample, some incident electrons scatter from the electron cloud and nucleus of the constituent atoms. Scattering may be elastic (electrons do not lose kinetic energy) or inelastic (electrons transmit energy to the sample). The scattering angle of the electrons is related to the microstructure of the material; scattering from an amorphous material will occur over a broad range of angles, whereas scattering from a crystal will peak at discrete angles contingent on the arrangement of atoms in the sample. Inelastic scattering may also

cause the sample to emit other forms of radiation (*e.g.*, X-rays, secondary electrons, Auger electrons). These signals are passed through a series of optics to form an image, scattering pattern, or spectrum. This array of information projected from a TEM sample enables rigorous characterization of nanostructured materials.¹⁰⁸

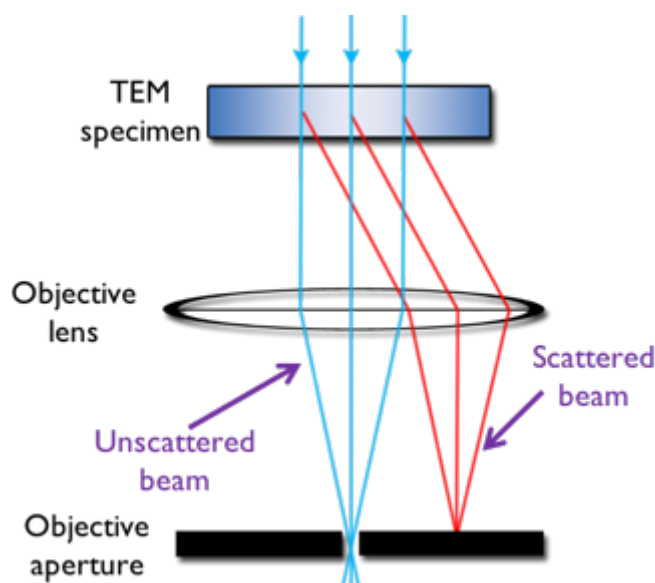


Figure 2.1. Simplified ray diagram of the electron beam in a transmission electron microscope.

2.6.2 TEM imaging and electron diffraction

TEM image interpretation relies on evaluating contrast, the difference in intensity between two adjacent distinct regions. For amorphous organic samples, contrast typically results from variations in the mass and thickness of the sample; thicker or denser regions of the sample cause the incident electrons to scatter more because the electrons encounter more atoms. Thus, the resulting scattering pattern is comprised of two types of beams: (i) the direct beam and (ii) scattered beam. An objective aperture is placed in the beam path so that only the direct beam passes to the detector. In the resulting “bright-field” image, the darker areas represent thicker or denser regions (Figure 2.2).

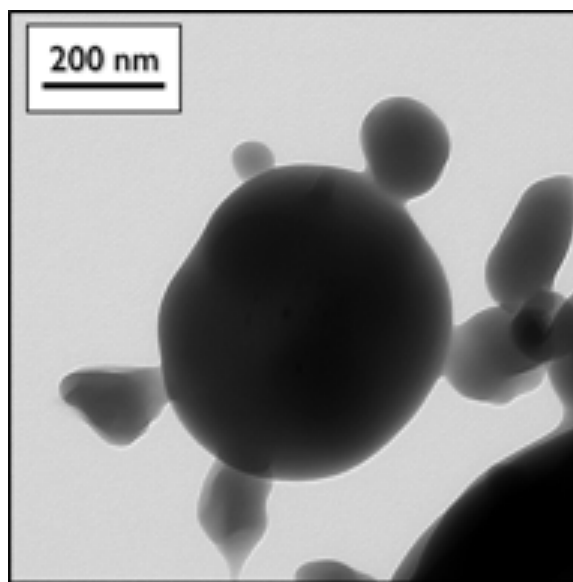


Figure 2.2. Bright-field TEM image of 10 wt% griseofulvin and 90 wt% HPMCAS 126 SD particles.

Unlike amorphous samples, the electron scattering pattern of a crystalline sample contains sharp spots produced by Bragg diffraction (see Figure 2.3B). Not only do sharp diffraction spots confirm a sample is at least partially crystalline, but also the reflections may be indexed to verify or elucidate the crystal structure and orientation. Analysis of electron diffraction patterns is analogous to the analysis of X-ray diffraction patterns. By placing the objective aperture over a reflection so that only specific diffraction electrons pass to the detector, crystalline regions of the sample may be imaged. In the “dark-field” TEM image in Figure 2.3C, the intensely white domains represent crystals that have an orientation that satisfies Bragg’s law with the electron beam. The grey and dark regions may be amorphous or they contain crystals that have an orientation that does not satisfy Bragg’s law with the beam.¹⁰⁸

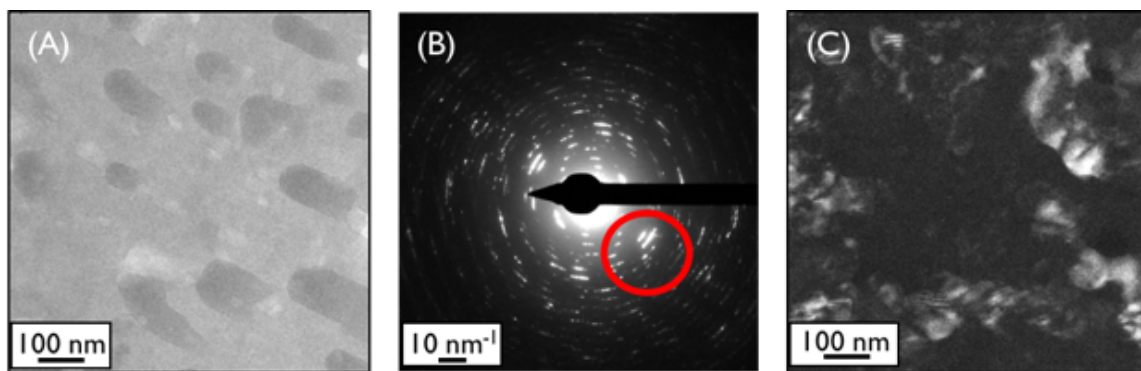


Figure 2.3. (A) Bright-field TEM image, (B) electron diffraction pattern, and (C) dark-field TEM image of a spin coated griseofulvin film. Red circle in (B) represents approximate position of objective aperture during the collection of (C).

Although the main utility of TEM is collection of a diffraction pattern and image from the same region of interest, the influence of beam damage must be considered. Unlike hard materials, which are fairly resistant to beam damage, soft matter (such as the organic molecules and polymers studied in this dissertation) are very sensitive to electron dosage. Electron irradiation may cause incipient radical formation, leading to irreversible chemical changes and destruction of crystallinity in the material. Figure 2.4 illustrates this effect of beam damage on a spin coated film of phenytoin. After a cumulative beam dosage of $1000 \text{ e}^-/\text{nm}^2$, the electron diffraction pattern exhibited intense diffraction spots. After a dosage of $26000 \text{ e}^-/\text{nm}^2$, however, the diffraction spots disappeared and only diffuse scattering was observed. Because soft matter is sensitive to beam damage, electron dosage must be carefully minimized to preserve the microstructure of the pristine sample.

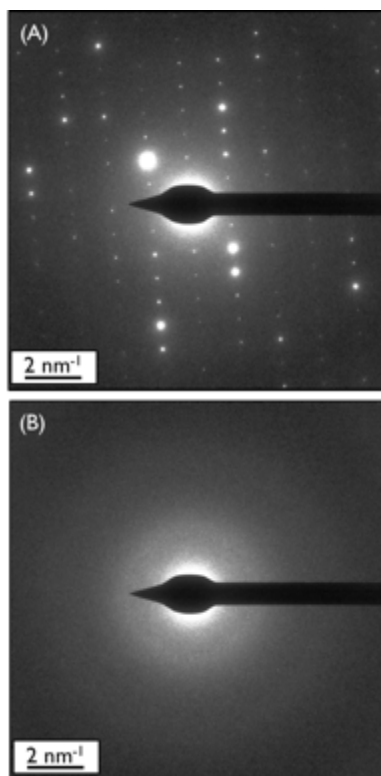


Figure 2.4. Electron diffraction pattern of a spin coated phenytoin thin film after a cumulative electron dose of (A) 1000 and (B) 26000 e^-/nm^2 .

2.6.5 Scanning TEM (STEM) and high-angle annular dark-field (HAADF) imaging

The preceding sections detailed imaging and electron diffraction for conventional TEM, in which a parallel and wide beam (relative to the size of the region of interest) irradiates the sample. Alternately, bright- and dark-field images may be collected using scanning transmission electron microscopy (STEM), in which a narrow collimated electron probe (~ 1 nm in diameter) rasters across a region of interest. Instead of placing an objective aperture in the beam path, the bright- and dark-field signals are collected by separate detectors (see Figure 2.5). STEM also offers a third mode of image collection: high-angle annular dark-field (HAADF) imaging. For HAADF imaging, contrast arises from mass-thickness and atomic number variations. Another advantage of STEM is that the narrow electron beam diameter allows sampling of structural features smaller than 10 nm in size, which is necessary to achieve nanoscale spatial resolution for EDS and EELS. Many

modern-day transmission electron microscopes are capable of performing both conventional TEM and STEM.¹⁰⁸

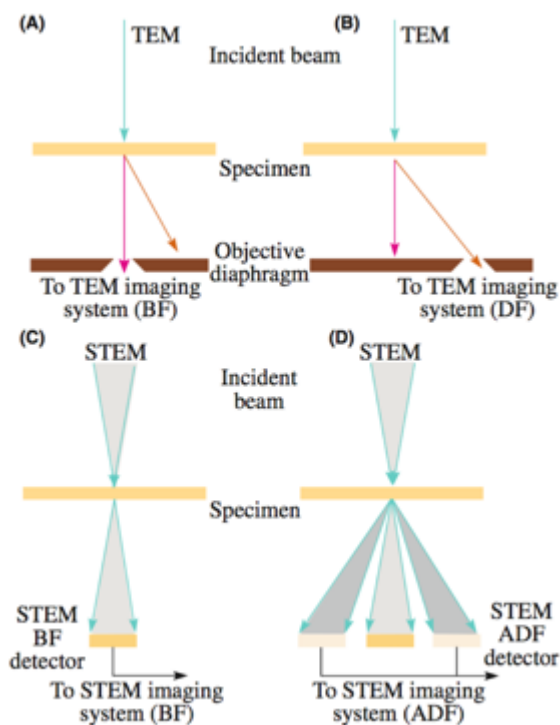


Figure 2.5. Comparison of electron beam optics for conventional TEM and STEM. For conventional TEM, the objective aperture may be shifted to collect either a (A) bright-field (BF) TEM image or (B) a dark-field (DF) TEM images. For STEM, separate detectors record either (C) bright-field STEM images or (D) annular dark-field (ADF) STEM images. Adapted from Williams, D.; Carter, C. *Transmission Electron Microscopy*, 2nd ed; Springer: Boston, 2009. Copyright Springer Science.¹⁰⁸

2.6.6 Energy dispersive X-ray spectroscopy

Although they are routine characterization techniques, TEM imaging and electron diffraction are limited. Imaging forms 2D projections of 3D samples, which may cause ambiguous or incorrect evaluation of nanostructure. Electron diffraction patterns may contain artifacts caused by crystal defects that obscure interpretation of the crystallographic properties of a material. To overcome these shortcomings, analytical electron microscopy

techniques, which characterize secondary signals emitted by the TEM sample, may be used to reveal the chemical composition of a material with high spatial resolution.

The most important secondary signal emitted by a TEM sample is X-ray emission. As an incident electron passes through a material, it penetrates the electron cloud of various atoms. If the incident electron interacts with a core electron and transfers a critical amount of energy, the core electron becomes excited and is ejected into an unfilled energy level, leaving behind an electron hole in the inner shell. To return the atom to its ground state, an outer-shell electron may relax into the hole in the inner-shell. This relaxation results in the emission of various photons, such as an X-ray, with an energy that is “characteristic” of the ionized atom. The emitted X-rays may be collected by an energy dispersive X-ray spectroscopy (EDS) detector that sits above the TEM sample.

Figure 2.6 features an EDS X-ray spectrum of griseofulvin. The spectrum contains four peaks produced by constituent atoms of the molecule: carbon, oxygen, and chlorine. The chlorine peaks (K_α and K_β refer to different types of transitions) serve as characteristic tags that allow for the molecule to be spatially mapped within a SD particle (see Chapter 5). EDS spectra may also be quantitatively analyzed to calculate the local composition of a material. The weight concentration ratio of arbitrary elements A and B, C_A and C_B , are related to the peak intensities by the *Cliff-Lorimer* equations:

$$\frac{C_A}{C_B} = \frac{1}{k_{AB}} \frac{I_A}{I_B} \quad (2.1)$$

$$k_{AB} = \frac{(\sigma\omega a)_A/M_A}{(\sigma\omega a)_B/M_B} \quad (2.2)$$

I_i is the characteristic peak intensity for the i th element, k_{AB} is the *Cliff-Lorimer* factor, σ is the ionization cross-section, ω is the fluorescence yield, a is the relative transition

probability, and M_i is the molecular weight. σ and ω may be approximated by the equations:

$$\sigma = \frac{\pi e^4 b_s n_s}{E_0 E_c} \ln \frac{c_s E_0}{E_c} \quad (2.3)$$

$$\omega = \frac{Z^4}{\zeta + Z^4} \quad (2.4)$$

e is electron charge, E_0 is electron beam energy, E_c is ionization energy, n_s is number of electrons in the ionization subshell, b_s and c_s are ionization constants, Z is atomic number, and ζ is a fluorescence constant.¹⁰⁸

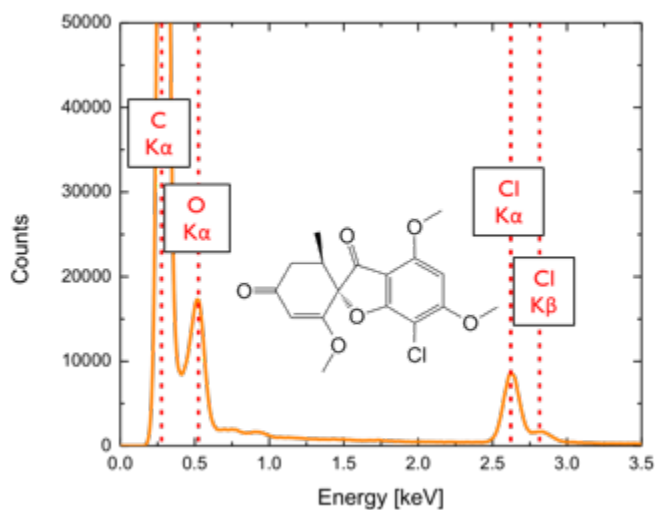


Figure 2.6. Experimental EDS spectrum and chemical structure of griseofulvin. Characteristic peaks are observed for carbon, oxygen, and chlorine. K_α and K_β refer to different types of electron transitions.

2.6.7 Electron energy-loss spectroscopy

Inelastic scattering may also be studied by directly evaluating the transmitted electron beam using electron energy-loss spectroscopy (EELS). In this technique, the

transmitted beam first passes through a magnetic prism that deflects the electrons. Because the deflection angle of the electron is inversely proportional to its kinetic energy, *viz.* speed, the magnetic prism separates the electron beam similar to how a glass prism disperses white light into a rainbow. The dispersed beam then enters an EELS spectrometer. While EDS only evaluates composition, EELS may elucidate composition, chemical bonding, and electronic properties. EELS also achieves better signal-to-noise than EDS because the transmitted electron beam has excellent counting statistics, whereas the rarity of X-ray emission from a TEM sample causes EDS counting statistics to be poor.^{108,109}

Figure 2.7 is an EELS spectrum from a thin film of griseofulvin. The spectrum contains several pieces of unique information. The peak at 0 eV is the zero-loss peak, which is created by electrons that undergo only elastic scattering or no scattering at all. The area between 5 and 50 eV, known as the low-loss regime, assesses electrons that interacted with outer-shell electrons in the material. The intensities in zero-loss peak and low-loss regime are related to sample thickness by:

$$t = \lambda_p \ln \left(1 + \frac{I_{LL}}{I_{ZLP}} \right) \quad (2.5)$$

$$\lambda_p = \frac{2a_0 m_0 v^2}{E_p \ln(1 + \beta^2 / \theta^2)} \quad (2.6)$$

λ_p is the mean free path length of inelastic scattering, I_{LL} is the integrated intensity of the deconvoluted low-loss EELS spectrum, and I_{ZLP} is the integrated intensity of the zero-loss peak spectrum, a_0 is the Bohr radius, m_0 is the rest mass of an electron, v is the velocity of the incident electron (modified to account for relativistic effects), E_p is the plasmon energy, β is the collection semi-angle, and θ is the plasmon scattering angle. For a composite material (such as a polymer blend or a SD), a multiple least-square (MLS) analysis may be used to estimate composition from the low-loss regime. This analysis,

which assumes the low-loss spectrum of the composite is a linear combination of the pure species, may be described by:

$$S_{comp} = \sum_i a_i S_i \quad (2.7)$$

$$a_i = \frac{w_i \xi_i / M_i}{\sum_i w_i \xi_i / M_i} \quad (2.8)$$

i is the index of each component, a_i is a fitting coefficient, and S_i is the reference spectra of the pure drug, w_i is the weight fraction, ξ_i is the inelastic scattering cross section, and M_i is the molecular mass of the pure species.^{110,111,112} The area past 50 eV, known as the high-loss regime, features ionization “edges” created by beam interactions with the core electrons. Similar to peaks in an EDS spectrum, ionization edges may be analyzed to evaluate elemental composition.^{108,109}

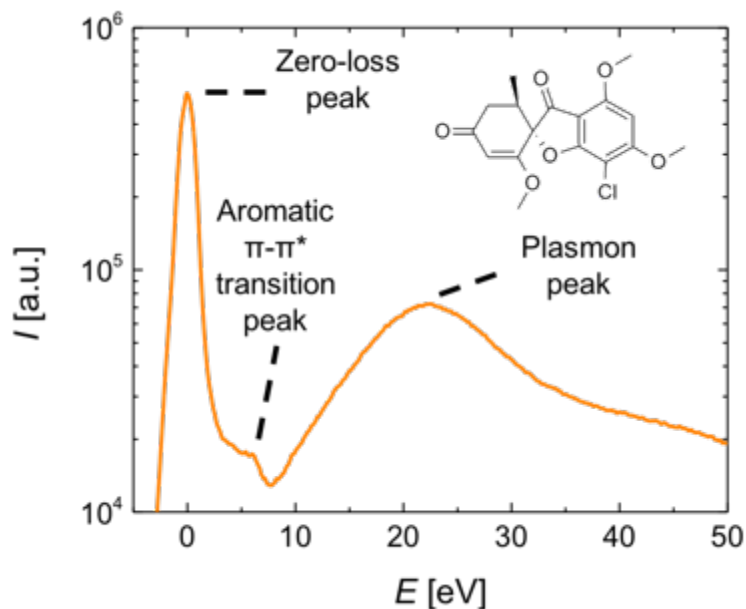


Figure 2.7. Experimental EELS spectrum and chemical structure of griseofulvin. Appearance of π - π^* transition is consistent with aromatic structure of the molecule.

2.6.8 Cryogenic transmission electron microscopy (cryo-TEM)

The high-vacuum environment of a TEM forbids the loading of most liquid samples into the microscope. While there have been recent advances in imaging liquids *in situ* using flow-cell holders,¹¹³ the most practiced strategy for imaging complex fluid nanostructure is thermal fixation. In this method, a small volume of liquid ($< 10 \mu\text{L}$) is placed on a TEM grid. The grid is blotted by filter paper to remove excess liquid and subsequently plunged into a cryogen (*e.g.*, liquid ethane, nitrogen, or helium). Because plunging cools the grid at a rate of $\sim 100,000 \text{ K/s}$, the liquid does not crystallize, which would destroy the fluid structure, but instead vitrifies so that the sample retains its original structure. The sample is then placed into a cryo-transfer holder maintained at cryogenic temperatures and directly imaged. While cryo-TEM is a powerful technique, the sample preparation process and microscope itself may introduce several artifacts that complicate image interpretation. Ice or solvent crystals may form due to incomplete vitrification or poor temperature control.

The cryogenic temperature of the holder may also induce deposition of water vapor or hydrocarbon contaminants onto the sample surface.¹¹⁴

2.6.9 TEM sample preparation and instrumentation

TEM imaging, electron diffraction, and EELS measurements were performed using a FEI Tecnai G2 F30 cryogenic transmission electron microscope at an accelerating voltage of 300 kV. Crystal detection samples were prepared by spreading a small amount of SD from a spatula onto a 300-mesh copper TEM grid that had either a lacey carbon or a thin (15–25 nm) amorphous sheet substrate. EELS samples were prepared using the spin coating method described in Section 2.3.

For the crystal detection measurement (Chapter 3), the sample was cooled to -180 °C using a cryogenic sample holder filled with liquid nitrogen to reduce the rate of beam damage. Electron diffraction patterns, dark-field TEM images, and bright-field TEM images were collected under low-dose conditions to preserve the sample crystallinity. Specifically, particles in a region of interest (ROI) were inspected in bright-field TEM at low magnification ($4700\times$) using an electron dose rate of $\lesssim 10$ e⁻/nm²s. Alignments at a higher magnification ($39,000\times$) were executed on sacrificial areas far removed from the desired ROI. A selected-area aperture was introduced into the electron beam path to reduce the sampled ROI to an area of ~ 1 μm². Selected-area electron diffraction patterns of the ROI were recorded under an electron dose rate of ~ 50 e⁻/nm²s. Dark-field TEM images were collected after centering the objective aperture over selected Bragg peaks in the electron diffraction pattern. Bright-field TEM images were captured after centering the objective aperture over the direct electron beam. Electron diffraction patterns were indexed using the DiffTools plug-in for Gatan DigitalMicrograph.¹¹⁵ Single crystal diffraction patterns of various drugs were simulated using Web Electron Microscopy Applications Software.¹¹⁶

For drug and HPMCAS concentration measurements (Chapter 5), EELS spectra were collected in STEM mode using a post-column Gatan Image Filter. Radiation damage was minimized using the same low-dose condition strategy as the crystal detection measurements. The electron beam energy distribution, defined as the zero-loss peak full-width at half maximum, was 0.9 eV. EELS spectra were collected from ROIs by rastering the electron beam over an area of a chosen size for a collection time of 10 s. For collection area sizes of $200\text{ nm} \times 200\text{ nm}$, $100\text{ nm} \times 100\text{ nm}$, and $50\text{ nm} \times 50\text{ nm}$, the electron dosage was 2800, 11000, and $46000\text{ e}^-/\text{nm}^2$, respectively. HAADF STEM images were recorded after EELS spectra acquisition. Collection of conventional TEM EELS spectra is described in Appendix C.2. EELS spectra were analyzed using custom-made Matlab scripts.

EDS measurements (Chapter 4) were implemented using a FEI Tecnai G2 F30 transmission electron microscope at an accelerating voltage of 300 kV in STEM mode. Samples were made by sprinkling SD powder onto a 300-mesh copper TEM grid with a lacey carbon substrate. EDS spectra were collected at acquisition times of 10 s. Spectrum map data were recorded by collecting EDS spectra from a ROI in a grid pattern where each lattice point was separated by 10 nm. Spectrum maps were analyzed using ImageJ.

Cryo-TEM samples of dissolution media were made using a FEI Vitrobot Mark III automated vitrification device. Glow discharge was applied to a 200-mesh copper TEM grid with a lacey carbon support film to increase the surface energy of the grid. The grid was then placed into the sample chamber of the vitrification device, which had a relative humidity and temperature of 100% and $26\text{ }^\circ\text{C}$, respectively. SD dissolution was initiated using the method described in Section 2.7. After centrifugation of dissolution media at various time points, a $2\text{ }\mu\text{L}$ aliquot of the supernatant was collected and deposited onto the aforementioned TEM grid. The grid was then immediately plunged into a pool of liquid ethane to vitrify the dissolution media. Vitrified samples were stored at cryogenic temperature until imaging. Cryo-TEM imaging and electron diffraction were accomplished using a FEI Tecnai Spirit BioTWIN transmission electron microscope with an accelerating

voltage of 120 kV. The temperature of the sample during imaging was maintained between -179 to -175 °C.

2.7 Microcentrifuge dissolution and solubility assays

For dissolution measurements, a SD was loaded into a 1.5 mL microcentrifuge tube. Phosphate-buffered saline (PBS, 82 mM sodium chloride, 20 mM sodium phosphate dibasic, 47 mM potassium phosphate monobasic, pH 6.5) at 37 °C was added to the microcentrifuge tube to achieve the desired targeted drug concentration (*e.g.*, to achieve a concentration of 1000 $\mu\text{g/mL}$, 12 mL of PBS was added to 12 mg of 10 wt% phenytoin SD). The sample was then mixed in a vortex mixer for 1 min and placed in an isothermal aluminum sample holder at 37 °C. At various time points (4, 10, 20, 40, 90, 180, and 360 min), the sample was centrifuged at 13000 *g* for 1 min. 50 μL of the supernatant was collected and subsequently diluted with 350 μL of methanol. The remaining solution was re-vortexed for 30 s and placed back in the aluminum sample holder until the next time point.

For solubility measurements, 4 mg of crystalline drug (phenytoin or probucol) was loaded into a 1.5 mL microcentrifuge tube with a small stir bar and deluged with 1.2 mL of solution of HPMCAS dissolved in PBS (concentrations of 1, 3, and 9 mg/mL were used). Samples were sealed with ParafilmTM, vortexed for 1 min, placed in a sand bath heated to 37 °C, and stirred for 72 hrs. The samples were then centrifuged at 13000 *g* for 1 min. Aliquots of the supernatant were collected, passed through a 0.25 μm GHP filter, and diluted by 350 μL of methanol.

The diluted aliquots for both dissolution and solubility assays were analyzed by high-performance liquid chromatography using an Agilent 1260 liquid chromatograph system with multi-wavelength UV-vis detection and a reversed-phase EC-C18 column (Poroshell 120, 4.6 \times 50 mm, particle size 2.7 μm , Agilent). The mobile phase was 45:55 and 96:4 (v/v) MeCN/H₂O for SDs containing phenytoin and probucol, respectively. For

both drugs, calibration curves ranging from 10–1000 $\mu\text{g/mL}$ were developed. All dissolution and solubility measurements were repeated in triplicate.

2.8 Light and X-ray scattering of polymer solutions and dissolution media

As shown in Chapter 6, scattering techniques are powerful tools for characterizing not only polymer solutions, but also dissolution media of SDs. By fitting scattering data to appropriate models, nanostructure, polymer-solvent interactions, and polymer-drug interactions can be revealed. The following sections detail scattering techniques that use either light or X-rays as the radiation source.

2.8.1 Basic scattering theory

For all types of radiation, elastic scattering of a plane wave traveling through a molecular mixture is produced by two separate processes. First, concentration fluctuations caused by thermal motion of the particulates in the mixture give rise to incoherent scattering (angle-independent). The amplitude of scattering created by these composition fluctuations (*i.e.*, the scattering power) is proportional to specific material properties. Second, intra- or interparticulate spatial correlations produce scattered waves that have a phase relationship characteristic of the pair correlation function of the scatterers in the material. This coherent scattering (angle-dependent) may be expressed in terms of the scattering vector, \vec{q} :

$$|\vec{q}| = q = \frac{4\pi}{\lambda} \sin\left(\frac{\theta}{2}\right) \quad (2.9)$$

λ is the wavelength of radiation and θ is the angle between incident and scattered waves. q , which has dimensions of inverse length, describes the length scale probed by scattered radiation. For $q^{-1} \ll L$, where L is a relevant length scale of the material, constituents

behave as point scatterers, so no structural information may be obtained. As q^{-1} increases, the influence of structure on the scattering pattern becomes more apparent. This concept may be mathematically expressed as a form factor, $P(q)$.

While the basic physics of scattering is universal to all radiation sources, light and X-ray scattering are distinguished by the relevant material property that defines scattering power and the accessible q range. Scattering power contrast is proportional to the incremental refractive index increment $\left(\frac{\partial n}{\partial c}\right)^2$ for light and electron density for X-ray. The λ and q range for both light and X-ray scattering are listed in Table 2.2.

Table 2.2. Comparison of λ and q for light and X-ray scattering.

Radiation source	λ [nm]	q [nm⁻¹]
Light	350 to 700	0.007 to 0.05
X-rays	0.1 to 1	0.01 to 1

2.8.2 Static light scattering (SLS)

For solutions containing polymers with modest molecular weight ($10^3 \lesssim M_w \lesssim 10^5$ g/mol), the q range probed by light scattering reveals information regarding the size of polymer structures in solution, but not the shape. Intensity of light scattered from a dilute polymer solution may be expressed by Equation 2.10, which is a convolution of three factors: the mean amplitude of the concentration fluctuations, the phase relationship between the scattered waves, and a contrast factor.

$$R_{\theta} = KcM_wP(q)(1 - 2A_2cM_wP(q)) \quad (2.10)$$

$$R_{\theta} = \frac{I_{ex}r^2}{I_0} \quad (2.11)$$

$$K = \frac{4\pi(\partial n/\partial c)^2n^2}{\lambda^4N_A} \quad (2.12)$$

$$P(q) = 1 - \frac{q^2R_g^2}{3} + \dots \quad (2.13)$$

R_{θ} is the Rayleigh ratio (essentially a normalized intensity), K is the optical constant, c is concentration (g/mL), $P(q)$ is the form factor, A_2 is the second virial coefficient, M_w is weight-average molecular weight of the polymer, I_{ex} is the excess scattering intensity, r is the sample-to-detector distance, I_0 is the incident light intensity, n is the solution index of refraction, λ is the wavelength of the incident light, N_A is Avogadro's number, q is the scattering vector, and R_g is the radius of gyration of the polymer in solution. By recasting Equation 2.10 in a linear form, the fundamental *Zimm* equation may be obtained:

$$\frac{Kc}{R_{\theta}} = \frac{1}{M_w} \left(1 + \frac{q^2R_g^2}{3} + \dots \right) + 2A_2c + \dots \quad (2.14)$$

Light scattering data may be analyzed using Equation 2.14 to form a *Zimm* plot (see Figure 2.8).¹¹⁷ By extrapolating the data to both zero-angle and zero-concentration, thermodynamic (M_w and A_2) and structural (R_g) parameters may be simultaneously obtained.^{5,118} To correct for the effect of the third virial coefficient, A_3 , Berry proposed a modified *Zimm* equation that cast A_3 in terms of A_2 :¹¹⁹

$$\sqrt{\frac{Kc}{R_\theta}} = \frac{1}{M_w^{1/2}} \left(1 + \frac{q^2 R g^2}{6} + \dots \right) + 2A_2 c + \dots \quad (2.15)$$

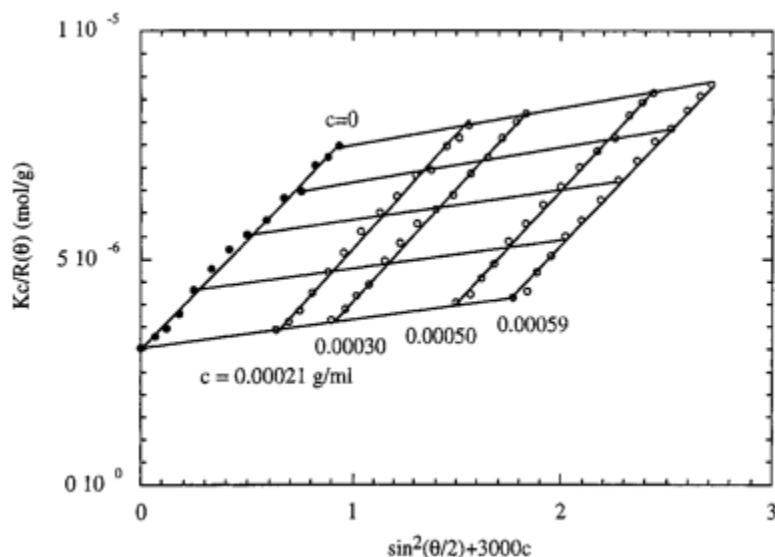


Figure 2.8. Zimm plot of methylcellulose in water at 20 °C. Image adapted from Kobayashi, K.; Huang, C. I.; Lodge, T. P. *Macromolecules* 1999, 32, 7070–7077. Copyright the American Chemical Society.¹¹⁷

2.8.3 Dynamic light scattering (DLS)

The concentration fluctuations that give rise to scattering have a characteristic relaxation time, τ , related to the structure of the particle or particles in solution. τ may be extracted by calculating the second-order time autocorrelation function of the scattering intensity, $g^{(2)}$, and fitting the function to the *Siegert* relation:

$$g^{(2)}(q, t) = \frac{1}{\langle |I_s(\tau)|^2 \rangle} \lim_{T \rightarrow \infty} \left(\frac{1}{T} \right) \int_0^T I_s(\tau) I_s^*(t + \tau) d\tau = 1 + \beta |g^{(1)}(q, t)|^2 \quad (2.16)$$

$g^{(1)}$ is the first-order time autocorrelation functions, I_s is the scattered intensity, t is time, and T is the total time interval.¹¹⁸ Figure 2.9 displays the autocorrelation functions for multicompartiment micelle systems.¹²⁰ To directly calculate τ from Equation 2.15, $g^{(1)}$

must be defined *a priori*. Common $g^{(1)}$ models are a single exponential decay for systems that are monodisperse and double exponential decay for systems that have two well-separated relaxation modes. The distribution may also be estimated by taking an inverse Laplace transform of either $g^{(1)}$ or $g^{(2)}$ (see Figure 2.9B), but this method is prone to producing artifacts. For dilute particle solutions ($c \rightarrow 0$), τ may be related to the particle hydrodynamic radius, R_h , by the equations:

$$R_h = \frac{kT}{6\pi\eta_s D} \quad (2.17)$$

$$D = \frac{1}{q^2\tau} \quad (2.18)$$

k is Boltzmann's constant, T is temperature, η_s is solvent viscosity, and D is the tracer diffusion coefficient.^{5,118}

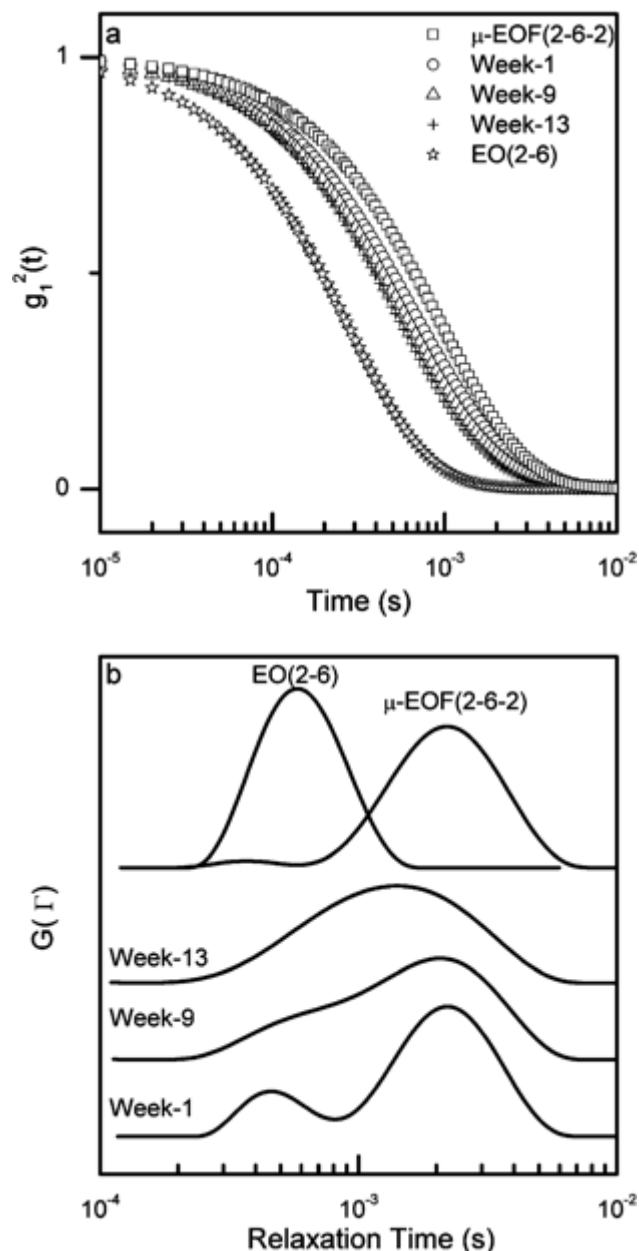


Figure 2.9. (A) Second-order time autocorrelation functions and (B) inverse Laplace transform results for dynamic light scattering measurements of multicompartment micelles at various time points. Adapted from Li, Z.; Hillmyer, M. A.; Lodge, T. P. *Macromolecules* 2006, 39, 765–771. Copyright the American Chemical Society.¹²⁰

2.8.4 Light scattering sample preparation and instrumentation

To prepare samples for static light scattering measurements (Chapter 6), HPMCAS 912 was first dissolved in tetrahydrofuran to form a 2 wt% solids solution. The solution was successively passed through 0.45 and 0.25 μm PTFE filters. The filtered solution was

then spray dried using the process described in section 2.3. The resulting dried polymer was dissolved in PBS to form a stock solution with a concentration of 0.25 mg/mL HPMCAS. Aliquots of the stock solution were subsequently diluted to form 11 additional static light scattering samples that had concentrations ranging from 0.01–0.235 mg/mL HPMCAS. To prepare samples for dynamic light scattering measurements (Chapter 6), HPMCAS 912 was dissolved directly in PBS or tetrahydrofuran to form solutions with a concentration of 9 mg/mL HPMCAS. The solution was then passed through a 0.25 μm filter (GHP or PTFE for PBS and tetrahydrofuran, respectively) into a dynamic light scattering sample tube.

Both experiments were performed using a Brookhaven BI-200SM light scattering instrument with a wavelength of 637 nm, laser power of 30 mW, and an avalanche photodiode detector with a pinhole size set to 1 mm and 200 μm for static light scattering and dynamic light scattering, respectively. Data analysis was performed using custom-made Matlab scripts.

2.8.5 Small-angle X-ray scattering sample preparation and instrumentation

Dissolution media of various SDs were characterized using synchrotron-sourced SAXS (Chapter 6) performed at DND-CAT (beamline 5-ID-D) at the Advanced Photon Source in Argonne National Laboratory (Argonne, IL). The sample-to-detector distance and X-ray wavelength were 8500 nm and 0.729 Å, respectively. Samples were prepared by loading a SD into a 20 mL scintillation vial. PBS at 37 °C was added to the scintillation vial to achieve the desired targeted drug concentration. The vial was vortexed for 1 min and placed in an aluminum vial holder heated to 37 °C. At specific time points (4, 10, 20, 40, 90, 180, and 360 min), the vial was vortexed to remix the dissolution media. Approximately 0.1 mL of the solution was collected and injected into a 1.5 mm quartz capillary. The solution was re-inserted into the vial holder and held at 37 °C. The aliquot

capillary was immediately placed in a multi-capillary heating stage set to 37 °C. 2D SAXS scattering patterns were then recorded and subsequently integrated to form 1D intensity (arbitrary units) vs. q . SAXS data analysis was performed using custom-made Matlab scripts.

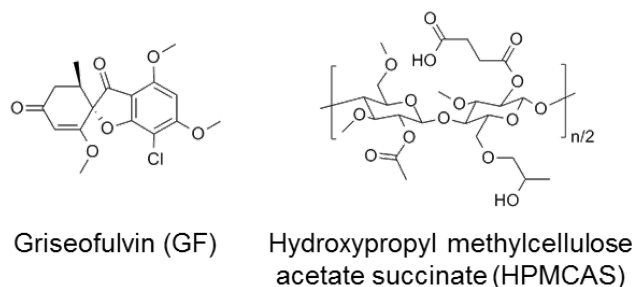
Chapter 3: Detection of pharmaceutical drug crystallites in solid dispersions by transmission electron microscopy[†]

3.1 Introduction

Trace levels of drug crystallinity (≈ 5 vol%) within a SD are hypothesized to have a damaging influence on solubility enhancement. However, the traditional methods for characterizing crystallinity in solid dispersions (i.e., wide-angle X-ray scattering and differential scanning calorimetry) lack the sensitivity for detecting small amounts of crystals. To overcome this limitation, I demonstrate the use of TEM for evaluating the crystallinity of solid dispersions. The model API is griseofulvin (GF), a well-studied drug that has a strong tendency to crystallize.^{121,122} The model excipient is hydroxypropyl methylcellulose acetate succinate (HPMCAS), one of the most promising excipients.^{41,42} The molecular structures of GF and HPMCAS are shown in Scheme 3.1. The crystallinity of GF/HPMCAS solid dispersions are assessed using WAXS, differential scanning calorimetry, and TEM. We compare the crystal detection sensitivity of each of the techniques, and use TEM to directly observe small amounts of nanoscale crystals in solid dispersions of GF and HPMCAS.

[†] Reproduced and modified with permission from Ricarte, R.G.; Lodge, T.P.; Hillmyer, M.A. *Molecular Pharmaceutics* **2015**, *12*, 983–990.

Scheme 3.1. Molecular structures of griseofulvin (GF) and hydroxypropyl methylcellulose acetate succinate (HPMCAS).



3.2 Experimental details

3.2.1 Materials

Griseofulvin (GF) (Sigma-Aldrich, 97+%) and tetrahydrofuran (Acros Organics, 99.9%, stabilized with BHT) were used as received. Hydroxypropyl methylcellulose acetate succinate (HPMCAS) (AFFINISOL™ 126 G, 14 wt% acetate, 6 wt% succinate, The Dow Chemical Company) was dried under vacuum at 70 °C for at least 12 h prior to use.

3.2.2 Preparation of solid dispersions by spray drying

Solid dispersions of varying GF loading were prepared by spray drying. Solid dispersions with GF loadings of 5, 10, and 50 wt%, spray dried GF (pure drug), and spray dried HPMCAS (pure polymer) were used for this study. For each sample, the required amounts of GF and HPMCAS were first dissolved in tetrahydrofuran to form a precursor solution that had a total solids loading of 2 wt%. The precursor solution was then sprayed by a mini spray dryer (Bend Research) using the following operating conditions: nitrogen flow rate = 12.8 L/min, inlet temperature = 68 °C, solution flow rate = 0.65 mL/min. The outlet temperature ranged between 24–27 °C. The solid dispersion was collected from filter paper in the spray dryer and subsequently dried under reduced pressure at ambient temperature for at least 12 h. Solid dispersions were stored in a desiccator under reduced

pressure at ambient temperature until use. The resultant particle morphologies were investigated using scanning electron microscopy (see Appendix A.1). A physical mixture containing 3 vol% spray dried GF (pure drug) and 97 vol% spray dried HPMCAS (pure polymer) was prepared by mixing the two solid components with a mortar and pestle.

3.2.3 *Wide-angle X-ray scattering (WAXS)*

Approximately 50 mg of solid dispersion were loaded into a 0.5 mm-deep zero-background sample holder and analyzed at ambient temperature by a Bruker-AXS D5005 diffractometer with a Cu K α source ($\lambda = 1.54 \text{ \AA}$). The operating voltage and current were 45 kV and 40 mA, respectively. Diffraction patterns were collected from a scattering vector (q) range of 4–28 nm⁻¹ with a scan rate of 0.01 nm⁻¹s⁻¹. Overall crystallinity was estimated by dividing the area of the Bragg peaks after background subtraction by the total area of the diffraction pattern (this ratio corresponds to vol%), while the crystal grain size was calculated using the Scherrer equation, a routine procedure.¹⁰⁷

3.2.4 *Modulated differential scanning calorimetry (MDSC)*

MDSC was run using a Discovery DSC (TA Instruments). 5–8 mg of solid dispersion were placed inside TzeroTM aluminum pans with standard lids. While under nitrogen gas with a flow rate of 50 mL/min, each sample was heated from 0–160 °C using the following parameters: average temperature heating rate = 1 °C/min, temperature modulation amplitude = 1 °C, temperature modulation period = 40 s. During this heating cycle, total, reversing, and non-reversing heat flow curves were recorded. The solid dispersion glass transition temperature (T_g) was determined from the reversing heat flow curve, while the crystallization temperature and enthalpy (T_c and ΔH_c , respectively) were estimated from the non-reversing heat flow curve. All solid dispersions were examined by MDSC in triplicate.

3.2.5 Transmission electron microscopy (TEM)

TEM analysis of solid dispersions was performed using a FEI Tecnai G2 F30 cryogenic transmission electron microscope at an accelerating voltage of 300 kV. Samples were prepared by spreading a small amount of solid dispersion from a spatula onto a 300-mesh copper TEM grid with either a lacey carbon or a thin (15 to 25 nm) amorphous carbon substrate film. To reduce the rate of electron beam damage, the sample was cooled to -180 °C by using a cryogenic sample holder filled with liquid nitrogen. To preserve the crystallinity of the particles in each TEM sample, low-dose conditions were used to obtain electron diffraction patterns, dark-field TEM images, and bright-field TEM images. Briefly, particles in a region-of-interest (ROI) were first surveyed in bright-field TEM at low magnification ($4700\times$) using an electron dose rate of $\lesssim 10 \text{ e}^-/\text{nm}^2\text{s}$. Focusing and beam alignment at a higher magnification ($39,000\times$) were performed on a sacrificial area far removed from the desired ROI. A selected-area aperture was inserted into the electron beam path to restrict the field of view to an area of $\sim 1 \mu\text{m}^2$. Selected-area electron diffraction patterns of the ROI were then collected using an electron dose rate of $\sim 50 \text{ e}^-/\text{nm}^2\text{s}$. Dark-field TEM images were recorded after centering the objective aperture on various diffraction spots in the electron diffraction pattern. Bright-field TEM images were finally obtained after centering the objective aperture on the direct electron beam. Electron diffraction patterns were evaluated with the DiffTools plug-in for Gatan DigitalMicrograph.¹¹⁵ Kinematical simulations of GF single crystal diffraction patterns were performed using Web Electron Microscopy Applications Software.¹¹⁶

3.2.6 *In situ* WAXS

In situ WAXS diffraction patterns of 10 and 50 wt% GF solid dispersions were recorded by a Bruker D8 Discover diffractometer with a Cu K α source filtered with a nickel foil ($\lambda = 1.54 \text{ \AA}$). Approximately 50 mg of solid dispersion were loaded into a 0.8 mm-deep, zero-background, temperature-controlled sample holder. The sample holder was

inserted into the sample chamber and immersed under nitrogen gas with a flow rate of 15 mL/min. First, a diffraction pattern was recorded with the sample stage at 25 °C. Second, the sample stage was heated at a rate of 1 °C/min to an elevated temperature above the T_c of the solid dispersion (130 °C for 50 wt% GF solid dispersion and 140 °C for 5 and 10 wt% GF solid dispersions). Third, diffraction patterns were recorded continuously over a period of at least 2 h. After *in situ* WAXS, the sample was removed from the sample holder, ground into a powder using a spatula, and analyzed by TEM.

3.2.7 Growth of GF crystals from a 50 wt% GF solid dispersion on a TEM grid

Glow discharge was performed on a TEM grid with a thin amorphous carbon substrate film to increase the surface energy of the film.^{123,124} The TEM grid was exposed to plasma for 1 min at a pressure of 500 millitorr and 50 DC amperes. A 50 wt% GF solid dispersion was then deposited on the modified TEM grid. Using a temperature-controlled oven, the sample was heated from 0 to 130 °C at a ramp rate of 1 °C/min and held at 130 °C for 12 h. The sample was then removed from the oven and analyzed by TEM.

3.3 Results

3.3.1 Wide-angle X-ray scattering of solid dispersions

Representative WAXS patterns of GF/HPMCAS solid dispersions with varying GF loadings are shown in Figure 3.1. The sharp Bragg peaks in the diffraction pattern of spray dried GF indicate that the sample is highly crystalline. From these data, the overall crystallinity and minimum crystal grain size of spray dried GF were estimated to be 90 vol% overall and 50 nm, respectively. Conversely, the WAXS patterns of 5, 10, and 50 wt% GF solid dispersions are broad with no clear Bragg peaks. This is typically attributed to fully amorphous drug in the solid dispersion.^{125,126,127} The practical lower limit of crystal detection for laboratory-scale WAXS experiments, however, is approximately 5 vol% overall.⁶⁰ This reported detection limit is corroborated by our WAXS study of a physical

mixture of 5 vol% GF and 95 vol% hydroxypropyl methylcellulose (Figure 3.2). Therefore, these diffraction patterns only confirm that the 5, 10, and 50 wt% GF solid dispersions have an overall crystallinity lower than 5 vol%. Consistent with these observations, the WAXS diffraction pattern of a physical mixture of 3 vol% spray dried GF and 97 vol% spray dried HPMCAS showed no clear Bragg peaks, even though the WAXS diffraction pattern of spray dried GF shows that it is mostly crystalline. Thus, WAXS can detect crystals in the spray dried GF, but cannot conclusively establish the complete absence of crystals in the GF/HPMCAS solid dispersions.

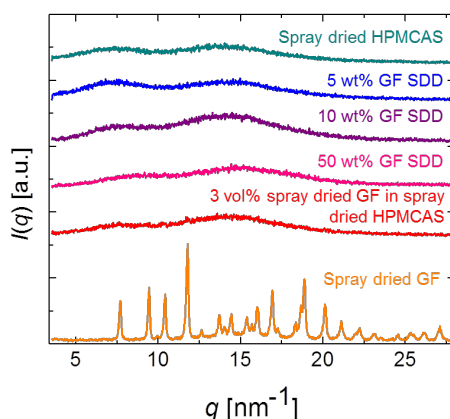


Figure 3.1. WAXS of solid dispersions with varying GF loading. Curves were vertically shifted for clarity. Spray dried GF (orange curve) has sharp Bragg peaks, indicating the presence of crystal domains. Spray dried HPMCAS, and 5, 10, and 50 wt% GF solid dispersions (teal, blue, pink, and purple curves, respectively) do not exhibit Bragg peaks. The physical mixture of 3 vol% spray dried GF in spray dried HPMCAS (red curve) also does not exhibit Bragg peaks.

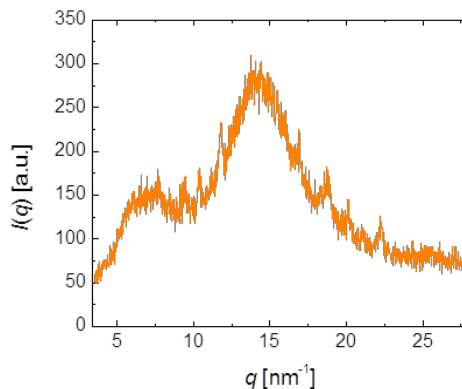


Figure 3.2. WAXS of the physical mixture of 5 vol% GF and 95 vol% hydroxypropyl methylcellulose. The broad Bragg peaks confirm that the lower limit of detection for our WAXS studies is ~ 5 vol%.

3.3.2 MDSC of solid dispersions

Figure 3.3 shows the modulated differential scanning calorimetry (MDSC) heat flow curves for 5, 10, and 50 wt% GF solid dispersion samples. In MDSC the total heat flow curve mimics the conventional DSC heat curve, the reversing heat curve accounts for changes in the heat capacity of the sample, and the non-reversing heat curve catalogs all other thermal events.¹²⁸ The T_g values of the solid dispersions correspond to the inflection point of the increase in the reversing heat flow curves. The 5, 10, and 50 wt% GF solid dispersions each only exhibit single T_g values at 110, 100, and 84 °C, respectively, suggesting that GF is molecularly dispersed throughout the polymer matrix in the solid dispersions.

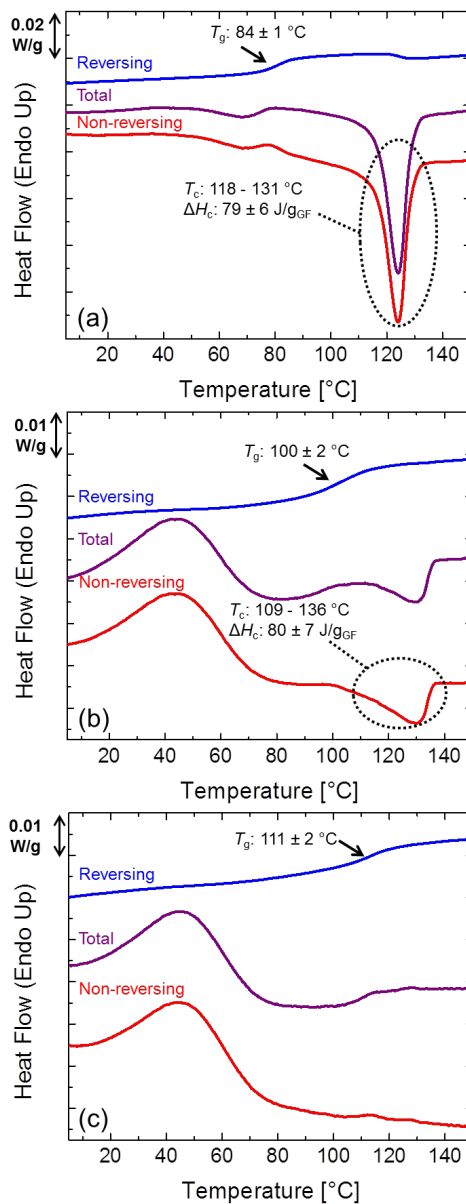


Figure 3.3. Modulated DSC heat flow curves of GF solid dispersions. Data were recorded upon first heating using an average temperature heating rate of 1 °C/min, a temperature modulation amplitude of 1 °C, and a temperature modulation period of 40 s. The reported T_g s, T_c s, and ΔH_c s represent the average of three DSC experiments, while the error bars represent the standard deviation. Curves were vertically shifted for clarity. (a) 50 wt% GF solid dispersion exhibits crystallization over a temperature range of 118 to 131 °C, while (b) 10 wt% GF solid dispersion displays crystallization over a temperature range of 109 to 136 °C. (c) 5 wt% GF solid dispersion does not show crystallization of the GF.

The total and non-reversing heat flow curves of the 50 wt% GF solid dispersion feature a sharp exothermic peak that is attributed to crystallization of GF (Figure 3.3a), with T_c range and ΔH_c of 118 to 131 °C and 79 J/g_{GF}, respectively. From the MDSC data, the degree of crystallinity was estimated by taking the ratio of ΔH_c of the solid dispersion to the $\Delta H_{melting}$ of pure GF. This ratio corresponds to wt%. To convert wt% to vol%, we assumed that all the GF in the solid dispersion was initially non-crystalline (as justified by the TEM analysis) and that the density of amorphous GF is 5% less than the density of crystalline GF, a typical value for APIs.^{129,130,131} The overall crystallinity of the entire 50 wt% GF solid dispersion after MDSC analysis was approximately 40 vol%. Furthermore, the reversing heat flow curve exhibits a decrease that coincides with T_c . This decrease was attributed to the expectation that crystalline GF should have a lower heat capacity than amorphous GF. The total and non-reversing heat flow curves of 10 wt% GF solid dispersion feature a broad crystallization peak with a T_c range of 109 to 136 °C (Figure 3.3b). The crystallinity of the entire 10 wt% GF solid dispersion after MDSC analysis was estimated to be approximately 5 vol% overall. In contrast to the higher GF loading solid dispersions, the 5 wt% GF solid dispersion does not exhibit a crystallization peak in its total and non-reversing heat flow curves (Figure 3.3c).

The 5 and 10 wt% GF solid dispersions also exhibit a broad endothermic peak around 40 °C in both total and non-reversing heat flow curves. This peak, which appears in several other studies,^{132,133,134} has been attributed to evaporation of bound water,¹³⁵ but we are not aware of any direct evidence that supports this hypothesis. Although the origin of this peak is ambiguous, annealing the sample at 80 °C prior to the full MDSC scan does not affect the T_g or crystallization of the solid dispersion (Figure 3.4). In summary, the MDSC data suggest the GF in the 10 and 50 wt% GF solid dispersions can crystallize upon heating, while the 5 wt% GF solid dispersion does not show any crystallization behavior.

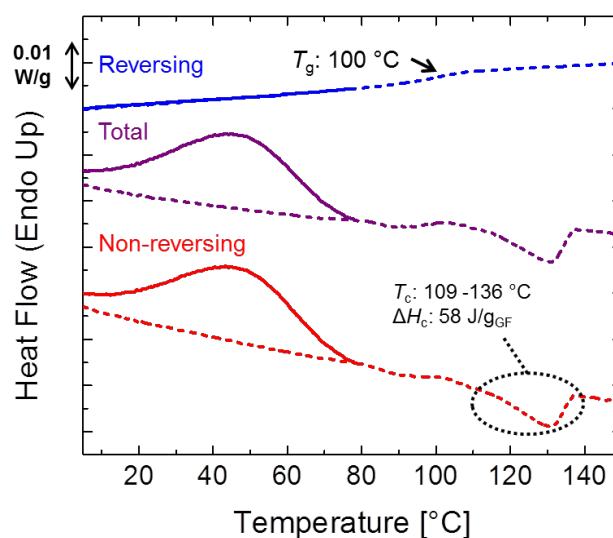


Figure 3.4. Modulated DSC heat flow curves of 10 wt% GF solid dispersion. When the solid dispersion was initially heated to 80 °C (solid lines), total and non-reversing heat curves exhibited an endothermic peak from 5 – 80 °C. After cooling the solid dispersion to 0 °C and then heating it to 150 °C, the endothermic peak disappeared. The T_g , T_c , and ΔH_c exhibited upon second heating were consistent with previously recorded values.

3.3.3 TEM of spray dried GF

Figure 3.5 shows TEM analysis of a spray dried GF particle. The ill-defined morphology of the spray dried GF particle observed in bright-field TEM (Figure 3.5a) is consistent with the scanning electron microscopy data (Appendix A.1). The presence of sharp diffraction spots in the electron diffraction pattern confirms that the observed particle is crystalline (Figure 3.5b). Furthermore, the indices of the 1-D intensity profile of the electron diffraction pattern match the indices of the WAXS diffraction pattern of bulk spray dried GF (Figure 3.5d), verifying that the particle is composed of GF crystals. Particles that produce fewer diffraction spots were also indexed to verify the presence of GF crystals (see Appendix A.2). Dark-field TEM of the particle provides real-space information about the GF crystals (Figure 3.5c); the intensely white regions correspond to the crystal domains of the particle that produce the diffraction pattern. The circle on Figure 3.5b (and all

subsequent diffraction patterns) indicates the location of the objective aperture during the dark field image acquisition.

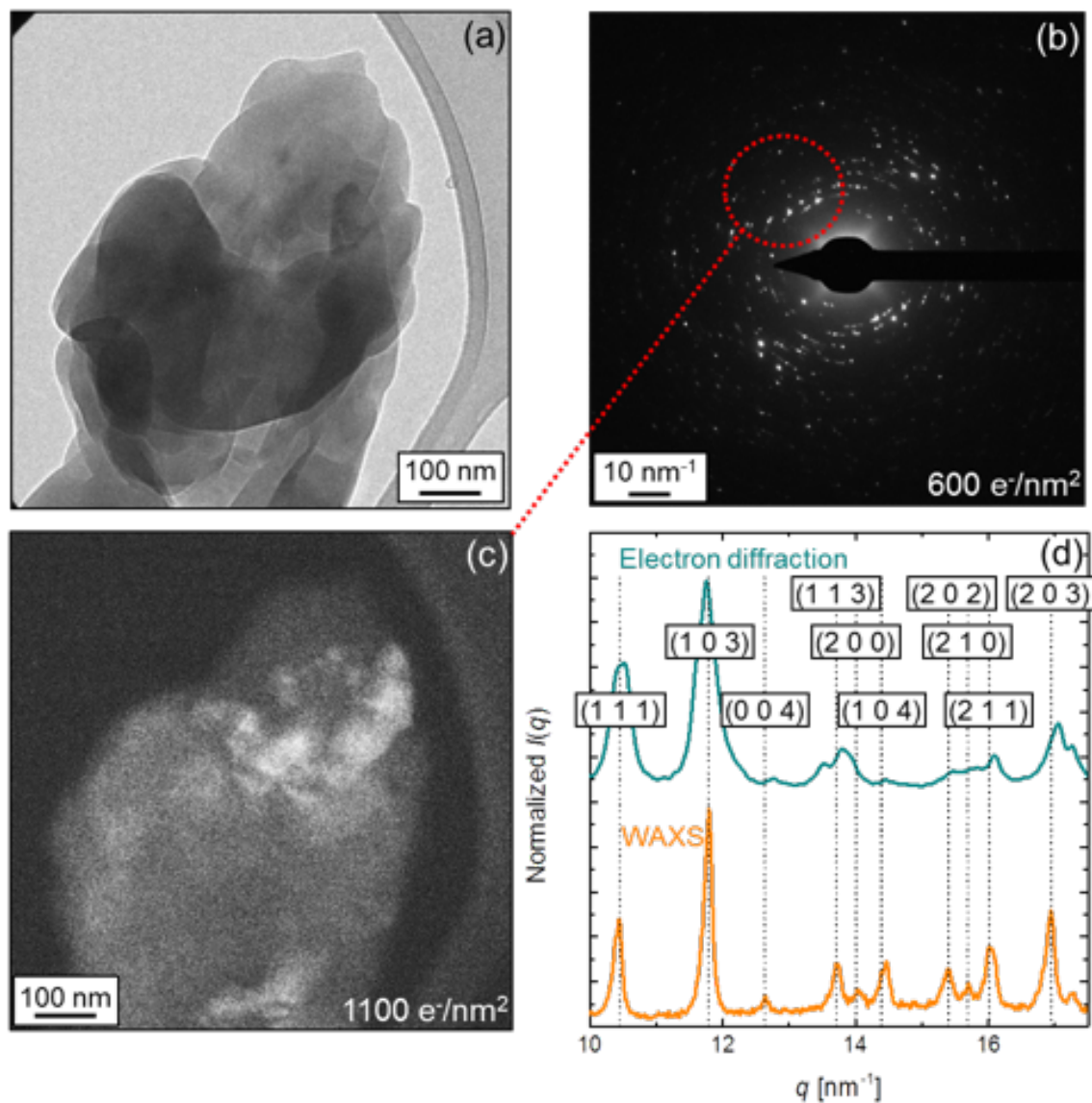


Figure 3.5. (a) Bright-field TEM of a spray dried GF particle. (b) Electron diffraction pattern of the spray dried GF particle in (a). The scale bar is the scattering vector. The value in the lower right-hand corner is the cumulative electron dose. (c) Dark-field TEM of the particle identifies the domains that produce the reflections encircled in (b). (d) The 1-D intensity profile of the electron diffraction pattern matches the WAXS diffraction pattern of bulk spray dried GF. Curves were shifted for clarity.

Figure 3.6 shows the TEM analysis of the physical mixture of 3 vol% spray dried GF and 97% vol% spray dried HPMCAS. Unlike WAXS, TEM identified GF crystals throughout the physical mixture, as evidenced by the electron diffraction pattern, dark-field image, and diffraction pattern indices of selected particles in the sample. This analysis demonstrates the improved crystal detection sensitivity of TEM over WAXS.

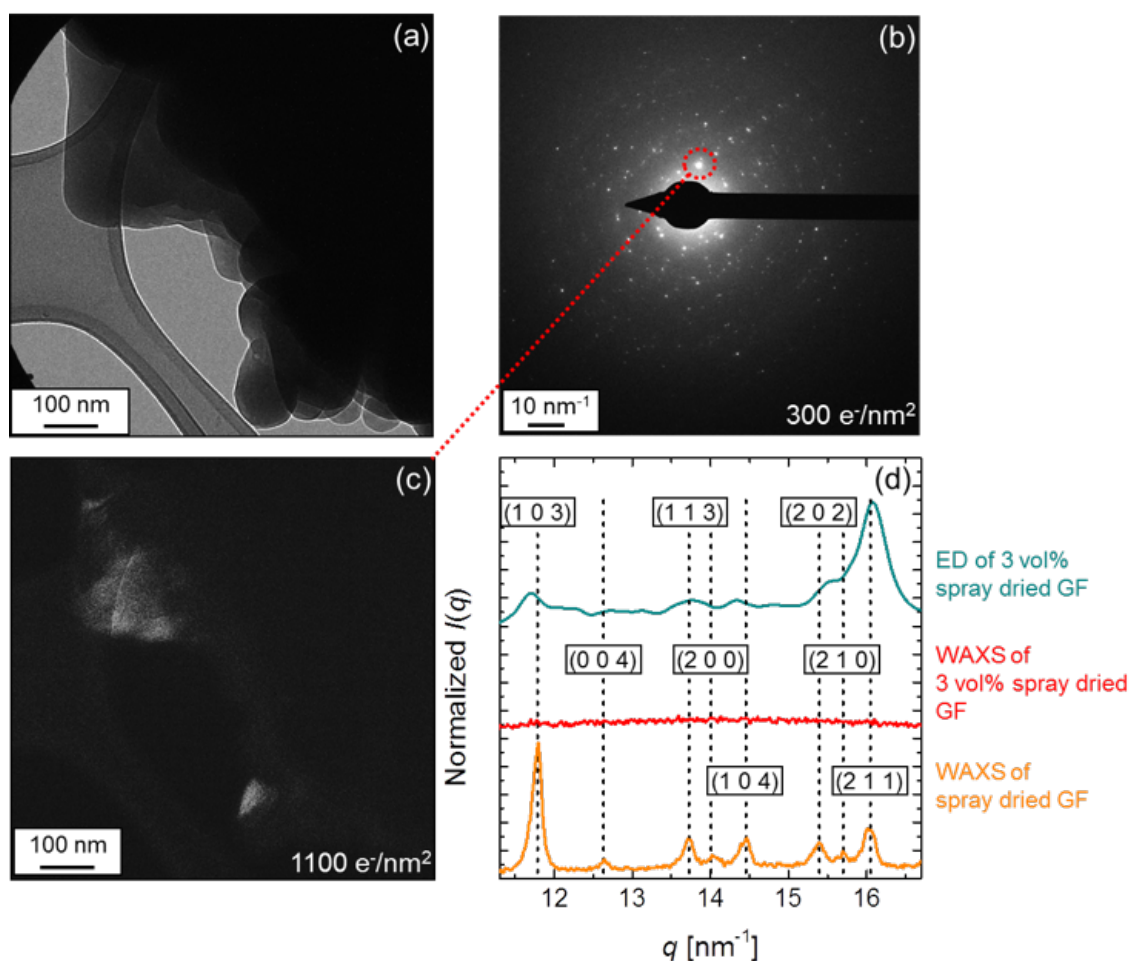


Figure 3.6. (a) Bright-field TEM of particles in a 3 vol% spray dried GF in spray dried HPMCAS physical mixture. The (b) electron diffraction pattern and (c) dark-field TEM of the particles confirm the presence of crystals in the ROI, while (d) the peak positions of the electron diffraction pattern 1-D intensity profile coincide with the peaks of the WAXS diffraction pattern of spray dried GF. The curves in (d) were vertically shifted for clarity.

3.3.4 TEM analysis of solid dispersions

We examined GF/HPMCAS solid dispersions using TEM to further evaluate the crystallinity and to complement the WAXS studies. With TEM we did not detect GF crystals in any of the solid dispersions (Figure 3.7), corroborating the WAXS results. Annealing of GF solid dispersions on a temperature-controlled sample stage during *in situ* WAXS analysis was performed to induce GF crystallization. Following *in situ* WAXS, the annealed samples were studied by TEM. Figure 3.8a features the *in situ* WAXS analysis of a 50 wt% GF solid dispersion. While the WAXS diffraction pattern of the solid dispersion is initially smooth, sharp Bragg peaks appear upon annealing, confirming the growth of GF crystals. Based on the WAXS diffraction pattern, the overall crystallinity and minimum crystal grain size after annealing were estimated to be 40 vol% (consistent with the MDSC results) and 40 nm, respectively. TEM analysis of the post-annealed *in situ* WAXS sample (Figures 3.8b, 3.8c, and 3.8d) further verified the presence of GF crystals.

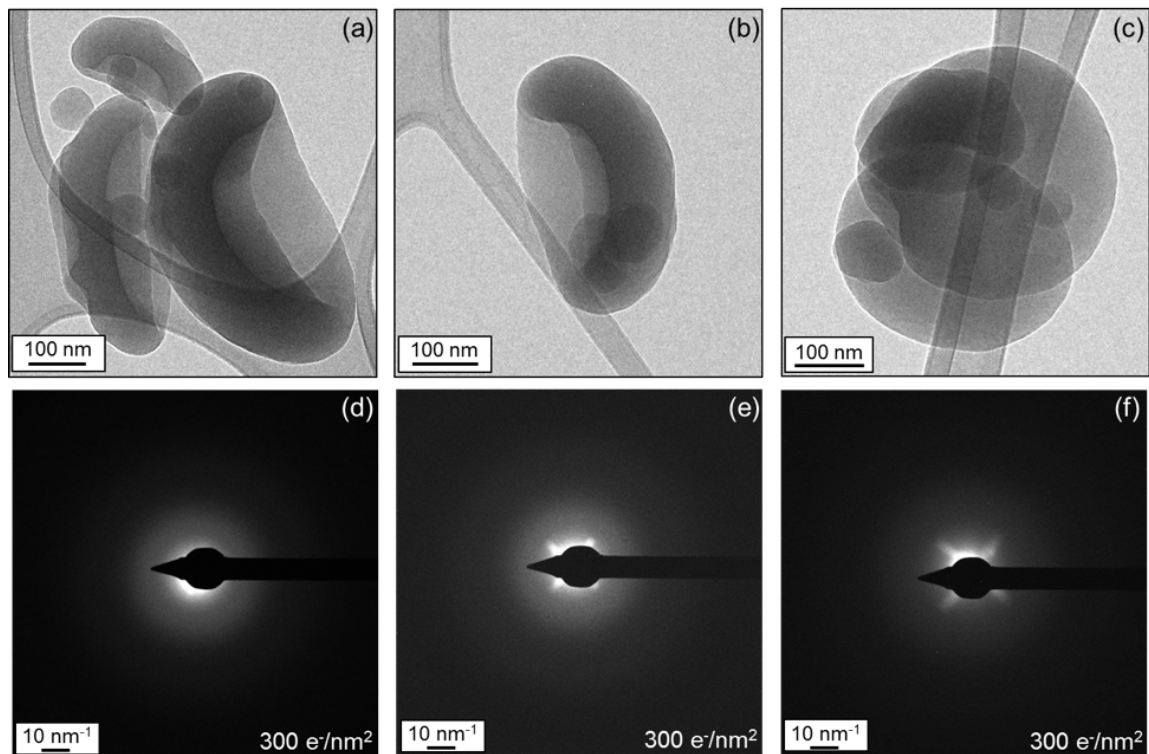


Figure 3.7. Bright-field TEM images of (a) 5, (b) 10, and (c) 50 wt% GF solid dispersion particles. The corresponding electron diffraction patterns of (d) 5, (e) 10, and (f) 50 wt% GF solid dispersion particles do not exhibit sharp diffraction spots, indicating the GF in the particles is fully amorphous.

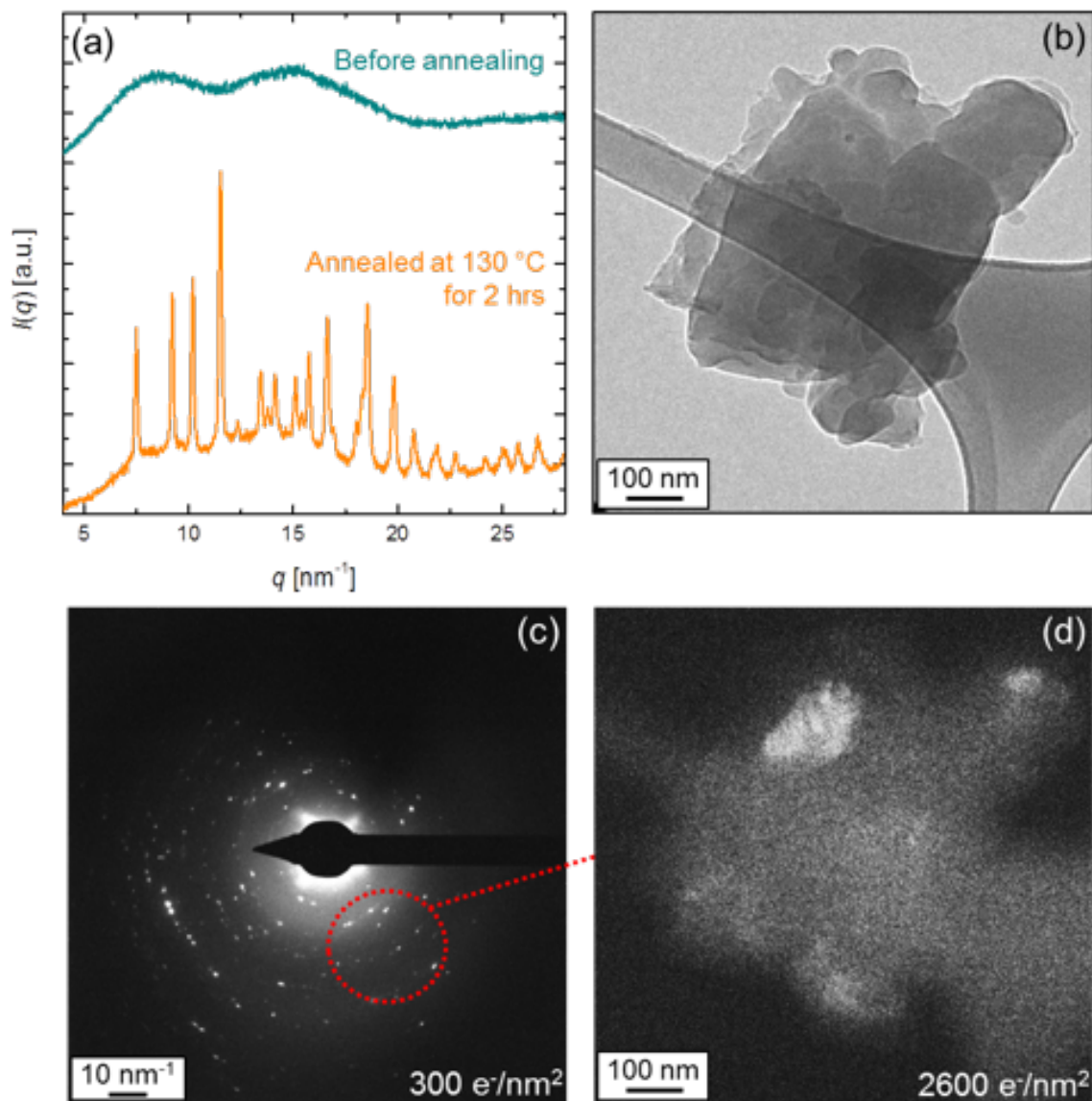


Figure 3.8. (a) *In situ* WAXS of 50 wt% GF solid dispersion before and after annealing at 130 °C. (b) Bright-field TEM, (c) electron diffraction, and (d) dark-field TEM provide direct observation of crystals in the post-annealed *in situ* WAXS sample. The dark-field TEM image in (d) is sampled from the circled diffraction spots in (c).

Figure 3.9a presents the *in situ* WAXS analysis of 5 wt% GF solid dispersion. Consistent with the MDSC analysis, no clear Bragg peaks developed during annealing. Yet, TEM analysis of the post-annealed *in situ* WAXS sample (Figures 3.9b, 3.9c, and 3.9d) uncovered GF crystals in the specimen. We also analyzed the data from an annealed 10 wt% GF solid dispersion (Figure 3.10) and were able to uncover GF crystals in that

sample as well. These results demonstrate that TEM has superior crystal detection sensitivity as compared to both WAXS and MDSC.

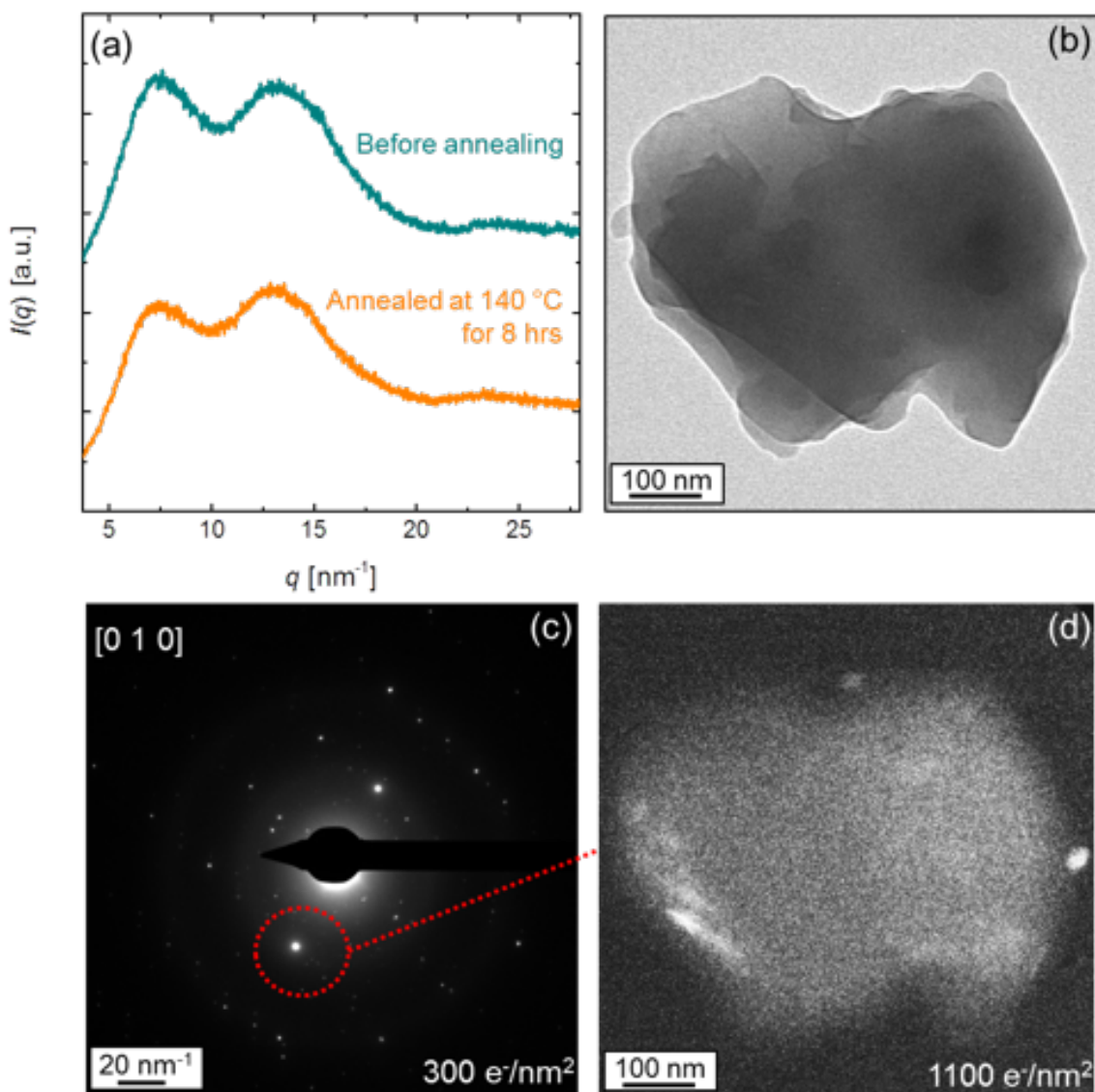


Figure 3.9. (a) *In situ* WAXS of 5 wt% GF solid dispersion before and after annealing at 140 °C. Similar to the modulated DSC results, the diffraction patterns of the sample during annealing do not show signs of crystallinity. (b) Bright-field TEM, (c) electron diffraction, and (d) dark-field TEM reveal that some particles in the post-annealed *in situ* WAXS sample contained GF crystals.

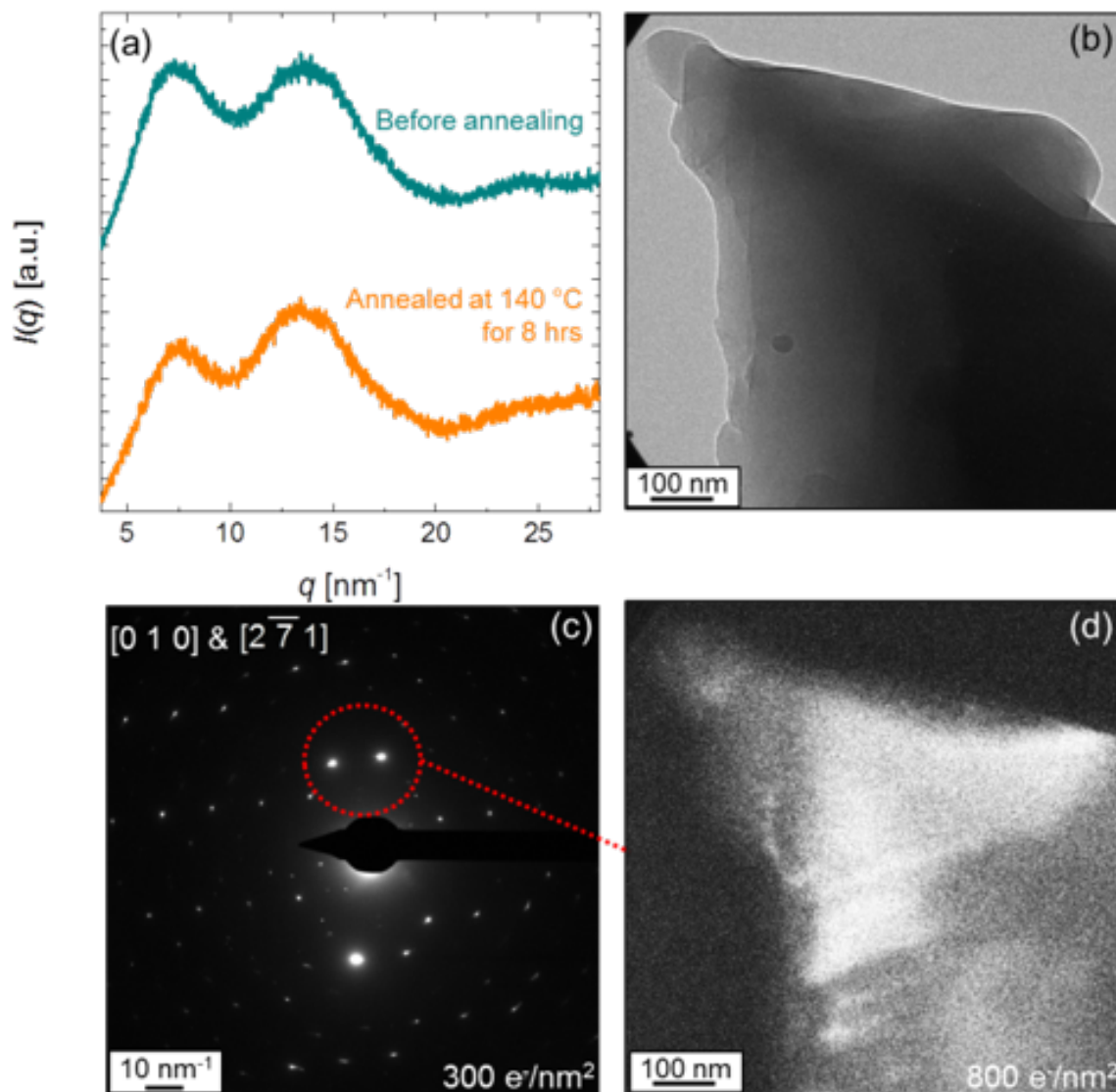


Figure 3.10 (a) *In situ* WAXS of 10 wt% GF solid dispersion before and after annealing at 140 °C. The diffraction patterns of the sample during annealing do not show signs of crystallinity, disagreeing with the modulated DSC results. (b) Bright-field TEM, (c) electron diffraction, and (d) dark-field TEM confirm that some particles in the post-annealing *in situ* WAXS sample are crystalline.

To further explore the utility of TEM for studying solid dispersions, a TEM sample of 50 wt% GF solid dispersion was thermally annealed in an oven to induce the growth of GF crystals. Though some particles did not exhibit crystallization and instead formed droplets (Figure 3.11), GF crystals were detected. Figure 3.12 features a narrow (~ 300 nm wide) GF crystal that grew from the remnants of a solid dispersion particle. Large GF

crystals ($\sim 30 \mu\text{m}$ long) were also observed (Figure 3.13). This analysis of the *in situ* growth of GF crystals suggests that the mechanism of crystal growth in a solid dispersion could be studied by TEM.

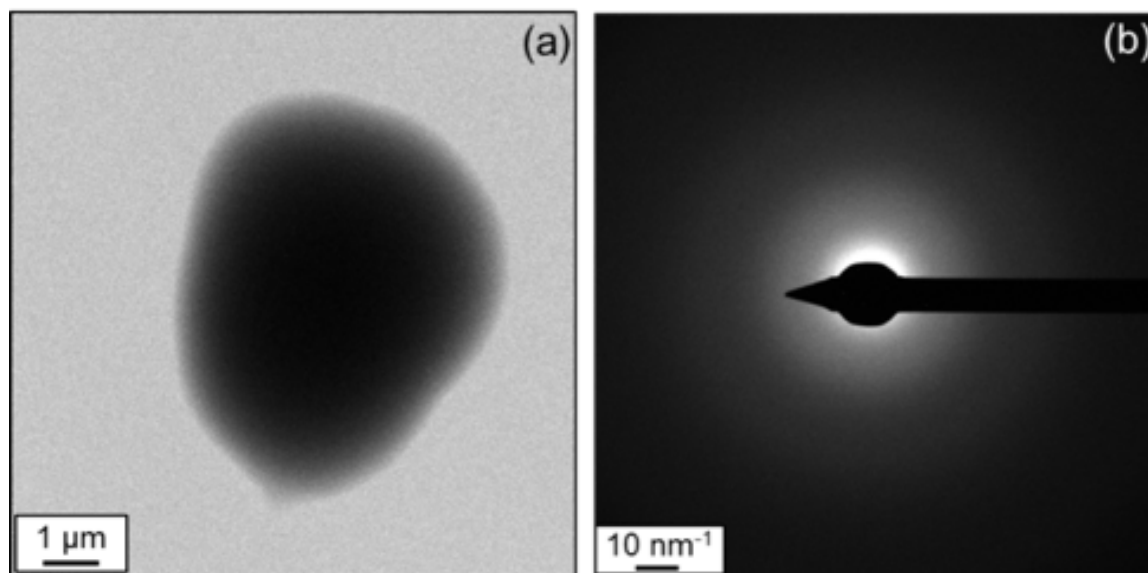


Figure 3.11. (a) Bright-field TEM image and (b) electron diffraction pattern of droplet observed in the post-annealed TEM sample of 50 wt% GF solid dispersion. Lack of clear diffraction spots indicates the droplet is amorphous.

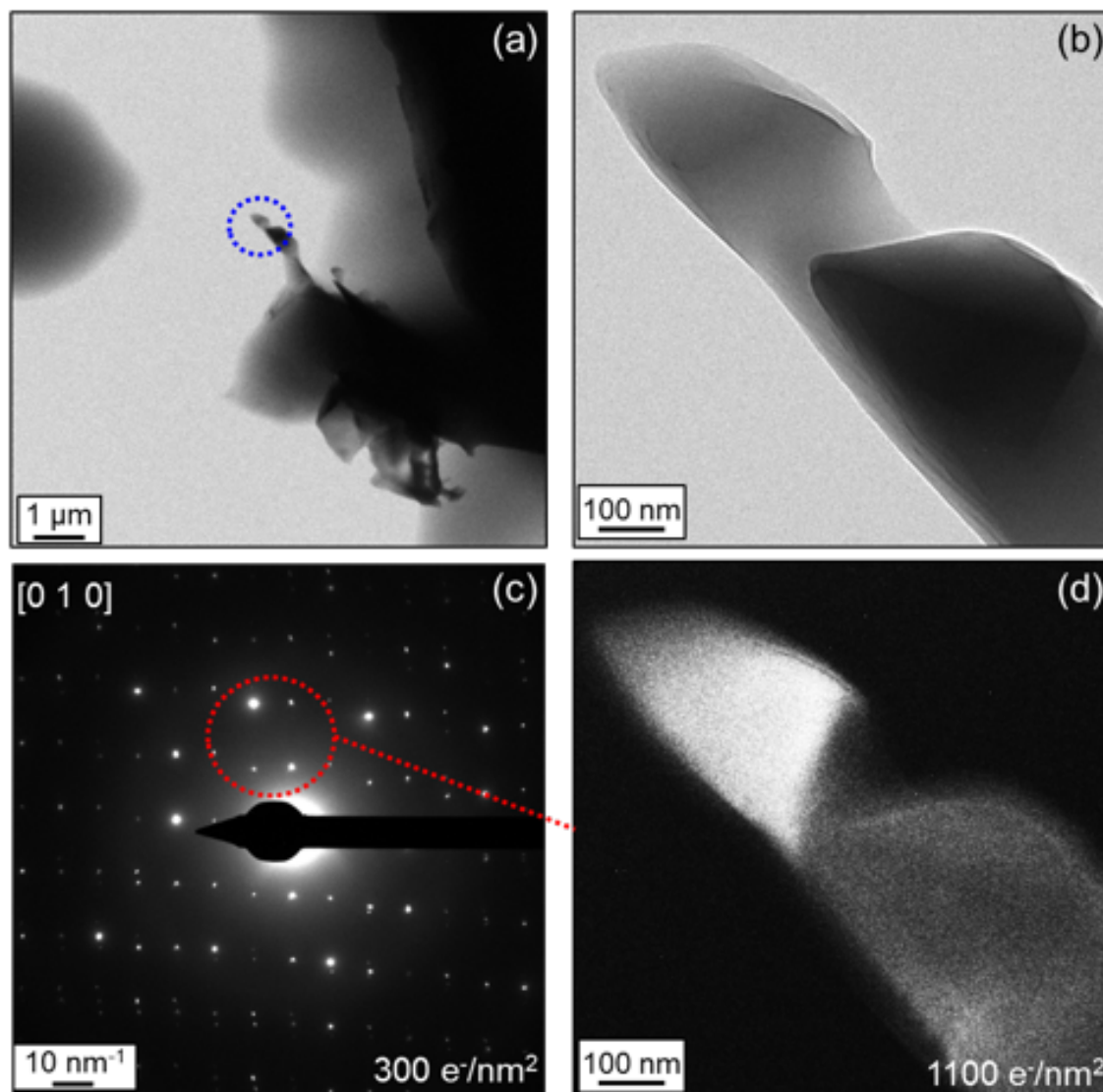


Figure 3.12. (a) Bright-field TEM of 50 wt% GF solid dispersion that was annealed on a TEM grid at 130 °C for 12 hrs. The circled region is captured at a higher magnification in (b). The (c) electron diffraction pattern and (d) dark-field TEM confirm the aforementioned region is crystalline.

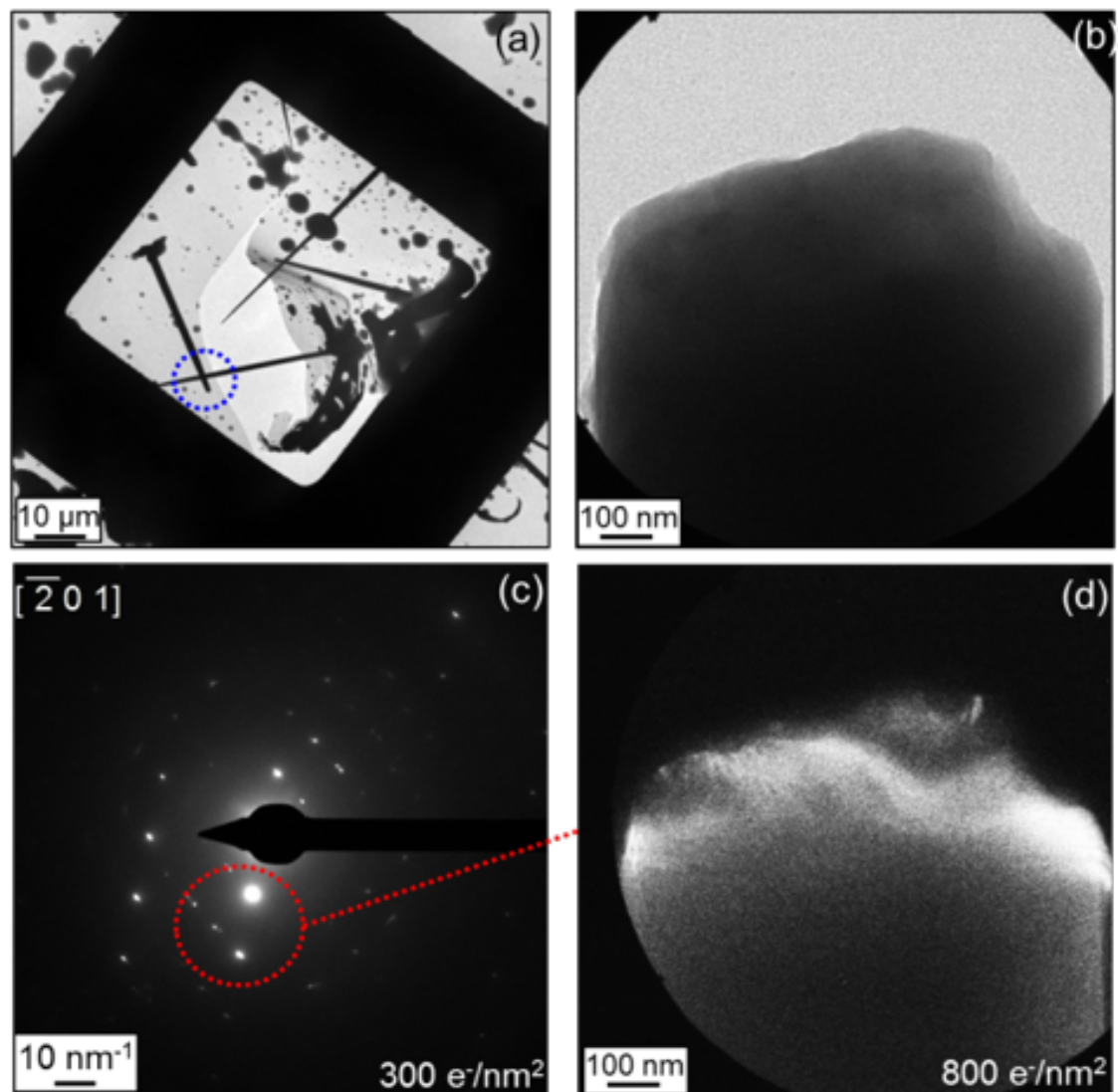


Figure 3.13. (a) Bright-field TEM of a large crystal (30 μm long) in the post-annealed TEM sample of 50 wt% GF solid dispersion. The circled region is magnified in (b). The (c) electron diffraction pattern and (d) dark-field TEM image confirm the crystal is GF.

3.4 Discussion

TEM offers substantial advantages over WAXS, MDSC, and other microscopy techniques for detecting crystals in solid dispersions. First, as demonstrated by the physical mixtures and solid dispersions of GF and HPMCAS, TEM achieves significantly improved crystal detection sensitivity. Second, TEM offers nanoscale spatial resolution. Unlike optical microscopy techniques, TEM can detect crystals that are smaller than the diffraction-barrier of visible light.⁶⁶ Electron diffraction patterns have been recorded from

nanoparticles as small as 5 nm.¹³⁶ This spatial resolution allows for single-particle screening of drug crystals. Additionally, because organic molecules typically have a critical nucleation diameter of ~ 10 to 20 nm,⁵ I expect that any drug crystal in a solid dispersion should be large enough to produce a distinguishable electron diffraction signal. Third, TEM can identify drug crystals in a wide variety of drug-excipient pairs. Since electron diffraction patterns provide crystal structure information, drug crystals in a solid dispersion may be unambiguously identified and located. Fourth, TEM offers fast and facile data collection. Image and diffraction pattern acquisition take seconds. TEM grids may hold thousands of particles; assuming the particles that stick to the grid are representative of the entire ensemble, a statistically significant amount of particles may be sampled.

Beam damage, however, is a major challenge for using TEM to study solid dispersions. GF, like most organic materials,¹³⁷ is sensitive to the electron beam of a transmission electron microscope; exposure to the beam ultimately destroys GF crystals (see Appendix A.3). Therefore, a low electron dose must be used to preserve any possible drug crystals. Nevertheless, when paired with other techniques, TEM analysis offers complementary information about the structural and thermodynamic properties of solid dispersions. For GF/HPMCAS solid dispersions, our TEM study of the post-annealed *in situ* WAXS samples suggests that the equilibrium solubility of GF in AFFINISOL™ 126 G HPMCAS is less than 5 wt%. I also performed preliminary FT-IR studies to further probe the specific chemical interactions between GF and HPMCAS (see Appendix A.4).

Furthermore, TEM allowed observation of the diverse structures – *i.e.*, droplets (Figure 3.11) and GF crystals – that developed during the annealing of the TEM sample of 50 wt% GF solid dispersion. We speculate that the structural diversity is caused by heterogeneous distribution of solid dispersion particles throughout the TEM grid. Presumably, when the TEM sample was annealed above the T_g of 50 wt% GF solid dispersion, isolated particles formed small droplets, while particles that touched each other or were agglomerated formed large droplets. The GF in the large droplets should be more

likely to nucleate. A similar mechanism was observed for the nucleation of poly(ethylene oxide) crystals from droplets on an isotactic polystyrene substrate.¹³⁸ Still, more studies must be performed to determine how the structures in this system developed.

While the broader utility of this methodology hinges on the capacity to estimate the degree of crystallinity of a solid dispersion, quantification may be challenging. Prolonged electron beam exposure eradicates API crystals, and crystals with orientation that does not satisfy Bragg's law do not exhibit a diffraction signal. Thus, electron diffraction and dark field imaging may capture only a fraction of crystals within a sampling area. Nevertheless, the strength of this TEM approach is that it probes crystallinity at the local level. Information obtained by TEM is complementary to bulk crystal detection techniques and may provide deep insight into the growth mechanism of API crystals in a solid dispersion.

3.5 Conclusion

We explored the utility of TEM for characterizing crystallinity and structure of solid dispersions. TEM achieves nanoscale spatial resolution and allows for unambiguous identification of drug crystals. Using TEM, we detected GF crystals in annealed solid dispersions, even in cases where WAXS and MDSC failed to detect crystals. Based on our annealing studies, we posit that the solubility of GF in HPMCAS is below 5 wt%, suggesting that GF has poor affinity for HPMCAS. The *in situ* growth of GF crystals in a TEM sample of 50 wt% GF solid dispersion was also achieved. Due to the high spatial resolution and sensitivity, TEM is a powerful and complementary tool for evaluating solid dispersions and potentially other nanoengineered pharmaceutical materials.

Chapter 4: Energy-dispersive X-ray spectroscopy of solid dispersions

4.1 Introduction

Solid dispersions (SDs) are designed so that the active pharmaceutical ingredient (API) and polymer excipient form a homogeneous material. However, standard techniques for characterizing SD miscibility, such as differential scanning calorimetry, cannot confirm if the two species intimately mix at the nanoscale (see Appendix B). To overcome this limitation, I explored the use of energy-dispersive X-ray spectroscopy (EDS) to evaluate spatial distribution of the API griseofulvin (GF) within a HPMCAS SD. First, simulations of the scanning transmission electron microscopy (STEM) beam trajectory through GF are performed to predict the spatial resolution of the technique. Then, X-ray spectrum maps of GF SDs are collected to demonstrate that spatial distribution can be evaluated. Finally, EDS spectra are quantitatively analyzed to determine if the concentration sensitivity of the technique is sufficient for detecting phase separation in SDs.

4.2 Experimental details

4.2.1 Materials

Griseofulvin (GF) (Sigma-Aldrich, 97+%) and tetrahydrofuran (Acros Organics, 99.9% stabilized with BHT) were used as received. Hydroxypropyl methylcellulose acetate succinate (HPMCAS) (AFFINISOL™ HPMCAS 126G, 14 wt% acetate, 6 wt% succinate,

The Dow Chemical Company) was dried at reduced pressure at 70 °C for at least 12 h prior to use.

4.2.2 Preparation of solid dispersions by spray drying

Solid dispersions (SDs) with GF loadings of 1, 5, 10, 50 wt%, spray dried GF, and spray dried HPMCAS were used in this study. To prepare each sample, GF and HPMCAS were first dissolved in tetrahydrofuran to form a 2 wt% solids solution. The precursor solution was then sprayed by a mini spray dryer (Bend Research) using a nitrogen flow rate of 12.8 L/min, inlet temperature of 68 °C, and solution flow rate of 0.65 mL/min. The outlet temperature, which was not controlled, fluctuated between 24–27 °C. The solid dispersion was collected from filter paper set at the outlet of the spray dryer, dried under reduced pressure at ambient temperature for at least 12 h, and stored in a desiccator under reduced pressure at ambient temperature until use.

4.2.3 STEM electron beam trajectory simulations

Monte-Carlo simulations of the scanning transmission electron microscopy (STEM) electron beam trajectory through a sample of GF was performed using the software CASINO v3.2.¹³⁹ 10^6 electrons with an accelerating voltage of 300 kV were simulated, while the initial electron beam diameter was set to 5 nm. The simulated electron trajectory data were analyzed using custom-made MatlabTM (version R2012a) scripts.

4.2.4 STEM EDS sample preparation and instrumentation

TEM samples were prepared by spreading SD powder onto a TEM grid with a lacey carbon support film. STEM EDS measurements were performed using a FEI Tecnai G2 F30 transmission electron microscope at an accelerating voltage of 300 kV. Spectra were acquired using 10 s collection times. Spectrum map data were recorded by collecting EDS

spectra from several spots, separated by 10 nm each, in a region-of-interest. Spectra maps were analyzed using ImageJ.

4.3 Results and discussion

4.3.1 Simulations of STEM electron beam trajectory

Because the expected critical nucleation size for an API crystal is ~ 10 nm,⁵ phase separation between API and excipient is posited to occur on a similar length scale. To determine if EDS can resolve features at this spatial resolution, the trajectory of the incident electrons passing through a TEM sample of GF were modeled. Using the software CASINO v3.2,¹³⁹ the trajectories of 10^6 incident electrons with an energy of 300 kV were simulated (Figure 4.1A). As the electrons penetrated deeper into the sample, they scattered from C, O, and Cl atoms of GF, causing the electron beam diameter (defined as the full-width half-maximum (FWHM) of the incident electron radial distribution) to spread. As seen in Figure 4.1B and Table 4.1, the electron beam diameter was ~ 10 nm at sample depths below 300 nm (approximately the upper end of thickness for TEM samples). This suggested EDS can achieve a sufficient spatial resolution for resolving phase separated domains in a SD.

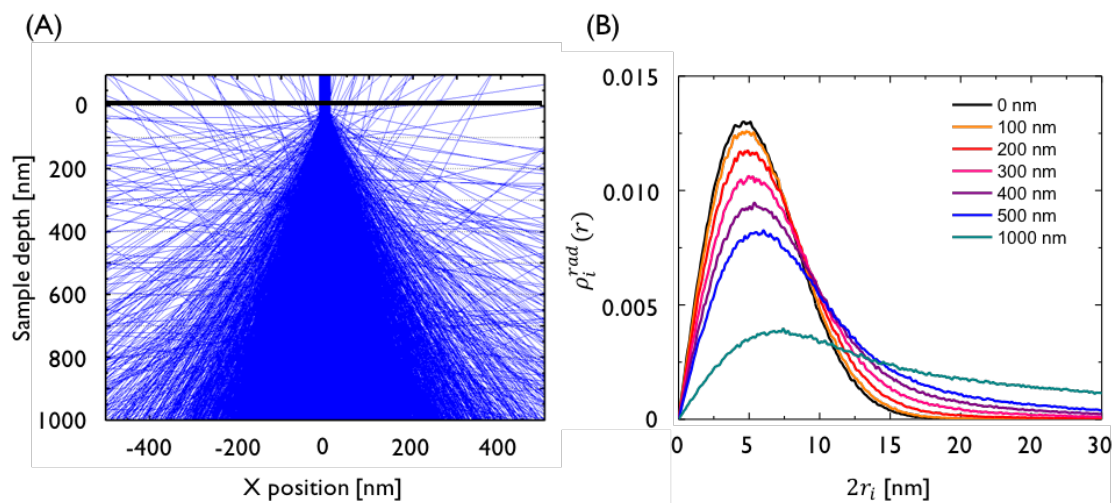


Figure 4.1. (A) Simulated trajectories of 10^6 300 kV incident electrons traveling through a GF sample. (B) Spatial distribution of electrons at various sample depths. r_i is the distance of the electron from the beam center, while ρ_i^{rad} is the fraction of electrons at a particular distance. The initial electron beam diameter was 5 nm.

Table 4.1. Full-width half-maximum (FWHM) of incident electrons at various sample depths.

Sample depth [nm]	FWHM [nm]
0	5
100	6
200	8
300	12
400	16
500	21
1000	52

4.3.2 Elemental spectrum maps of griseofulvin and HPMCAS

Figure 4.2 compares experimental EDS spectra of spray dried HPMCAS and GF particles. The spectra, normalized by the total area under the curve, contained peaks representative of the constituent atoms of each molecule. While HPMCAS and GF are both

comprise C and O atoms, only GF contained Cl atoms. The Cl peaks in the GF EDS spectra served as a signal that qualitatively distinguished API from excipient.

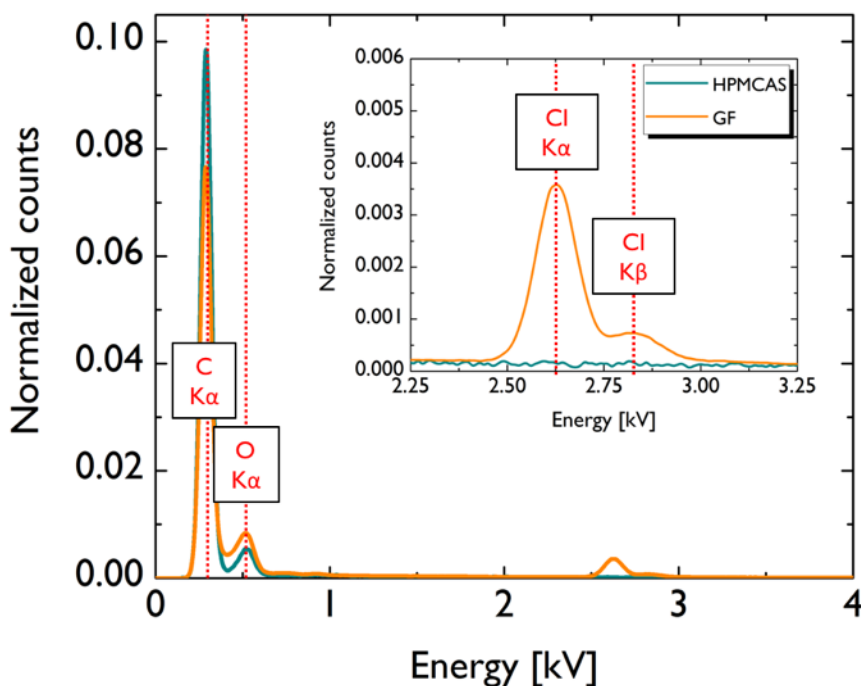


Figure 4.2. Comparison of EDS spectra for HPMCAS and GF. Inset is a magnification of the Cl peaks.

EDS spectrum maps of the Cl $K\alpha$ peak enabled evaluation of the spatial distribution of GF. To create a spectrum map, EDS spectra were collected from discrete spots (arranged in a grid like manner and separated by 10 nm) in a region-of-interest. The C, O, and Cl $K\alpha$ peaks of each spectra were integrated and visualized in a spectrum map (each pixel represents a single spectrum). Figure 4.3 features elemental spectrum maps of a spray dried GF particle adhered to the lacy carbon support film of the TEM grid. Both the particle and support film are seen in the C $K\alpha$ map, but only the particle is detected in O and Cl $K\alpha$ maps. Cl maps of spray dried HPMCAS (Figure 4.4) showed that the particles completely

disappeared, thereby demonstrating that Cl correlated with the presence of GF and not polymer.

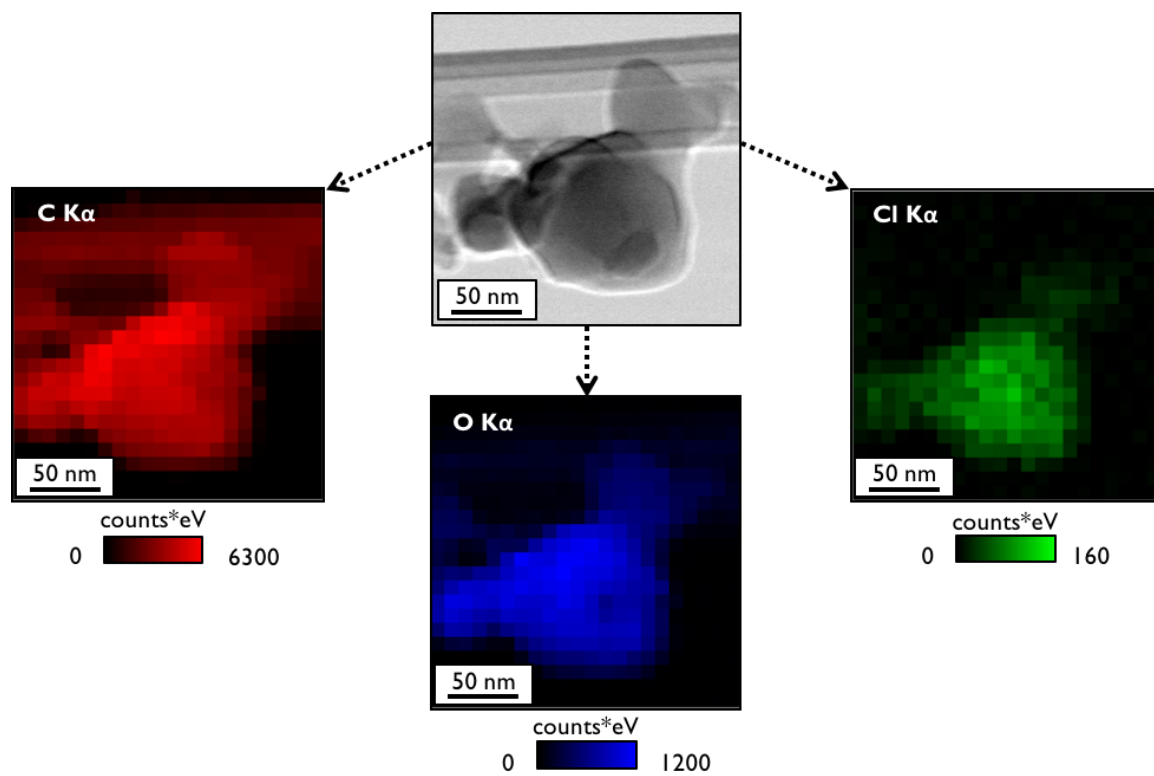


Figure 4.3. HAADF TEM image (middle-top) and elemental maps of a spray dried GF particle. The spatial distribution of C, O, and Cl may be isolated.

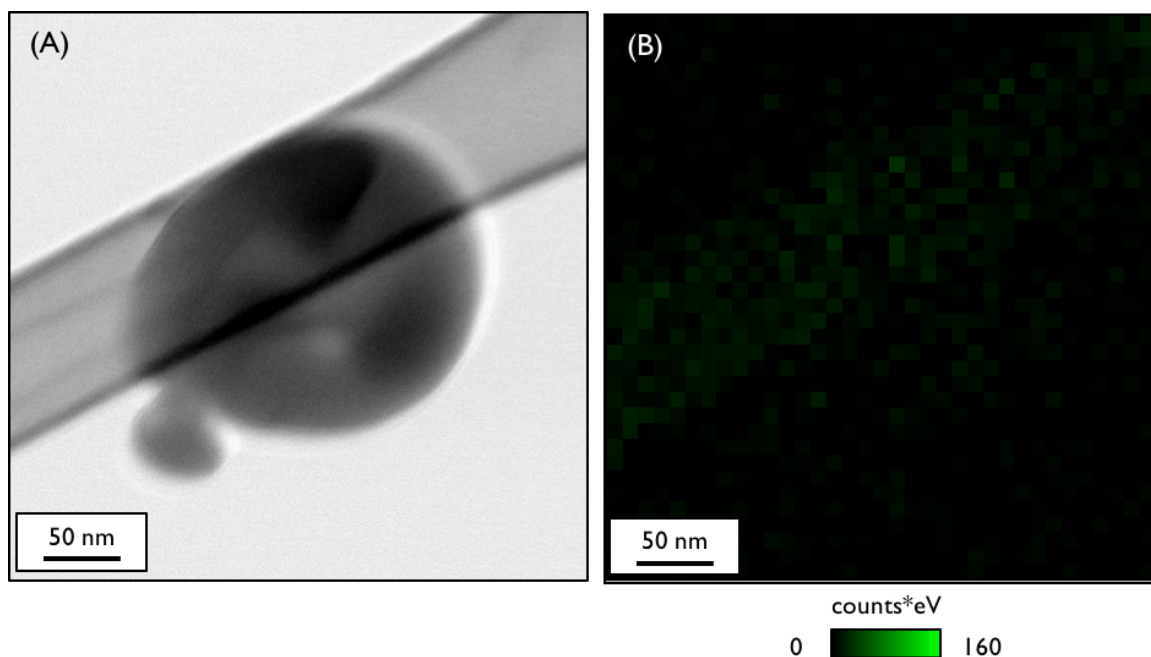


Figure 4.4. (A) HAADF TEM image and (B) Cl K α map of a spray dried HPMCAS particle. The particle cannot be seen in the Cl map.

EDS characterization of 10 wt% GF SDs showed that Cl maps recreated the particles. As seen in Figure 4.5, the Cl signal is isolated to the particle, confirming GF can be detected in the HPMCAS matrix of the SD. Although the uniform Cl signal across the particle implied the spatial distribution of GF was homogeneous, further analyses were needed to evaluate the concentration resolution of EDS.

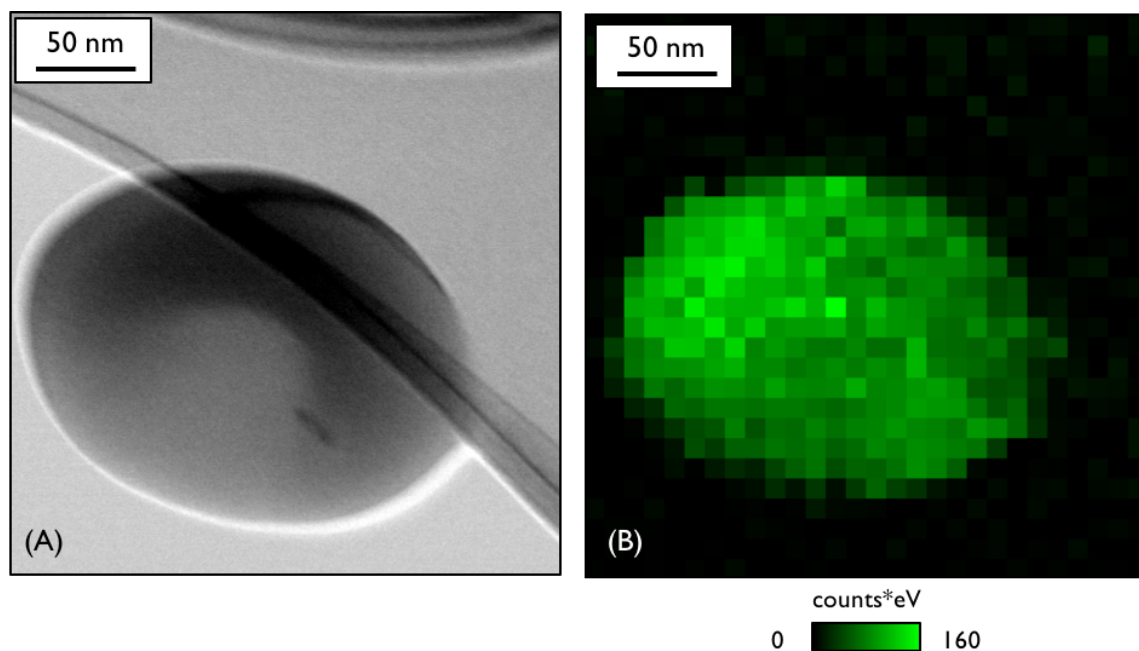


Figure 4.5. (A) HAADF TEM image and (B) Cl K α map of a 10 wt% GF SD particle. The particle is recreated in the Cl map.

4.3.3 Quantification of EDS spectra

The concentration ratio of two distinct elements in a region-of-interest may be quantified by Equations 2.1 and 2.2, which are analogous to Beer's law, although k_{AB} is dependent on the TEM sample and microscope operating parameters. Using these equations, theoretical EDS spectrum for EDS were calculated. Comparison between theoretical and experimental spectra revealed spray dried GF emitted Cl and O signals that have intensities consistent with the predictions, but the C signal intensity was much stronger than expected (Figure 4.6 and Table 4.2). This deviation from theory could be the result of two distinct phenomena. (i) Excess C X-rays were emitted by the TEM grid itself. Although the electron beam was localized on the particle, spurious electrons or X-rays emitted from the sample may have excited electrons in the lacey carbon support film. (ii) The Cl and O X-rays may be absorbed by the particles themselves. Absorption is especially likely to occur in very thick samples.¹⁰⁸

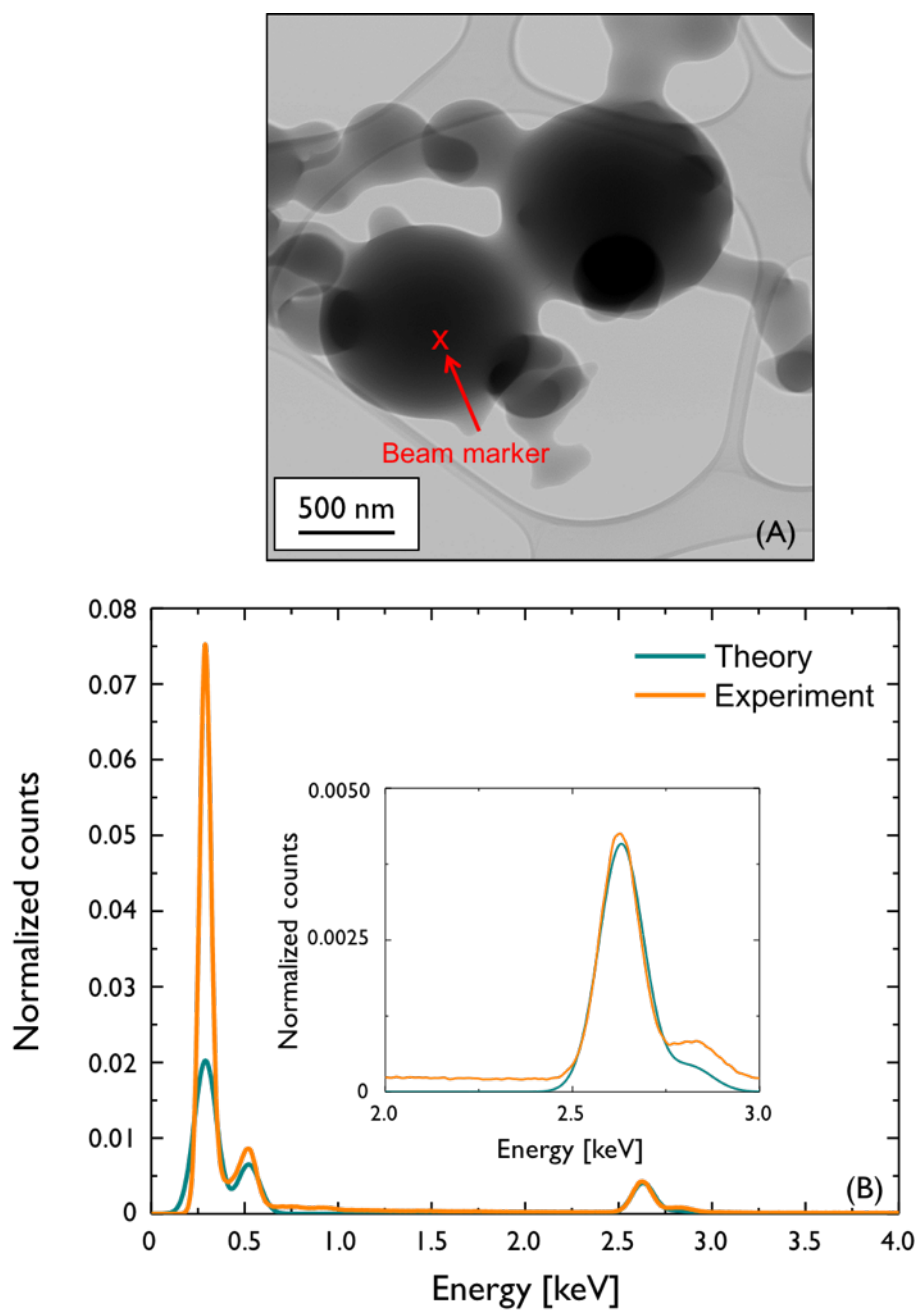


Figure 4.6. (A) HAADF TEM image of spray dried GF particles. An EDS spectrum was collected from the spot marked by the red X. (B) Comparison of theoretical and experimental EDS spectra for GF (same data as Figure 4.2). Inset is a magnification of the Cl peaks. Spectra were normalized by the height of the Cl $K\alpha$ peak.

Table 4.2. Comparison of theoretical and experimental EDS spectrum peak intensities for GF.

A/B	Theo. I_A/I_B for pure GF	Exp. I_A/I_B for pure GF
Cl K α / C K α	0.2	0.07
Cl K α / O K α	0.6	0.4
Cl K α / Cl K β	10	5

To probe the influence of thickness, EDS spectra were collected from spray dried GF particles with thicknesses varying from 100–1000 nm (Figure 4.7A and Table 4.3). Although the particles were homogeneous (they only contained GF), the peak intensity deviation from the theory increased as the thickness decreased. Deterioration of both $I_{Cl\ K\alpha}/I_{C\ K\alpha}$ and $I_{Cl\ K\alpha}/I_{O\ K\alpha}$ ratios, rather than just the $I_{Cl\ K\alpha}/I_{C\ K\alpha}$ ratio, suggested X-rays emitted by the lacey carbon support film were not the only reason for the deviation from theory. Furthermore, the measured peak ratios for spray dried GF SDs were identical between drug loadings of 1 and 50 wt% (Figure 4.7B and Table 4.4).

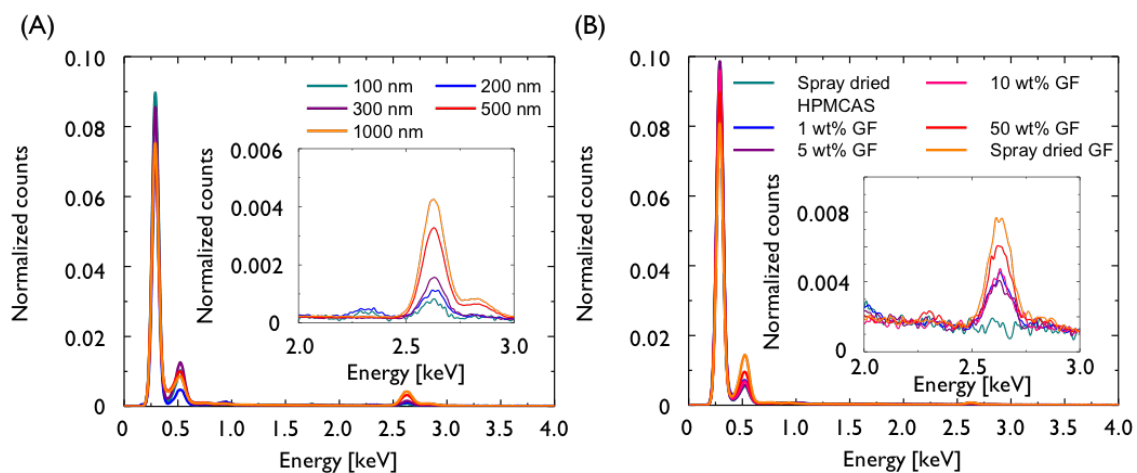


Figure 4.7. (A) EDS spectra for spray dried GF particles with different thicknesses. (B) EDS spectra for SD particles with a thickness of 300 nm and varying GF loading. Insets for both plots are magnifications of the Cl peaks. All spectra were normalized by the total area under the curve.

Table 4.3. Measured peak ratio intensities for spray dried GF particles with varying thickness. The theoretical values for $I_{ClK\alpha}/I_{CK\alpha}$ and $I_{ClK\alpha}/I_{OK\alpha}$ are 0.2 and 0.6, respectively.

Spray dried GF	Exp.	Exp.
particle thickness [nm]	$I_{ClK\alpha}/I_{CK\alpha}$	$I_{ClK\alpha}/I_{OK\alpha}$
1000	0.07	0.4
500	0.05	0.3
300	0.02	0.1
200	0.02	0.2
100	0.01	0.1

Table 4.4. Measured peak ratio intensities for 300 nm thick GF SD particle with varying drug loading.

GF loading	Theo.	Exp.	Theo.	Exp.
[wt%]	$I_{ClK\alpha}/I_{CK\alpha}$	$I_{ClK\alpha}/I_{CK\alpha}$	$I_{ClK\alpha}/I_{OK\alpha}$	$I_{ClK\alpha}/I_{OK\alpha}$
100	0.2	0.02	0.6	0.1
50	0.1	0.007	0.2	0.04
10	0.01	0.004	0.02	0.05
5	0.0006	0.004	0.0005	0.05
1	7×10^{-6}	0.004	4×10^{-6}	0.04
0	0	0	0	0

These observations showed that the measured Cl signal in the EDS spectra only provided qualitative, not quantitative, information regarding the spatial distribution of GF SDs. Therefore, EDS likely cannot be used to detect phase separated domains in SDs. The insufficient concentration resolution presumably resulted due to low X-ray emission from GF. Not only is ionization of the Cl atom rare, but the probability that ionization produces

an X-ray is also miniscule. However, the signal intensity of photons emitted from GF could possibly be increased by using a technique that only probes ionization and not X-ray emission, such as electron energy-loss spectroscopy. Exploration of electron energy-loss spectroscopy is discussed in Chapter 5. While EDS is ultimately unsuitable for characterizing GF SDs, the high spatial resolution of the technique makes it potentially useful for characterizing soft matter systems that involve higher concentrations of heteroatoms.

4.4 Conclusions

Energy-dispersive X-ray spectroscopy was explored as a tool for characterizing the spatial distribution of API and polymer in a solid dispersion. Simulations of the electron beam trajectory through a griseofulvin sample predicted that the technique could achieve a spatial resolution of ~ 10 nm. Elemental spectrum maps demonstrated that the spatial distribution of GF in a SD particle could be evaluated. Unfortunately, quantitative analysis of EDS spectra from GF showed that the concentration resolution of the technique was not sufficient for detecting phase separation between GF and HPMCAS.

Chapter 5: Nanoscale concentration quantification of pharmaceutical actives in amorphous polymer matrices by electron energy-loss spectroscopy[†]

5.1 Introduction

As discussed in Chapter 4, nanoscale characterization is needed to elucidate the spatial distribution of drug and polymer within a solid dispersion (SD). While energy-dispersive X-ray spectroscopy (EDS) can isolate drug and polymer within high spatial resolution, it cannot identify phase separation in SDs due to the poor signal of the X-ray spectra. An alternate technique, electron energy-loss spectroscopy (EELS), achieves a stronger signal-to-noise ratio than EDS because it relies on the collection of electrons that pass through the TEM sample, rather than X-rays. In this chapter, we demonstrate the use of EELS to measure the local concentration of drug and polymer throughout various SDs. We first use EELS on an SD system composed of the model polymer hydroxypropyl methylcellulose acetate succinate (HPMCAS),⁴¹ and the model API phenytoin, which has a strong tendency to crystallize. The local concentration of phenytoin within the HPMCAS matrix can be quantified with high accuracy and sub-100 nm spatial resolution by using a multiple least-squares analysis algorithm and reference spectra from the individual

[†] Reproduced and modified with permission from Ricarte, R.G.; Lodge, T.P.; Hillmyer, M.A. *Langmuir* **2016**, *32*, 7411–7419.

components. We then extend this technique to other APIs and propose other small molecule/polymer blend systems that may be suitable for this method of analysis.

5.2 Experimental details

5.2.1 Materials

Phenytoin, carbamazepine, naproxen, griseofulvin, itraconazole (Sigma-Aldrich), and tetrahydrofuran (Acros Organics, 99.9%, stabilized with BHT) were used as received. Hydroxypropyl methylcellulose acetate succinate (HPMCAS) (AFFINISOL™ 126 G, 12 wt% acetate, 7 wt% succinate, The Dow Chemical Company) was dried prior to use by heating at 70 °C under reduced pressure for at least 12 h. 200-mesh TEM grids with an ultrathin (nominally 3-4 nm) C support film (Electron Microscopy Sciences) were used to prepare samples for EELS analysis.

5.2.2 Preparation of SDs by spin coating

Spin-coated SDs of 10, 25, and 50 wt% drug, spin-coated drug, and spin-coated HPMCAS were used for this study. The appropriate amounts of drug and HPMCAS were dissolved in tetrahydrofuran to create a precursor solution with a total solids loading of 2 wt%. A ~ 10 µL drop of the solution was passed through a 0.2 µm PTFE syringe filter and placed onto a 200-mesh copper TEM grid that was supported by a 1 cm x 1 cm silica wafer. The TEM grids had an ultrathin amorphous carbon film to uphold the SD. The TEM samples were spun at 2500–3000 rpm for 1 min, dried under reduced pressure at ambient temperature for at least 12 h, and stored in a desiccator under reduced pressure at ambient temperature until use.

5.2.3 High-angle annular dark-field scanning transmission electron microscopy and electron energy-loss spectroscopy

A FEI Tecnai G2 F30 cryogenic transmission electron microscope at an accelerating voltage of 300 kV was used to collect high-angle annular dark-field scanning TEM images (HAADF STEM) and electron energy-loss spectroscopy (EELS) data. The microscope was equipped with a HAADF detector (inner and outer angles of 50 and 200 mrad, respectively) and a post-column Gatan Image Filter. The energy distribution of the electron beam, determined by the full-width at half maximum of the zero-loss peak, was 0.9 eV. To minimize radiation damage of the spin-coated SD TEM samples, regions of interest were surveyed in conventional bright-field TEM at a low magnification (9400 \times) using an electron dose rate of $\lesssim 10 \text{ e}^-/\text{nm}^2\text{s}$. At higher magnifications (40,000 \times and above), HAADF STEM image focusing and EELS spectrum alignment were performed on a sacrificial area that was far removed from the desired regions of interest. EELS spectra were then collected from the regions of interest by using "Focus" mode, in which the beam was rastered over an area of chosen size for an acquisition time of 10 s. The collection area size was varied among 200 nm \times 200 nm, 100 nm \times 100 nm, and 50 nm \times 50 nm; the electron dosages for each collection area size were 2800, 11000, and 46000 e^-/nm^2 , respectively. For each sample, EELS spectra were collected from at least 50 different regions of interest on the TEM grid. The beam was blocked before and after spectrum acquisitions to prevent damage of the sample. HAADF STEM images were collected after EELS spectra collection. Acquisition of conventional TEM EELS spectra is described in the Appendix C.2.

5.2.4 Quantification of drug concentration in spin-coated SDs from EELS spectra

To extract the zero-loss and low-loss EELS spectra from the raw EELS spectrum, the Fourier-log deconvolution routine in the Gatan Digital Micrograph software was used. The reflected tail zero-loss peak identification and modifier were chosen for the deconvolution. For each deconvoluted low-loss spectrum, the data below 3.5 eV and above

50.0 eV were removed and the contribution from the amorphous carbon film of the TEM grid was subtracted (see Appendix C.3). The intensity of each deconvoluted low-loss EELS spectrum was normalized by the integrated intensity of the spectrum. Average reference spectra of pure drugs and HPMCAS were calculated by summing at least 50 truncated spectra collected from each material and dividing the sum by the total integrated intensity. Reference spectra were created for different EELS spectra collection area sizes.

A multiple least-squares (MLS) analysis was used to quantify the concentration of a drug from the deconvoluted low-loss EELS spectrum. This analysis, which assumes that the experimental EELS spectrum of the SD is a linear combination of pure drug and HPMCAS spectra, may be described by:

$$S_{SD} = \sum_i a_i S_i \quad (5.1)$$

where S_{SD} is the predicted SD EELS spectrum (in units of normalized intensity), i is the index of each component, a_i is a fitting coefficient, and S_i is the reference spectra of the pure drug or HPMCAS. a_i is equal to:

$$a_i = \frac{w_i \xi_i / M_i}{\sum_i w_i \xi_i / M_i} \quad (5.2)$$

where w_i is the weight fraction of the i th species, ξ_i is the inelastic scattering cross section, and M_i is the molecular mass of the drug molecule or average HPMCAS substituted anhydroglucose unit. LENZPLUS was used to calculate ξ_i for various drugs and HPMCAS (see Table C.1).¹⁰⁹ For the deconvoluted low-loss EELS spectra of the drug:HPMCAS SDs,

MLS fitting was only performed on the range between 3.5 and 9.5 eV, which contains the π - π^* transition peak, because this range exhibited the largest contrast between the drug and HPMCAS spectra. All MLS analysis calculations were performed using custom-made MATLAB (version R2012a) scripts.

5.2.5 Annealing of 25 wt% phenytoin spin-coated SD TEM sample

A 25 wt% phenytoin spin-coated SD TEM sample was annealed using a Discovery differential scanning calorimeter (TA Instruments). First, the TEM sample was placed inside a Tzero™ aluminum pan with a standard lid. Then, while immersed under nitrogen gas flow with a rate of 50 mL/min, the sample pan was heated from 0–160 °C using the following modulated differential scanning calorimetry (DSC) parameters: average temperature heating rate = 1 °C/min, temperature modulation amplitude = 1 °C, temperature modulation period = 40 s. Modulated DSC mode was used to mimic an experiment on the 25 wt% phenytoin spray-dried dispersion sample (see Appendix C.4).

5.3 Results and discussion

5.3.1 EELS of HPMCAS and phenytoin

Figure 5.1A shows a high-angle annular dark-field (HAADF) STEM image of a spin-coated HPMCAS film. While TEM imaging does not provide much information about this uniform HPMCAS film, the raw EELS spectrum of HPMCAS in Figure 5.1C reveals the electronic fingerprint. The peak at 0 eV is caused by electrons that undergo elastic scattering or no scattering, and is referred to as the zero-loss peak.¹⁰⁸ Created by interactions between the incident electrons of the beam and the valence shell electrons of the HPMCAS, a broad plasmon peak at 25 eV is commonly observed in molecules that contain a high fraction of carbon atoms.^{140,141} Figure 5.1B displays a HAADF STEM image of a spin-coated phenytoin film. The film has holes and a jagged surface texture, presumably due to crystallization of phenytoin during the spin-coating process. The raw

EELS spectrum of phenytoin in Figure 5.1D not only contains the zero-loss and plasmon peaks, but also has a sharp π - π^* transition peak at 7.5 eV. Unlike conventional TEM imaging, we can use this spectroscopic signal to distinguish between HPMCAS and phenytoin.

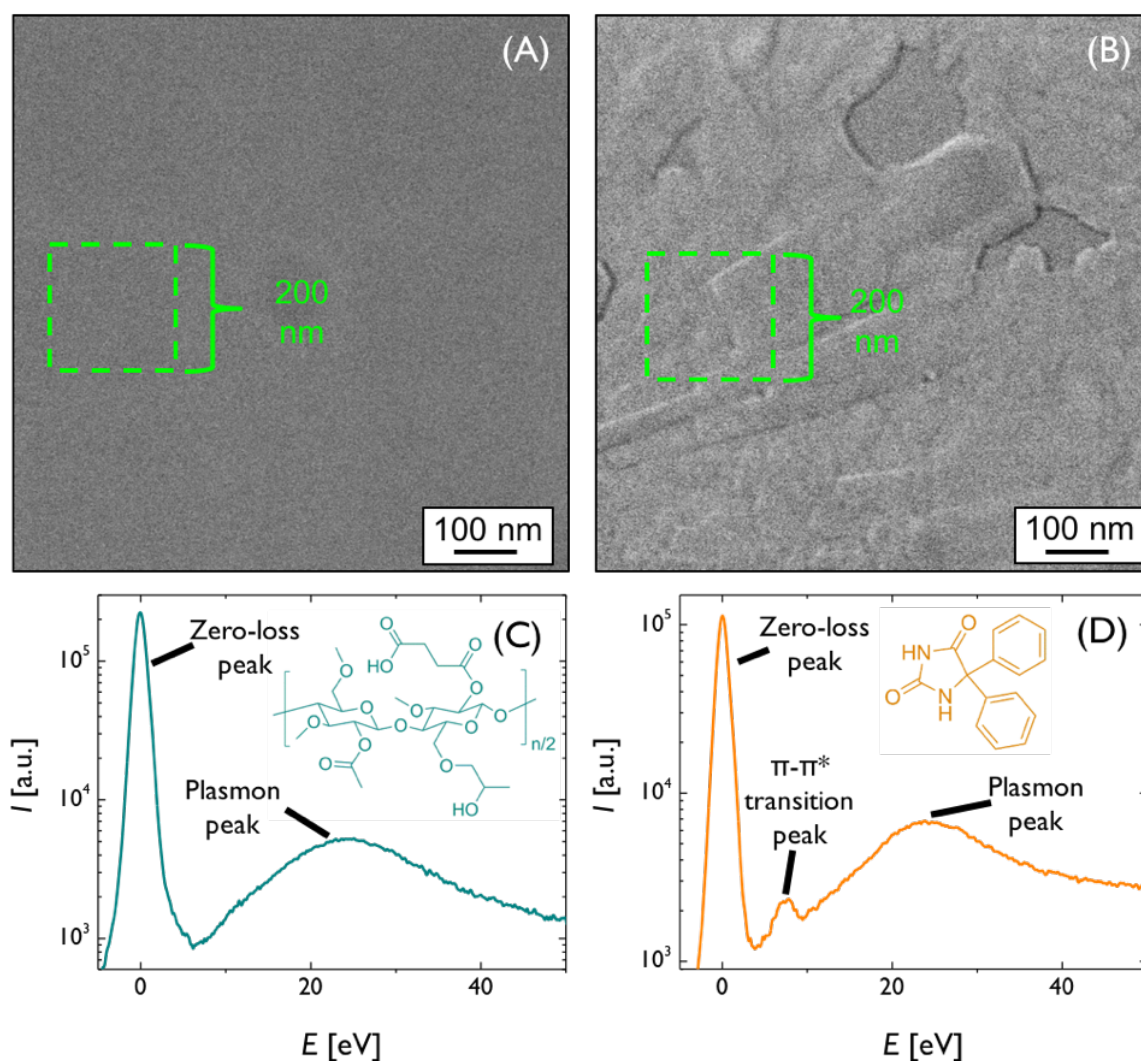


Figure 5.1. High-angle annular dark-field (HAADF) STEM image of spin-coated (A) HPMCAS and (B) phenytoin films. The outlined regions are the areas from which EELS spectra were collected. EELS spectra and molecular structures of (C) HPMCAS and (D) phenytoin. The pictured structure of HPMCAS is merely illustrative; it does not represent the actual substitution pattern. The y-axis is the intensity (I) and the x-axis is the energy-loss exhibited by a particular electron (ΔE). The HPMCAS spectrum only has the zero-loss and plasmon peaks, while the phenytoin spectrum contains the zero-loss, plasmon, and π - π^* transition peaks.

5.3.2 Quantification of phenytoin concentration for spin-coated HPMCAS and phenytoin

Figure 5.2 shows the histograms of the measured phenytoin concentrations from STEM EELS for spin-coated HPMCAS and phenytoin. The average measured concentrations are consistent with the expected concentrations (0 and 100 wt% for HPMCAS and phenytoin, respectively) and the standard deviations of the measured concentrations match the values we observed for the phenytoin:HPMCAS SDs.

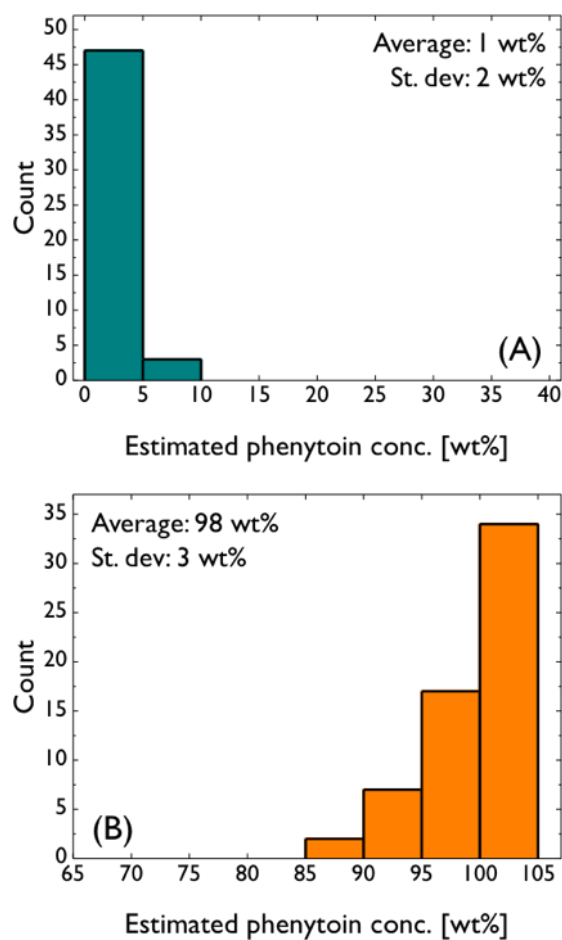


Figure 5.2. Histograms of measured concentrations for (A) spin-coated HPMCAS and (B) spin-coated phenytoin.

5.3.3 EELS of spin-coated SDs with varying phenytoin concentration

Figure 5.4 presents HAADF STEM images of spin-coated SDs with different loadings of phenytoin (10, 25, and 50 wt% drug). The square marks in the images, spots from where EELS spectra were collected, are artifacts of beam damage (see Appendix C.1 for bright-field TEM images of the SDs). Although the concentration of phenytoin varies significantly, TEM imaging cannot distinguish amongst these films and shows no features that signal the presence of HPMCAS or phenytoin, due to the small difference in electron density of the two species.

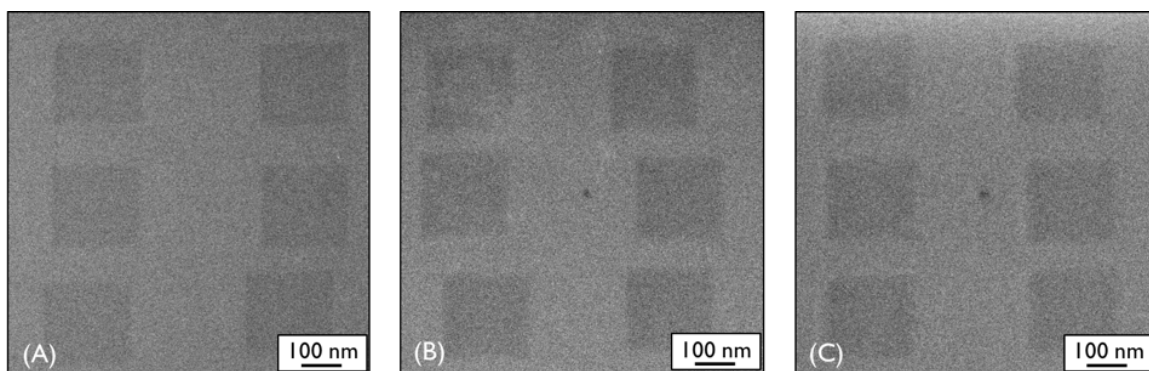


Figure 5.3. HAADF STEM images of (A) 10, (B) 25, and (C) 50 wt% phenytoin spin-coated dispersion films. TEM imaging cannot distinguish among these films. The square marks, caused by radiation damage, were areas from which EELS spectra were collected.

EELS, however, can distinguish among solid dispersions with different phenytoin loadings. Figure 5.4 contains experimental and predicted spectra, as calculated by Eqn. 1, for spin-coated SDs of varying phenytoin concentration. The spectra show that the intensity of the π - π^* transition peak in the EELS spectrum increases as the phenytoin concentration increases. Furthermore, the shape of each experimental spectrum qualitatively matches the shape of its corresponding predicted spectrum (no fitting was performed in this step). This

agreement not only corroborates the assumptions required for the MLS analysis (as described in the Section 5.2.4), but also allows for phenytoin concentration quantification.

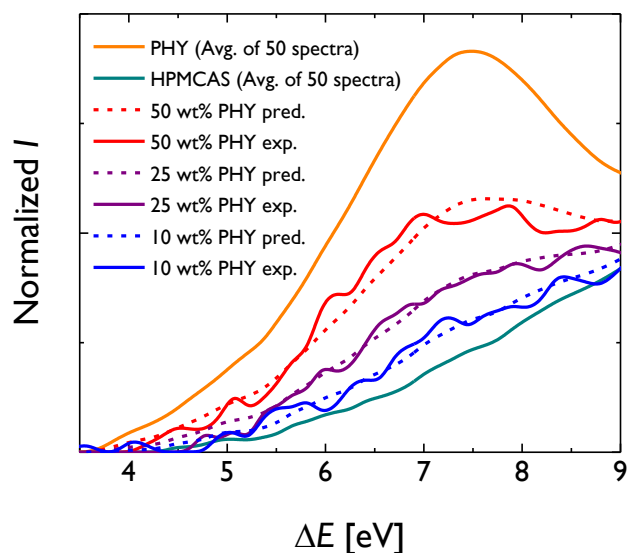


Figure 5.4. Comparison of experimental and predicted EELS spectra for 10, 25, and 50 wt% phenytoin (PHY) spin-coated dispersions. The y-axis is the normalized spectrum intensity (Normalized I) and the x-axis is the energy-loss of each electron (ΔE). The HPMCAS and phenytoin spectra are each averages of 50 spectra. The representative experimental spectra qualitatively match the predicted spectra.

5.3.4 Quantification of phenytoin concentration in spin-coated SDs

For the 10, 25, and 50 wt% phenytoin spin-coated SDs, EELS spectra from 50 different regions on each film were evaluated. The spectra were acquired using a collection area size of $200 \text{ nm} \times 200 \text{ nm}$, and the aforementioned MLS model was used to calculate the phenytoin concentration. Histograms of the calculated phenytoin concentrations from 50 different regions for each SD show that the average calculated concentrations match the nominal concentrations (Figure 5.5), suggesting that the use of the MLS analysis is valid for the phenytoin:HPMCAS system. Furthermore, the concentration histograms are monomodal and exhibit a standard deviation of 4–5 wt%, much larger than the error expected due to spectrum noise,¹¹² but consistent with the experimental error reported in

the literature (~ 4 wt% for measurements of water and biomacromolecule concentrations in biological cryosections).^{142,143} We posit that the major source of this error is random experimental uncertainty. In particular, the subtraction of the contribution of the amorphous carbon support film from the deconvoluted low-loss EELS spectrum may create an uncertainty of ~ 4 wt% (see Appendix C.3 for further discussion of this point). Statistical fluctuations in the local concentration of drug and polymer may also cause the measured concentration to deviate from bulk concentration. These fluctuations, due in part to chain connectivity, are assumed to occur on a length scale of approximately the Kuhn length (~ 10 – 20 nm for cellulosic polymers).^{71,72,73,144,145} Therefore, given that the EELS spectra collection area size used was $200 \text{ nm} \times 200 \text{ nm}$ and thus much larger than the Kuhn length of a cellulosic polymer, such concentration fluctuations likely have little influence on the calculated concentration uncertainty. Based on these factors, we assume that 4 wt% is the minimum calculated concentration error for SD samples that are supported by an amorphous carbon film. Hence, we interpret the histograms to be strong evidence that for drug loadings of 10–50 wt% the phenytoin and HPMCAS in the SDs are intimately mixed at a length scale of 200 nm. This result, which supports studies that suggest that HPMCAS intimately mixes with phenytoin up to a drug loading of at least 50 wt%,^{25,42} implies that HPMCAS is an effective excipient for stabilizing glassy phenytoin.

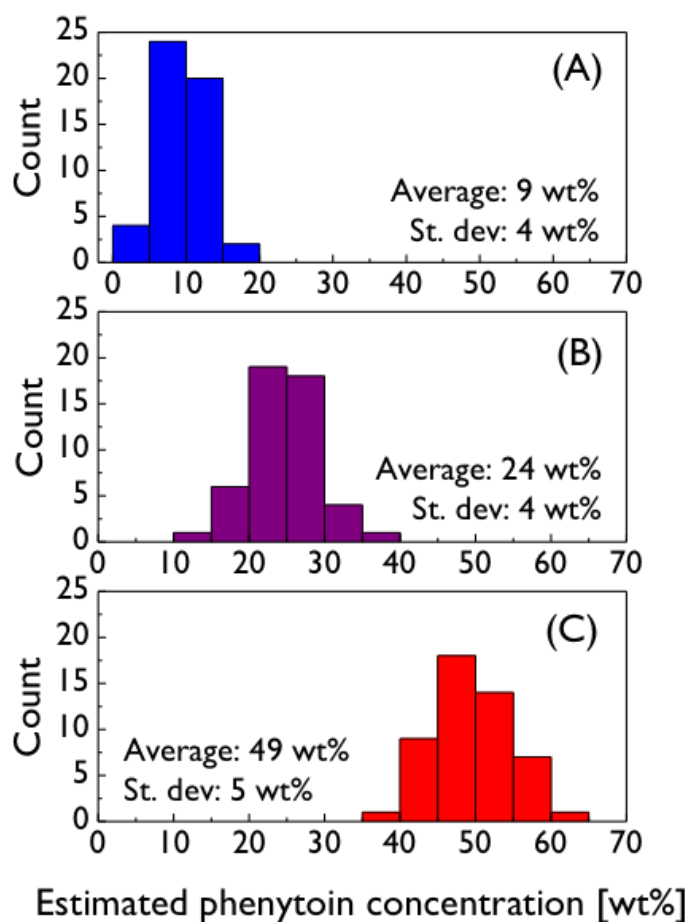


Figure 5.5. Histograms of measured concentrations, as calculated by the EELS MLS noise-weighted algorithm, for 50 spots in (A) 10, (B) 25, and (C) 50 wt% spin-coated SDs. The average measured concentrations agree with the nominal phenytoin loadings of the dispersions.

These data, however, do not conclusively rule out phase separation in phenytoin:HPMCAS SDs, as phase separated domains of phenytoin or HPMCAS could be smaller than 100 nm in size. To further investigate the possibility of phase separation in the phenytoin:HPMCAS spin-coated SDs, we also quantified the phenytoin concentration from EELS spectra that were acquired from much smaller collection area sizes of 100 nm \times 100 nm and 50 nm \times 50 nm. Figure 5.5 features the phenytoin and HPMCAS EELS spectra for collection area sizes of 200 nm \times 200 nm, 100 nm \times 100 nm, and 50 nm \times 50

nm. The electron dosage for these collection area sizes was 2800, 11000, and 46000 e^-/nm^2 , respectively. For phenytoin, the intensity of the $\pi-\pi^*$ transition peak intensity decreases as the collection area size decreases. Conversely, the $\pi-\pi^*$ region in the HPMCAS spectrum increases in intensity as the collection area size decreases. These changes in the spectra may be caused by the increase in electron dosage at smaller collection area sizes. When exposed to radiation, aromatic rings can break to create aliphatic crosslinks, thereby eliminating a π -bond from the molecule, while saturated C-H bonds can cleave to form an unsaturated C=C bond.¹⁴⁶ Further experiments are needed to fully understand the influence of electron beam damage on the phenytoin and HPMCAS spectra.

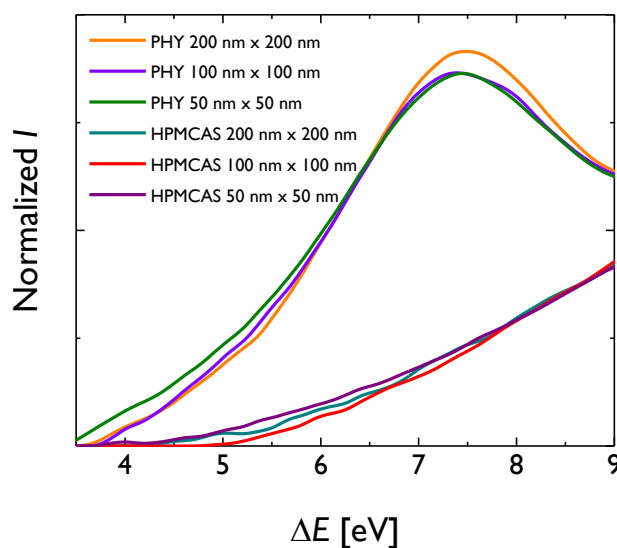


Figure 5.6. Phenytoin and HPMCAS EELS spectra for various collection area sizes. Each spectrum is an average of at least 50 experimental spectra. For phenytoin, the $\pi-\pi^*$ transition peak intensity decreases as the collection area decreases. For HPMCAS, the $\pi-\pi^*$ transition region slightly increases in intensity as the collection area decreases.

As an example, Figures 5.6 compares the concentration histograms of a 25 wt% phenytoin spin-coated dispersion for different collection area sizes (the 10 and 50 wt% phenytoin spin-coated SDs analyses are located in the Figures 5.7 and 5.8, respectively). At smaller collection area sizes, the average calculated concentrations still match the

nominal drug loadings, but the standard deviation of the calculated concentrations increased. The monomodal calculated concentration histograms again suggest that phenytoin and HPMCAS are not phase separated. The increase in the concentration variance may possibly be caused by two separate factors. First, the influence of statistical fluctuations in local drug and polymer concentration should increase as the collection area decreases. The smallest collection area size probed in this experiment ($50 \text{ nm} \times 50 \text{ nm}$) is only 2–3 times larger than the expected length scale of concentration fluctuations for phenytoin:HPMCAS SDs. Second, the increase in electron dosage may damage the SD in a way that skews the calculated concentration. Electron irradiation causes irreversible chemical changes to soft materials *via* incipient radical formation. These chemical changes would likely corrupt the shape of the measured EELS spectra and shift the calculated concentration away from the concentration of the pristine material.^{146,147,148} Further studies are required to resolve the role of these processes. Nevertheless, these studies show that TEM and EELS can overcome the spatial resolution barriers that inhibit other imaging techniques.

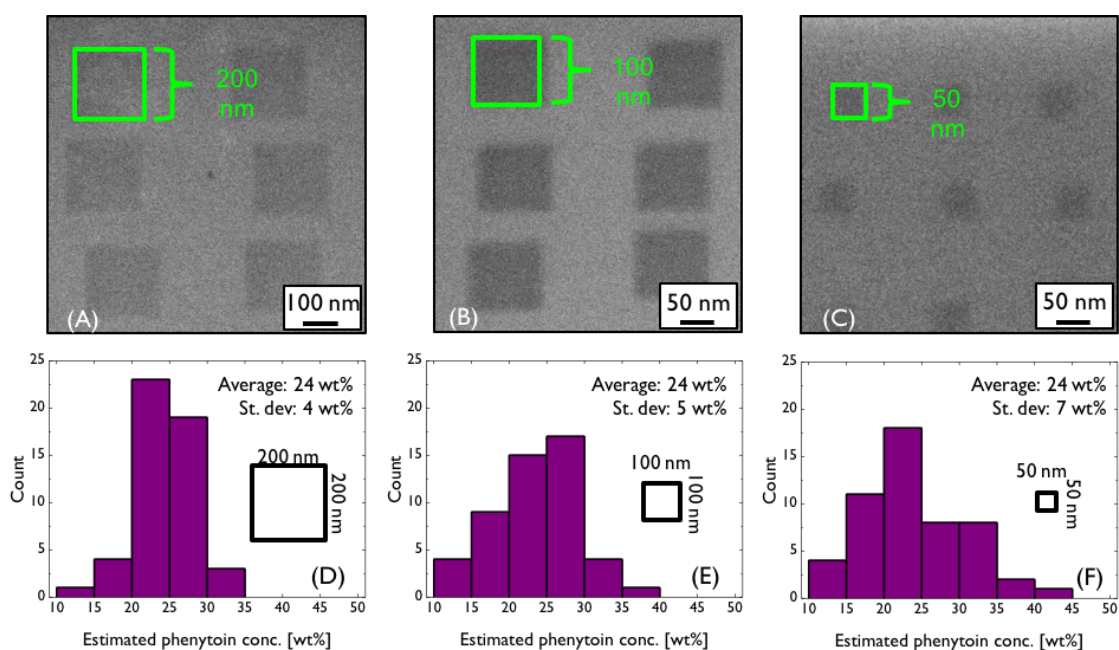


Figure 5.6. Histograms of measured concentrations, as calculated by the EELS MLS noise-weighted algorithm, for 50 spots in (A) 10, (B) 25, and (C) 50 wt% spin-coated SDs. The average measured concentrations agree with the nominal phenytoin loadings of the dispersions.

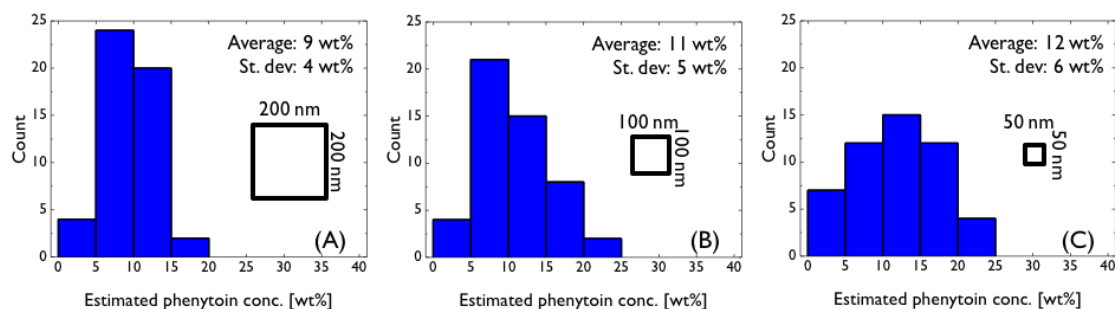


Figure 5.7. Histograms of measured concentrations from 50 spots on a 10 wt% phenytoin spin-coated SD. The EELS spectrum collection area sizes are (A) 200 nm \times 200 nm, (B) 100 nm \times 100 nm, and (C) 50 nm \times 50 nm.

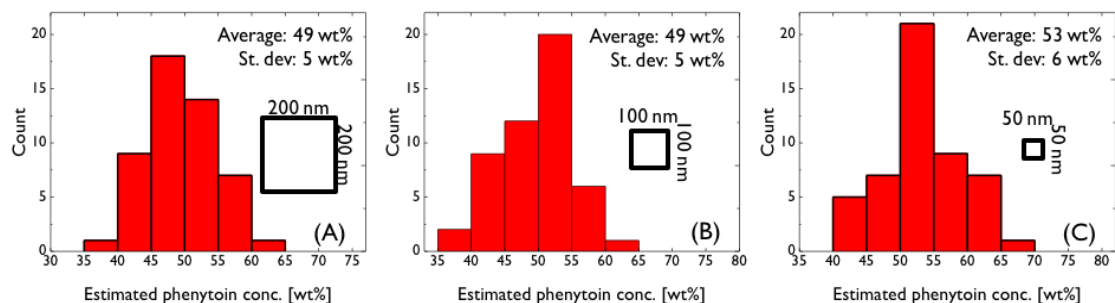


Figure 5.8. Histograms of measured concentrations from 50 spots on a 50 wt% phenytoin spin-coated SD. The EELS spectrum collection area sizes are (A) 200 nm \times 200 nm, (B) 100 nm \times 100 nm, and (C) 50 nm \times 50 nm.

5.3.5 EELS of an annealed 25 wt% phenytoin spin-coated SD

To further demonstrate the sub-100 nm spatial resolution of EELS, we collected spectra from a 25 wt% phenytoin spin-coated SD that was heated to 140 °C, which is above the crystallization temperature of the 25 wt% phenytoin spray-dried SD (Appendix C.4). Unlike the virgin sample, the annealed SD exhibits non-uniform topology and nanostructures. For the region captured in Figure 5.9A, EELS spectra were collected from

regions "X" and "Y". Though "X" and "Y" were only separated by less than 50 nm, the phenytoin concentrations of the two regions were substantially different (Figure 5.9B). "X" is likely a region of crystalline phenytoin, while "Y" is likely a region of amorphous phenytoin and HPMCAS. A lower magnification HAADF TEM image of the region is given in Figure 5.10. By using EELS, we may directly elucidate the composition of the nanostructures in the sample with high spatial resolution.

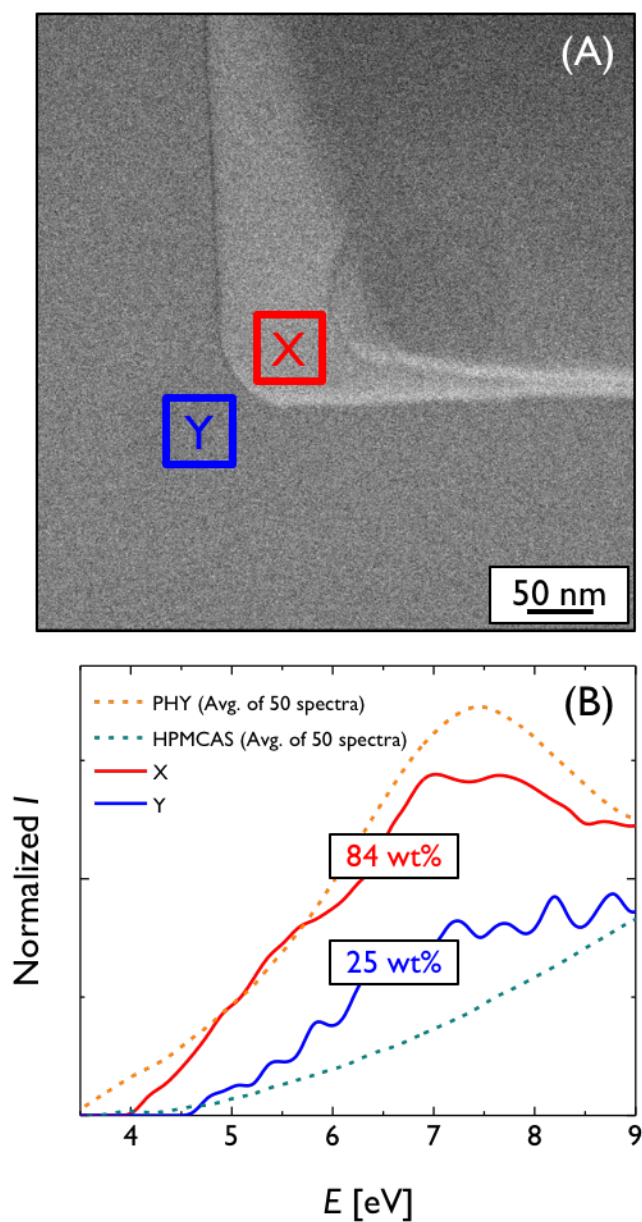


Figure 5.9. (A) HAADF STEM image of a 25 wt% phenytoin spin-coated dispersion film that was annealed to 140 °C. EELS spectra were collected from the regions "X" and "Y". (B) EELS spectra from regions "X" and "Y". Though the regions are separated by less than 50 nm, the phenytoin concentrations in these two regions are drastically different. Phenytoin (PHY) and HPMCAS EELS spectra are shown for comparison.

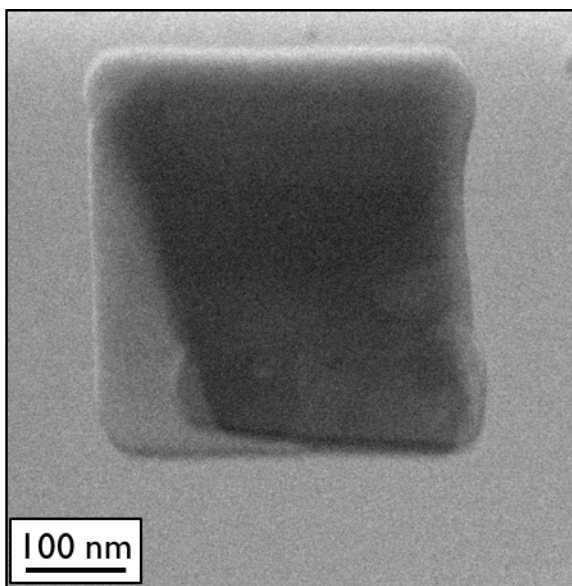


Figure 5.10. Low magnification HAADF TEM image of annealed 25 wt% phenytoin SD.

5.3.6 Application of EELS for detecting other aromatic-ring containing drug molecules

The use of the EELS MLS analysis should be useful for SDs containing not only phenytoin, but also other APIs. To further test the versatility of this strategy, we collected EELS spectra from four other drug molecules containing aromatic motifs: carbamazepine, naproxen, itraconazole, and griseofulvin. As seen in Figure 7, each drug exhibits a unique π - π^* transition peak in the EELS spectrum. The intensity and breadth of the π - π^* transition peak is intimately tied to molecular structure.¹⁴⁹

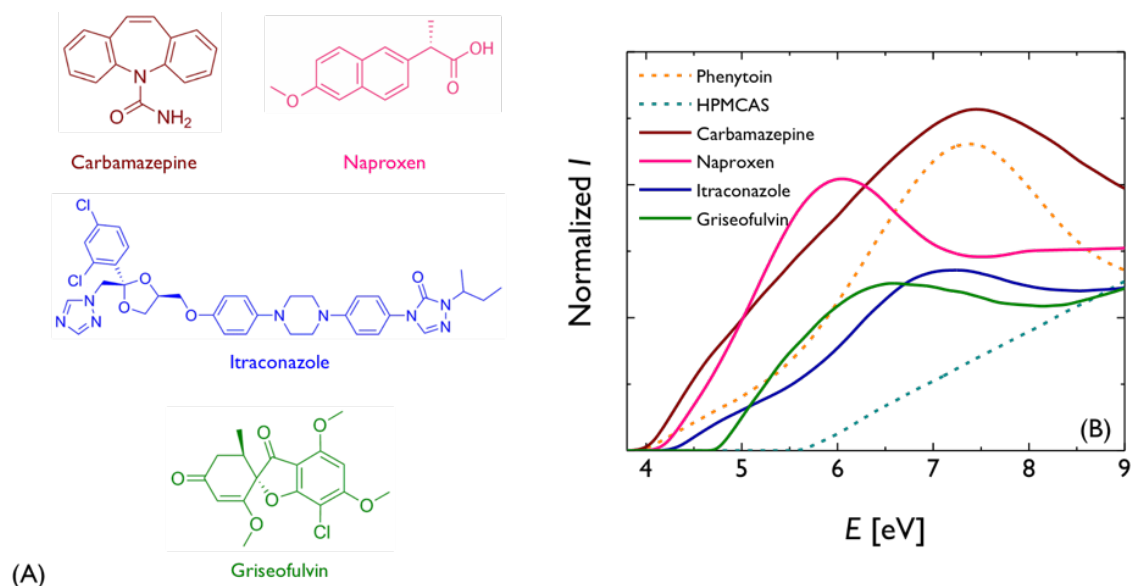


Figure 5.11. (A) Molecular structures of carbamazepine, naproxen, itraconazole, and griseofulvin. (B) Conventional TEM EELS spectra of the four additional APIs. Each spectrum is the average of at least 50 experimental spectra. The molecules, which all contain aromatic rings, each exhibit a unique EELS spectrum. Phenytoin and HPMCAS, the dashed lines, are included for comparison.

To probe the accuracy and precision of the concentration quantification for different molecules, we analyzed EELS spectra from SDs that contained 10 wt% of carbamazepine, naproxen, itraconazole, or griseofulvin (Figure 5.12). The concentration quantification was accurate and precise for the SDs that had carbamazepine or naproxen (molecules that exhibit a relatively strong $\pi-\pi^*$ transition signal), but was both inaccurate and imprecise for the SDs that had itraconazole or griseofulvin (molecules that exhibited a relatively weak $\pi-\pi^*$ transition signal). This observation implies that the reliability of the MLS analysis is contingent on the strength of the associated $\pi-\pi^*$ transition peak relative to the HPMCAS EELS spectrum. Furthermore, this result supports the finding of Yakovlev *et al.* that the uncertainty of the concentration calculated by the EELS MLS analysis is inversely related to the difference between the pure species spectra.¹¹²

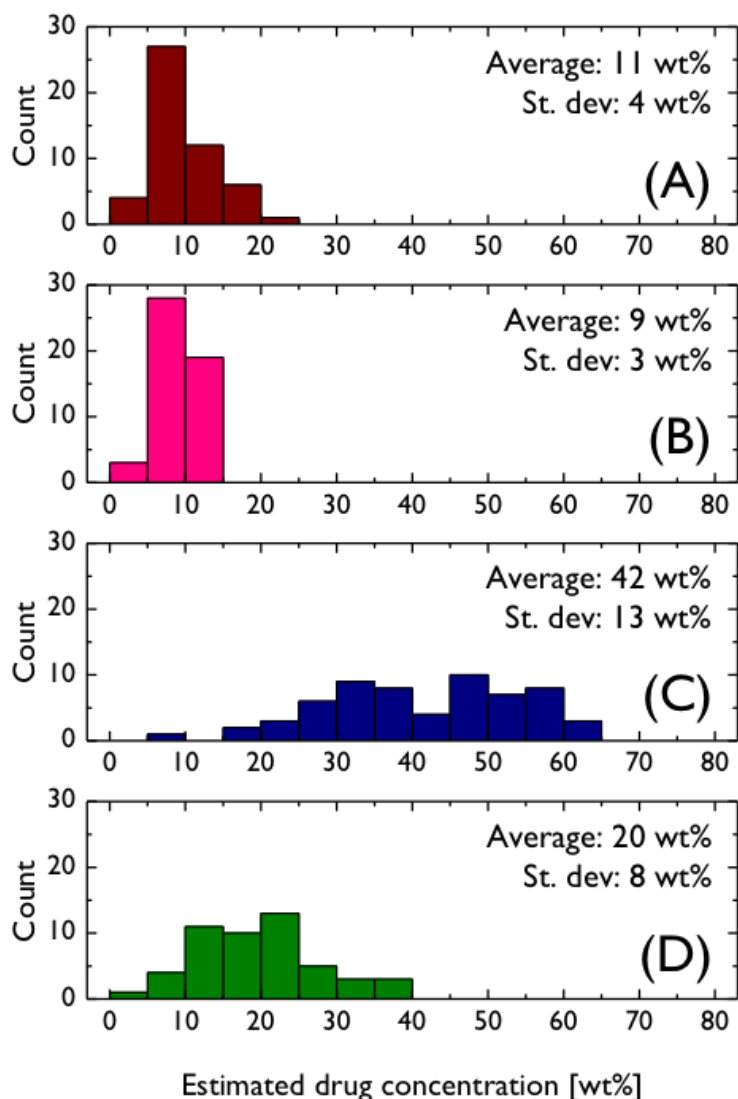


Figure 5.12. Histograms of measured concentrations from 50 spots for 10 wt% drug solid dispersions featuring HPMCAS as the excipient and either (A) carbamazepine, (B) naproxen, (C) itraconazole, or (D) griseofulvin as the drug. The ELS MLS analysis is accurate and precise for carbamazepine and naproxen, which have strong π - π^* transition peaks, while the analysis is inaccurate and imprecise for itraconazole and griseofulvin, which have weak π - π^* transition peaks.

The findings in this work suggest that EELS will be a useful tool for resolving many questions regarding SD design. This technique may potentially be used to characterize with sub-100 nm the miscibility of a single API in various non-aromatic excipients (*e.g.*, Soluplus®, Eudragit®, other cellulose derivatives)^{54,150} and to elucidate the relationship between API spatial distribution and SD performance. Potentially, the influence of

temperature and humidity on the API nanoscale spatial distribution may also be evaluated by EELS. Furthermore, the EELS MLS analysis described in this work could be generalized for binary blends in which one component has a relatively strong π - π^* transition signal and the other component does not. Many soft materials fit this criterion. For example, many polymer binary blends and block polymers commonly have an aromatic component and a non-aromatic component. Many of these aromatic polymers – such as poly(styrene), poly(2-vinylpyridine), and polycarbonate – exhibit strong π - π^* transition signals.^{112,149,151,152} Materials that contain an encapsulated fluorophore are also excellent candidates for this analysis. Fluorophores, typically polycyclic aromatic hydrocarbons, exhibit sharp π - π^* transition signals.¹⁵³ The transparency and flexibility of the EELS MLS analysis suggest it may be useful for characterizing a wide variety of systems.

The main challenge that prevents the use of EELS MLS analysis as a routine characterization tool for soft materials is electron beam damage. Extended irradiation of the sample materials may cause structural changes or non-linear phenomenon to occur, thereby compromising the linearity assumption of the MLS analysis. The effect of beam damage may be diminished by using reference spectra of the pure species components that were collected at the same conditions as the blend materials (as was done in this work).¹⁴⁸ Also, the rate of beam damage can be reduced by cooling the sample to cryogenic conditions.¹¹² By minimizing the influence of electron beam damage and other random experimental uncertainty, the accuracy and precision of the EELS MLS analysis may be improved.

5.4 Conclusions

We demonstrated EELS characterization of SDs. The technique may be used to quantify the local concentration of drug throughout the polymer matrix with high accuracy and sub-100 nm resolution. Analysis of phenytoin:HPMCAS SDs suggests the drug and polymer are intimately mixed throughout the dispersion, even at high drug loadings.

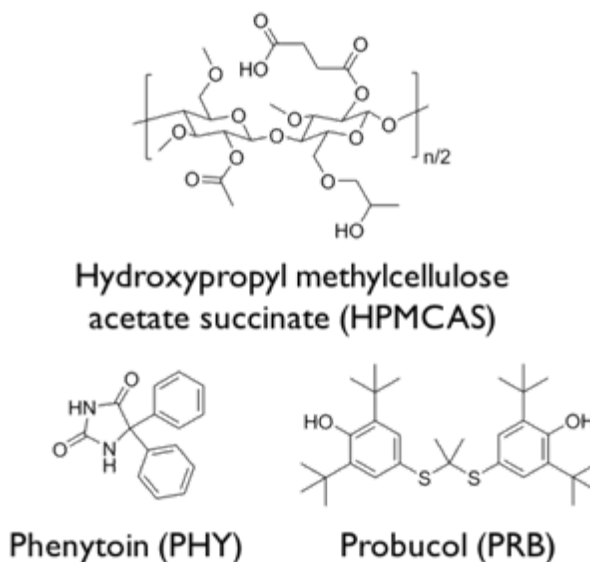
Furthermore, we established the utility of EELS for characterizing other drug molecules. EELS is therefore a potentially powerful and complementary tool for evaluating the spatial distribution and structure-property relationships of a wide variety of small molecule-polymer blends.

Chapter 6: Direct observation of nanostructures during dissolution of polymer/drug particles

6.1 Introduction

The use of a solid dispersion (SDs) may significantly enhance the apparent solubility of a pharmaceutical drug, but the role of the polymer excipient is poorly understood. For example, hydroxypropyl methylcellulose acetate succinate (HPMCAS, Scheme 6.1) is an effective excipient for some drugs, but it is not a panacea. To address this ambiguity, the work in this chapter elucidates the influence of polymer and drug on SD dissolution in phosphate buffered saline by directly evaluating nanostructures in solution. First, aqueous solution behavior of HPMCAS, a polymer considered to be one of the most effective excipients, is characterized. Then, dissolution of HPMCAS SDs, containing either phenytoin or probucol (Scheme 6.1) as the API, is investigated. Although both of these drugs have poor aqueous solubility, phenytoin and probucol have very disparate physical properties (see Figure D.1). Using a combination of cryogenic transmission electron microscopy, small-angle X-ray scattering, and electron diffraction, a direct correlation between SD dissolution profiles and the presence of nanoparticles, <100 nm in size, was revealed. Finally, the repercussions and potential universality of these discoveries are discussed.

Scheme 6.1. Chemical structures of hydroxypropyl methylcellulose acetate succinate (HPMCAS), phenytoin, and probucol. The pictured structure of HPMCAS is merely illustrative and not representative of the actual substitution pattern.



6.2 Experimental Section

6.2.1 Materials

Phenytoin, probucol (Sigma-Aldrich), and tetrahydrofuran (Acros Organics, 99.9%, stabilized with BHT) were used as received. Hydroxypropyl methylcellulose acetate succinate (AFFINISOLTM HPMCAS 912 G, 10 wt% acetate, 11 wt% succinate, reported M_n , M_w , and D of 60 kg/mol, 140 kg/mol, and 2.4, respectively, The Dow Chemical Company) was dried prior to use for 12 h under reduced pressure at a temperature of 70 °C. Phosphate buffered saline (PBS, pH = 6.5) was prepared using Milli-Q water, 20 mM sodium phosphate dibasic heptahydrate (Fisher, 98%), 47 mM potassium phosphate monobasic (J.T. Baker, $\geq 99\%$), and 82 mM sodium chloride (Fisher, $\geq 99\%$).

6.2.2 Preparation of SDs by spray drying

Spray dried SDs of 3.2, 10, 25, and 50 wt% phenytoin or 10, 25, and 50 wt% probucol, and HPMCAS were studied in this work. Specified amounts of drug and HPMCAS were dissolved in tetrahydrofuran to form a 2 wt% solution. The precursor solution was then spray dried by a mini spray dryer (Bend Research) using a nitrogen flow rate of 12.8 standard liters per min, an inlet temperature of 68 °C, and a solution flow rate of 0.65 mL/min. The outlet temperature, which was not controlled, fluctuated between 24 and 27 °C. SD powder was recovered from filter paper placed in the outlet of the spray dryer, subsequently dried under reduced pressure at ambient temperature for at least 12 h, and stored in a desiccator under reduced pressure at ambient temperature until use. SD morphology was characterized by scanning electron microscopy. All SDs were determined to be homogenous and fully amorphous materials within the detection limits of wide-angle X-ray scattering and modulated differential scanning calorimetry (see Figures D.4 and D.5).

6.2.3 Dynamic light scattering (DLS)

Samples were prepared by directly dissolving HPMCAS in PBS or tetrahydrofuran and passing the solutions through 0.2 µm filters (GHP and PTFE for PBS and tetrahydrofuran, respectively) into clean glass tubes. DLS was conducted on a Brookhaven BI-200SM light scattering instrument with a wavelength of 637 nm, laser power of 30 mW, and an avalanche photodiode detector with a 200 µm pinhole. Measurements were made at 11 angles ranging from 30–120°.

6.2.4 Static light scattering (SLS)

To prepare samples for SLS, HPMCAS was dissolved in tetrahydrofuran to form a 2 wt% HPMCAS solution, successively passed through 0.45 and 0.25 µm PTFE filters,

and spray dried. The resulting dried polymer was dissolved in PBS to form a 0.25 mg/mL HPMCAS stock solution. Aliquots of the stock solution were diluted to form 11 additional SLS samples that had concentrations ranging from 0.010–0.235 mg/mL. SLS measurements were performed using the Brookhaven BI-200SM light scattering instrument described above. The pinhole size was set to 1 mm and measurements were made at 13 angles ranging from 30–102°.

6.2.5 Microcentrifuge dissolution and solubility assays

For each dissolution measurement, a SD was loaded into a 1.5 mL microcentrifuge tube. PBS was added to the SD at 37 °C to achieve the desired targeted drug concentration (*e.g.*, to obtain 1000 µg/mL of phenytoin, 1.2 mL of PBS was added to 12 mg of 10 wt% phenytoin SD). Dissolution media were vortexed for 1 min and placed in an isothermal aluminum microcentrifuge tube holder held at 37 °C. At 4, 10, 20, 40, 90, 180, and 360 min, the dissolution media was centrifuged at 13000 g for 1 min, a 50 µL aliquot of the supernatant was collected and subsequently diluted by 350 µL of methanol, and the remaining dissolution medium was re-vortexed for 30 s and returned to the microcentrifuge tube holder. During aliquot collection, the samples are typically outside the 37 °C sample holder for ~ 2 min. For solubility measurements, 4 mg of crystalline drug (phenytoin or probucol) was loaded into a 1.5 mL microcentrifuge tube with a small stir bar and covered with 1 mL solution of HPMCAS dissolved in PBS. The sample was sealed with Parafilm™, vortexed for 1 min, placed in a sand bath heated to 37 °C, and stirred for 72 hrs. Then, the solubility media were centrifuged at 13000 g for 1 min. 50 µL aliquots of the supernatant were collected, passed through a 0.25 µm GHP filter, and diluted by 350 µL of methanol. Diluted aliquots for both measurements were analyzed by high-performance liquid chromatography using an Agilent 1260 liquid chromatograph system with multi-wavelength UV-vis detection and a reversed-phase EC-C18 column (Poroshell 120, 4.6 ×

50 mm, particle size 2.7 μm , Agilent). The mobile phase was 45:55 and 96:4 (v/v) MeCN/H₂O for SDs containing phenytoin and probucol, respectively. For both drugs, calibration curves ranging from 10–1000 $\mu\text{g/mL}$ were developed. All dissolution and solubility measurements were repeated in triplicate.

6.2.6 Cryogenic transmission electron microscopy (Cryo-TEM)

Samples of vitrified SD dissolution media were made using an FEI Vitrobot Mark III automated vitrification device. Glow discharge was applied to a 200-mesh copper TEM grid with a lacey carbon support film to increase the surface energy of the grid. The grid was then placed into the sample chamber of the Vitrobot, which had a relative humidity and temperature of 100% and 26 °C, respectively. SD dissolution was initiated using the method described previously. After centrifugation of dissolution media at various time points, a 2 μL aliquot of the supernatant was collected and deposited onto the aforementioned TEM grid. The grid was then immediately plunged into a pool of liquid ethane to vitrify the dissolution media. Vitrified samples were stored at cryogenic temperature until imaging. Cryo-TEM imaging and electron diffraction were executed using a FEI Tecnai Spirit BioTWIN transmission electron microscope with an accelerating voltage of 120 kV. During imaging, the sample was maintained between -179 and -175 °C. Electron diffraction patterns of dissolution media structures were collected using low-dose conditions. Briefly, a region of interest (ROI) was identified in bright-field TEM at low magnification (4700 \times) using an electron dose rate of $\lesssim 10 \text{ e}^-/\text{nm}^2\text{s}$. Higher magnification (49000 \times) alignments were made on an area far removed from the desired ROI. To reduce the size of the sampled ROI, a selected-area aperture with an area of $\sim 1 \mu\text{m}^2$ was inserted into the electron beam path. Electron diffraction patterns were recorded using an electron dose rate of $\sim 150 \text{ e}^-/\text{nm}^2\text{s}$ and indexed using the DiffTools plug-in for Gatan DigitalMicrographTM.¹¹⁵

6.2.7 Small-angle X-ray scattering (SAXS)

SAXS experiments were conducted at DND-CAT (beamline 5-ID-D) at the Advanced Photon Source in Argonne National Laboratory (Argonne, IL). The sample-to-detector distance was 8.5 m. Dissolution media samples were generated by loading SDs into 20 mL scintillation vials and adding PBS at 37 °C to achieve the desired targeted drug concentration. The vials were vortexed for 1 min and heated in an aluminum vial holder at 37 °C. At 4, 10, 20, 40, 90, 180, and 360 min, the vials were vortexed to remix the dissolution media. At each time point, approximately 0.1 mL of dissolution media was collected and injected into a 1.5 mm quartz capillary. The remaining solution was replaced into the vial holder and held at 37 °C. The aliquot capillary was immediately placed in a multi-capillary heating stage set to 37 °C. After closing the hutch door (a process that takes ~ 2 min), 2D SAXS scattering patterns of the aliquots were recorded and subsequently integrated to create 1D intensity (arbitrary units) vs. q patterns. SAXS patterns were analyzed using custom-made MATLAB (version R2012a) scripts. Background was removed from the SAXS patterns by subtracting a high q baseline and a PBS reference pattern.

6.3 Results

6.3.1 Characterization of HPMCAS solutions

The 912 G grade of HPMCAS (roughly equal weight fractions of acetate and succinate substituents) was chosen as the model excipient to balance hydrophobicity and aqueous solubility. Figure 6.1A shows the hydrodynamic radius (R_h) distribution, as calculated by REPES of the DLS data, for 9 mg/mL of HPMCAS dissolved in PBS. The peaks around 10 nm are consistent with the expected R_h of linear HPMCAS chains with a

molecular weight $\sim 10^5$ g/mol. There was also a peak around 100 nm. The collected second-order auto correlation functions, (g_2), were also fit to a double exponential model:

$$g_2(q, t) = \beta |g_1(q, t)|^2 + BG \quad (6.1)$$

$$g_1(q, t) = f \exp(-\Gamma_1 t) + (1 - f) \exp -\Gamma_2 t \quad (6.2)$$

β is the spatial coherence factor, g_1 is the first-order auto correlation function, BG is the background, f is the fractional intensity of the first mode, t is time, Γ_1 is the decay rate of the first mode, and Γ_2 is the decay rate of the second mode. The double exponential fits (featured in Figure 6.2A) agrees with the REPES analysis, although the systematic error in the residuals suggests that this simplified model is not completely appropriate (see Figure 6.2B). The linear relationship between Γ for both modes and the square of the scattering vector (q) verifies the relaxations are diffusive (Figure 6.2C). Table 6.1 contains the values for all fitted parameters.

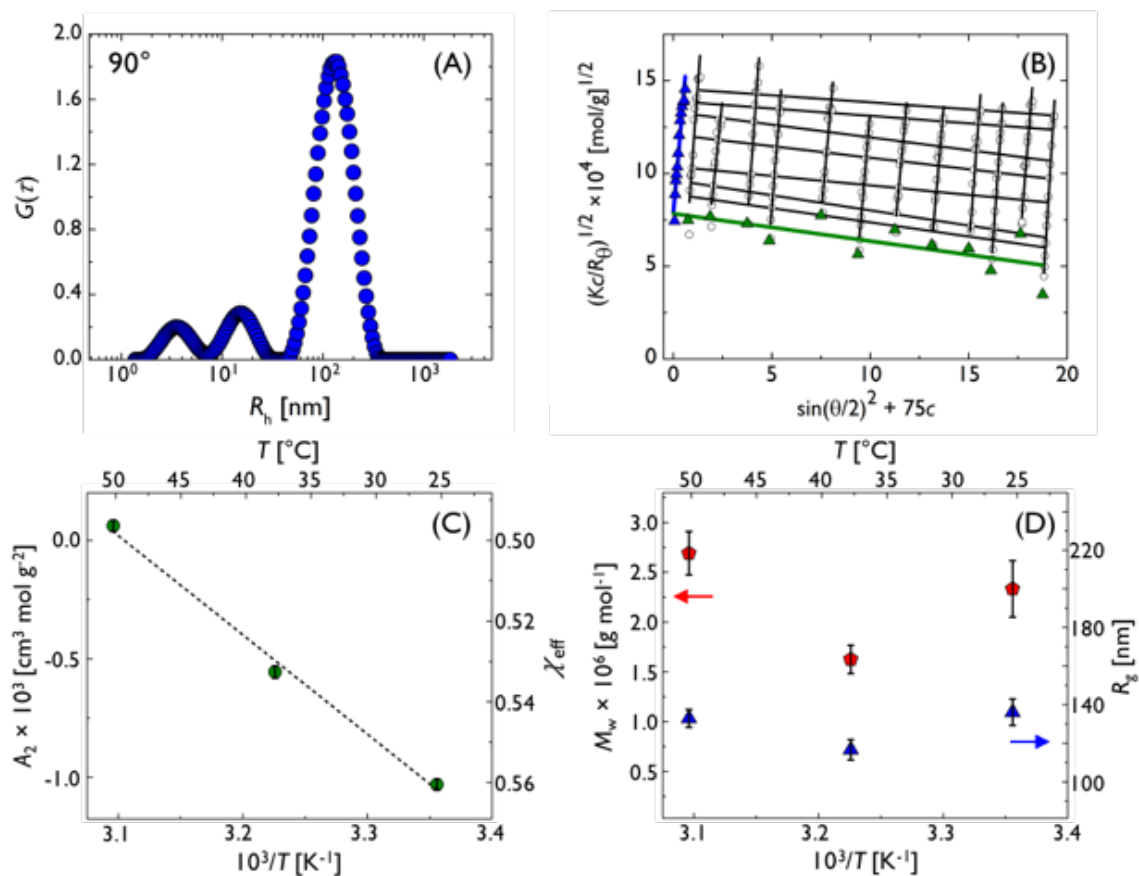


Figure 6.1. (A) Hydrodynamic radius distribution of HPMCAS in PBS buffer at 37 °C. The distribution was calculated by performing a REPES analysis on the 90° autocorrelation function measured by DLS. (B) Berry-modified Zimm plot of HPMCAS in PBS at 37 °C. The open black circles are the measured data, while the green and blue lines are the zero-angle and zero-concentration extrapolations, respectively. (C) Second virial coefficient, A_2 , and χ_{eff} of HPMCAS in PBS for various temperatures. PBS is a poor solvent for HPMCAS at 25 and 37 °C. (D) Molecular weight, M_w , and radius of gyration, R_g , of HPMCAS in PBS.

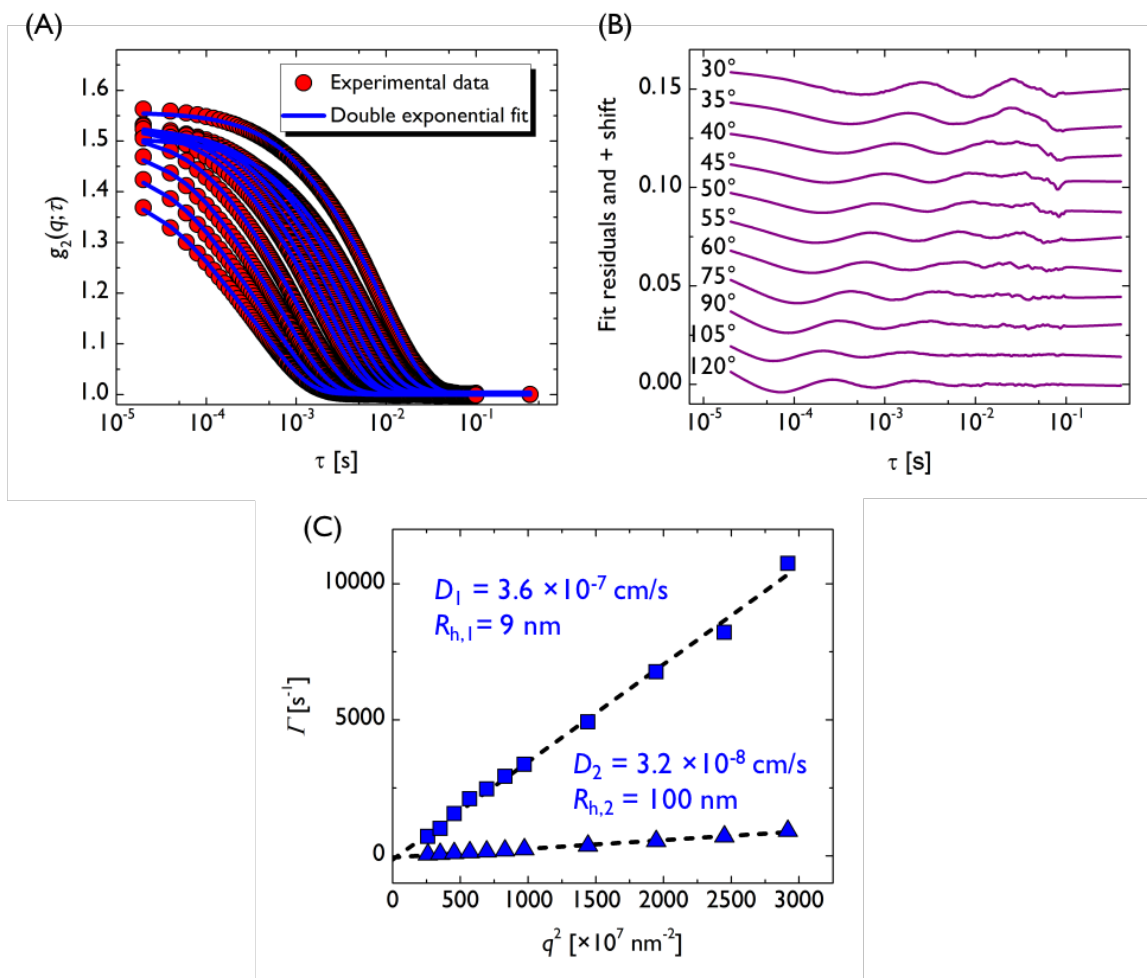


Figure 6.2. Additional DLS data of 9 mg/mL of HPMCAS in PBS at 37°C. (A) Comparison of autocorrelation functions versus double exponential fit. (B) Double exponential fit residuals. (C) Decay rate (Γ) versus q^2 for both modes of double exponential fit.

Table 6.1. Fitted parameters from double exponential fit of second-order autocorrelation functions for 9 mg/mL HPMCAS in PBS at 37°C.

Angle [°]	B	β	f	Γ_1 [1/s]	Γ_2 [1/s]
30	1.0004	0.56	0.90	49	720
35	1.004	0.50	0.89	73	1000
40	1.0038	0.52	0.90	100	1600
45	1.0021	0.53	0.90	130	2100
50	1.0025	0.53	0.90	160	2500
55	1.0003	0.53	0.89	200	2900
60	1.0025	0.53	0.88	240	3400
75	1.0006	0.52	0.86	380	4900
90	0.9996	0.49	0.84	540	6800
105	1.0006	0.45	0.82	710	8200
120	1.001	0.40	0.81	920	11000

As light scattering is more sensitive to larger objects, the numerical fraction of the larger structure is likely quite low.⁵ While several reports have suggested that the amphiphilicity of HPMCAS causes it to form aggregates or a gel in solution,^{41,42,49,154} no evidence of aggregates was observed using cryo-TEM for solutions of HPMCAS in PBS (Figure 6.3). Alternately, during synthesis of HPMCAS the acetate and succinate moieties not only add to the hydroxyl groups on the anhydroglucose backbone of HPMCAS, but also react with the hydroxypropyl substituent to form oligomeric side chains. Succinic anhydride may also induce chain coupling.^{45,155} To distinguish between aggregates and cross-linked chains, we compared the R_h distribution of HPMCAS dissolved in PBS to that in tetrahydrofuran at 25 °C (Figure 6.4). Despite the different solvents, the R_h distributions are nearly identical. The persistence of the slower mode suggests that the 100 nm structure primarily reflects a low concentration of covalently-linked HPMCAS chains.

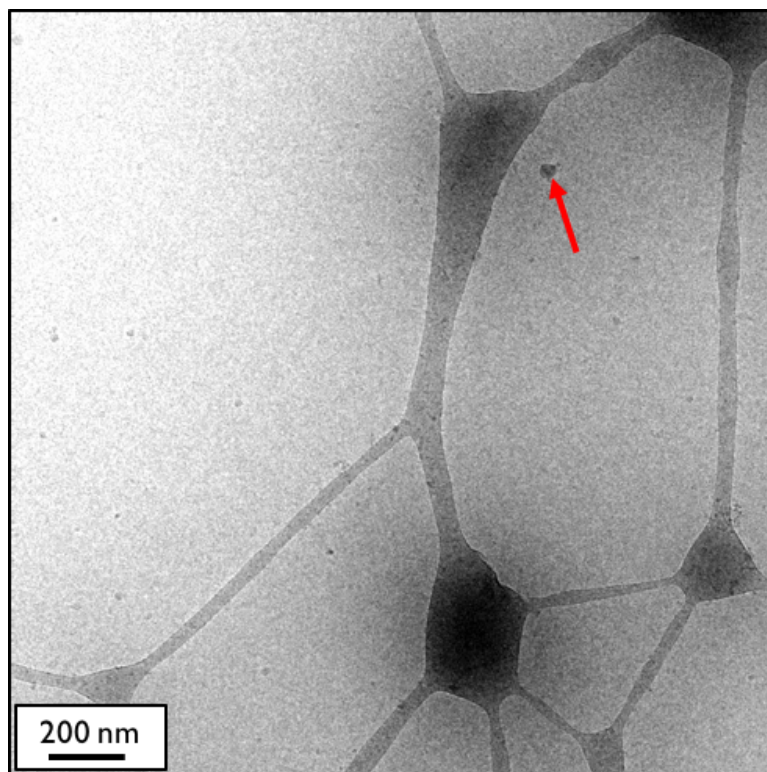


Figure 6.3. Cryo-TEM of 9 mg/mL HPMCAS in PBS solution. The red arrow points to an ice crystal artifact.

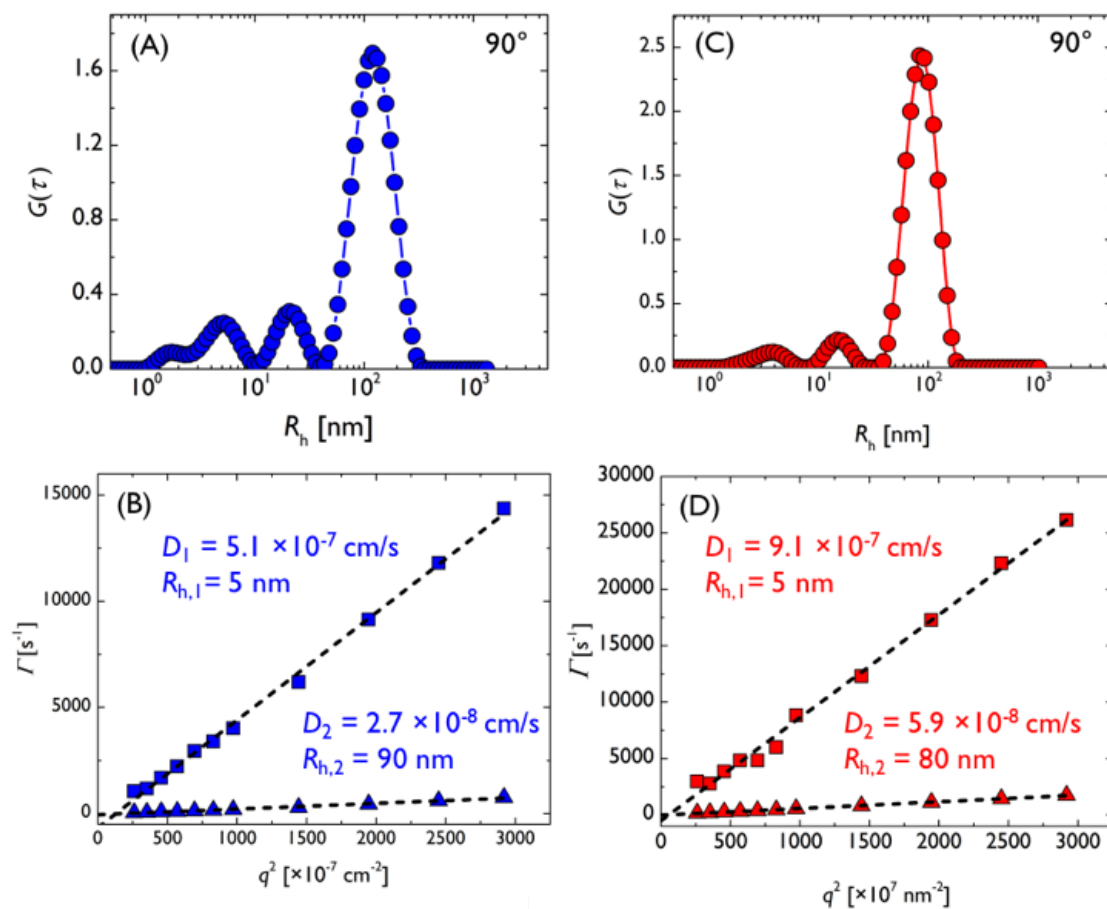


Figure 6.4. (A) REPES analysis and (B) double exponential fit analysis for 8 mg/mL of HPMCAS in PBS at 25 °C. (C) REPES analysis and (D) double exponential fit analysis for 8 mg/mL of HPMCAS in tetrahydrofuran at 25 °C.

To further probe the solution behavior of HPMCAS, SLS was performed on dilute solutions (≤ 0.25 mg/mL) in PBS. Static light scattering (SLS) data were fit to the Berry-modified Zimm equation:¹¹⁹

$$\sqrt{\frac{Kc}{R_\theta}} = \frac{1}{M_w^{1/2}} \left(1 + \frac{q^2 R_g^2}{6} + \dots \right) + 2A_2 c + \dots \quad (6.3)$$

R_θ is the Rayleigh ratio, K is the optical constant, c is concentration (g/mL), A_2 is the second virial coefficient, M_w is weight-average molecular weight of the polymer, q is the scattering vector, and R_g is the radius of gyration of the polymer in solution. Figure 6.1B, 6.5A, and 6.5B are the Berry-modified Zimm plots for the solutions at 37 °C, 25, and 50 °C, respectively. Figures 6.5C-E magnify the zero-concentration extrapolation lines at 25, 37, and 50°C. The zero-angle and zero-concentration extrapolations were used to estimate the second virial coefficient, A_2 , weight-average molecular weight, M_w , and radius of gyration, R_g . An effective interaction parameter, χ_{eff} , was calculated by

$$\chi_{eff} = \frac{1}{2} - \frac{M_0^2 \bar{V}_s A_2}{\bar{V}_p^2} \quad (6.4)$$

M_0 is the polymer repeat unit molecular weight, \bar{V}_s is the solvent molar volume, \bar{V}_p is the polymer average repeat unit molar volume. Based on the temperature dependence of A_2 and χ_{eff} , HPMCAS dissolved in PBS displays an upper critical solution temperature phase diagram (Figure 6.1C). At 25 and 37 °C, PBS is a poor solvent for HPMCAS, indicating there is a thermodynamic driving force for HPMCAS to preferentially interact with itself (and/or possibly other species) rather than with water molecules. At 50 °C, PBS is approximately a theta solvent for HPMCAS.⁵ Both M_w and R_g are essentially invariant with temperature (Figure 6.1D). The measured R_g is consistent with the 100 nm mode observed by DLS, and given the observation of 100 nm structures in different solvents, temperatures, and across orders of magnitude in concentration, strongly suggests that HPMCAS solutions contain species resulting from chain coupling.

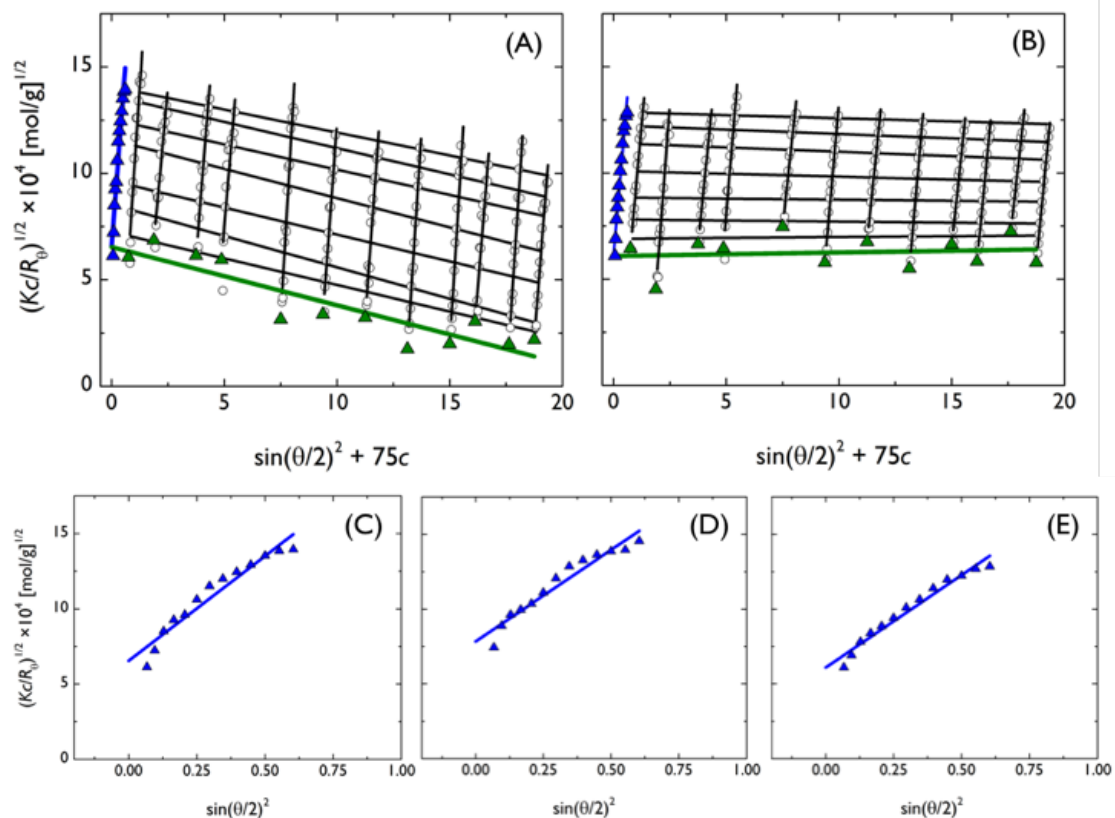


Figure 6.5. Berry-modified Zimm plots of HPMCAS in PBS at (A) 25 and (B) 50 °C. Zero-concentration extrapolation lines at (C) 25, (D) 37, and (E) 50 °C.

6.3.2 Dissolution of phenytoin and HPMCAS SDs

Figure 6.6 features dissolution profiles of phenytoin (PHY) and HPMCAS SDs with varying drug loading. The 10 wt% PHY SD dissolution profile plateaus at 600 $\mu\text{g}/\text{mL}$ and then rapidly decays after 20 min. The 20 wt % PHY SD dissolution profile decays from 600 $\mu\text{g}/\text{mL}$ after 4 min, while the 50 wt% SD dissolution profile stays at a low concentration over 6 hours. The observed trends show that PHY, a drug with a strong tendency to crystallize (Figure D.1), can be temporarily stabilized in solution by HPMCAS. The polymer, however, has minimal influence on the solubility of crystalline PHY (Figure 6.7), confirming that the dissolution profiles reflect kinetic phenomena.

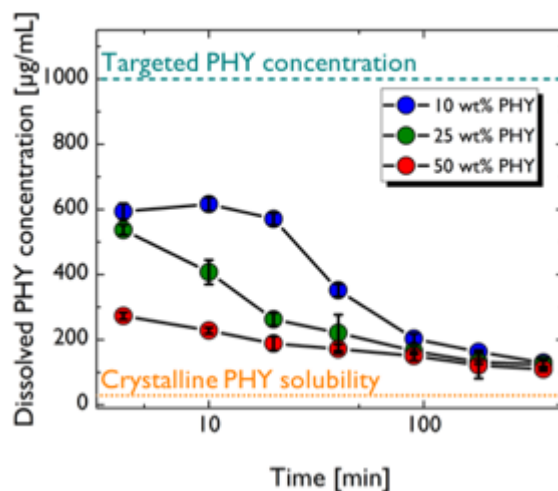


Figure 6.6. Dissolution profiles of PHY:HPMCAS SDs with various drug loadings.

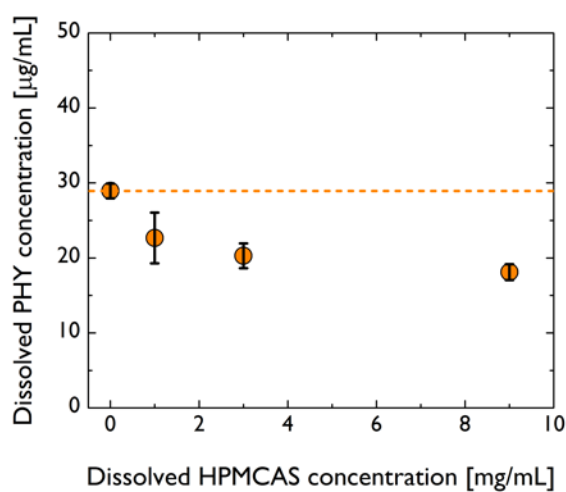


Figure 6.7. Measured solubility of crystalline phenytoin in HPMCAS solutions. The polymer had minimal influence on the solubility of the crystalline drug.

To further elucidate the dissolution mechanism, PHY:HPMCAS SD dissolution media were characterized using both cryo-TEM and small-angle X-ray scattering (SAXS). For the 10 wt% PHY SD, cryo-TEM revealed that the dissolution media contained nanoparticles that persisted over 90 min, with a constant volumetric average radius of 15 ± 3 nm (Figure 6.8A), much smaller than the large mode structures in HPMCAS solutions observed by light scattering and also other previously reported dissolution aggregates.¹⁶

Figure 6.9 contains additional cryo-TEM images of 10 wt% PHY SD dissolution media. These nanoparticles are not detected during the dissolution of spray dried HPMCAS particles (Figure 6.10). SAXS further corroborates the presence of nanoparticles in the dissolution media (Figure 6.8B). The shoulder in the SAXS patterns between 4–90 min confirms the presence of structures ≈ 100 nm in size, while the decaying shoulder intensity verifies the gradual disappearance of the structures. SAXS patterns of centrifuged dissolution media also display the same trend (Figure 6.11). Additionally, beginning at 20 min, an upturn in the SAXS pattern emerges at $q < 0.3 \text{ nm}^{-1}$. This upturn, coinciding with the first time point in which PHY crystals are observed in the dissolution media by optical microscopy,¹⁵⁶ possibly indicates the onset of PHY crystallization from solution.

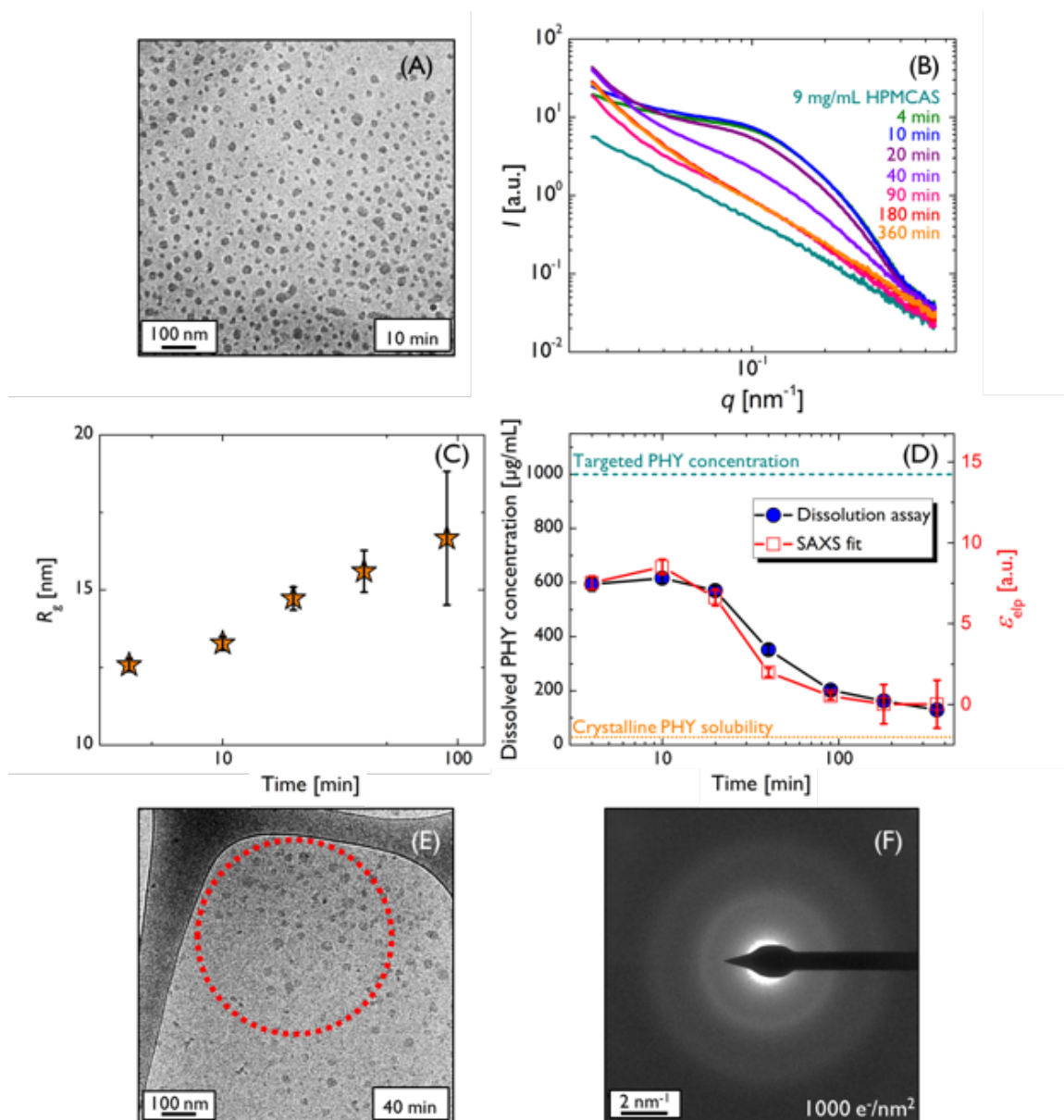


Figure 6.8. (A) Cryo-TEM image of 10 wt% phenytoin SD dissolution media at 10 min. (B) SAXS patterns of 10 wt% phenytoin SD dissolution media at various time points. The characteristic shoulder confirmed the presence of a metastable nanostructure in solution. (C) Radius of gyration, R_g , estimated by fitting SAXS pattern to Equation 6.5 using a triaxial ellipsoid form factor. (D) Comparison of dissolution profile and estimated ellipsoid scaling parameters. Measured drug concentration directly correlated with the presence of nanoparticles in the dissolution media. (E) Low-dose cryo-TEM image and (F) electron diffraction pattern of 10 wt% phenytoin dissolution media at 40 min. Red circle represents position of SAD aperture during acquisition. Lack of sharp diffraction spots suggested nanoparticles are amorphous.

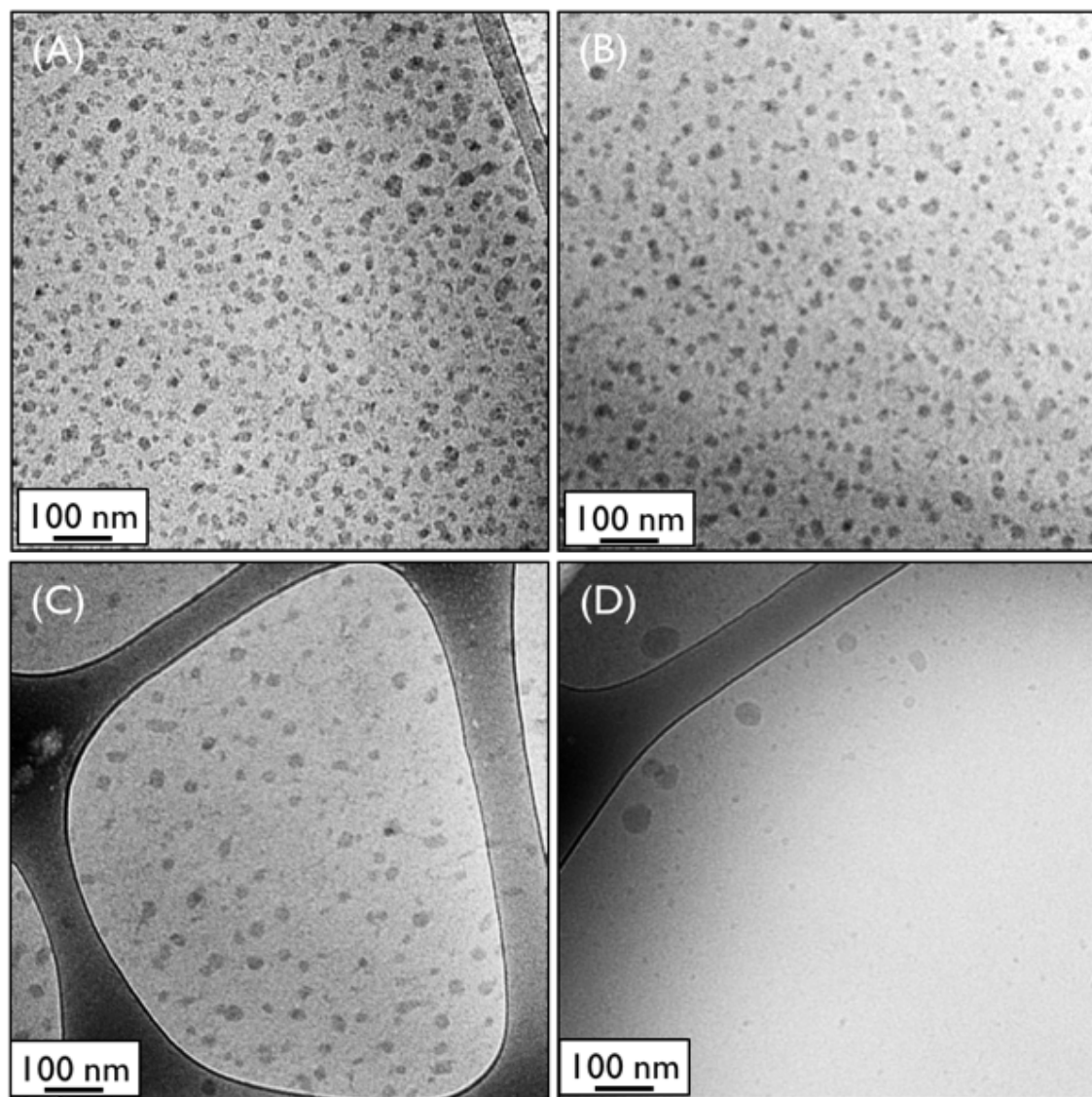


Figure 6.9. Cryo-TEM images of 10 wt% PHY SD dissolution media at (A) 4, (B) 20, (C) 40, and (D) 90 min.

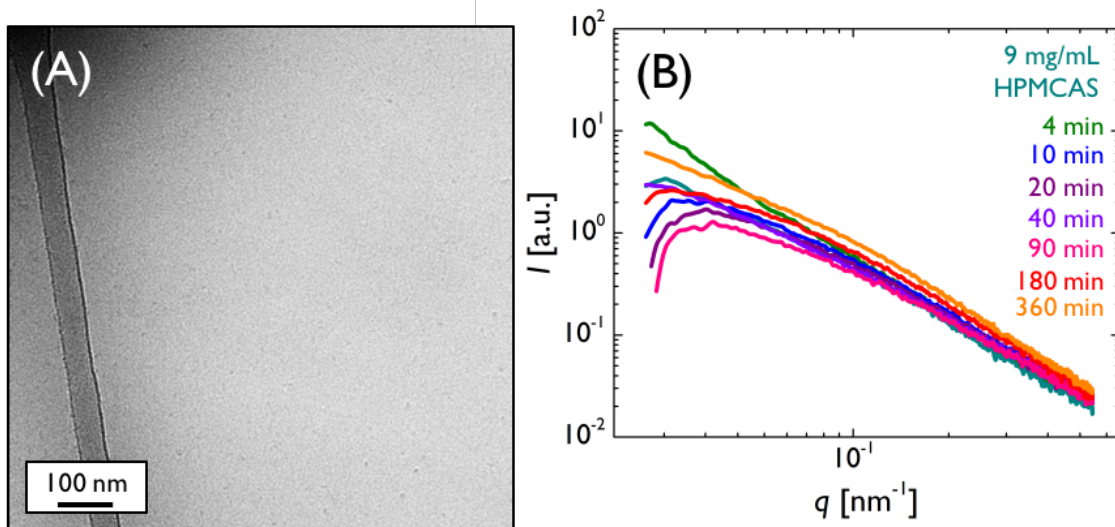


Figure 6.10. Characterization of spray dried HPMCAS dissolution media (targeted concentration of 9 mg/mL). (A) Cryo-TEM of dissolution media at 4 min. (B) SAXS patterns.

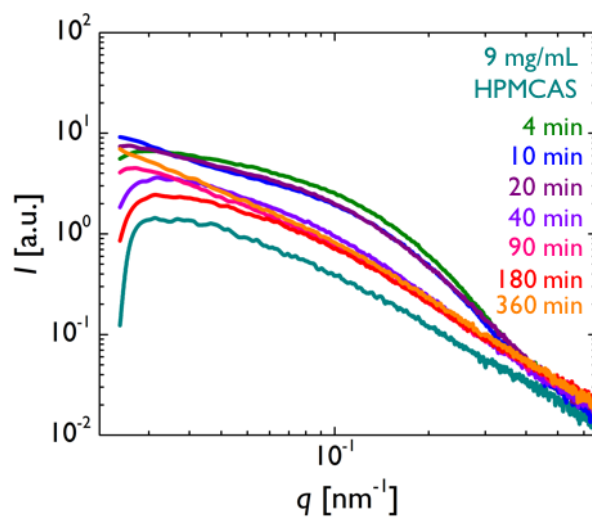


Figure 6.11. SAXS patterns of centrifuged 10 wt% PHY SD dissolution media.

SAXS patterns may be quantitatively analyzed by fitting the scattering intensity, $I(q)$, to an empirical model that is a sum of form factor scattering from nanoparticles (first term) and pure HPMCAS (second term):

$$I(q) = P_{np}(q) + \beta q^{-\gamma} + BG \quad (6.5)$$

$P_{np}(q)$ is a form factor that describes nanoparticle shape, β and γ are power law constants, and BG is the background. Because the nanoparticles observed in the cryo-TEM images were jagged, a triaxial ellipsoid form factor was used to describe the nanoparticle shape:^{S157}

$$P_{elp}(q) = \frac{2}{\pi} \varepsilon_{elp} \int_0^{\pi/2} \int [\Phi(qr(a, b, c, \theta, \varphi))]^2 \sin \theta \, d\theta d\varphi \quad (6.6)$$

$$\Phi(x) = \frac{3[\sin(x) - x \cos(x)]}{x^3} \quad (6.7)$$

$$r(a, b, c, \theta, \varphi) = \sqrt{(a^2 \sin^2 \varphi + b^2 \cos^2 \varphi) + c^2 \cos^2 \theta} \quad (6.8)$$

$$R_g = \sqrt{\frac{a^2 + b^2 + c^2}{5}} \quad (6.9)$$

ε_{elp} is the ellipsoid scattering intensity scaling factor, q is the scattering vector, Φ is the square root of the hard sphere form factor, a , b , and c are semi-axes lengths, and R_g is the ellipsoid radius of gyration. Figure 6.12A compares the SAXS patterns to the model fits, Figure 6.12B features the extracted semi-axes lengths, and Table 6.2 lists values of all fit parameters. From 4 to 90 min, the estimated nanoparticle R_g increased slightly (Figure 6.8C). The estimated values of ε_{elp} , which assess scattering caused solely by the nanoparticles, exhibited a trend identical to the dissolution profile (Figure 6.8D). Thus, measured drug concentration directly correlates with the presence of nanoparticles in solution.

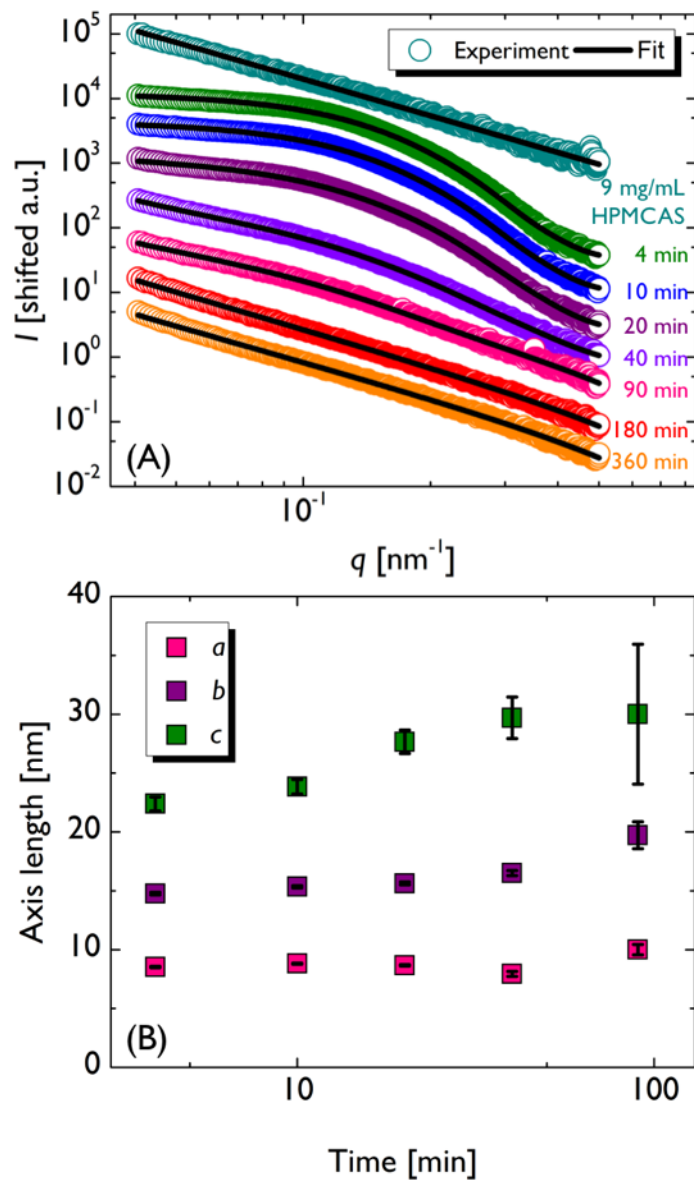


Figure 6.12. (A) Comparison of experimental SAXS data versus triaxial ellipsoid form factor model fit. (B) Ellipsoid semi-axes lengths extracted from model fitting. SAXS pattern for 9 mg/mL HPMCAS solution was fit only to a power law model.

Table 6.2. Fitted parameters from triaxial ellipsoid form factor model fit of 10 wt% PHY SD dissolution media SAXS patterns.

Time [min]	ε_{elp} [a.u.]	a	b	c	β	γ	BG [a.u.]
4	7.5	8.5	15	22	0.003	1.2	0.014
10	8.5	8.8	15	24	0.008	1.2	0.0008
20	6.6	8.7	16	28	0.005	1.8	0.002
40	2.0	7.9	17	30	0.006	2.1	0.003
90	0.5	10	20	30	0.011	1.7	-0.014
180	0.02	2.1	15	20	0.009	1.9	-0.010
360	0.02	2	11	20	0.011	1.9	-0.013
9 mg/mL HPMCAS	-	-	-	-	0.023	1.3	-0.051

The nanoparticles in the 10 wt% PHY SD dissolution media may also be described by a polydisperse sphere form factor:

$$P_{sph}(q) = \varepsilon_{sph} \int_0^{\infty} p(R) \Phi^2(qR) dR \quad (6.10)$$

$$p(R) = \frac{z^{z+1}}{\Gamma(z+1)} \frac{R^{z-1}}{R_{avg}^z} \exp\left(\frac{-zR}{R_{avg}}\right) \quad (6.11)$$

ε_{sph} is the polydisperse sphere scattering intensity scaling factor, p is the normalized Schulz-Zimm distribution,¹⁵⁸ R is the radius, q is the scattering vector, Φ is the square root of the hard sphere form factor (Equation 6.7), z is the Schulz-Zimm distribution width parameter, and R_{avg} is the average radius. Figure 6.13 is a comparison between the SAXS patterns and polydisperse sphere form factor model fit, Figure 6.14 shows R_{avg} , z , and ε_{sph} , and Table 6.3 features values for all fit parameters. Fitting the data to a polydisperse sphere form factor gave similar results.

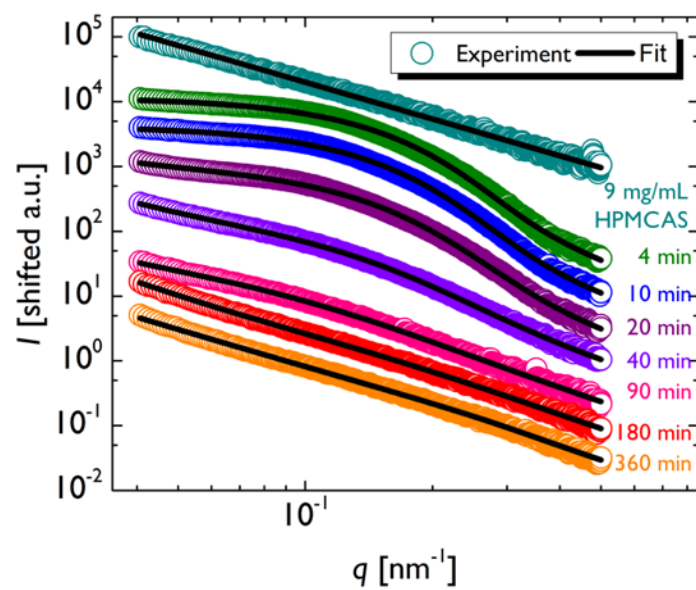


Figure 6.13. Comparison of experimental SAXS data versus polydisperse sphere form factor model fit. SAXS pattern for 9 mg/mL HPMCAS solution was fit only to a power law model.

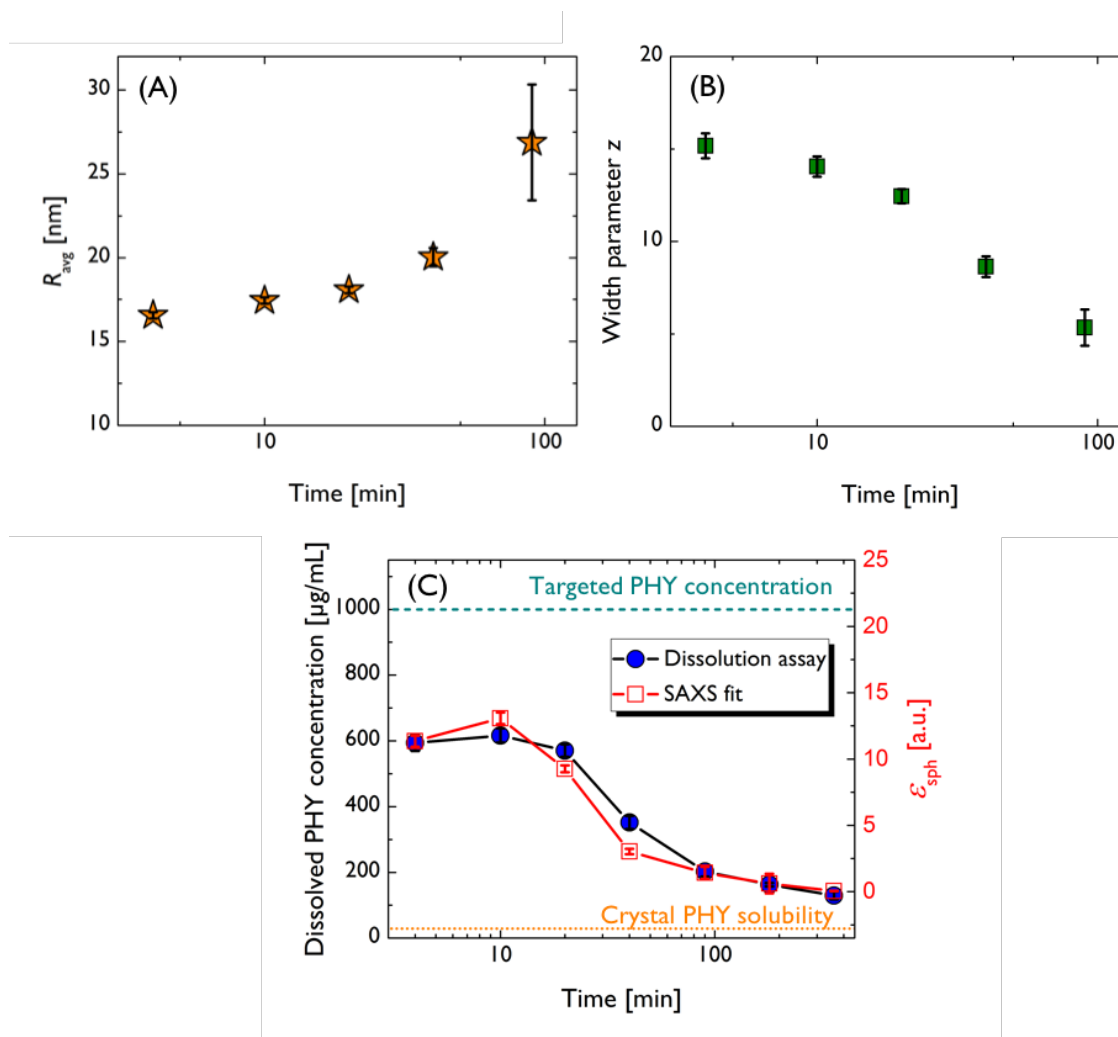


Figure 6.14. (A) Average radius (R_{avg}) and (B) Schulz-Zimm distribution width parameter (z) extracted from polydisperse sphere form factor model fit for 10 wt% PHY SD dissolution media. (C) Comparison of 10 wt% PHY SD dissolution profile and sphere scattering intensity scaling factor (ϵ_{sph}).

Table 6.3. Fitted parameters from polydisperse sphere form factor model fit of 10 wt% PHY SD dissolution media SAXS patterns.

Time [min]	ϵ_{sphere} [a.u.]	R_{avg}	z	β	γ	BG [a.u.]
4	11	17	15	0.0036	1.2	0.005
10	13	17	14	0.0016	1.2	0.009
20	9.3	18	12	0.0018	2.3	0.006
40	3	20	8.6	0.0052	2.2	0.003
90	1.4	27	5.3	0.0063	1.8	-0.002
180	0.61	20	3.4	0.0021	2.4	0.004
360	0.047	10	75	0.0089	1.9	-0.005
9 mg/mL HPMCAS	-	-	-	0.023	1.3	-0.051

To determine whether the nanoparticles are crystalline PHY, electron diffraction patterns of 10 wt% SD dissolution media were collected under low-dose conditions. While electron diffraction patterns of crystalline drug exhibit strong Bragg peaks,¹⁵⁹ the absence of Bragg peaks in the dissolution media diffraction patterns suggests that the nanoparticles are amorphous structures (Figures 6.8E and 6.8F), consistent with observations by Taylor *et al.*¹⁶

The dissolution profiles of SDs with higher PHY loading also correlated with the presence of nanoparticles. For the 25 wt% PHY SD, cryo-TEM and SAXS verified that at 4 min, when the measured PHY concentration was at 600 $\mu\text{g/mL}$, the dissolution media contained nanoparticles with a similar average size as the 10 wt% PHY SD dissolution media (Figures 6.15A and 6.16A, respectively). After 10 min, when the PHY concentration begins to decrease, the nanoparticles disappeared from solution (Figures 6.15B and 6.15B). For the 50 wt% PHY SD, nanoparticles were not detected at any time point (Figures 6.17). These results demonstrate that achievement and stabilization of high PHY concentrations corresponds to nanoparticle formation.

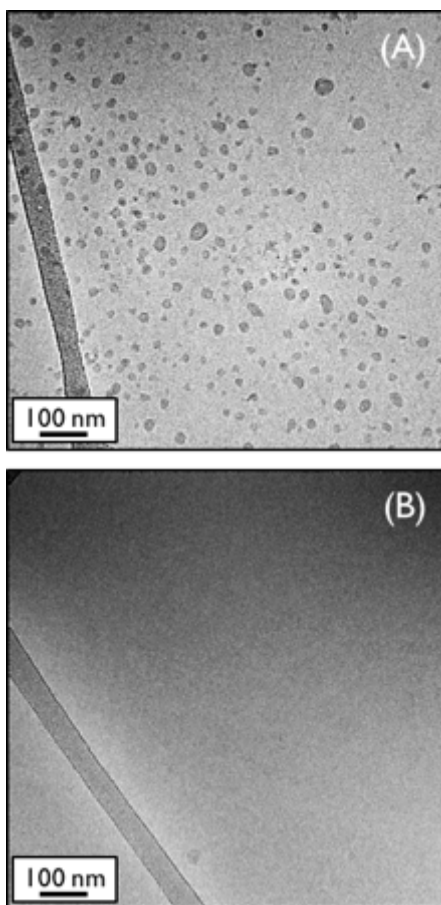


Figure 6.15. Cryo-TEM images of 25 wt% phenytoin dissolution media at (A) 4 min and (B) 10 min.

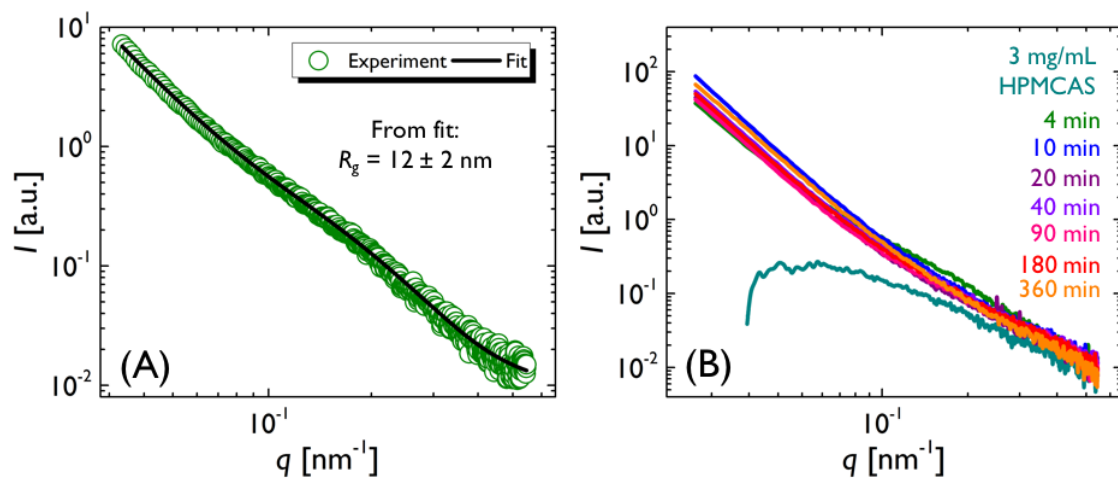


Figure 6.16. (A) Comparison of SAXS pattern and triaxial ellipsoid form model fit for 25 wt% PHY SD dissolution media at 10 min. (B) SAXS patterns of 25 wt% PHY SD dissolution media at various time points.

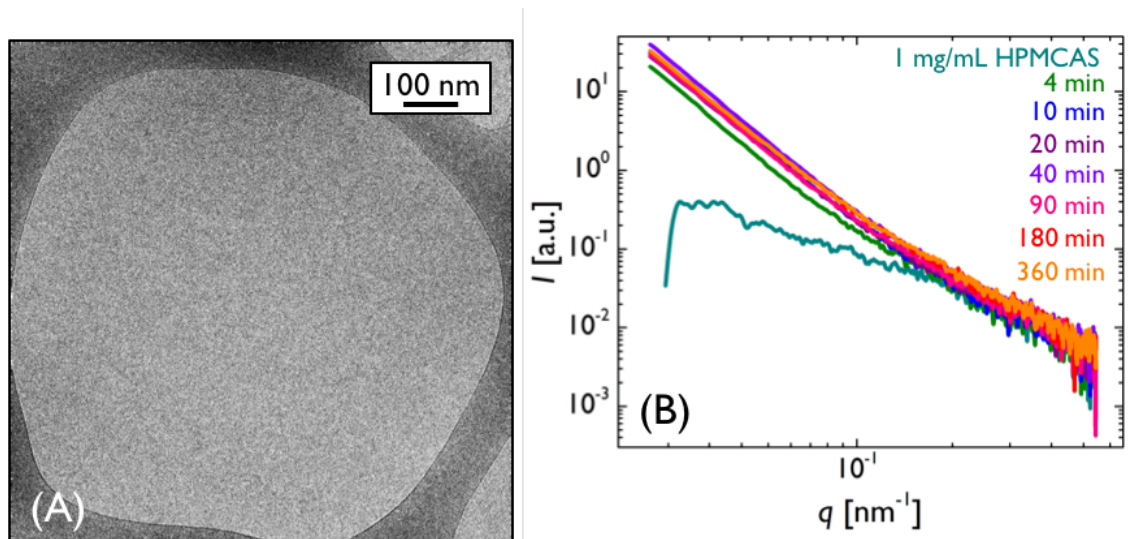


Figure 6.17. Characterization of 50 wt% PHY SD dissolution media. (A) Cryo-TEM image at 4 min. (B) SAXS patterns at various time points.

The influence of targeted drug concentration on PHY SD dissolution was investigated. Figure 6.18A is the dissolution profile for 10 wt% PHY SD with a targeted drug concentration of 300 $\mu\text{g}/\text{mL}$. In this case, dissolution of the SD results in lower concentrations of both drug and polymer relative to the measurement where 1000 $\mu\text{g}/\text{mL}$ of drug was targeted. Concentration decreased at 360 min, likely caused by crystallization or precipitation of drug from solution. Nanoparticles were not detected in the dissolution media by both cryo-TEM and SAXS (Figures 6.18B and 6.18C). Figure 6.18D is the dissolution profile for 3.2 wt% PHY SD with a targeted drug concentration of 300 $\mu\text{g}/\text{mL}$. While the polymer concentration is much higher, still no nanoparticles were detected by cryo-TEM and SAXS (Figures 6.18E and 6.18F). These observations strongly suggest nanoparticles only form above some critical PHY concentration.

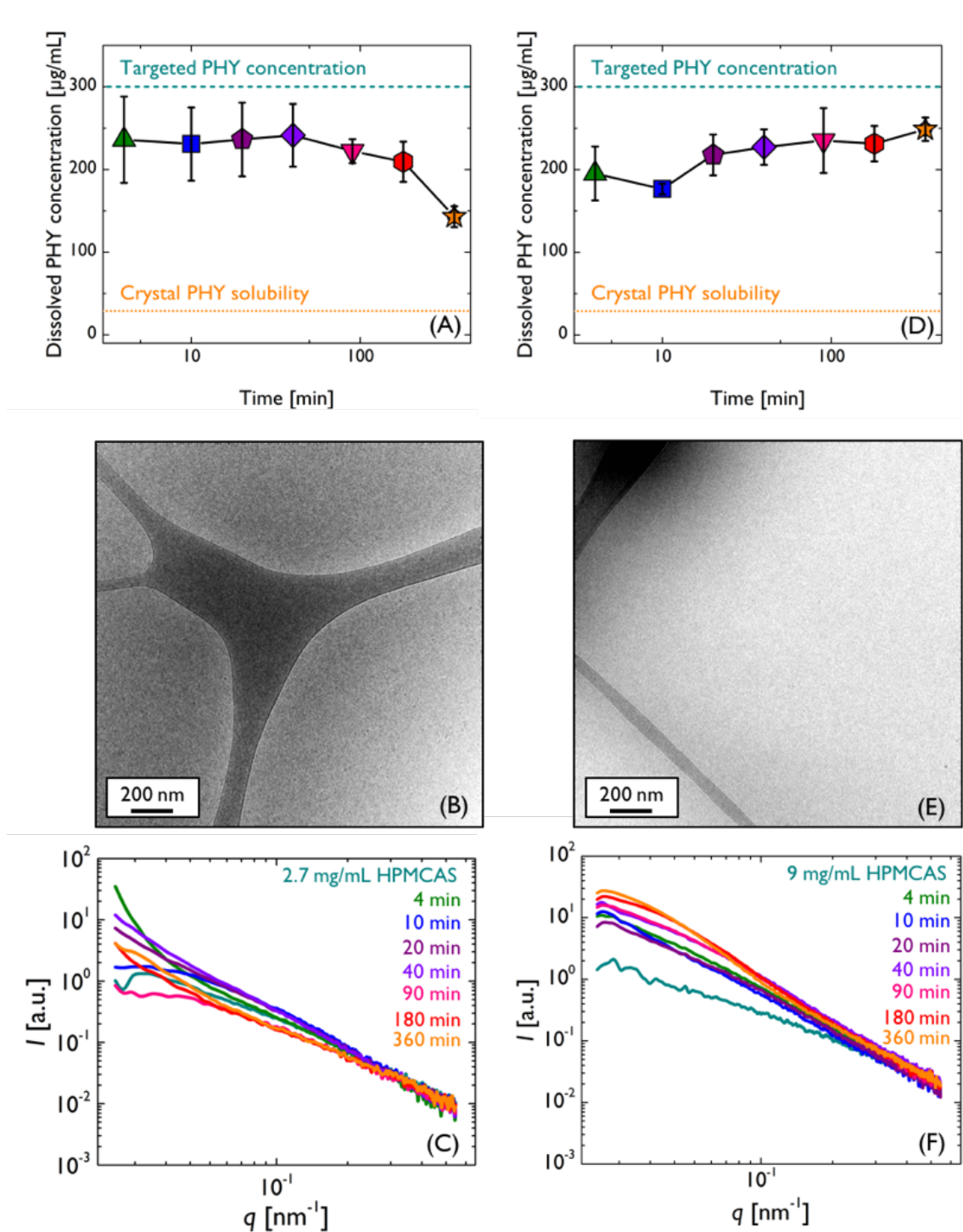


Figure 6.18. Dissolution profiles for PHY SDs with a targeted drug concentration of 300 $\mu\text{g/mL}$. (A) Dissolution profile, (B) cryo-TEM of dissolution media at 4 min, and (C) SAXS patterns of dissolution media for 10 wt% PHY SD. (D) Dissolution profile, (E) cryo-TEM of dissolution media at 4 min, and (F) SAXS patterns of dissolution media for 3.2 wt% PHY SD.

6.3.3 Dissolution of probucol and HPMCAS SDs

Figure 6.19A presents the dissolution profiles of probucol (PRB) and HPMCAS SDs. Increased PRB loading decreased the release rate of drug, a trend unlike the behavior of PHY SDs, but observed for other API:excipient pairings.^{94,95,96} Once the concentration was relatively high, PRB remained in solution. The lack of a concentration decrease is likely related to the relatively weak crystallization tendency of PRB (Figure D.1). Measurements of crystalline PRB solubility in HPMCAS solutions (Figure 6.19B) were overestimated because the solubility media contained both fully dissolved PRB and nanoscale crystals, as confirmed by electron diffraction (Figure 6.19C and 6.19D), that passed through the filter. The PRB crystals, initially many microns in size (Figure D.3B), were smaller than 200 nm in the solubility media. This shrinking in size qualitatively confirmed HPMCAS increased the solubility of crystalline PRB. The poor solvent quality of PBS at 37 °C potentially induces HPMCAS and PRB to interact in solution.

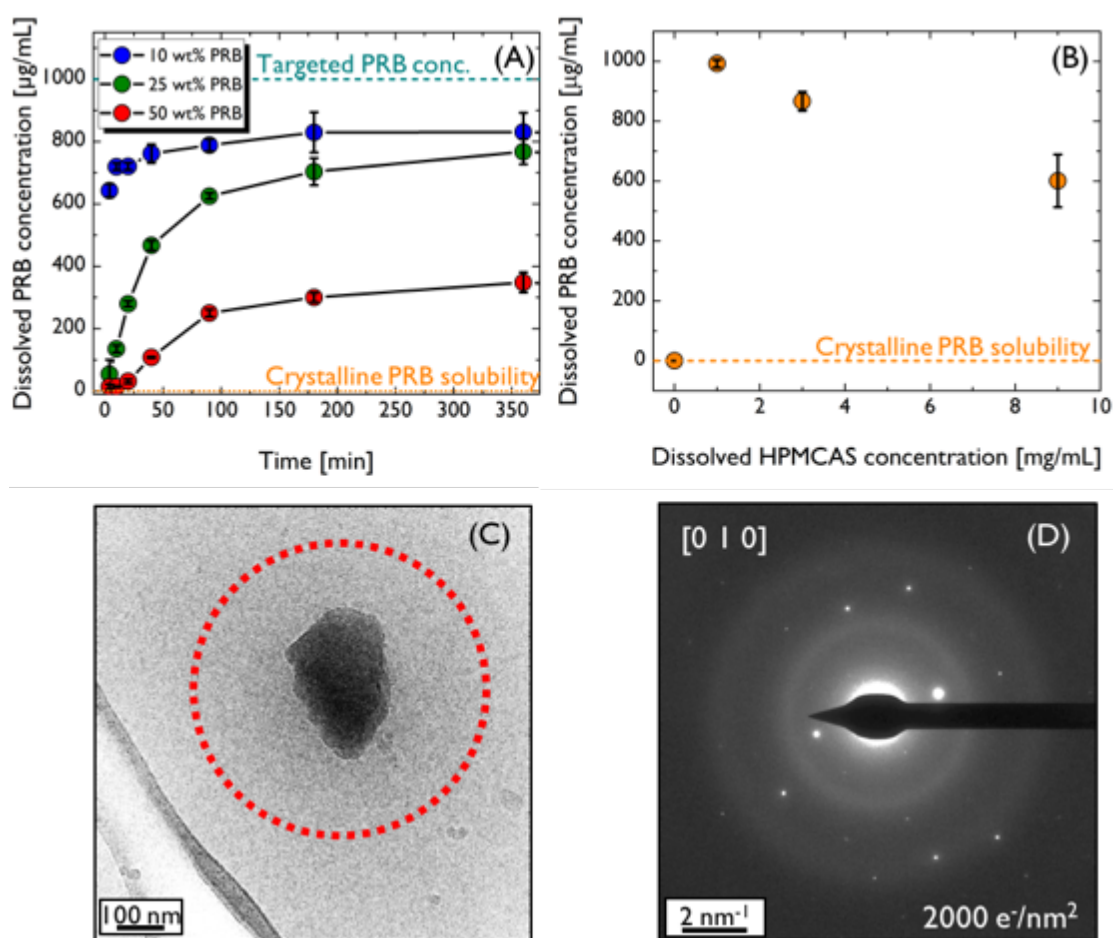


Figure 6.19. (A) Dissolution profiles of probucol:HPMCAS SDs with various drug loadings. (B) Solubility of crystalline probucol in HPMCAS solutions. Measured concentrations were overestimates because the solubility media contained both fully dissolved and nanocrystalline drug. (C) Low-dose cryo-TEM image and (D) electron diffraction pattern of probucol solubility media with 1 mg/mL of HPMCAS. Indexing of diffraction spots confirmed particle is crystalline probucol. Zone-axis and electron dosage are located in the top-left and bottom-right corners of (D), respectively.

In contrast to the solubility measurements, dissolution profiles of PRB SDs correlated with amorphous nanoparticles, not PRB crystals. Cryo-TEM showed the 10 wt% PRB SD dissolution media contained spherical nanoparticles that endured for the entire dissolution assay (Figures 6.20A and 6.21). The volumetric average radius measured from cryo-TEM images at 4, 90, and 360 min were 20 ± 5 nm, 16 ± 4 nm, and 19 ± 4 nm, respectively. SAXS patterns of the dissolution media also exhibited a characteristic

shoulder (Figure 6.20B), although the low electron density of PRB caused this feature to have a weaker intensity than the corresponding feature for 10 wt% PHY SD. The SAXS patterns were quantitatively analyzed by fitting the data to Equation 6.5. Because the nanoparticles observed in the cryo-TEM images were spherical, a polydisperse sphere form factor with a Schulz-Zimm distribution was used to describe the nanoparticle shape (see Figure 6.22). From this form factor, the average sphere radius, R_{avg} , Schulz-Zimm distribution width parameter, z , and sphere scattering intensity scaling factor, ϵ_{sphere} , were estimated. Table 6.4 lists the extracted values of all fit parameters. The growth of nanoparticle size and decrease of dispersity (R_{avg} increased from 20 to 30 nm (6.20C), and z increased from 10 to 30 (Figure 6.23B)) may be described by Ostwald ripening models:

160

$$R_{avg} = \sqrt[n]{kt + R_0^n} \quad (6.12)$$

k is the ripening rate, t is time, and R_0 is the initial particle size. n is the exponent that reflects the mechanism of growth. An n value of 2 suggests the rate limiting step is incorporation of solute into the particle, while a value of 3 indicates growth is diffusion-limited. Because both exponents describe the data (Table 6.5), the mechanism of growth cannot be distinguished. Identical trends between ϵ_{sphere} and dissolution profile established that high PRB concentration coincides with nanoparticles in solution. Additionally, electron diffraction of the dissolution media strongly suggests the nanoparticles are amorphous (Figures 6.20E and 6.20F). Despite the dissimilarity between the physical properties of the APIs, the hydrophobicity of both PRB and PHY likely causes the APIs to form amorphous nanoparticles with HPMCAS during SD dissolution.

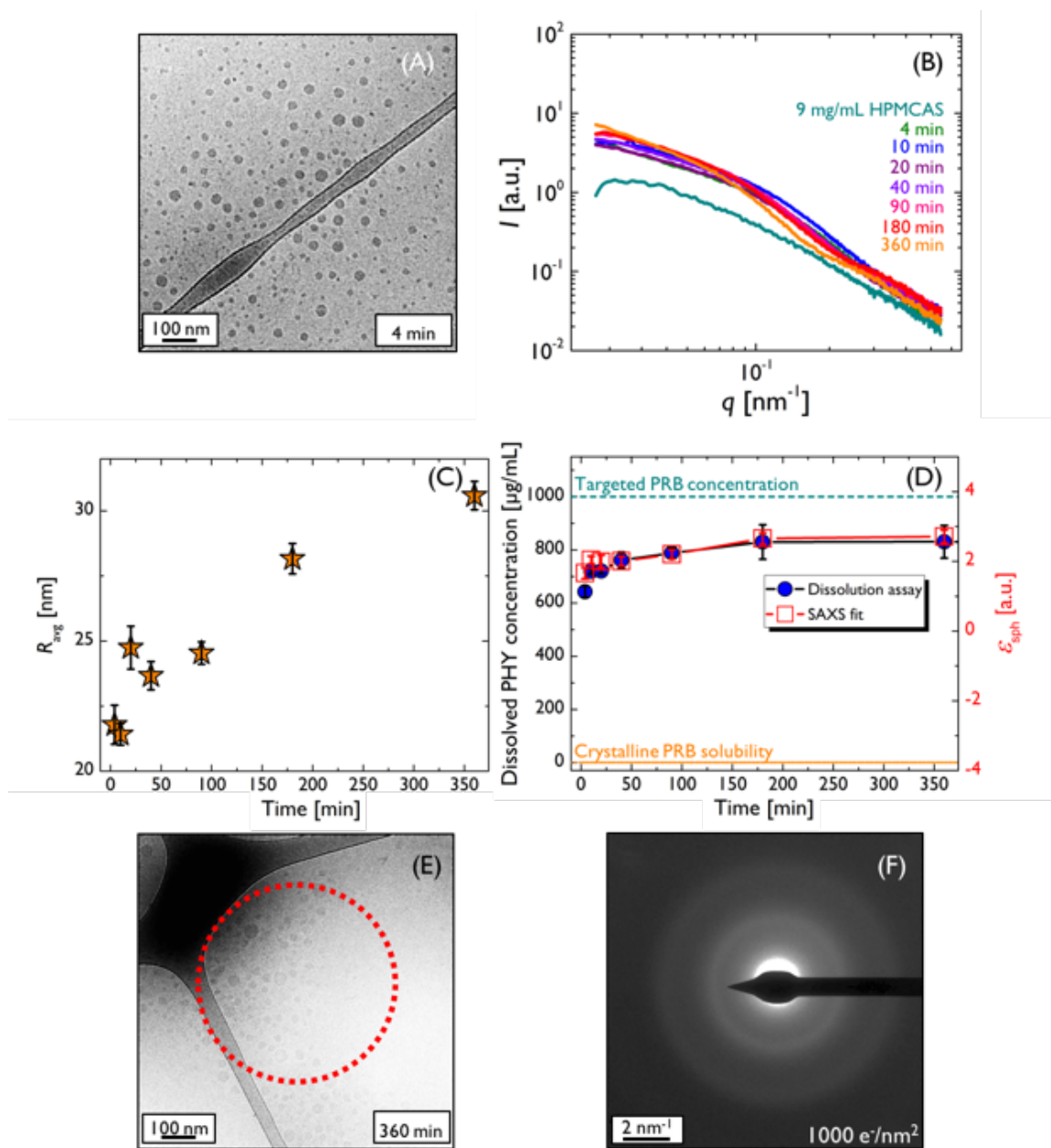


Figure 6.20. (A) Cryo-TEM image of 10 wt% probucol SD dissolution media at 4 min. (B) SAXS patterns of 10 wt% probucol SD dissolution media at various time points. Characteristic shoulder confirmed presence of nanostructures. (C) Average radius of gyration, R_{avg} , of nanoparticles estimated by fitting SAXS patterns to Equation 6.5 using a polydisperse sphere form factor with a Schulz-Zimm distribution. (D) Comparison of dissolution profile and estimated polydisperse sphere scaling parameters. Measured drug concentration directly correlated with the presence of nanoparticles in the dissolution media. (E) Low-dose cryo-TEM image and (F) electron diffraction pattern of 10 wt% probucol SD dissolution media. Red circle represents position of SAD aperture. Electron diffraction patterns suggested nanoparticles are amorphous.

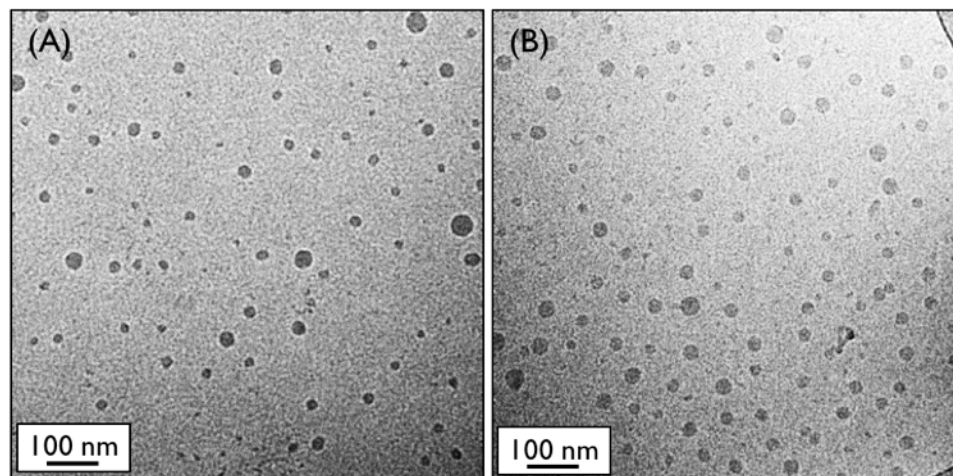


Figure 6.21. Cryo-TEM of 10 wt% PRB dissolution media at (A) 90 and (B) 360 min.

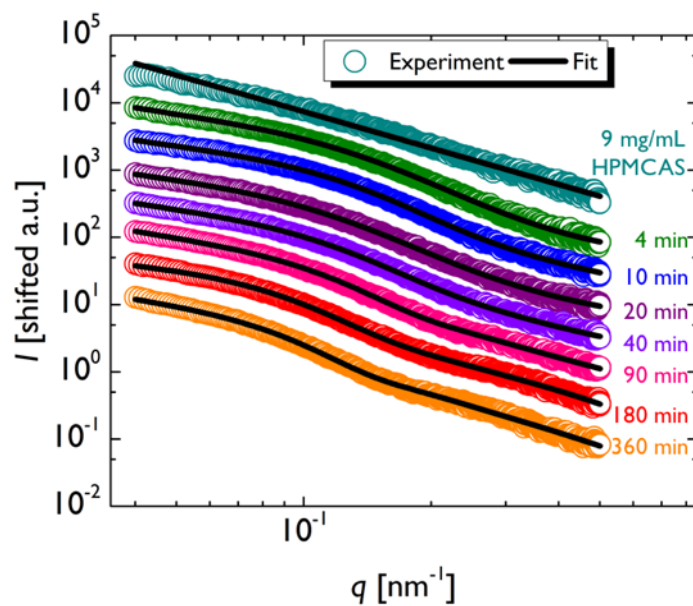


Figure 6.22. Comparison of SAXS patterns and polydisperse sphere form factor model fit for 10 wt% PRB SD dissolution media. SAXS pattern for 9 mg/mL HPMCAS solution was fit to a power law model.

Table 6.4. Fitted parameters from polydisperse sphere form factor model fit of 10 wt% PRB SD dissolution media SAXS patterns.

Time [min]	ε_{sphere} [a.u.]	R_{avg}	z	β	γ	BG [a.u.]
4	1.7	22	7	0.003	1.9	0.012
10	2.0	21	11	0.008	1.6	0.009
20	2.0	25	8	0.006	1.7	0.011
40	2.0	24	12	0.009	1.6	0.006
90	2.2	25	22	0.011	1.6	0.0002
180	2.7	28	20	0.016	1.4	-0.012
360	2.7	31	31	0.011	1.6	-0.008
9 mg/mL HPMCAS	-	-	-	0.020	1.3	-0.043

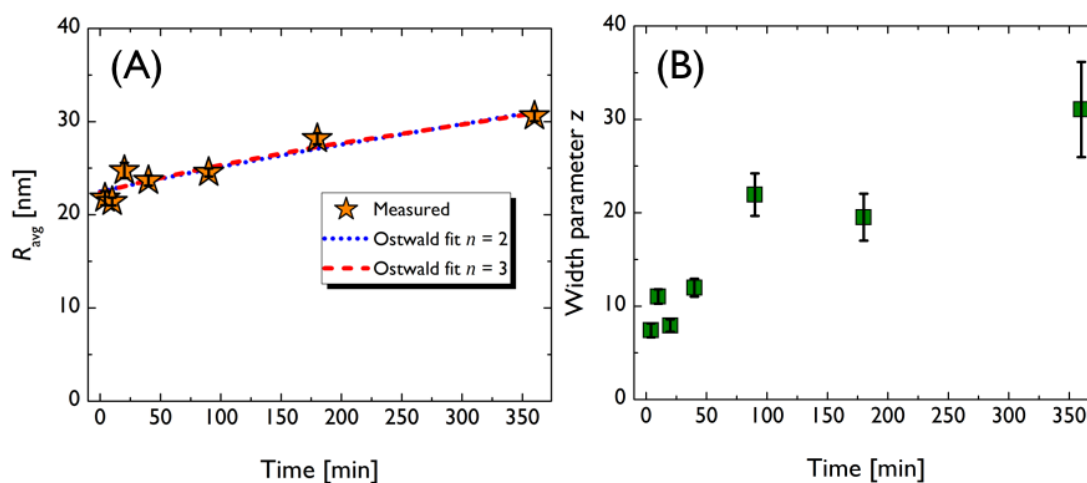


Figure 6.23. (A) Average radius (R_{avg}) and (B) Schulz-Zimm distribution width parameter (z) extracted from polydisperse sphere form factor model fit for 10 wt% PRB SD dissolution media.

Table 6.5. Fitted parameters from Ostwald ripening model fit of 10 wt% PRB SD dissolution media nanoparticles.

n	k [nm ^{n} /min]	R_0 [nm]
2	1.3	23
3	53	23

Cryo-TEM confirms that the lag in the higher PRB loading SD dissolution profiles is mirrored by delayed nucleation of nanoparticles. For 25 wt% PRB SD, the dissolution media at 4 min is not populated by spherical nanoparticles, but instead contains larger structures with ill-defined shapes (Figure 6.24A). These structures are likely disintegrating spray dried SD particles. Coinciding with the increase of PRB concentration, over time the nanoparticles become more spherical and much larger in size relative to the structures in the 10 wt% PRB dissolution media (Figure 6.24B; the volumetric average radius of the nanoparticles at 360 min was 70 ± 40 nm). Although the structures are large, electron diffraction patterns strongly suggest the nanoparticles are amorphous (Figures 6.24C and 6.24D). SAXS patterns of the dissolution media display a small shoulder, but the large size dispersity of the nanoparticles smears the patterns and obscures quantitative analysis (Figure 6.25). The prolonged onset in the 50 wt% PRB dissolution profile also corresponds to delayed nanoparticle nucleation, while the higher drug to polymer ratio leads to much larger nanoparticle sizes (Figure 6.26; the volumetric average radius of the nanoparticles at 360 min is 180 ± 60 nm). While the dissolution behavior for PRB SDs differs greatly from PHY SDs, high concentration of PRB still parallels the appearance of nanoparticles in the dissolution media.

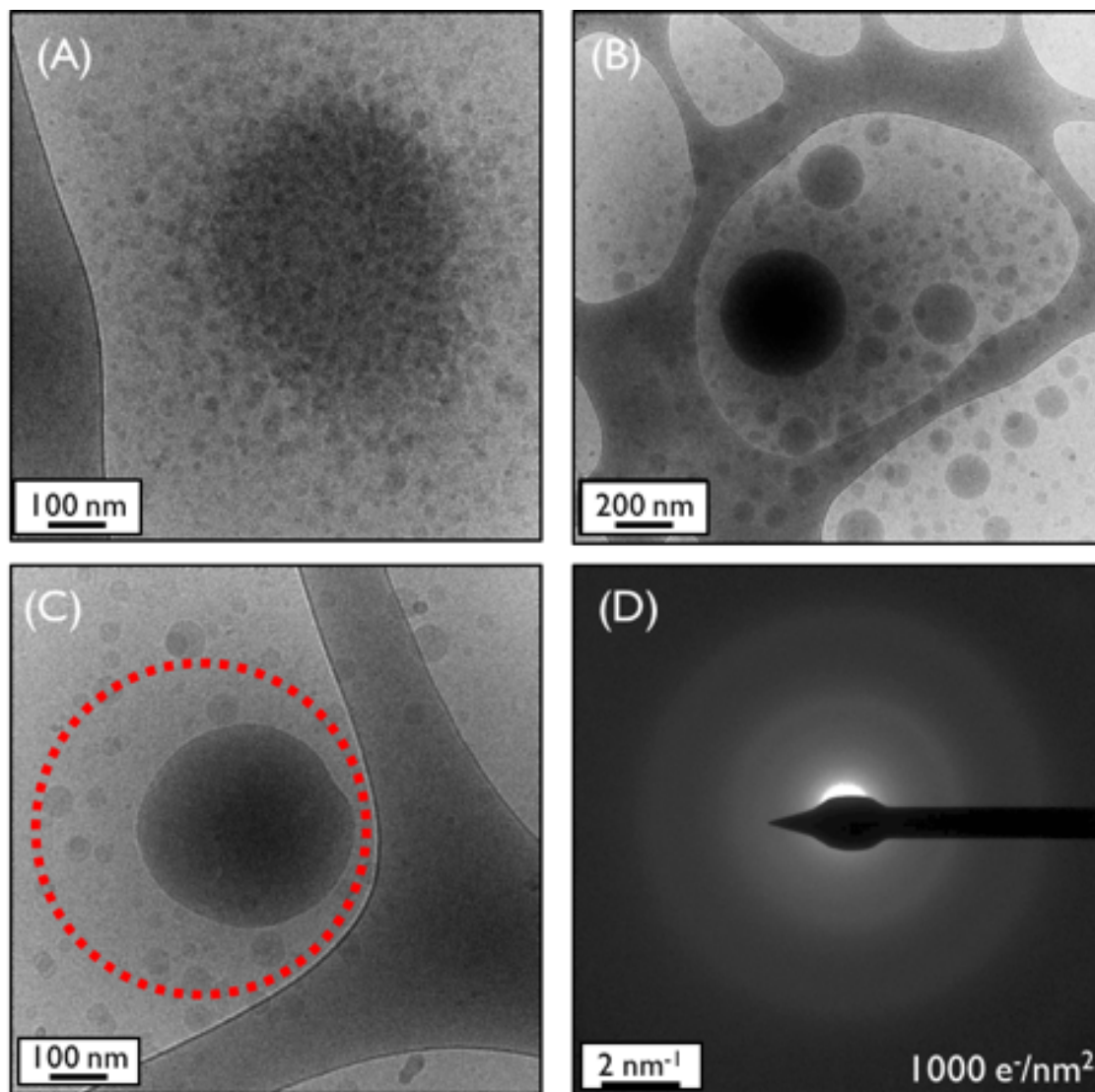


Figure 6.24. 25 wt% probucol SD dissolution media at (A) 4 min and (B) 360 min. (C) Low-dose cryo-TEM image and (D) electron diffraction pattern at 360 min. Electron diffraction pattern suggested nanoparticles are amorphous.

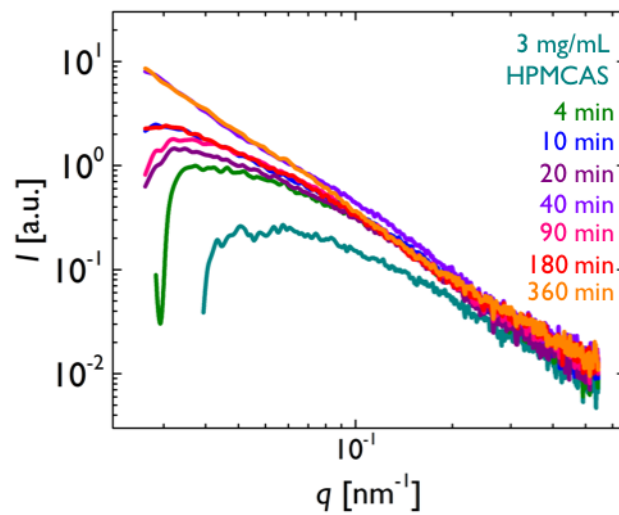


Figure 6.25. SAXS patterns of 25 wt% SD PRB dissolution media.

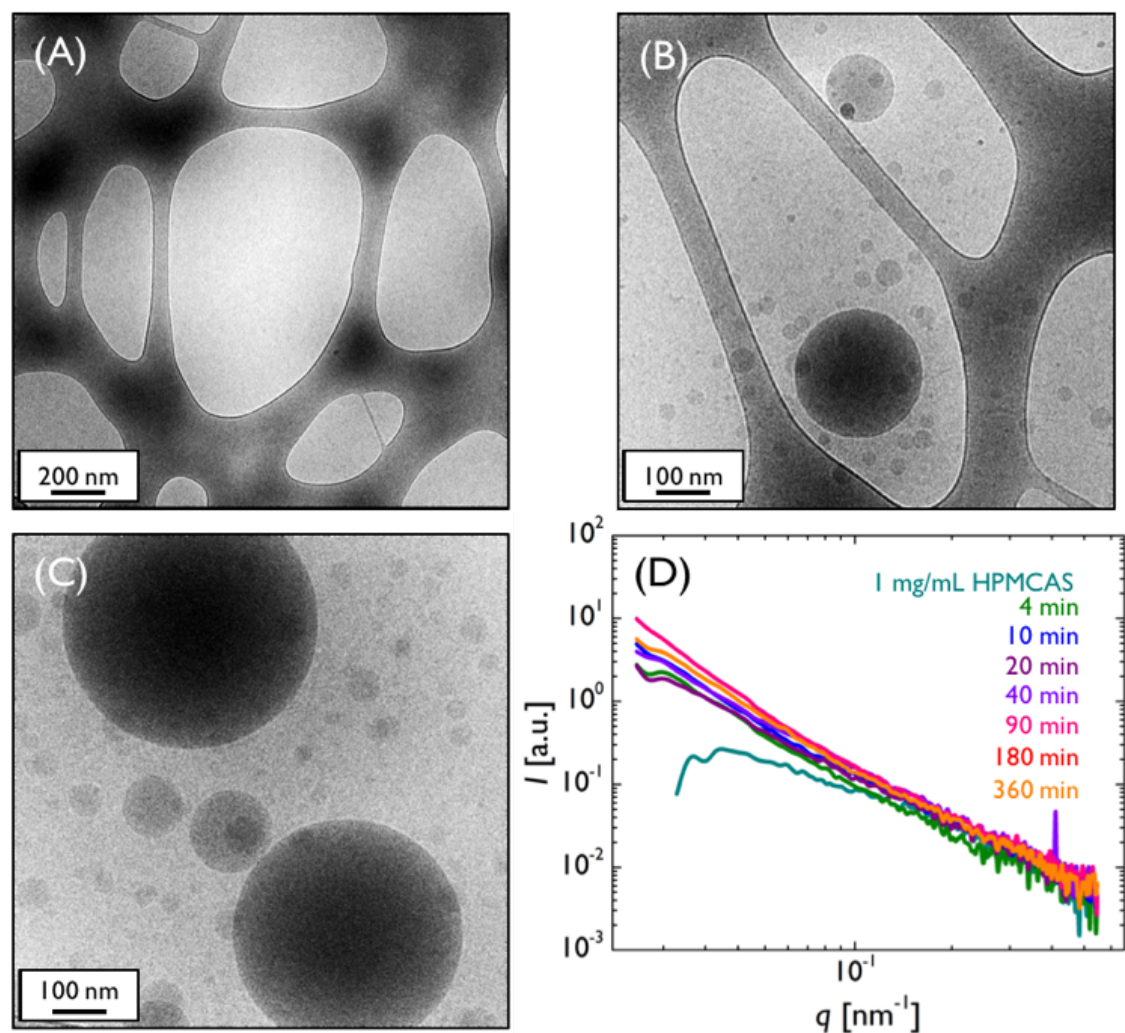


Figure 6.26. Cryo-TEM images of 50 wt% PRB SD dissolution media at (A) 4, (B) 40, and (C) 360 min. (D) SAXS patterns of 50 wt% PRB SD dissolution media.

Figure 6.27 exhibits the dissolution profile and nanostructure characterization for the 10 wt% PRB SD dissolution at a targeted drug concentration of $300 \mu\text{g/mL}$. The detection of nanoparticles in the dissolution media suggests the critical nanoparticle concentration for PRB is lower than $300 \mu\text{g/mL}$. The weak intensity of the shoulder in the SAXS patterns prevents quantitative analysis.

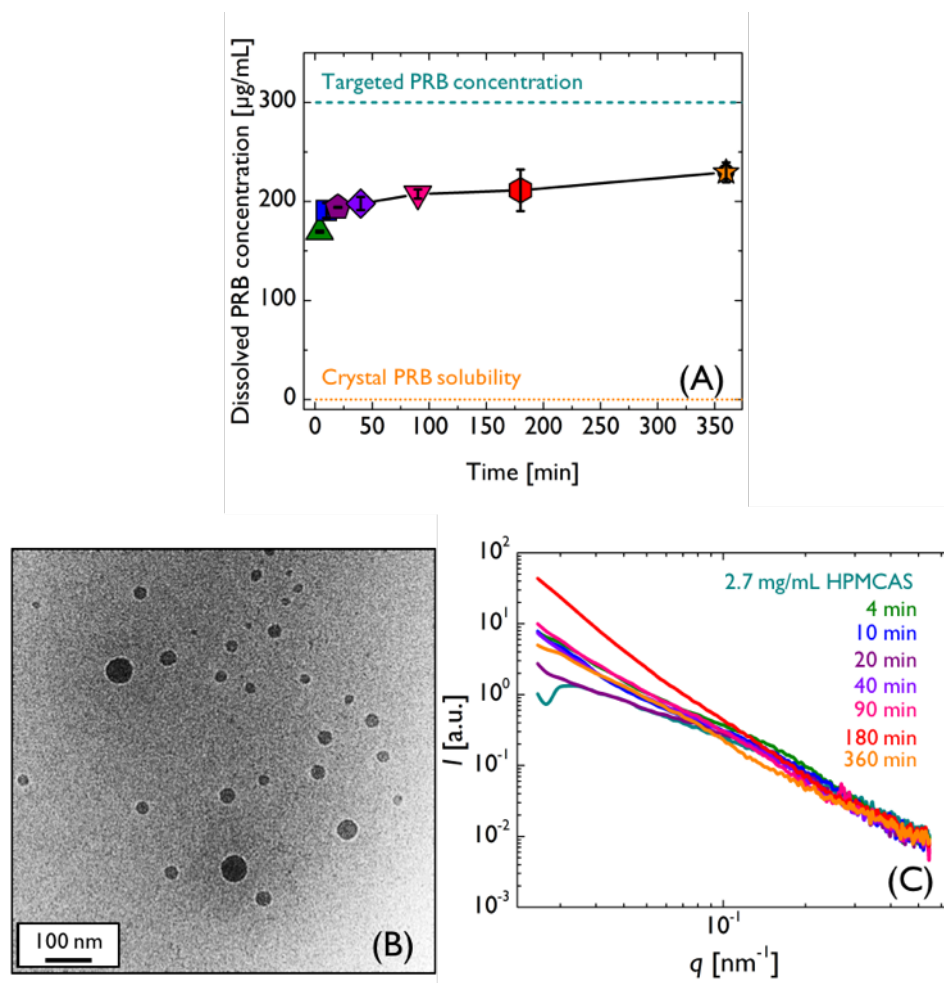


Figure 6.27. Dissolution profiles for 10 wt% PRB SD with a targeted drug concentration of 300 µg/mL. (A) Dissolution profile, (B) cryo-TEM of dissolution media at 360 min, and (C) SAXS patterns of dissolution media.

6.4 Discussion

This work directly confirms that formation of amorphous nanoparticles is essential for achieving and maintaining enhanced solubility of hydrophobic drugs that come from SDs. Although PRB and PHY have very different physical properties, dissolution profiles of SDs containing these drugs reflected the nanostructure evolution within the dissolution medium. Conclusions drawn from this work (and others)¹⁶ imply correlation between dissolution and nanoparticles applies not only HPMCAS SDs, but possibly many other polymeric drug delivery systems. Nanoparticle formation may possibly be a critical step

that is neglected by current theoretical models of drug release from polymeric matrices.^{161,99}

These studies also clarify the role of HPMCAS during SD dissolution. Contrary to many theories,^{41,42,154} the colloidal structure of HPMCAS in solution appears to have little relevance in the mechanism. Instead, A_2 measurements suggest that unfavorable interactions between HPMCAS and PBS at 37 °C drive polymer to interact with hydrophobic drug. The success of HPMCAS at stabilizing drug in solution seems to be tied to crystallization tendency of the API, but electron diffraction of both PHY and PRB SD dissolution media suggests the polymer inhibits drug crystallization by impeding nucleation, rather than slowing crystal growth. Furthermore, the connection between PRB:HPMCAS ratio and ensuing nanoparticle size hints that increased polymer concentration leads to lower interfacial tension between API and water, resulting in smaller droplets—reminiscent of trends observed for oil:water emulsions stabilized by surfactants.^{162,163}

This investigation potentially establishes a fundamental criterion for rational SD design: API and excipient must form nanostructures to achieve high concentration of drug in solution. Screening of excipients for a particular API may be streamlined to focus only on polymers that form amorphous nanoparticles with the drug. Thus, nanoscale characterization tools—such as the cryo-TEM, electron diffraction, and SAXS assays developed for this work—will be essential for identifying optimal formulations. These findings also raise deeper questions regarding the SD dissolution mechanism. Although nanoparticles can readily form in the dissolution media, the bioavailability of drug in these structures is not known. Some theories propose the nanoparticles compensate drug loss, resulting from both crystallization and permeation through the gastrointestinal membrane, by replenishing the dissolved drug concentration.¹⁶ However, the nanoparticles can potentially adhere to the mucus lining of the gut, leading to facilitated transport of drug.¹⁶⁴

Nanoparticle formation itself could possibly lead to enhanced drug efficacy, although more studies are needed to clarify this relationship. Moreover, the structure and stability of the nanoparticles may also be influenced by the native surfactants in the intestinal fluid.¹⁶⁵ Resolving these questions and other structure-property relationships will likely involve even more rigorous nanoscale characterization of SD dissolution.

6.5 Conclusions

I investigated the dissolution mechanism for HPMCAS SDs featuring PHY or PRB as the API. The poor solvent quality of PBS at 37 °C possibly served as the driving force for HPMCAS to interact with drug. Characterization by cryo-TEM and SAXS showed that both PHY and PRB SD dissolution directly correlated with the appearance of nanoparticles in the dissolution media. Drug identity, loading, and targeted drug concentration were critical factors that affected the nanoparticle size, shape, and formation kinetics. The relationship between dissolution and nanostructure potentially extends to other polymer:drug systems.

Chapter 7: Conclusions and suggestions for future directions

7.1 Project summary

The use of solid dispersions (SDs) can surmount the solubility limitations of many pharmaceutical drugs, but the primitive understanding of structure-property relationships for these materials inhibits rational SD design. Furthermore, the complexity of some excipients, such as hydroxypropyl methylcellulose acetate succinate (HPMCAS), obscures elucidation of the polymer:drug interactions. To resolve these uncertainties, I developed several novel strategies for characterizing solid dispersions in both the solid-state and during dissolution. These tools, which achieved spatial resolutions and sensitivity superior to the traditional techniques, probed the nanoscale phenomena that govern SD material properties.

In Chapter 3, I demonstrated the use of transmission electron microscopy (TEM) to evaluate the crystallinity of griseofulvin:HPMCAS SDs. TEM, providing both real-space images and electron diffraction patterns, was used to unambiguously detect griseofulvin crystals in a physical mixture of spray dried griseofulvin and spray dried HPMCAS that had an overall crystallinity of ~ 3 vol%, below the practical lower limit of detection for laboratory-scale wide-angle X-ray scattering (WAXS). Using both TEM and WAXS, I did not find crystals in griseofulvin:HPMCAS SDs that had drug loadings of 5, 10, and 50 wt%. I detected griseofulvin crystals in annealed 5 wt% griseofulvin SD using TEM, but

did not detect crystals in the same sample using *in situ* WAXS and modulated differential scanning calorimetry, thereby confirming the superior crystal detection sensitivity of TEM. I also performed TEM analysis on the *in situ* growth of griseofulvin crystals in a TEM sample of 50 wt% griseofulvin SD. Based on this study, TEM has significant potential for characterizing trace levels of crystallinity in SDs.

In Chapter 4, I tested the use of energy-dispersive X-ray spectroscopy (EDS) for mapping the spatial distribution of griseofulvin throughout a SD particle. Based on Monte-Carlo simulations of the TEM electron beam trajectory through a sample of griseofulvin, the spatial resolution of EDS was predicted to be ~ 10 nm, sufficient for detecting phase separated domains of drug in the HPMCAS SDs. In the EDS spectrum for spray dried griseofulvin, the Cl $K\alpha$ peak served as a signal that distinguished the drug from HPMCAS. By tracking this spectroscopic signature, the spatial distribution of griseofulvin was isolated in particles of spray dried griseofulvin and 10 wt% griseofulvin SD. Quantitative analysis of EDS spectra for SDs with varying particle size and griseofulvin loading revealed that the Cl $K\alpha$ peak was too weak for calculating drug concentration. The inadequate concentration resolution of the technique was attributed to the poor counting statistics of the collected X-rays. Based on this deficiency, EDS was judged to be a limited tool for characterizing SDs.

In Chapter 5, I explored electron energy-loss spectroscopy (EELS) as a tool for evaluating the composition of phenytoin:HPMCAS spin-coated SDs. To overcome weak elemental signals recorded by EDS, I used the π - π^* transition peak in the EELS spectrum to detect phenytoin within the HPMCAS matrix of the SD. The phenytoin concentrations for SDs with drug loadings of 10, 25, and 50 wt% were calculated using a multiple least-squares analysis. Measuring the concentration of 50 different regions in each SD, I concluded that HPMCAS and phenytoin were intimately mixed at a length scale of 200 nm for drug loadings up to 50 wt%. At length scales below 100 nm, the variance of the measured drug concentration increased; I speculated that this increase was due to statistical

fluctuations in local phenytoin concentration and electron irradiation. I also analyzed an annealed 25 wt% phenytoin SD and showed that EELS resolves concentration differences between regions less than 50 nm apart. These findings indicated EELS is a powerful tool for quantifying, with high accuracy and sub-100 nm spatial resolution, the composition of many polymer drug delivery systems.

In Chapter 6, I investigated the solution behavior of HPMCAS and dissolution of HPMCAS SDs in phosphate buffered saline. Dynamic and static light scattering measurements of HPMCAS solutions showed that the polymer formed both 10 and 100 nm structures (likely linear and cross-linked polymer chains, respectively) in solvent. Static light scattering also revealed phosphate buffered saline at 37 °C and below is a poor solvent for HPMCAS, potentially inducing the polymer to interact with itself or other species in solution. Characterization of the dissolution of HPMCAS SDs—featuring either phenytoin or probucol as the hydrophobic drug—showed that polymer and drug formed amorphous nanoparticles (<100 nm in size) in solution. Using a combination of cryogenic transmission electron microscopy, small-angle X-ray scattering, and electron diffraction, a direct correlation between SD dissolution profiles and nanostructure evolution was discovered for both drugs. The size, shape, and lifespan of the nanoparticles were affected by drug identity, loading, and targeted concentration. These findings confirm SD dissolution is a manifestation of nanoscale phenomena and suggest nanoparticle formation is universal to many other polymeric drug delivery systems.

7.2 Future research directions

The discoveries discussed in Chapter 6 illuminate critical steps of the SD dissolution mechanism. The correlation between solubility enhancement and nanoparticle formation may be universal not only to HPMCAS SDs, but other polymer:drug pairings, as well. Probuco and phenytoin occupy extreme quadrants of the hydrophobicity vs. crystallization tendency phase space (Figure D.1), so the dissolution of SDs featuring

hydrophobic APIs with more modest properties (*i.e.*, a smaller partition coefficient and lower free energy of crystallization) should be studied, such as griseofulvin, nifedipine, carbamazepine, and ketoprofen. Ionizable APIs—*e.g.*, nilutamide and bifonazole—possibly exhibit more complex nanoparticle behavior. Furthermore, the influence of excipient identity on nanostructure evolution in solution must also be investigated. For example, poly(*N*-isopropylacrylamide-*co*-*N,N*-dimethylacrylamide) (poly(NIPAm-*co*-DMA)) has recently been identified as an excellent excipient for phenytoin.¹⁶⁶ Preliminary SAXS characterization of SDs featuring phenytoin and poly(NIPAm-*co*-DMA) show that the dissolution profile corresponds to nanostructural changes in the solution (Appendix D.4). HPMC esters of substituted succinates, another outstanding novel excipient for phenytoin,⁵⁷ possibly forms nanoparticles with API.

While nanoparticles are potentially ubiquitous to SD systems, the spatial distribution of drug and polymer within the structures is not known. To probe the structure, alternate techniques must be developed to complement the cryo-TEM and SAXS assays discussed in Chapter 6. In particular, small-angle neutron scattering (SANS) contrast matching experiments might offer a way to isolate the spatial distribution of drug or polymer within the nanoparticles. In this measurement, the SANS intensity is proportional to the scattering length density differences between polymer, drug, and solvent.¹¹⁸ Tuning the scattering length density of phosphate buffered saline by altering the ratio of H₂O to D₂O may eliminate scattering from either polymer or drug and isolate the other species. The resulting scattering profile can then be fit to particular models to extract quantitative information regarding the structure or population of nanostructures. To achieve sufficient contrast between the isolated species and solvent, the use of deuterated polymer or drug will likely be needed. Furthermore, due to the lengthy collection times for SANS (ranges from 30 min to hours), this measurement will be limited to polymer:drug pairings that exhibit stable dissolution profiles. For formulations that display an unstable dissolution profile, more accurate quantitative information regarding the nanoparticle structure or

concentration may be acquired by modifying the SAXS assay to collect absolute intensity scattering profiles. Instead of collecting discrete aliquots at various time points, the dissolution media can be continuously pumped through a quartz capillary and heated stage. Because the background scattering intensity throughout the experiment is constant, time-resolved absolute intensity scattering patterns may be obtained. The intensity of the SAXS patterns may be improved by using APIs that have a large electron density (*e.g.*, carbamazepine, naproxen, and itraconazole). The flow-cell equipment for this experiment is available at the 5ID-D beamline at the Advanced Photon Source of Argonne National Laboratory. To selectively image drug or polymer in dissolution media, energy-filtered TEM can possibly be used. Similar to EELS, this technique images electrons that have a specific energy. By isolating electronic signatures that correspond to drug or polymer, more accurate assignment of phases can be achieved.

Despite the advances in understanding the HPMCAS SD dissolution mechanism, the structure of the polymer in solution is still ambiguous. Light scattering experiments in Chapter 6 strongly insinuate HPMCAS solutions contain cross-linked chains, but the data are not conclusive. SAXS and SANS scattering patterns of HPMCAS solutions lack a plateau regime (Appendix D), suggesting the length scale that dominates the scattering intensity is larger than 100 nm. To collect scattering data at much lower q (and consequently, larger length scales), ultra-small-angle neutron scattering (USANS) may be used. With USANS, the q range is expanded to $0.0003\text{--}0.1\text{ nm}^{-1}$,¹⁶⁷ likely sufficient observing the Rayleigh and Guinier regimes of the scattering pattern for HPMCAS in solvent. The scattering data could potentially be fit to a model to deduce the structure of HPMCAS in solution.

The suite of analytical tools developed in this dissertation not only clarify nanoscale properties of HPMCAS SDs, but also enable the ability to directly characterize the relationship between the physical stability of the SD in the solid-state and the ultimate dissolution profile. As mentioned in Chapters 1, 3, and 5, small traces of API crystallinity

or phase separation are hypothesized to have remarkably detrimental influence on the solubility enhancement of an SD formulation. To test this hypothesis, the morphology of the SD may be tracked before and during dissolution. Crystallinity and phase separation within the SD can be induced (either by heating the material above T_g or exposing it to high humidity) and characterized by electron diffraction or EELS. Subsequently, the influence of these properties on the resulting dissolution media nanostructure may be studied using cryo-TEM and SAXS.

The results described in this dissertation show that the structure-property relationships of SD materials are complex and only partially understood. Thus, rigorous characterization is essential for comprehending these materials and enabling rational SD design.

Bibliography

- ¹Macarron, R. *Drug Discov. Today* **2006**, *11*, 277–279.
- ²Kawabata, Y.; Wada, K.; Nakatani, M.; Yamada, S.; Onoue, S. *Int. J. Pharm.* **2011**, *420*, 1–10.
- ³Babu, N. J.; Nangia, A. *Cryst. Growth Des.* **2011**, *11*, 2662–2679.
- ⁴Liu, H.; Taylor, L. S.; Edgar, K. J. *Polymer* **2015**, *77*, 399–415.
- ⁵Hiemenz, P. C.; Lodge, T. P. *Polymer Chemistry*, 2nd ed.; Boca Raton, FL, 2007.
- ⁶Merisko-Liversidge, E.; Liversidge, G. G.; Cooper, E. R. *Eur. J. Pharm. Sci.* **2003**, *18*, 113–120.
- ⁷Van Eerdenbrugh, B.; Vermant, J.; Martens, J. A.; Froyen, L.; Van Humbeeck, J.; Augustijns, P.; Van Den Mooter, G. *J. Pharm. Sci.* **2009**, *98*, 2091–2103.
- ⁸Peltonen, L.; Hirvonen, J. *J. Pharm. Pharmacol.* **2010**, *62*, 1569–1579.
- ⁹Miller, J. M.; Beig, A.; Krieg, B. J.; Carr, R. A.; Borchardt, T. B.; Amidon, G. E.; Amidon, G. L.; Dahan, A. *Mol. Pharm.* **2011**, *8*, 1848–1856.
- ¹⁰Cabral, H.; Kataoka, K. *J. Control. Release* **2014**, *190*, 465–476.
- ¹¹Hancock, B. C.; Parks, M. *Pharm. Res.* **2000**, *17*, 397–404.
- ¹²Murdande, S. B.; Pikal, M. J.; Shanker, R. M.; Bogner, R. H. *J. Pharm. Sci.* **2010**, *99*, 1254–1264.
- ¹³Murdande, S. B.; Pikal, M. J.; Shanker, R. M.; Bogner, R. H. *Pharm. Res.* **2010**, *27*, 2704–2714.
- ¹⁴Murdande, S. B.; Pikal, M. J.; Shanker, R. M.; Bogner, R. H. *J. Pharm. Sci.* **2011**, *100*, 4349–4356.
- ¹⁵Janssens, S.; Van den Mooter, G. *J. Pharm. Pharmacol.* **2009**, *61*, 1571–1586.
- ¹⁶Taylor, L. S.; Zhang, G. G. *Z. Adv. Drug Deliv. Rev.* **2016**, *101*, 122–142.
- ¹⁷Baird, J. A.; Taylor, L. S. *Adv. Drug Deliv. Rev.* **2012**, *64*, 396–421.

- ¹⁸Shanbhag, A.; Rabel, S.; Nauka, E.; Casadevall, G.; Shivanand, P.; Eichenbaum, G.; Mansky, P. *Int. J. Pharm.* **2008**, *351*, 209–218.
- ¹⁹Raijada, D.; Müllertz, A.; Cornett, C.; Munk, T.; Sonnergaard, J.; Rantanen, J. *J. Pharm. Sci.* **2014**, *103*, 900–908.
- ²⁰Janssens, S.; De Zeure, A.; Paudel, A.; Van Humbeeck, J.; Rombaut, P.; Van den Mooter, G. *Pharm. Res.* **2010**, *27*, 775–785.
- ²¹Wegiel, L. A.; Zhao, Y.; Mauer, L. J.; Edgar, K. J.; Taylor, L. S. *Pharm. Dev. Technol.* **2013**, *7450*, 1–11.
- ²²Gallardo, D.; Skalsky, B.; Kleinebudde, P. *Pharm. Dev. Technol.* **2008**, *13*, 413–423.
- ²³Ting, J. M.; Navale, T. S.; Bates, F. S.; Reineke, T. M. *ACS Macro Lett.* **2013**, *2*, 770–774.
- ²⁴Ting, J. M.; Navale, T. S.; Bates, F. S.; Reineke, T. M. *Macromolecules* **2014**, *47*, 6554–6565.
- ²⁵Ting, J. M.; Navale, T. S.; Jones, S. D.; Bates, F. S.; Reineke, T. M. *ACS Biomater. Sci. Eng.* **2015**, *1*, 978–990.
- ²⁶Qi, S.; Gryczke, A.; Belton, P.; Craig, D. Q. M. *Int. J. Pharm.* **2008**, *354*, 158–167.
- ²⁷Rumondor, A. C. F.; Ivanisevic, I.; Bates, S.; Alonzo, D. E.; Taylor, L. S. *Pharm. Res.* **2009**, *26*, 2523–2534.
- ²⁸Taylor, L. S.; Zografu, G. *Pharm. Res.* **1997**, *14*, 1691–1698.
- ²⁹Marsac, P. J.; Konno, H.; Rumondor, A. C. F.; Taylor, L. S. *Pharm. Res.* **2008**, *25*, 647–656.
- ³⁰Rumondor, A. C. F.; Konno, H.; Marsac, P. J.; Taylor, L. S. *J. Appl. Polym. Sci.* **2010**, *117*, 1055–1063.
- ³¹Ilevbare, G. A.; Liu, H.; Edgar, K. J.; Taylor, L. S. *Mol. Pharm.* **2013**, *10*, 2381–2393.
- ³²Klemm, D.; Heublein, B.; Fink, H.-P.; Bohn, A. *Angew. Chemie Int. Ed.* **2005**, *44*, 3358–3393.
- ³³Raina, S. A.; Alonzo, D. E.; Zhang, G. G. Z.; Gao, Y.; Taylor, L. S. *Mol. Pharm.* **2014**, *11*, 3565–3576.
- ³⁴Abbou Oucherif, K.; Raina, S.; Taylor, L. S.; Litster, J. D. *CrystEngComm* **2013**, *15*, 2197–2205.

- ³⁵Weuts, I.; Van Dycke, F.; Voorspoels, J.; De Cort, S.; Stokbroekx, S.; Leemans, R.; Brewster, M. E.; Xu, D.; Segmuller, B.; Turner, Y. T. A.; Roberts, C. J.; Davies, M. C.; Qi, S.; Craig, D. Q. M.; Reading, M. *J. Pharm. Sci.* **2011**, *100*, 260–274.
- ³⁶Liu, H.; Ilevbare, G. A.; Cherniawski, B. P.; Ritchie, E. T.; Taylor, L. S.; Edgar, K. J. *Carbohydr. Polym.* **2014**, *100*, 116–125.
- ³⁷Ilevbare, G. A.; Liu, H.; Edgar, K. J.; Taylor, L. S. *Cryst. Growth Des.* **2013**, *13*, 740–751.
- ³⁸Pereira, J. M.; Mejia-Ariza, R.; Ilevbare, G. A.; McGettigan, H. E.; Sriranganathan, N.; Taylor, L. S.; Davis, R. M.; Edgar, K. J. *Mol. Pharm.* **2013**, *10*, 4640–4653.
- ³⁹Dong, Y.; Mosquera-Giraldo, L. I.; Taylor, L. S.; Edgar, K. J. *Biomacromolecules* **2016**, *17*, 454–465.
- ⁴⁰Dong, Y.; Mosquera-Giraldo, L. I.; Troutman, J.; Skogstad, B.; Taylor, L. S.; Edgar, K. J. *Polym. Chem.* **2016**, *7*, 4953–4963.
- ⁴¹Friesen, D. T.; Shanker, R.; Crew, M.; Smithey, D. T.; Curatolo, W. J.; Nightingale, J. A. S. *Mol. Pharm.* **2008**, *5*, 1003–1019.
- ⁴²Curatolo, W.; Nightingale, J. A.; Herbig, S. M. *Pharm. Res.* **2009**, *26*, 1419–1431.
- ⁴³Shin-Etsu Chemical Co. Ltd. (Tokyo, Japan) Product literature on AQOAT.
- ⁴⁴Babcock, W.C.; Friesen, D.T.; Lyon, D.K.; Miller, W.K.; Smithey, D.T. Pharmaceutical Compositions With Enhanced Performance Comprising A HPMCA Polymer. European Patent 1,753,402. October 01, 2008. Espacenet Patent search. <https://worldwide.espacenet.com/publicationDetails/biblio?CC=EP&NR=1753402B1&KC=B1&FT=D> (accessed September 8, 2016).
- ⁴⁵Petermann, O.; Sprehe, M.; Miller, W.K. Process of Preparing an Esterified Cellulose Ether in The Presence of an Alkali Metal Carboxylate and an Aliphatic Carboxylic Acid. United States Patent 218,291. August 6, 2015. Free Patents Online. <http://www.freepatentsonline.com/y2015/0218291.html> (accessed September 10, 2016).
- ⁴⁶Xiang, T.-X.; Anderson, B. D. *Mol. Pharm.* **2014**, *11*, 2400–2411.
- ⁴⁷Fukasawa, M.; Obara, S. *Chem. Pharm. Bull.* **2004**, *52*, 1391–1393.
- ⁴⁸Chen, R. *Int. J. Polym. Anal. Charact.* **2009**, *14*, 617–630.
- ⁴⁹Chen, R.; Ilasi, N.; Sekulic, S. S. *J. Pharm. Biomed. Anal.* **2011**, *56*, 743–748.

- ⁵⁰Shah, Navnit.; Sandhu, Harpreet; Choi, Duk Soon; Chokshi, Hitesh; Malick, A. Waseem. *Amorphous Solid Dispersions: Theory and Practice*, 1st ed.; New York, New York, 2014.
- ⁵¹Flory, P. J.; Krigbaum, W. R. *Annu. Rev. Phys. Chem.* **1951**, *2*, 383–402.
- ⁵²Huggins, M. L. *J. Chem. Phys.* **1941**, *9*, 440.
- ⁵³Pajula, K.; Taskinen, M.; Lehto, V.; Ketolainen, J.; Korhonen, O. *Mol. Pharm.* **2010**, *7*, 795–804.
- ⁵⁴Tian, Y.; Booth, J.; Meehan, E.; Jones, D. S.; Li, S.; Andrews, G. P. *Mol. Pharm.* **2013**, *10*, 236–248.
- ⁵⁵Tian, Y.; Caron, V.; Jones, D. S.; Healy, A.-M.; Andrews, G. P. *J. Pharm. Pharmacol.* **2014**, *66*, 256–274.
- ⁵⁶Roe, R.J. *Methods of X-ray and Neutron Scattering in Polymer Science*, 1st ed.; New York, NY, 2000.
- ⁵⁷Yin, L.; Hillmyer, M. A. *Mol. Pharm.* **2014**, *11*, 175–185.
- ⁵⁸Rumondor, A. C. F.; Stanford, L. A.; Taylor, L. S. *Pharm. Res.* **2009**, *26*, 2599–2606.
- ⁵⁹Chiou, W. L. *J. Pharm. Sci.* **1977**, *66*, 989–991.
- ⁶⁰Yamamura, S.; Takahira, R.; Momose, Y. *Pharm. Res.* **2007**, *24*, 880–887.
- ⁶¹Trasi, N. S.; Taylor, L. S. Effect of polymers on nucleation and crystal growth of amorphous acetaminophen. *CrystEngComm* **2012**, *14*, 5188-5197.
- ⁶²Trasi, N. S.; Taylor, L. S. Effect of Additives on Crystal Growth and Nucleation of Amorphous Flutamide. *Cryst. Growth Des.* **2012**, *12*, 3221–3230.
- ⁶³MicroscopyU. Principles of Birefringence. <http://www.microscopyu.com/techniques/polarizedlight/principles-of-birefringence> (accessed September 12, 2016).
- ⁶⁴Ghebremeskel, A. N.; Vemavarapu, C.; Lodaya, M. *Int. J. Pharm.* **2007**, *328*, 119–129.
- ⁶⁵Kestur, U. S.; Taylor, L. S. *CrystEngComm* **2010**, *12*, 2390-2397.
- ⁶⁶Hänninen, P. *Nature* **2002**, *419*, 802–802.
- ⁶⁷Kwei, T. K. *J. Polym. Sci. Polym. Lett. Ed.* **1984**, *22*, 307–313.

- ⁶⁸Brekner, M. J.; Schneider, H. A.; Cantow, H. J. *Polymer* **1988**, *29*, 78–85.
- ⁶⁹Gupta, P.; Bansal, A. K. *J. Pharm. Pharmacol.* **2005**, *57*, 303–310.
- ⁷⁰Marsac, P. J.; Li, T.; Taylor, L. S. *Pharm. Res.* **2009**, *26*, 139–151.
- ⁷¹Lodge, T. P.; McLeish, T. C. B. *Macromolecules* **2000**, *33*, 5278–5284.
- ⁷²Savin, D. A.; Larson, A. M.; Lodge, T. P. *J. Polym. Sci., Part B: Polym. Phys.* **2004**, *42*, 1155–1163.
- ⁷³He, Y.; Lutz, T. R.; Ediger, M. D. *J. Chem. Phys.* **2003**, *119*, 9956–9965.
- ⁷⁴Lodge, T. P.; Wood, E. R.; Haley, J. C. *J. Polym. Sci., Part B: Polym. Phys.* **2006**, *44*, 756–763.
- ⁷⁵Qian, F.; Huang, J.; Zhu, Q.; Haddadin, R.; Gawel, J.; Garmise, R.; Hussain, M. *Int. J. Pharm.* **2010**, *395*, 232–235
- ⁷⁶Konno, H.; Taylor, L. S. *J. Pharm. Sci.* **2006**, *95*, 2692–2705.
- ⁷⁷Konno, H.; Taylor, L. S. *Pharm. Res.* **2008**, *25*, 969–978.
- ⁷⁸Bhattacharya, S.; Suryanarayanan, R. *J. Pharm. Sci.* **2009**, *98*, 2935–2953.
- ⁷⁹Kothari, K.; Ragoonanan, V.; Suryanarayanan, R. *Mol. Pharm.* **2015**, *12*, 1477–1484.
- ⁸⁰Mehta, M.; Kothari, K.; Ragoonanan, V.; Suryanarayanan, R. *Mol. Pharm.* **2016**, *13*, 1339–1346.
- ⁸¹Mehta, M.; Suryanarayanan, R. *Mol. Pharm.* **2016**, *13*, 2661–2666.
- ⁸²Tobyn, M.; Brown, J.; Dennis, A. B.; Fakes, M.; Gao, Q.; Gamble, J.; Khimyak, Y. Z.; McGeorge, G.; Patel, C.; Sinclair, W.; Timmins, P.; Yin, S. *J. Pharm. Sci.* **2009**, *98*, 3456–3468.
- ⁸³Paudel, A.; Geppi, M.; Van den Mooter, G. *J. Pharm. Sci.* **2014**, *103*, 2635–2662.
- ⁸⁴Aso, Y.; Yoshioka, S.; Miyazaki, T.; Kawanishi, T. *Chem. Pharm. Bull.* **2009**, *57*, 61–64.
- ⁸⁵Yuan, X.; Sperger, D.; Munson, E. J. *Mol. Pharm.* **2014**, *11*, 329–337.
- ⁸⁶Vogt, F. G.; Yin, H.; Forcino, R. G.; Wu, L. *Mol. Pharm.* **2013**, *10*, 3433–3446.

- ⁸⁷Nanoscience Instruments. Atomic Force Microscopy. <http://www.nanoscience.com/technology/afm-technology/> (accessed September 13, 2016).
- ⁸⁸Marsac, P. J.; Rumondor, A. C. F.; Nivens, D. E.; Kestur, U. S.; Stanciu, L.; Taylor, L. S. *J. Pharm. Sci.* **2010**, *99*, 169–185.
- ⁸⁹Dazzi, A.; Glotin, F.; Carminati, R. *J. Appl. Phys.* **2010**, *107*, 124519.
- ⁹⁰Qi, S.; Belton, P.; Nollenberger, K.; Gryczke, A.; Craig, D. Q. M. *Pharm. Res.* **2011**, *28*, 2311–2326.
- ⁹¹Li, N.; Taylor, L. S. *Mol. Pharm.* **2016**, *13*, 1123–1136.
- ⁹²Narasimhan, B.; Peppas, N. A. *J. Pharm. Sci.* **1997**, *86*, 297–304.
- ⁹³Qian, F.; Wang, J.; Hartley, R.; Tao, J.; Haddadin, R.; Mathias, N.; Hussain, M. *Pharm. Res.* **2012**, *10*, 2765–2776.
- ⁹⁴Simonelli, A. P.; Mehta, S. C.; Higuchi, W. I. *J. Pharm. Sci.* **1969**, *58*, 538–549.
- ⁹⁵Alonzo, D. E.; Gao, Y.; Zhou, D.; Mo, H.; Zhang, G. G. Z.; Taylor, L. S. *J. Pharm. Sci.* **2011**, *100*, 3316–3331.
- ⁹⁶Jackson, M. J.; Kestur, U. S.; Hussain, M. A.; Taylor, L. S. *Mol. Pharm.* **2016**, *13*, 223–231.
- ⁹⁷Corrigan, O.I. *Drug. Dev. Ind. Pharm.* **1985**, *11*, 697–724.
- ⁹⁸Siepmann, J.; Kranz, H.; Bodmeier, R.; Peppas, N. A. *Pharm. Res.* **1999**, *16*, 1748–1756.
- ⁹⁹Siepmann, J.; Siepmann, F. *Int. J. Pharm.* **2013**, *453*, 12–24.
- ¹⁰⁰Hsieh, Y.L.; Ilevbare, G.A.; Van Eerdenbrugh, B.; Box, K.J.; Sanchez-Felix, M.V.; Taylor, L.S. *Pharm. Res.* **29**, 2012, 2738–2753.
- ¹⁰¹Ilevbare, G. A.; Liu, H.; Pereira, J.; Edgar, K. J.; Taylor, L. S. *Mol. Pharm.* **2013**, *10*, 3392–3403.
- ¹⁰²Mosquera-Giraldo, L. I.; Taylor, L. S. *Mol. Pharm.* **2015**, *12*, 496–503.
- ¹⁰³Indulkar, A. S.; Box, K. J.; Taylor, R.; Ruiz, R.; Taylor, L. S. *Mol. Pharm.* **2015**, *12*, 2365–2377.

- ¹⁰⁴Jackson, M. J.; Kestur, U. S.; Hussain, M. A.; Taylor, L. S. *Mol. Pharm.* **2016**, *13*, 223–231.
- ¹⁰⁵Almeida e Sousa, L.; Reutzel-Edens, S. M.; Stephenson, G. A.; Taylor, L. S. *Mol. Pharm.* **2015**, *12*, 484–495.
- ¹⁰⁶Raina, S.; Alonzo, D.; Zhang, G.Z.; Gao, Y.; Taylor, L. *Pharm. Res.* **2015**, *32*, 3660–3673.
- ¹⁰⁷Rohrer, G. *Structure and Bonding in Crystalline Materials*, 1st ed.; Cambridge University Press: New York, 2001.
- ¹⁰⁸Williams, D.; Carter, C. *Transmission Electron Microscopy*, 2nd ed; Springer: Boston, 2009.
- ¹⁰⁹Egerton, R. F. *Electron Energy-Loss Spectroscopy in the TEM*, 3rd ed.; Springer: New York, 2011.
- ¹¹⁰Sousa, A.; Aitouchen, A.; Libera, M. *Ultramicroscopy* **2006**, *106*, 130–145.
- ¹¹¹Yakovlev, S.; Misra, M.; Shi, S.; Firlar, E.; Libera, M. *Ultramicroscopy* **2010**, *110*, 866–876.
- ¹¹²Yakovlev, S.; Balsara, N. P.; Downing, K. H. *Ultramicroscopy* **2012**, *116*, 39–46.
- ¹¹³Klein, K. L.; Anderson, I. M.; De Jonge, N. *J. Microsc.* **2011**, *242*, 117–123.
- ¹¹⁴Talmon, Y. *Berichte der Bunsengesellschaft für Phys. Chemie* **1996**, *100*, 364–372.
- ¹¹⁵Mitchell, D. *Microsc. Res. Tech.* **2008**, *71*, 588–593.
- ¹¹⁶Zuo, J. M.; Mabon, J. C. *Microsc. Microanal.* **2004**, *10*, 1000–1001.
- ¹¹⁷Kobayashi, K.; Huang, C. I.; Lodge, T. P. *Macromolecules* **1999**, *32*, 7070–7077.
- ¹¹⁸Lodge, T.P. *Mikrochim. Acta* **1994**, *116*, 1–31.
- ¹¹⁹Berry, G. C. *J. Chem. Phys.* **1967**, *46*, 1338.
- ¹²⁰Li, Z.; Hillmyer, M. A.; Lodge, T. P. *Macromolecules* **2006**, *39*, 765–771.
- ¹²¹Baird, J. A.; Van Eerdenbrugh, B.; Taylor, L. S. *J. Pharm. Sci.* **2010**, *99*, 3787–3806.
- ¹²²Trasi, N. S.; Baird, J. A.; Kestur, U. S.; Taylor, L. S. *J. Phys. Chem. B* **2014**, *118*, 9974–9982.

- ¹²³Dubochet, J.; Ducommun, M.; Zollinger, M.; Kellenberger, E. *J. Ultrastruct. Res.* **1971**, *35*, 147–167.
- ¹²⁴Aebi, U.; Pollard, T. D. *J. Electron Microsc. Tech.* **1987**, *7*, 29–33.
- ¹²⁵Al-Obaidi, H.; Lawrence, M. J.; Al-Saden, N.; Ke, P. *Int. J. Pharm.* **2013**, *443*, 95–102.
- ¹²⁶Tian, Y.; Caron, V.; Jones, D. S.; Healy, A.M.; Andrews, G. P. *J. Pharm. Pharmacol.* **2014**, *66*, 256–274.
- ¹²⁷Li, B.; Wegiel, L. A.; Taylor, L. S.; Edgar, K. J. *Cellulose* **2013**, *20*, 1249–1260.
- ¹²⁸Verdonck, E.; Schaap, K.; Thomas, L. C. *Int. J. Pharm.* **1999**, *192*, 3–20.
- ¹²⁹Hancock, B. C.; Zografis, G. *J. Pharm. Sci.* **1997**, *86*, 1–12.
- ¹³⁰Van den Mooter, G.; Wuyts, M.; Bleton, N.; Busson, R.; Grobet, P.; Augustijns, P.; Kinget, R. *Eur. J. Pharm. Sci.* **2001**, *12*, 261–269.
- ¹³¹Hancock, B. C.; Carlson, G. T.; Ladipo, D. D.; Langdon, B. A.; Mullarney, M. P. *Int. J. Pharm.* **2002**, *241*, 73–85.
- ¹³²Six, K.; Berghmans, H.; Leuner, C.; Dressman, J.; Van Werde, K.; Mullens, J.; Benoist, L.; Thimon, M.; Meublat, L.; Verreck, G.; Peeters, J.; Brewster, M.; Van den Mooter, G. *Pharm. Res.* **2003**, *20*, 1047–1054.
- ¹³³Patel, V. I.; Dave, R. H. *AAPS PharmSciTech* **2013**, *14*, 620–628.
- ¹³⁴Worku, Z. A.; Aarts, J.; Singh, A.; Van den Mooter, G. *Mol. Pharm.* **2014**, *11*, 1094–1101.
- ¹³⁵Sethia, S.; Squillante, E. *Int. J. Pharm.* **2004**, *272*, 1–10.
- ¹³⁶Filippo, E.; Serra, A.; Buccolieri, A.; Manno, D. *J. Non. Cryst. Solids* **2010**, *356*, 344–350.
- ¹³⁷Knapek, E.; Dubochet, J. *J. Mol. Biol.* **1980**, *141*, 147–161.
- ¹³⁸Carvalho, J. L.; Dalnoki-Veress, K. *Phys. Rev. Lett.* **2010**, *105*, 237801.
- ¹³⁹Casino: monte Carlo Simulation of electron trajectory in solids.
<http://www.gel.usherbrooke.ca/casino/> (accessed October 29, 2016).
- ¹⁴⁰Stöckli, T.; Bonard, J.M.; Châtelain, A.; Lin Wang, Z.; Stadelmann, P. *Phys. Rev. B* **1998**, *57*, 15599–15612.

- ¹⁴¹Mkhoyan, K. A.; Contryman, A. W.; Silcox, J.; Stewart, D. A.; Eda, G.; Mattevi, C.; Miller, S.; Chhowalla, M. *Nano Lett.* **2009**, *9*, 1058–1063.
- ¹⁴²Sun, S.; Shi, S.; Leapman, R. *Ultramicroscopy* **1993**, *50*, 127–139
- ¹⁴³Sun, S. Q.; Shi, S.L.; Hunt, J. A.; Leapman, R. D. *J. Microsc.* **1995**, *177*, 18–30.
- ¹⁴⁴Kroon-Batenburg, L. M. J.; Kruiskamp, P. H.; Vliegthart, J. F. G.; Kroon, J. *J. Phys. Chem. B* **1997**, *101*, 8454–8459.
- ¹⁴⁵Salaniwal, S.; Kant, R.; Colby, R. H.; Kumar, S. K. *Macromolecules* **2002**, *35*, 9211–9218.
- ¹⁴⁶Yakovlev, S.; Libera, M. *Micron* **2008**, *39*, 734–740.
- ¹⁴⁷Egerton, R. F. *Ultramicroscopy* **2007**, *107*, 575–586.
- ¹⁴⁸Yakovlev, S.; Misra, M.; Shi, S.; Libera, M. *J. Microsc.* **2009**, *236*, 174–179.
- ¹⁴⁹Crececius, G.; Fink, J.; Ritsko, J. J.; Stamm, M.; Freund, H.J.; Gonska, H. *Phys. Rev. B* **1983**, *28*, 1802–1808.
- ¹⁵⁰Wegiel, L.; Mosquera-Giraldo, L. I.; Mauer, L. J.; Edgar, K. J.; Taylor, L. S. *Pharm. Res.* **2015**.
- ¹⁵¹Ritsko, J. J.; Bigelow, R. W. *J. Chem. Phys.* **1978**, *69*, 4162–4170.
- ¹⁵²Marletta, G.; Pignataro, S.; Oliveri, C. *Nucl. Instruments Methods Phys. Res. Sect. B Beam Interact. with Mater. Atoms* **1989**, *39*, 773–777.
- ¹⁵³Ritchie, T. J.; Macdonald, S. J. F. *Drug Discov. Today* **2009**, *14*, 1011–1020.
- ¹⁵⁴Ueda, K.; Higashi, K.; Yamamoto, K.; Moribe, K. *Mol. Pharm.* **2015**, *12*, 1096–1104.
- ¹⁵⁵Allen, T. C. *Text. Res. J.* **1964**, *34*, 331–336.
- ¹⁵⁶Li, Z.; Johnson, L.; Ricarte, R.G.; Yao, L.J.; Hillmyer, M.A.; Bates, F.S.; Lodge, T.P. *Submitted*.
- ¹⁵⁷Gapiński, J.; Szymański, J.; Wilk, A.; Kohlbrecher, J.; Patkowski, A.; Hołyst, R. *Langmuir* **2010**, *26*, 9304–9314.
- ¹⁵⁸Choi, S.-H.; Lodge, T. P.; Bates, F. S. *Phys. Rev. Lett.* **2010**, *104*, 047802.
- ¹⁵⁹Ricarte, R. G.; Lodge, T. P.; Hillmyer, M. A. *Mol. Pharm.* **2015**, *12*, 983–990.

- ¹⁶⁰Cabane, H.; Laporte, D.; Provost, A. *Contrib. to Mineral. Petrol.* **2005**, *150*, 37–53.
- ¹⁶¹Siepmann, J.; Peppas, N. A. *Adv. Drug Deliv. Rev.* **2012**, *64*, 163–174.
- ¹⁶²Porras, M.; Solans, C.; González, C.; Martínez, A.; Guinart, A.; Gutiérrez, J. M. *Colloids Surfaces A Physicochem. Eng. Asp.* **2004**, *249*, 115–118.
- ¹⁶³Fernandez, P.; André, V.; Rieger, J.; Kühnle, A. *Colloids Surfaces A Physicochem. Eng. Asp.* **2004**, *251*, 53–58.
- ¹⁶⁴Ensign, L. M.; Cone, R.; Hanes, J. *Adv. Drug Deliv. Rev.* **2012**, *64*, 557–570.
- ¹⁶⁵Otsuka, K.; Shono, Y.; Dressman, J. *J. Pharm. Pharmacol.* **2013**, *65*, 937–952.
- ¹⁶⁶Ting, J. M.; Tale, S.; Purchel, A. A.; Jones, S. D.; Widanapathirana, L.; Tolstyka, Z. P.; Guo, L.; Guillaudeu, S. J.; Bates, F. S.; Reineke, T. M. *ACS Cent. Sci.* **2016**, *2*, 748–755.
- ¹⁶⁷BT5 USANS – Ultra Small Angle Neutron Scattering.
<https://www.nist.gov/laboratories/tools-instruments/bt5-usans-ultra-small-angle-neutron-scattering> (accessed November, 4, 2016).

Appendix A: Supporting information for detection of pharmaceutical drug crystallites in solid dispersions by transmission electron microscopy[†]

A.1 GF/HPMCAS solid dispersion particle morphology

Scanning electron microscopy (SEM) analysis of solid dispersions was performed by either a Hitachi S-900 or S-4700 field emission gun scanning electron microscope. Samples were prepared by spreading solid dispersion with a spatula onto carbon conductive tape (Ted Pella Inc.) and coating the sample with 10 nm Au/Pd (60/40 w/w) in a 15 mTorr argon atmosphere using a Denton DV-502A high vacuum deposition system.

Figure A.1 features SEM images of GF/HPMCAS solid dispersions with varying GF loading. As GF loading increased the particles became more spherical. This change in morphology occurs because GF diffuses toward the center of the droplet during the spray drying process faster than HPMCAS.^{A1} Spray dried GF particles feature nanoscale grains; we posit that these grains are crystalline.

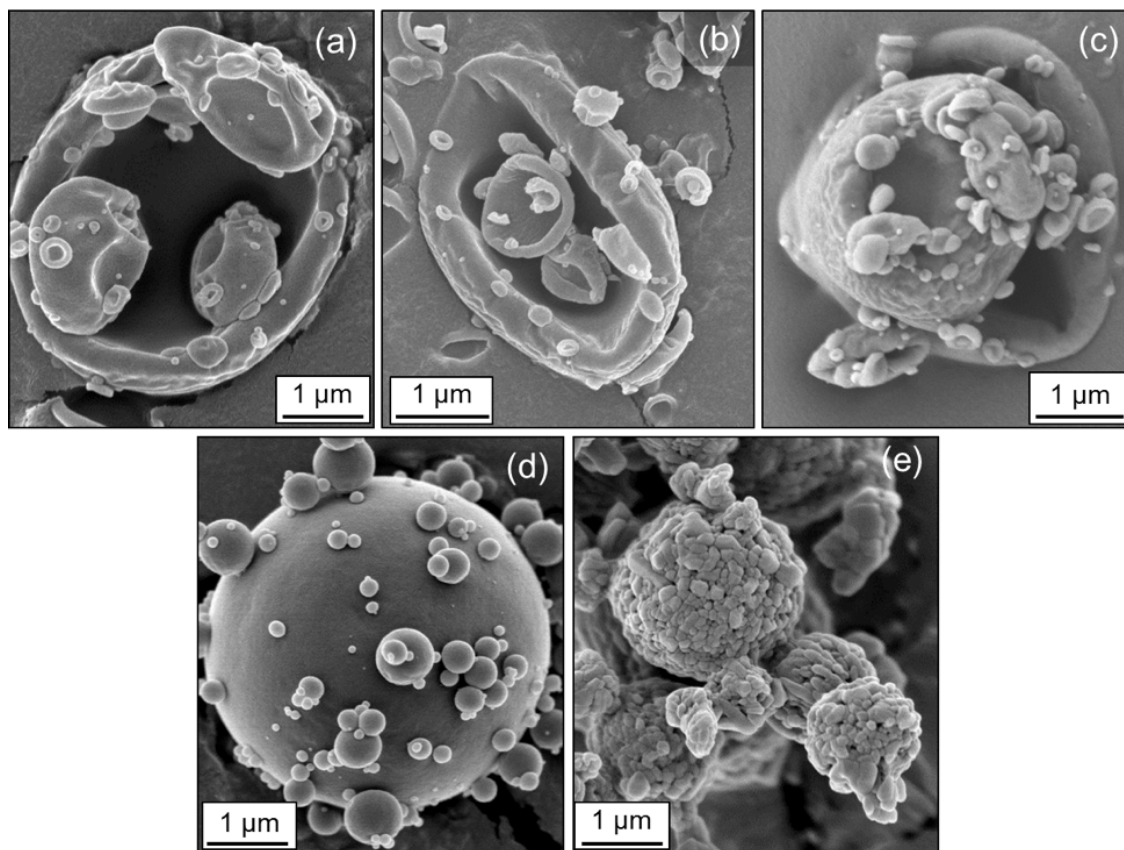


Figure A.1. Scanning electron microscopy images of solid dispersion particles. (a) Spray dried HPMCAS and (b) 5 and (c) 10 wt% GF solid dispersions exhibit a collapsed sphere particle morphology, (d) 50 wt% GF solid dispersion demonstrates a spherical particle morphology, and (e) spray dried GF features an ill-defined particle morphology.

A.2 Indexing of GF electron diffraction patterns

The GF crystal has tetragonal lattice geometry with the following lattice parameters: $a = 0.9$ nm and $c = 2.0$ nm.^{A2} d -spacings between crystal planes, d , were estimated by:

$$\frac{1}{d^2} = \frac{h^2 + k^2}{a^2} + \frac{l^2}{c^2} \quad (\text{A.1})$$

where a and c are lattice parameters, and h , k , and l are Miller indices. Interplanar angles, φ , were calculated by:

$$\cos \varphi = \frac{\frac{h_1 h_2 + k_1 k_2}{a^2} + \frac{l_1 l_2}{c^2}}{\sqrt{\frac{h_1^2 + k_1^2}{a^2} + \frac{l_1^2}{c^2}} \sqrt{\frac{h_2^2 + k_2^2}{a^2} + \frac{l_2^2}{c^2}}} \quad (\text{A.2})$$

where a and c are lattice parameters and h_i , k_i , and l_i are the Miller indices of the plane with spacing d_i .^{A3} Single crystal electron diffraction patterns were indexed in an iterative fashion. For each diffraction spot, the distance from the center of the diffraction pattern, R , was measured. The ratio of R for any two diffraction spots is related to the ratio of the d -spacings by

$$\frac{R_1}{R_2} = \frac{1/d_1}{1/d_2} \quad (\text{A.3})$$

Using this relation, the R ratio and the φ between various diffraction spot pairs were compared to estimate the zone axis of the diffraction.^{A4} A kinematical diffraction pattern simulation of the estimated zone axis was produced using Web Electron Microscopy Applications Software.^{A5} The simulated diffraction pattern was then compared with the experimental diffraction pattern to determine the accuracy of the zone axis estimate. Figure A.2 features the experimental and simulated diffraction pattern of a GF crystal.

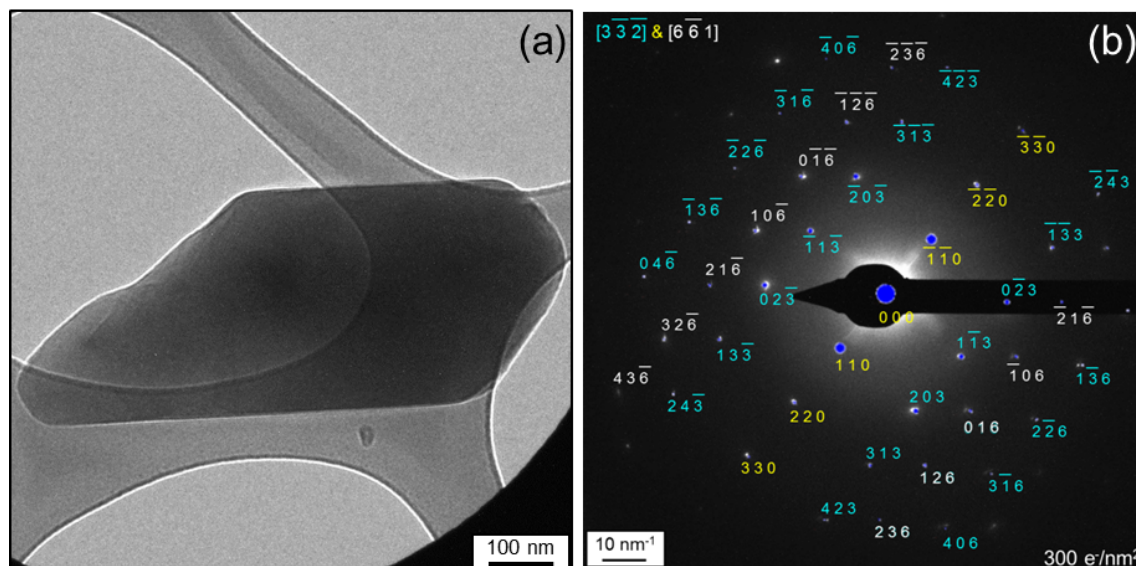


Figure A.2. (a) Bright-field TEM image and (b) electron diffraction pattern of GF crystal. The kinematical diffraction pattern simulation (blue dots) indicates the electron diffraction pattern samples two separate crystal grains. The zone axis of each grain is $[3 \bar{3} 2]$ (aqua) and $[6 \bar{6} 1]$ (white), respectively. The $\{1 1 0\}$ planes (yellow) belong to both zone axes.

A.3 Beam Sensitivity of GF crystals

To establish the maximum electron dose allowed for preserving GF crystals, electron diffraction patterns of $\sim 400 \text{ nm}$ spray dried GF particles were recorded under increasing electron beam exposure at both ambient temperature and $-180 \text{ }^{\circ}\text{C}$. At ambient temperature, the particle, featured in Figure A.3a, maintained a sufficient diffraction spot signal until a dosage of approximately $4000 \text{ e}^{-}/\text{nm}^2$ (see Supporting Information File "GF_beam_exposure_ambient.avi" at <http://pubs.acs.org/doi/suppl/10.1021/mp500682x>). At $-180 \text{ }^{\circ}\text{C}$, the particle, featured in Figure A.3b, exhibited a sufficient diffraction spot signal up to a dosage of $6000 \text{ e}^{-}/\text{nm}^2$ (see Supporting Information File "GF_beam_exposure_cryo.avi" at <http://pubs.acs.org/doi/suppl/10.1021/mp500682x>). Based on these trends, all subsequent electron diffraction studies were performed at $-180 \text{ }^{\circ}\text{C}$ using electron doses less than $6000 \text{ e}^{-}/\text{nm}^2$.

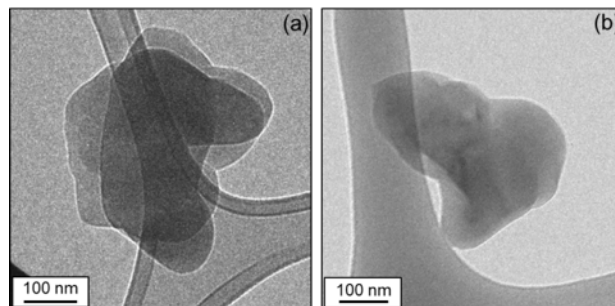


Figure A.3. Bright-field TEM images of spray dried GF particles at (a) ambient temperature and (b) $-180\text{ }^{\circ}\text{C}$. GF crystals can withstand a longer electron dose at $-180\text{ }^{\circ}\text{C}$ than ambient temperature.

A.4 Fourier transform infrared (FTIR) spectroscopy of solid dispersions

Solid dispersions were analyzed by a Bruker ALPHA Platinum FTIR spectrometer outfitted with a platinum attenuated total reflectance sampling module hosting a diamond crystal (single bounce). Samples were deposited directly on the diamond crystal plate. 128 scans were collected from a range of 4000 to 40 cm^{-1} with a resolution of 4 cm^{-1} .

Figure A.4 features FTIR spectra of solid dispersions with varying GF loading. Spray dried GF (pure drug) exhibits peaks at 1700 (ketone carbonyl stretching), 1660 (carbon-carbon double bond stretching), 1610 , 1600 , and 1580 cm^{-1} (carbon-carbon single bond stretching (in-ring)), while spray dried HPMCAS (pure polymer) exhibits at peak at 1740 cm^{-1} (ester carbonyl stretching). The ketone carbonyl stretching and carbon-carbon double and single bond stretching peaks for the 5, 10, and 50 wt% GF solid dispersions differ slightly from the spray dried GF spectrum. These discrepancies, however, are due to the GF in the solid dispersions being mostly amorphous. FTIR spectra of 100% amorphous GF, as recorded by Vasanthavada et al., has the same features as the spectra of the solid dispersions.⁶ Furthermore, neither the ester carbonyl stretch from HPMCAS nor the ketone carbonyl stretch from GF exhibit dramatic discrepancies from the pure polymer or pure amorphous drug spectra, respectively. Based on these spectra, we speculate that GF does not have any significant interactions with HPMCAS.

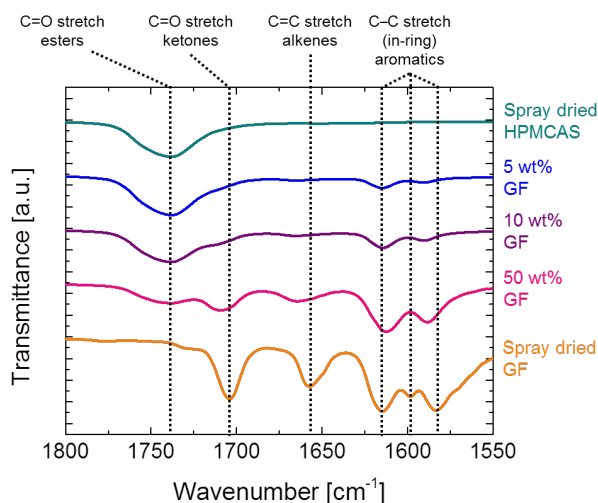


Figure A.4. FTIR spectra of solid dispersions with varying GF loading. Curves were shifted for clarity. No clear shift of the ketone carbonyl stretch peak was observed between the 5, 10, and 50 wt% GF solid dispersions (blue, purple, and pink curves, respectively) and the 100% amorphous GF spectra recorded by Vasanthavada et al.^{A6}

A.5. References

^{A1}Vehring, R. *Pharm. Res.* **2008**, *25*, 999–1022.

^{A2}Nirmala, K. A.; Sakegowda, D. S.; Duax, W. L. *J. Crystallogr. Spectrosc. Res.* **1982**, *12*, 415–423.

^{A3}Cullity, B.D.; Stock, S.R. *Elements of X-ray Diffraction*, 3rd ed.; Prentice Hall: Upper Saddle River, NJ, 2001.

^{A4}Williams, D.; Carter, C. *Transmission Electron Microscopy*, 2nd ed; Springer: Boston, 2009.

^{A5}Zuo, J. M.; Mabon, J. C. *Microsc. Microanal.* **2004**, *10*, 1000–1001.

^{A6}Vasanthavada, M.; Tong, W. Q.; Joshi, Y.; Kislalioglu, M. S. *Pharm. Res.* **2005**, *22*, 440–448.

Appendix B: Supporting information for energy-dispersive X-ray spectroscopy of solid dispersions

B.1 Modulated differential scanning calorimetry of griseofulvin:hydroxypropyl methylcellulose acetate succinate solid dispersions

Modulated differential scanning calorimetry was performed on SDs comprised of griseofulvin (GF) and hydroxypropyl methylcellulose acetate succinate solid dispersions (HPMCAS) in varying ratios (experimental method is described in Chapter 2.5). The pure GF glass transition temperature (T_g) was measured after heating the drug above its melting point (~ 220 °C). The reversing heat flow curves of each SD exhibit only a single T_g , suggests, but does not conclusively prove, that GF and HPMCAS are intimately mixed in each blend. Furthermore, the T_g s of SDs are lower than the T_g s of both HPMCAS and GF. More experiments are needed to understand the thermal properties of GF:HPMCAS SDs.

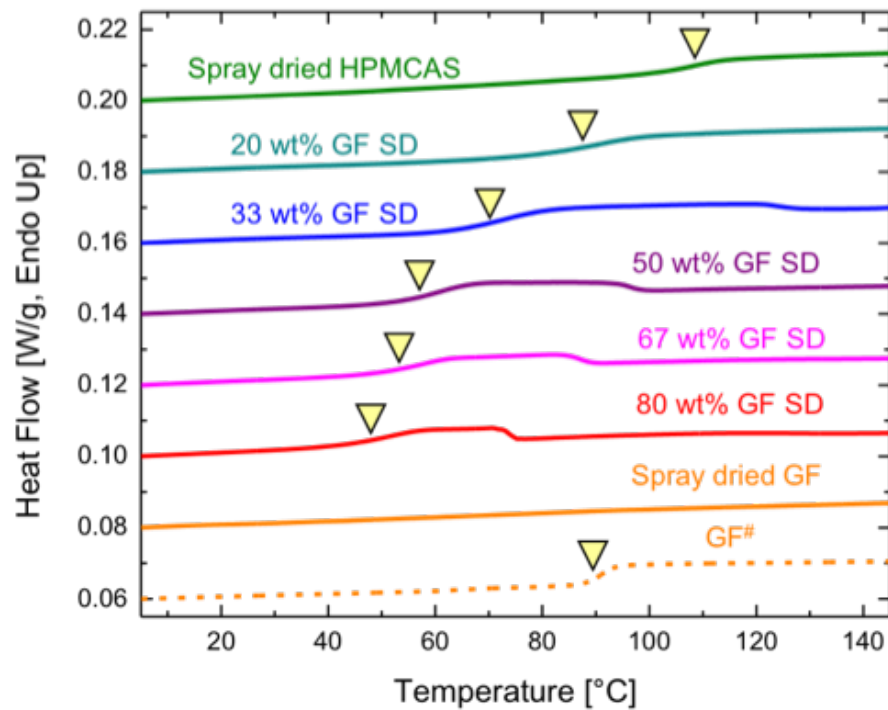


Figure B.1. MDSC reversing heat flow curves for GF SDs with varying drug loading, spray dried HPMCAS, and spray dried GF. #Conventional DSC trace of molten GF.

Appendix C: Supporting information for nanoscale concentration quantification of pharmaceutical actives in amorphous polymer matrices by electron energy-loss spectroscopy[†]

C.1 Cross-section and mean free path length of inelastic scattering for various species

Auto- Z_{eff} and LENZPLUS were used to approximate the effective atomic number (Z_{eff}) and inelastic scattering cross-section (ξ), respectively, of various drugs and the average HPMCAS anhydroglucose unit, as seen in Table C1.^{C1}

Table C.1. Z_{eff} , molecular weight, and ξ for various molecules.

Molecule name	Z_{eff}	Molecular weight [g/mol]	ξ [$\times 10^{-5} \text{ nm}^{-2}$]
HPMCAS anhydroglucose unit	3.9	252	8.50
Phenytoin	4.3	252	8.58
Carbamazepine	4.0	220	8.52
Naproxen	3.9	230	8.50
Griseofulvin	4.5	353	8.63
Itraconazole	4.3	706	8.58

The mean free path length of inelastic scattering, λ_p , was calculated by:

$$\lambda_p = \frac{2a_0 m_0 v^2}{E_p \ln \left(1 + \beta^2 / \theta^2 \right)} \quad (\text{C.1})$$

where a_0 is the Bohr radius, m_0 is the rest mass of an electron, v is the velocity of the incident electron (modified to account for relativistic effects), E_p is the plasmon energy, β is the collection semi-angle, and θ is the plasmon scattering angle.^{C1} For the molecules explored in this study, λ_p was ~ 165 nm. To simplify the MLS analysis, 165 nm was used as λ_p for subsequent concentration calculations.

C.2 Conventional TEM EELS characterization of phenytoin:HPMCAS spin-coated solid dispersions

Conventional TEM EELS spectra were collected from regions of interest by first inserting a 300 nm diameter selected-area aperture into electron beam path to confine the collection area size. The electron dosage for each spectrum acquisition was 2500 e⁻/nm². The beam was blanked before and after spectrum acquisition to minimize beam damage. Using diffraction mode, EELS spectra from at least 50 different regions of interest were collected from each sample. Bright-field TEM images of each region of interest were collected after spectrum acquisition.

Figure C.1A is a bright-field TEM image of a spin-coated HPMCAS film. Similar to Figure 5.1A, the HPMCAS film is uniform. Figure C.1C is a raw conventional TEM EELS spectrum of HPMCAS. This spectrum only exhibits the zero-loss and plasmon peaks. Figure C.1B is a bright-field TEM image of a spin-coated phenytoin film. Unlike the HPMCAS film, the phenytoin film has a jagged topology. The raw conventional TEM EELS spectrum of phenytoin, as seen in Figure C.1D, contains the zero-loss, plasmon, and π - π^* transition peaks.

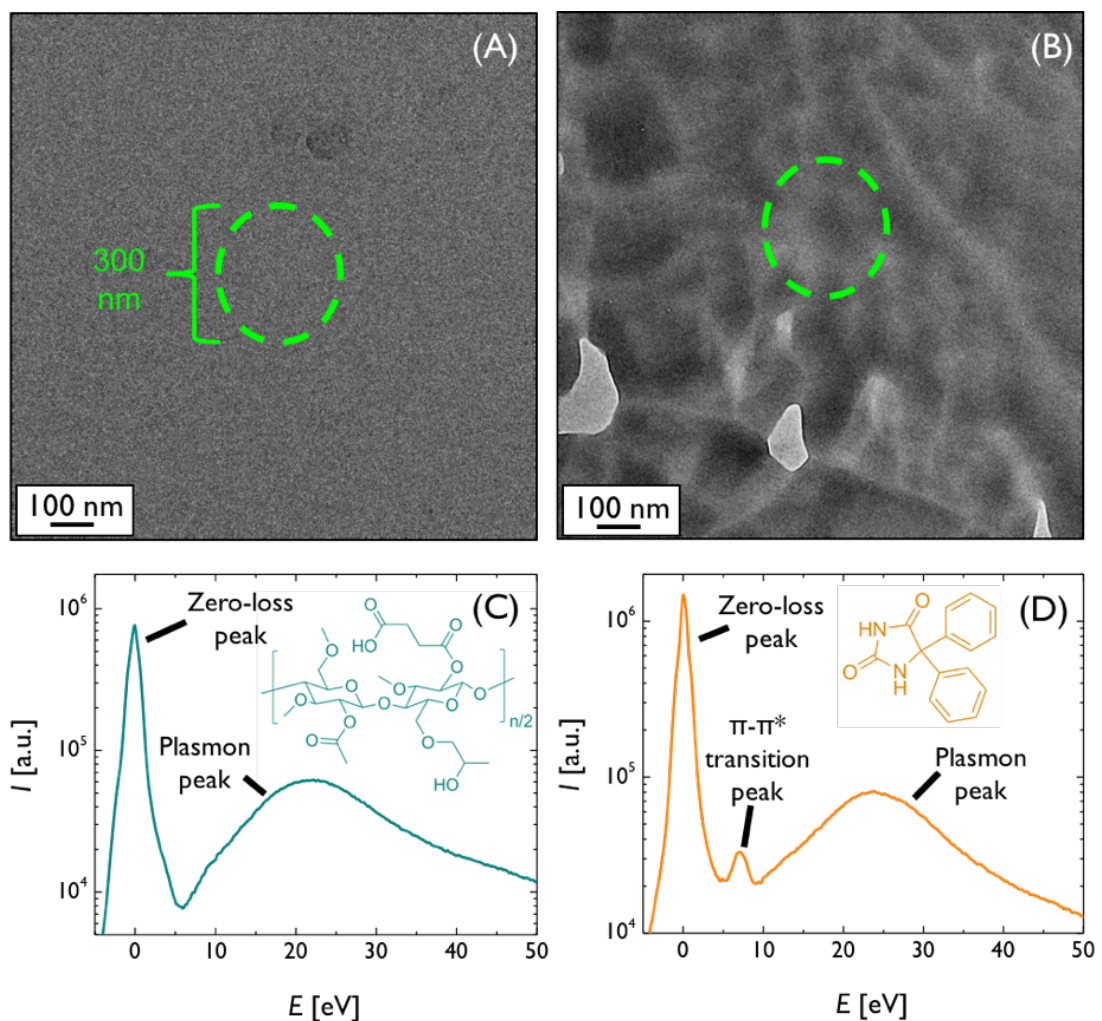


Figure C.1. Conventional bright-field TEM image of spin-coated (A) HPMCAS and (B) phenytoin films. The outlined regions are the areas where EELS spectra were collected. Conventional TEM EELS spectra and molecular structures of (C) HPMCAS and (D) phenytoin. The y-axis is the intensity (I) and the x-axis is the energy-loss exhibited by a particular electron (ΔE). Similar to the STEM EELS spectra, the HPMCAS spectrum only has the zero-loss and plasmon peaks, while the phenytoin spectrum has the zero-loss, plasmon, and π - π^* transition peaks.

Figure C.2 features bright-field TEM images of the 10, 25, and 50 wt% phenytoin spin-coated SDs. Because each film looks identical, TEM imaging cannot distinguish between the SDs. The conventional TEM EELS spectra, however, can distinguish each

film. As seen in Figure C.3, the π - π^* transition peak intensity increases as the phenytoin loading increases. The experimental spectra qualitatively match the predicted spectra.

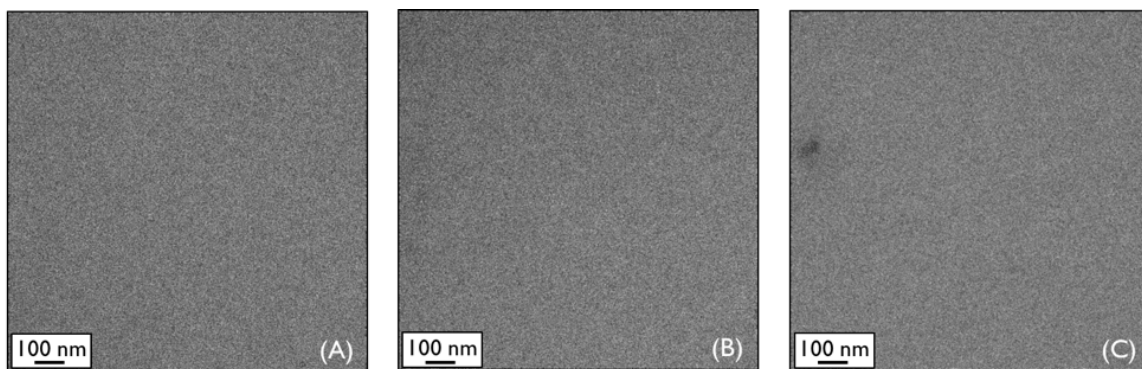


Figure C.2. Bright-field TEM images of (A) 10, (B) 25, and (C) 50 wt% phenytoin spin-coated dispersion films. TEM imaging cannot distinguish among these films.

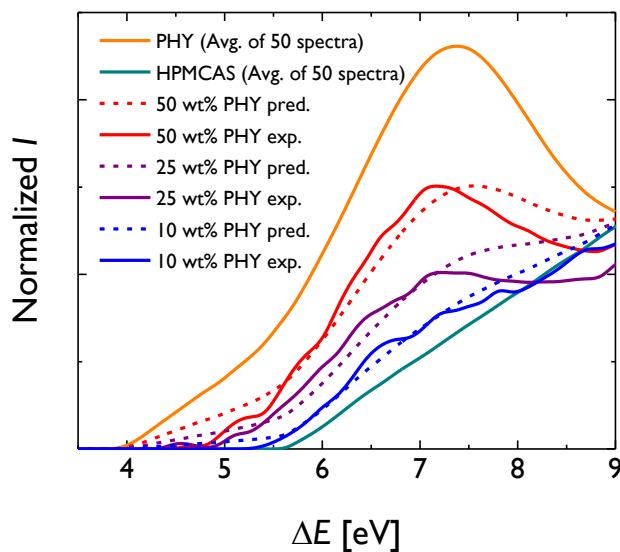


Figure C.3. Experimental and predicted conventional TEM EELS spectra for 10, 25, and 50 wt% phenytoin (PHY) spin-coated dispersions. The representative experimental spectra and predicted spectra qualitatively match.

Figure C.4 presents histograms of the measured phenytoin concentrations from conventional TEM EELS spectra for the 10, 25, and 50 wt% phenytoin spin-coated SDs.

Consistent with the STEM EELS results, the measured concentrations match the nominal SD loadings and have standard deviations of 3-6 wt%.

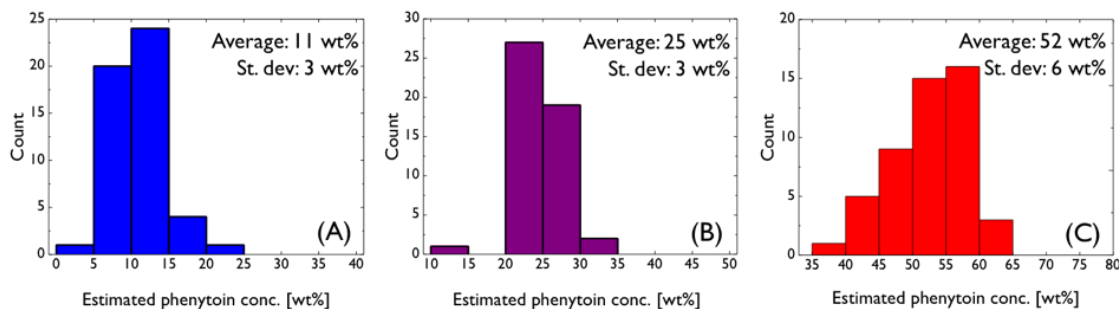


Figure C.4. Histogram of measured concentrations from 50 spots by conventional TEM EELS spectra, as calculated by the MLS noise-weighted algorithm, for (A) 10, (B) 25, and (C) 50 wt% phenytoin spin-coated dispersions. The average measured concentrations match the nominal phenytoin loadings of the dispersions.

C.3. Subtraction of amorphous C film contribution of EELS spectra

To isolate the single-scattering EELS spectra of phenytoin, HPMCAS, and SDs, the contribution of the amorphous C film was subtracted from each deconvoluted low-loss EELS spectrum. The reference spectrum of the amorphous C film, as seen in Figure C.5, was developed by collecting EELS spectra from ~ 50 different spots on a bare TEM grid that was covered with a thin (nominally 3 – 4 nm) amorphous film. The spectra were averaged and a quadratic spline was applied to the data set to smooth the curve. The isolated single-scattering EELS spectrum of the sample, S_{corr} , was calculated by:

$$S_{corr} = \frac{N_{raw}S_{raw} - N_C S_C}{N_{raw} - N_C} \quad (C.2)$$

where N_{raw} is number of electrons that scatter from both the SD sample and amorphous C film, S_{raw} is the normalized uncorrected deconvoluted low-loss EELS spectrum, N_C is the number of electrons that scatter from the amorphous C film only, S_C is the normalized amorphous C film EELS spectrum. N_{raw} and N_C are calculated by:

$$N = N_{dose} A \frac{t}{\lambda} \exp\left(-\frac{t}{\lambda}\right) \quad (\text{C.3})$$

$$t = \lambda_p \ln\left(1 + \frac{I_{LL}}{I_{ZLP}}\right) \quad (\text{C.4})$$

where N_{dose} is the electron dosage, A is the EELS spectrum collection area, t is the thickness of the sampled region of interest, λ_p is the mean free path length of inelastic scattering, I_{LL} is the integrated intensity of the deconvoluted low-loss EELS spectrum, and I_{ZLP} is the integrated intensity of the zero-loss peak spectrum. To use Eqn. C3, we assume that scattering of the electrons in the sample is described by Poisson statistics.

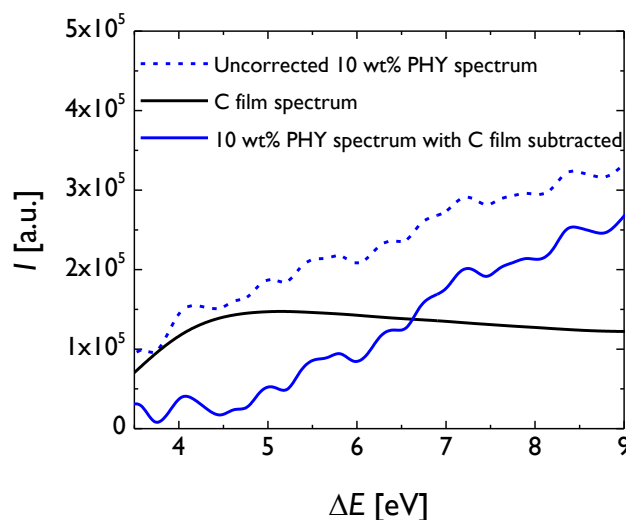


Figure C.5. Raw 10 wt% phenytoin (PHY) spin-coated SD, amorphous C film, and 10 wt% phenytoin spin-coated SD with C film subtracted EELS spectra. The thickness of the amorphous C film was assumed to be 16.5 nm.

Though collection of the amorphous C film EELS spectra was straightforward, calculating N_C , which is a function of the amorphous C film thickness, is non-trivial. While the amorphous C film is nominally 3 – 4 nm thick, the thickness calculated from the

EELS spectra is ~ 30 nm. This discrepancy may be caused by the presence of surface plasmons in the spectra. For thin samples ($\lesssim 25$ nm), a surface plasmon loss is more likely to occur than the bulk plasmon loss, thereby violating the Poisson statistic assumption required for Eqn. C3 to be valid. This uncertainty of the amorphous C film thickness is exacerbated by the addition of the spin-coated SD film. To mitigate this ambiguity, we assumed the average thickness of the amorphous C film was one-tenth of the mean free path length of inelastic scattering for C (*i.e.*, 16.5 nm). Figure C.5 details the C film subtraction from a raw EELS spectrum. While this assumption produces reasonable results, variation of the film thickness may skew the calculated concentrations. As seen in Figure C.6, the use of different amorphous C film thicknesses alters the calculated phenytoin concentration. Based on this analysis, we hypothesize that uncertainty of the film thickness, which likely varies by at least 2 nm, is a major influence on the standard deviation of the calculated concentration. Further experiments are needed to measure the calculated concentration error for SD TEM samples that lack the amorphous C film.

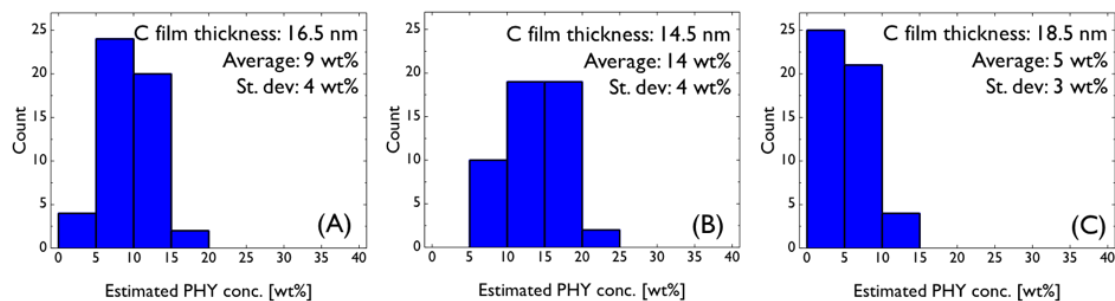


Figure C.6. Histograms of measured concentrations from 50 spots on a 10 wt% phenytoin spin-coated SD. The EELS spectrum of an amorphous C film with an assumed thickness of (A) 16.5 nm, (B) 14.5 nm, or (C) 18.5 nm was subtracted from the SD EELS spectra. Small variation in the amorphous C film thickness skews the calculated phenytoin concentration by 3–4 wt%.

C.4 Modulated differential scanning calorimetry of a 25 wt% phenytoin spray-dried dispersion

To prepare the 25 wt% phenytoin spray-dried dispersion, the required amounts of phenytoin and HPMCAS were first dissolved in tetrahydrofuran to create a solution with a total solids loading of 2 wt%. This solution was then sprayed by a mini spray dryer (Bend Research) using the following process parameters: nitrogen flow rate = 12.8 L/min, inlet temperature = 68 °C, solution flow rate = 0.65 mL/min. The outlet temperature was ~ 25 °C. The spray-dried dispersion was collected from a paper filter in the instrument, subsequently dried under reduced pressure at ambient temperature for 12 h, and stored in a desiccator under reduced pressure until use.

Modulated differential scanning calorimetry (DSC) of the 25 wt% phenytoin spray-dried dispersion was performed using a Discovery DSC (TA Instruments). The TEM sample was put into a Tzero™ aluminum pan with a standard lid. While exposed to a nitrogen gas flow with a rate of 50 mL/min, the sample pan was heated from 0–160 °C using the following parameters: average temperature heating rate = 1 °C/min, temperature modulation amplitude = 1 °C, temperature modulation period = 40 s. Figure C.7 shows the modulated DSC heat flow curves for the 25 wt% spray-dried SD. The T_g of the SD, as identified by the inflection point in the reversing heat curve, is 79 °C. The exothermic peak in the total and non-reversing heat curves is attributed to the crystallization of phenytoin in the SD. From this peak, the T_c and ΔH_c are 149 °C and 33 J/g_{PHY}, respectively. There is also a broad endothermic peak around 50 °C. While the source of this peak is unclear, we previously showed that this feature doesn't affect the T_g and T_c .^{C2}

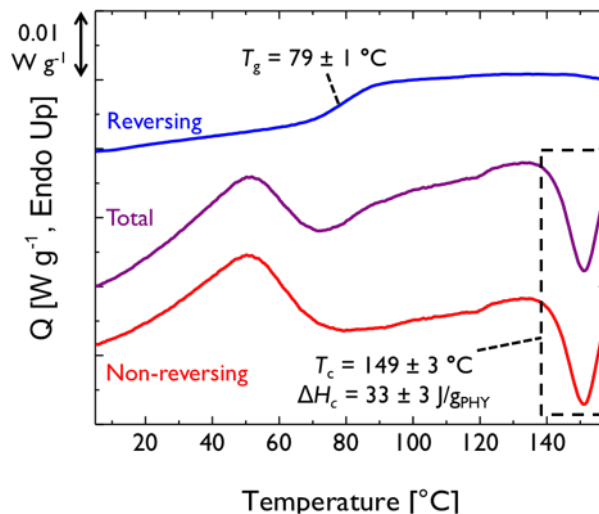


Figure C.7. Modulated DSC heat flow curves of a 25 wt% phenytoin spray-dried dispersion. Data were recorded during the first heating by using an average heating rate of 1 $^{\circ}\text{C}/\text{min}$, a temperature modulation amplitude of 1 $^{\circ}\text{C}$, and a temperature modulation period of 40 s. The reported T_g , T_c , and ΔH_c are the average of three DSC runs. Errors bars represent the standard deviations. Curves were shifted for clarity. The peak enclosed by the black box is caused by the crystallization of phenytoin.

C.5. References

^{C1}Egerton, R. F. *Electron Energy-Loss Spectroscopy in the TEM*, 3rd ed.; Springer: New York, 2011.

^{C2}Ricarte, R. G.; Lodge, T. P.; Hillmyer, M. A. *Mol. Pharm.* **2015**, *12*, 983–990.

Appendix D: Supporting Information for direct observation of nanostructures during dissolution of polymer/drug particles

D.1 Comparison of physical properties for various active pharmaceutical ingredients

Figure D.1 compares the octanol-water partition coefficient versus the free energy of crystallization (ΔG_{crys}) at 37 °C for various active pharmaceutical ingredients. ΔG_{crys} was calculated using:

$$\Delta G_{crys} = -\frac{\Delta H_f}{R} \left(\frac{T_m - T}{T_m T} \right) \quad (\text{D.1})$$

ΔH_f is the enthalpy of crystallization, T_m is the melting temperature, T is the temperature, and R is the universal gas constant. The properties for phenytoin were obtained from Ohm and Lippold,^{D1} while the attributes for all other drugs were found in Baird *et al.*^{D2}

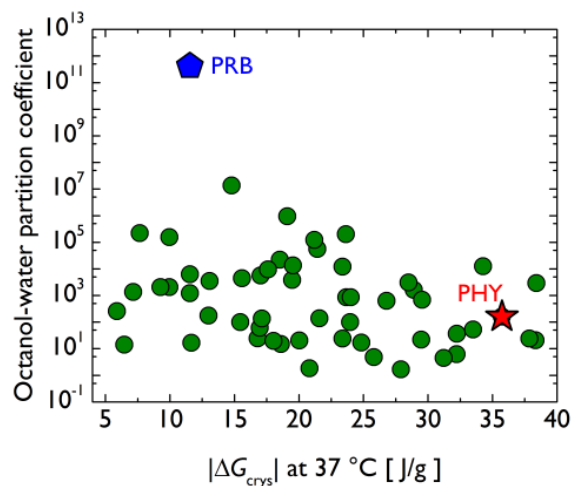


Figure D.1. Comparison of octanol-water partition coefficient versus free energy of crystallization at 37 °C for various active pharmaceutical ingredients. Probucole (PRB) and phenytoin (PHY) are highlighted.

Aqueous solubility of glassy API may be estimated by:

$$C_{glass} = C_{crys} \gamma \exp \frac{\Delta G_{crys}}{RT} \quad (D.2)$$

γ is the activity coefficient of glassy drug saturated with water (ranges from 0.5–1 for various drugs) and C_{crys} is the solubility of crystalline API.^{D3} Table D.1 lists the crystalline and expected glassy solubilities for phenytoin and probucole.

Table D.1. Crystalline and expected glassy aqueous solubility at 37°C for phenytoin and probucole.

Drug	C_{crys} [$\mu\text{g/mL}$]	C_{glass} [$\mu\text{g/mL}$]	
		$\gamma = 1$	$\gamma = 0.5$
Phenytoin	30	960	480
Probucole	4×10^{-8}	4×10^{-7}	2×10^{-7}

D.2. Solid-state characterization of phenytoin and probucol solid dispersions

All SDs studied in this work had deflated sphere or sphere morphology, as determined by scanning electron microscopy (Figures D.2 and D.3A). No crystallinity was detected by wide-angle X-ray scattering for all SDs (Figure D.4), while the modulated differential scanning calorimetry reversing heat flow revealed all SDs had only 1 glass transition temperature, suggesting drug and HPMCAS were well-mixed (Figure D.5). Methods for wide-angle X-ray scattering and modulated differential scanning calorimetry are described in Ricarte *et al.*^{D4}

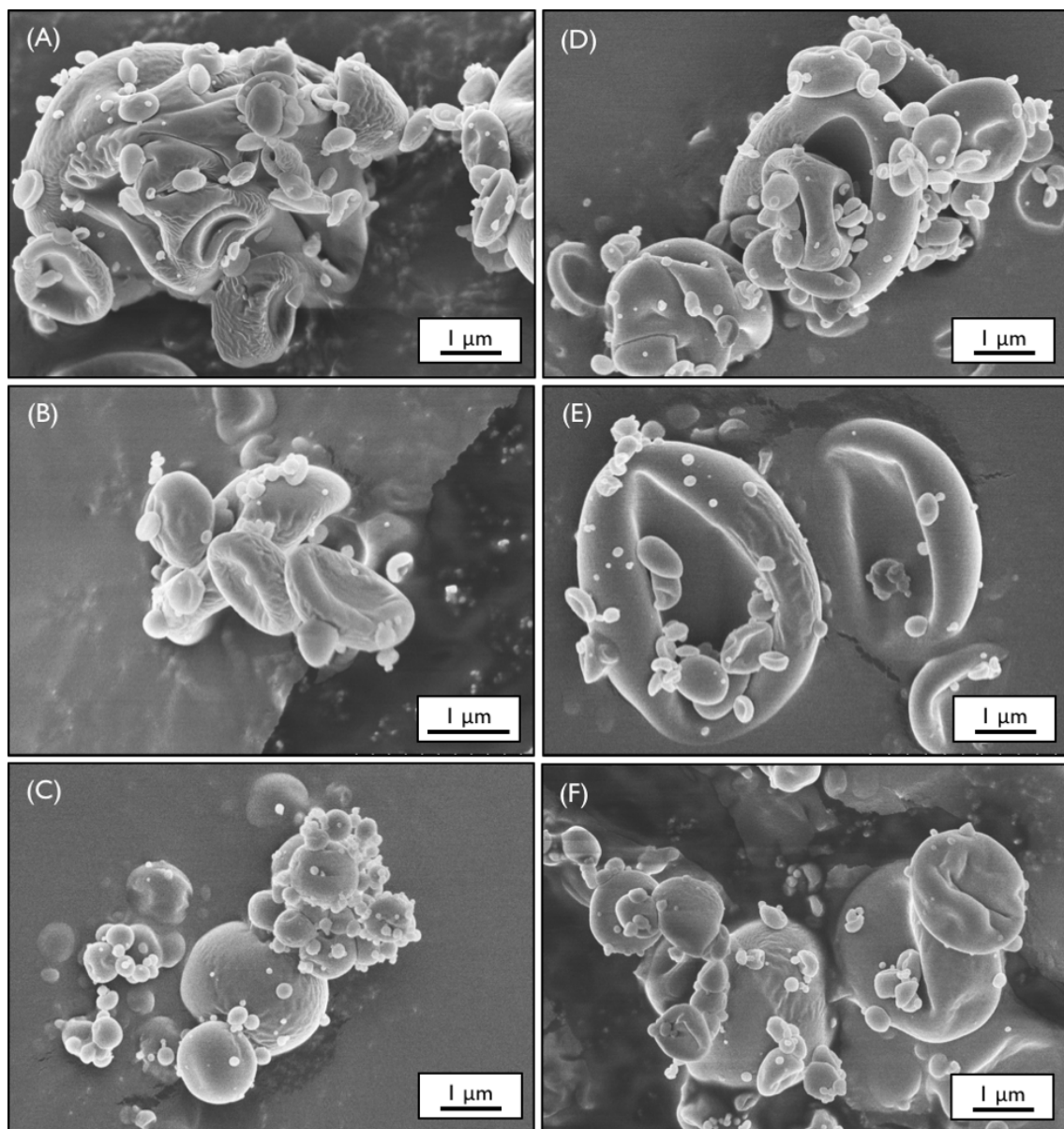


Figure D.2. Scanning electron microscopy images of (A) 10 wt% PHY, (B) 25 wt% PHY, (C) 50 wt% PHY, (D) 10 wt% PRB, (E) 25 wt% PRB, and (F) 50 wt% PRB SDSs.

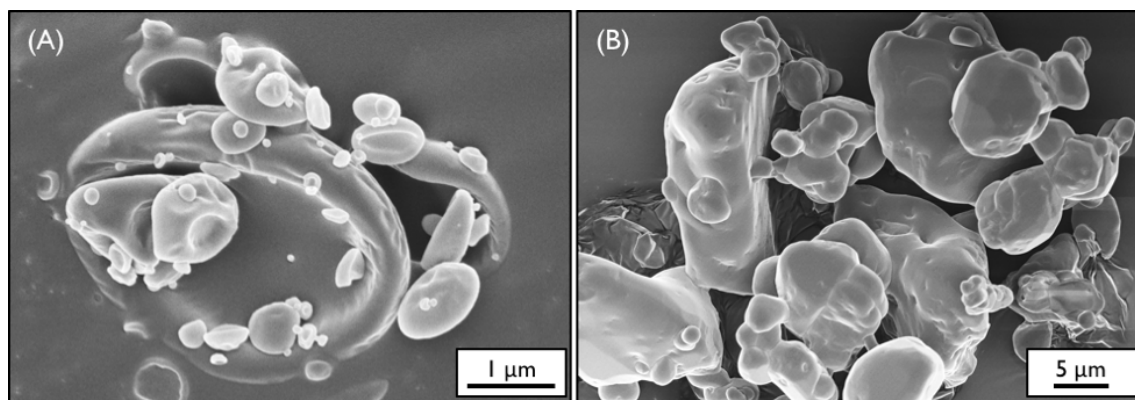


Figure D.3. Scanning electron microscopy images of (A) 3.2 wt% PHY and (B) crystalline probucol.

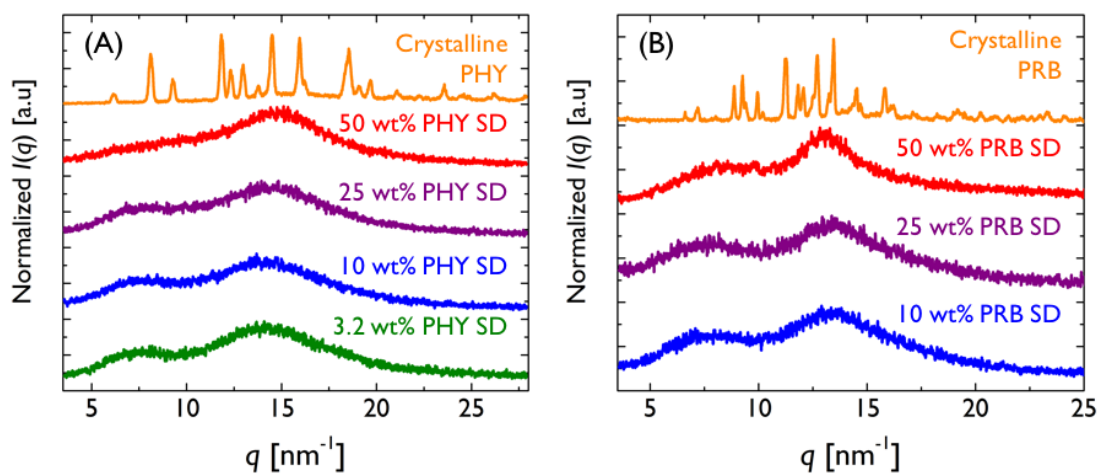


Figure D.4. Wide-angle X-ray scattering patterns of HPMCAS SDs featuring either (A) phenytoin or (B) probucol as the API. Patterns were shifted for clarity and normalized by the maximum intensity of the trace. Lack of Bragg peaks in SD patterns suggests API is amorphous.

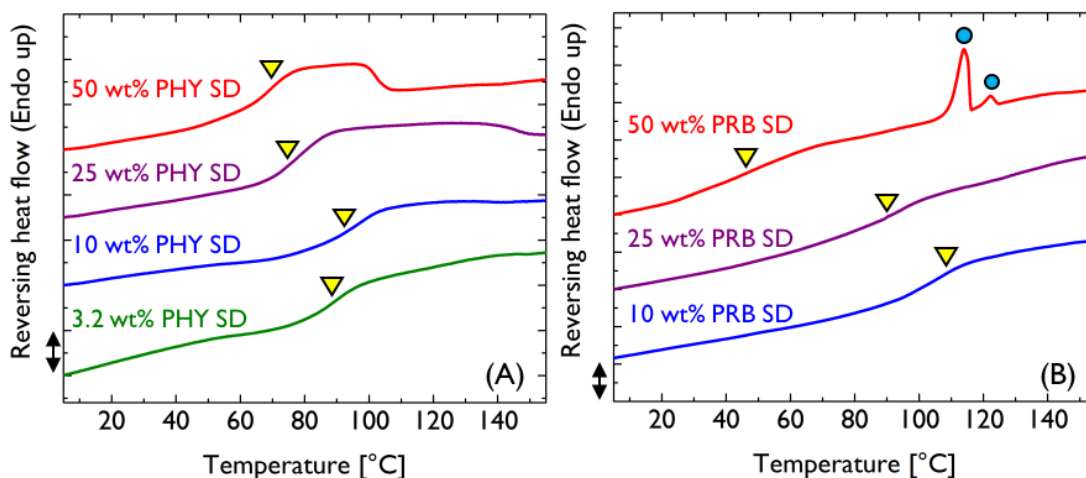


Figure D.5. Modulated differential scanning calorimetry reversing heat flow curves of HPMCAS SDs containing either (A) phenytoin and (B) probucol as the API. Data were vertically shifted for clarity. Double-headed arrows represent an increment of 5 mW/g. The triangles indicate the glass transition temperatures, while the circles mark artifacts caused by melting of probucol crystals that formed during heating.

D.3. PHY and PRB SDs dissolved in HPMCAS solutions

To achieve better understanding of nanoparticle formation, SDs featuring 25 wt% of either PHY or PRB were dissolved in PBS solutions containing 6 mg/mL of HPMCAS. Under these circumstances, PHY and PRB SDs exhibited very different behaviors. The 25 wt% PHY SD dissolved in the HPMCAS solution achieved a plateau similar to 10 wt% PHY SD, albeit at a slightly lower concentration (Figure D.6A). However, cryo-TEM showed that the dissolution media at early times contained both ellipsoid nanoparticles and branched worm-like structures (Figure D.6B). The ellipsoids had a volumetric average radius of 25 ± 7 nm, larger than the nanoparticles in the pure PBS solvent, and the worms had an arithmetic average radius of 12 ± 3 nm and lengths that spanned from 100–5000 nm. The appearance of the worms is possibly related to the semi-flexible nature of HPMCAS,⁵ but more experiments are needed to fully understand their origin. After 360 min, both ellipsoids and worms disappear from solution (Figure D.6C). SAXS of the dissolution media also confirm the metastable nature of the structures, but the complexity of the solution prohibits quantitative analysis (Figure D.7A). Nevertheless, sensitivity of

shape to dissolution solvent reveals that the nanoparticle nucleation in PHY SD dissolution media may occur both during the release of drug from the SD particles and after the drug is already dissolved in solution. Conversely, the 25 wt% PRB SD dissolved in the HPMCAS solution achieves an almost identical dissolution profile and nanostructure evolution as the SD dissolved in pure PBS (Figures D.6E). The minimal influence of the dissolution solvent implies that nanoparticle nucleation in PRB SD dissolution media only occurs as drug is released from the SD particles. Conceivably, the extreme hydrophobicity of PRB induced nanoparticles to form once the glassy SD particles imbibed water. The contrasting behavior of PHY and PRB SDs shows that API physical properties dictate the nucleation and growth kinetics of the nanoparticles.

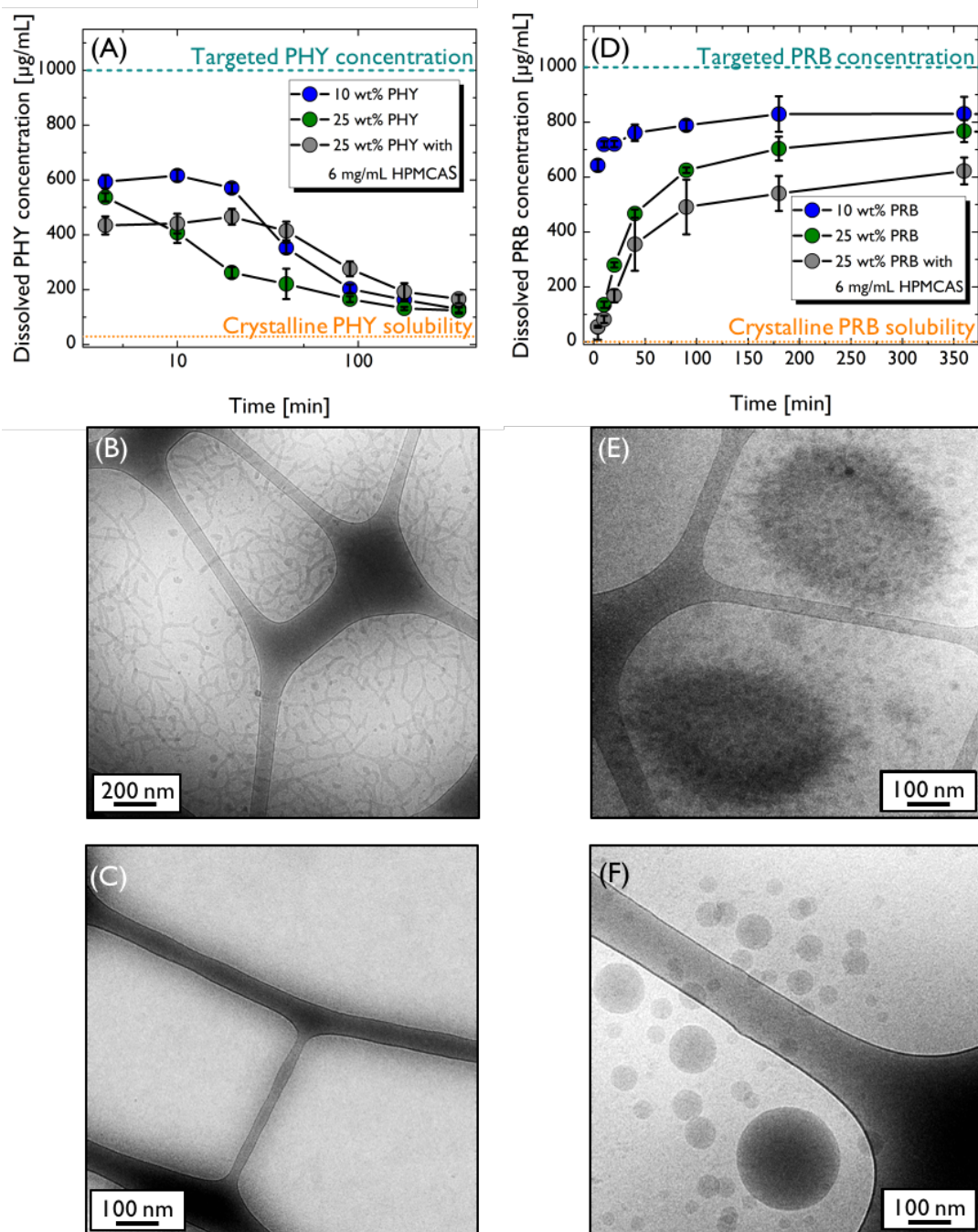


Figure D.6. (A) Dissolution profile 25 wt% phenytoin SD dissolved in HPMCAS solution compared with 10 and 25 wt% phenytoin SDs dissolved in PBS (same data as Figure 3A). (B) Cryo-TEM images of 25 wt% phenytoin SD dissolved in HPMCAS solution at 10 min and (C) 360 min. (D) Dissolution profile 25 wt% probucol SD dissolved in HPMCAS solution compared with 10 and 25 wt% probucol SDs dissolved in PBS (same data as Figure 6A). (E) Cryo-TEM images of 25 wt% probucol SD dissolved in HPMCAS solution at 4 min and (F) 360 min.

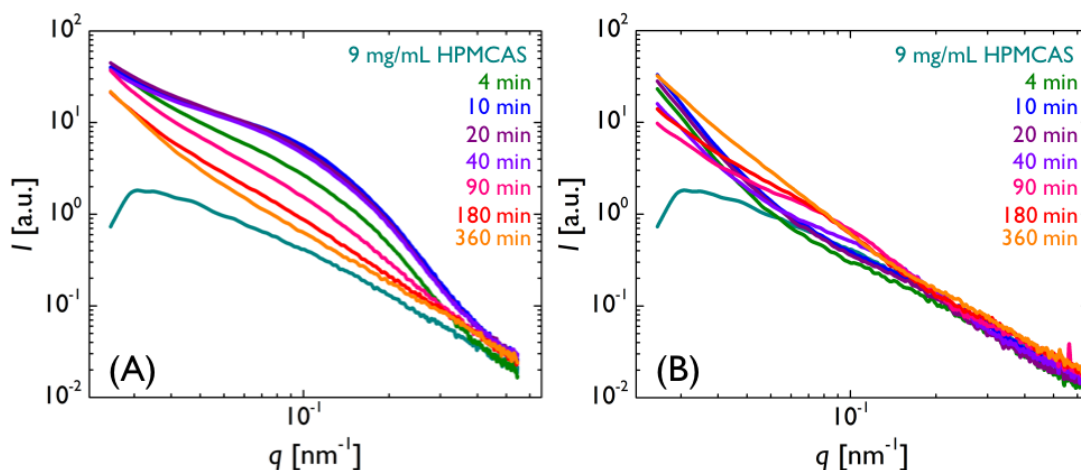


Figure D.7. SAXS patterns of (A) 25 wt% PHY SD and (B) 25 wt% PRB SD dissolved in 6 mg/mL HPMCAS solution.

D.4. Dissolution of poly(*N*-isopropylacrylamide-*co*-*N,N*-dimethylacrylamide) SDs

Poly(*N*-isopropylacrylamide-*co*-*N,N*-dimethylacrylamide) (poly(NIPAm-*co*-DMA)) is a polymer that was recently identified as an excellent excipient for stabilizing phenytoin in aqueous solution. Figure D.8A features the dissolution profile of a SD that is 90 wt% poly(NIPAm-*co*-DMA) and 10 wt% phenytoin.^{D6} Figure D.8B features SAXS patterns of the 10 wt% SD dissolution media at each time point. The transformation of the SAXS patterns strongly suggests that the dissolution profile of the SD directly correlates with nanostructure evolution in solution. More experiments are needed to identify the structures that form in the dissolution media.

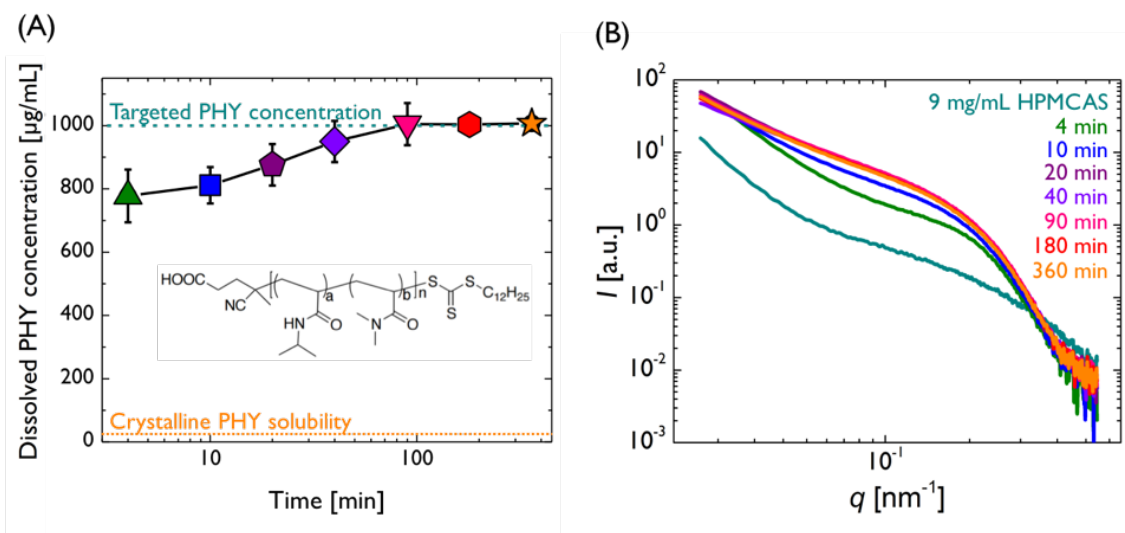


Figure D.8. (A) Dissolution profile of a 10 wt% PHY and 90 wt% poly(NIPAm-co-DMA) SD. Molecular structure of poly(NIPAm-co-DMA) is displayed as the inset. (B) SAXS patterns of dissolution media at various time points.

D.5. Small-angle neutron scattering of HPMCAS solutions

Small-angle neutron scattering (SANS) was used to probe the structure of HPMCAS in various solvents. SANS measurements were executed at the National Institute for Science and Technology on the NG7 30 m SANS instrument. The accessible q range was $0.009\text{--}3\text{ nm}^{-1}$. The contribution of incoherent scattering from solvent was removed from the patterns. Figure D.8 is a SANS pattern of a 9 mg/mL HPMCAS solution with deuterated phosphate buffered saline at $37\text{ }^{\circ}\text{C}$ as the solvent. Similar to the SAXS patterns of HPMCAS solutions, the SANS pattern exhibits a power-law scaling of -1.2 and lacks obvious Rayleigh and Guinier regimes. SANS patterns for solutions featuring either phosphate buffered saline or tetrahydrofuran at $25\text{ }^{\circ}\text{C}$ as solvent are identical to the aforementioned pattern, suggesting the solvent identity has minimal effect on the polymer structure in solution. More experiments are needed to fully understand the behavior of HPMCAS in solution.

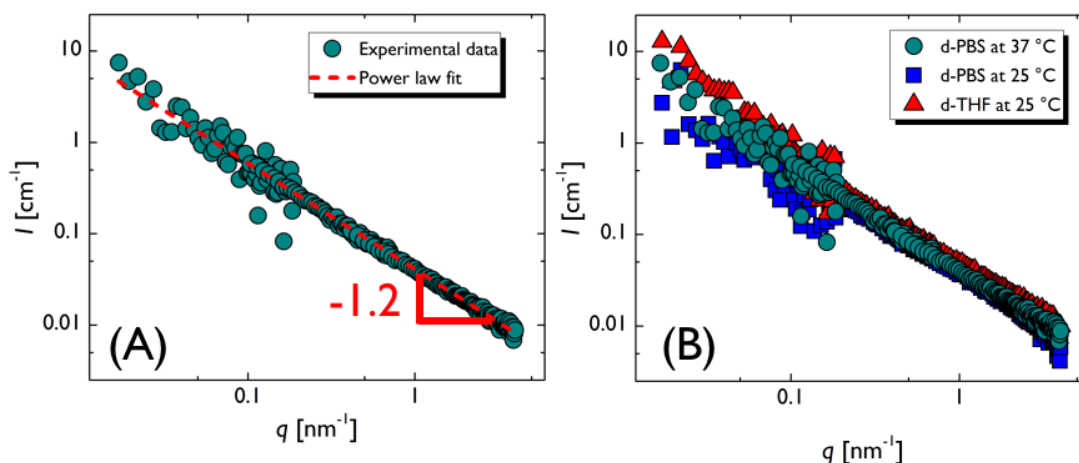


Figure D.9. (A) Experimental SANS pattern and power law fit of 9 mg/mL HPMCAS in deuterated phosphate buffered saline (d-PBS). (B) Comparison of experimental SANS patterns of 9 mg/mL HPMCAS solutions featuring either deuterated phosphate buffer or tetrahydrofuran as the solvent.

D.6. References

- ^{D1}Ohm, A.; B. C. Lippold. *Int. J. Pharm. Tech. Prod. Mfg.* **1985**, 6, 1.
- ^{D2}Baird, J. A.; Van Eerdenbrugh, B.; Taylor, L. S. *J. Pharm. Sci.* **2010**, 99, 3787–3806.
- ^{D3}Murdande, S. B.; Pikal, M. J.; Shanker, R. M.; Bogner, R. H. *J. Pharm. Sci.* **2010**, 99, 1254–1264.
- ^{D4}Ricarte, R. G.; Lodge, T. P.; Hillmyer, M. A. *Mol. Pharm.* **2015**, 12, 983–990.
- ^{D5}Burchard, W. Solubility and Solution Structure of Cellulose Derivatives. *Cellulose* **2003**, 10, 213–225.
- ^{D6}Ting, J. M.; Tale, S.; Purchel, A. A.; Jones, S. D.; Widanapathirana, L.; Tolstyka, Z. P.; Guo, L.; Guillaudeu, S. J.; Bates, F. S.; Reineke, T. M. *ACS Cent. Sci.* **2016**, 2, 748–755.